Nonequilibrium phase transitions in open quantum systems

열린 양자계에서의 비평형 상전이 현상

2021년 2월

서울대학교 대학원

물리·천문학부

조 민 재

이학박사학위논문

Nonequilibrium phase transitions in open quantum systems

열린 양자계에서의 비평형 상전이 현상

2021년 2월

서울대학교 대학원

물리·천문학부

조 민 재

Nonequilibrium phase transitions in open quantum systems

열린 양자계에서의 비평형 상전이 현상
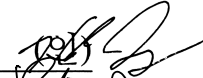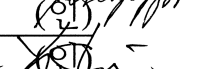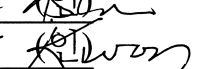
지도교수 강 병 남

이 논문을 이학박사 학위논문으로 제출함

2021년 2월
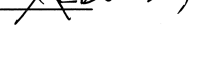
서울대학교 대학원

물리·천문학부

조 민 재

조민재의 박사 학위논문을 인준함

2020년 12월

위 원 장: 정 현 석   (인)

부위원장: 강 병 남   (인)

위   원: 백 용 주   (인)

위   원: 신 용 일   (인)

위   원: 천 천 안   (인)

Abstract

Nonequilibrium phase transitions in open quantum systems

Minjae Jo

Department of Physics and Astronomy

The Graduate School

Seoul National University

Recent advances in cold atomic physics offer a platform to explore non-equilibrium phase transition in open quantum many-body systems. Such nonequilibrium critical phenomena originate from the competition between quantum fluctuations (coherent Hamiltonian) and classical fluctuations (incoherent dissipation). In this regard, the fundamental question arises as to whether the system exhibits novel universal behavior in which the quantum fluctuations are relevant. If it does not exhibit novel universality, it may reduce to the classical universality, and is described as so-called "quantum-to-classical mapping". Many studies have been devoted to this question, but it has not been fully understood yet.

In this dissertation, we aim to investigate this question by considering the many-body physics of the quantum contact process (QCP), which is a generalization of the classical contact process belonging to the directed percolation (DP) class. The DP class is the most robust and well-studied class in classical nonequilibrium systems. The QCP has additional quantum processes to the DP class, and the quantum fluctuations may affect the universality class. Moreover, the QCP is experimentally feasible in ultra-cold Rydberg atomic systems.

Specifically, this dissertation presents recent studies related to critical phenomena of the QCP. Firstly, motivated by the Rydberg atomic experiment with the dipole-dipole interaction, we investigate QCP with the long-range interactions using the semi-classical approach. Generally, a system with long-range interaction can exhibit different universality from the corresponding system with short-range interaction. In this regard, we find that the novel classical universality is obtained for the regime where the long-range interaction is relevant, and it is called the "long-range tricritical DP class". For the regime where the long-range interaction is irrelevant, the mean-field phase diagram of our long-range model corresponds to that of the ordinary QCP. Next, we study the low-dimensional physics of the long-range tricritical directed percolation class using renormalization group theory and Monte Carlo simulation. Depending on the strength of the long-range interaction, we find that the universality class is changed from the mean-field long-range tricritical DP to ordinary tricritical DP.

To investigate the one-dimensional and two-dimensional QCP, we use machine learning and quantum simulations such as quantum jump Monte Carlo simulation and tensor network method. We find that in one dimension, there exists the crossover region, along which the critical exponents continuously varies from a quantum DP to the DP class. This indicates that the quantum coherent process is relevant to the critical phenomena. We also propose an experimental setting to investigate the crossover region.

In addition, we investigate the mean-field behavior of dissipative quantum systems using the permutational symmetry of fully-connected graph. Specifically, we consider the dissipative transverse Ising (DTI) model, driven-dissipative XY model, and QCP. We find that the DTI model exhibits a continuous phase transition for the entire parameter space, and the driven-dissipative XY model shows a discontinuous phase transition, contrary to the results from Keldysh formalism. Instead, those correspond to the fluctuationless MF approach. In addition, the phase transitions of QCP

shows that the transition line and universality class correspond to the semi-classical approach, whereas there exists a crossover region analogous to the one-dimensional QCP. Finally, we present the phase diagram of the QCP including the mean-field and low-dimensional cases.

Keywords: Open quantum systems, Nonequilibrium phase transition, Dissipative phase transitions, Quantum contact process, Semi-classical field theory, Machine learning, Finite-size scaling analysis

Student number: 2015-20353

Contents

List of Figures

List of Tables

Chapter 1

Introduction

Understanding the many-body systems has been one of the major challenges in theoretical physics. As in the Andersons's [1] "more is different", a large coupled degrees of freedom can behave completely different way, which cannot be understood sorely by the laws governing their microscopic components. Nonetheless, the many-body systems with different microscopic components can exhibit identical physics. This can be understood by the concept of the universality in which macroscopic physics does not depend on the microscopic details, but the symmetry, range of interactions, and spatial dimension. Based on the concept of universality, many-body systems are investigated for various classical and quantum systems.

One of the simplest examples is the classical Ising model. In the Ising model, the ferromagnetic system contains either a down or an up spin at each site of a d-dimensional lattice. The nearest-neighbor interaction denoted as J tends to align to the same direction; and temperature denoted as T makes the thermal fluctuations in spin states. When $T/J \ll 1$, the interaction dominates the thermal fluctuations, and all spin states tend to align in the same direction. This state is called the ferromagnetic phase. Otherwise, when $T/J \gg 1$, the thermal fluctuations dominate the interaction, and all spin states are random. This state is called the paramagnetic phase. Increasing the parameter T/J from a low temperature in the ferromagnetic phase, the spin alignment gets gradually randomized by the thermal fluctuations, and eventually becomes the paramagnetic phase at the critical point, Curie temperature T_c. Thus, the phase transition occurs between two phases. At the critical point T_c, the observables such

as the degree of spins alignment significantly fluctuate and diverge with power-law singularities. The exponent of the singularity of physical observables is described by critical exponents, and the complete set of the critical exponents forms the universality class. The critical phenomena of many-body systems can be categorized into universality classes and members of the same class have identical critical behavior. Examples include the liquid-gas transition and the (uniaxial) ferromagnetic-paramagnetic phase transition belonging to the 3D Ising class [2]. The universality classes derived through theoretical methods such as renormalization group approach [3] and Monte Carlo simulations are in good agreement with those found in experiments.

Naturally, interest turned to the closed quantum many-body systems, i.e. phase transitions are driven by quantum fluctuations rather than thermal fluctuations. For instance, the quantum Ising model. At zero temperature, the quantum phase transition occurs from the ferromagnetic phase to the paramagnetic phase depending on the strength of the transverse field. At the quantum critical point, the critical phenomena originate from the quantum fluctuations in contrast to the classical Ising model. Hence, the critical may be expected to behave differently from that of the classical model. Specifically, for the $1d$ quantum Ising model, quantum fluctuations affect the universal behavior and the critical exponents are different with $1d$ Ising exponents. Instead, the critical exponents of the $1d$ transverse Ising model correspond to the $2d$ Ising exponents. Thus, there exists so-called a quantum-to-classical mapping, where the d-dimensional quantum model corresponds to (d+1)-dimensional classical model. This concept was proposed based on the field-theoretical argument that imaginary time in the quantum system acts as an additional dimension in the corresponding classical system. By a quantum-to-classical mapping [4], many models in closed quantum systems are explained by the classical universality.

Meanwhile, recent experimental advances in open quantum systems opened the opportunity to realize the models showing the nonequilibrium phase transitions. In open quantum systems, the phase transition arises from the competition between co-

herent Hamiltonian dynamics and the incoherent dissipation process. These systems have intensely debated [5–17] whether the role of quantum fluctuations leads to a novel universality class [7, 17], or under what condition the universality class is classically described [9, 10, 12]. In this dissertation, we aim to investigate the possibility of the novel universality classes in open quantum systems. To be more specific, we consider the collective phenomena of the quantum contact process motivated the ultra-cold Rydberg atomic experiment. In what follows, we will present the motivation of the quantum contact process. To this end, we briefly introduce the classical contact process model, the experimental realization of the classical contact process, and the quantum contact process.

1.1 Classical contact process model

In nonequilibrium systems, the most robust universality class is the directed percolation (DP) universality, class. In other words, many models belong to the DP class; the examples are the Domany-Kinzel cellular automata [18], branching annihilating random walks with an odd number of offsprings [19], and the contact process model [20]. Among these models, the most well-known and simplest model for directed percolation (DP) universality class is the contact process. In the contact process, each element of the system is in an active or inactive state, and its state changes according to the following rules.

  i) Decay: an active particle becomes inactive at a rate of γ.

  ii) Branching: an inactive particle becomes active at a rate of κ when it contacts a neighboring active particle.

Depending on rates for decay and branching, the active sites may either spread over the whole system or disappear after some time. Once the inactive site becomes extinct where the dynamics become trapped in a nonfluctuating so-called "absorbing state". The system can enter this state, but cannot leave it. Thus, a detailed balance is violated.

If κ/γ is small, the system falls into an absorbing state. Otherwise, it is in an active state. Thus the system undergoes a continuous phase transition with the DP class (See Sec. 2 for more theoretical details).

Although the DP class is theoretically well established, the experimental realization of DP behavior has been elusive for two decades. It was only recently that the contact process model is realized using a cold Rydberg atomic experiment. This experiment will be introduced in the next section.

1.2　Rydberg atomic experiment

Let us consider the Rydberg atom represented by two spin states, $|\downarrow\rangle$ and $|\uparrow\rangle$ which are the eigenstates of the Pauli matrix of the z direction, where the up spin state indicates the Rydberg excitation. We start with the Hamiltonian in the rotating-wave approximation of the N coupled Rydberg atoms on a lattice as follows:

$$\hat{H}_R = \Omega \sum_{\ell}^{N} \hat{\sigma}_{\ell}^x + \Delta \sum_{\ell}^{N} \hat{n}_{\ell} + \sum_{\ell \neq m} \frac{V_{\ell m}}{2} \hat{n}_{\ell} \hat{n}_m, \tag{1.1}$$

where Ω and Δ are the Rabi frequency induced by the external laser and detuning strength, respectively. Here $\hat{\sigma}_{\ell}^i$ denotes the Pauli matrix, where the superscript and subscript stand for the spin axis and site index, respectively, and $\hat{n}_{\ell}$ means the number operator for the up spin at the ℓth site. Using the ladder operators $\hat{\sigma}^+ = |\uparrow\rangle\langle\downarrow|$ and $\hat{\sigma}^- = |\downarrow\rangle\langle\uparrow|$, we express the Pauli matrix of the x direction as $\hat{\sigma}^x = \hat{\sigma}^+ + \hat{\sigma}^-$ and with the projection $\hat{n} = |\uparrow\rangle\langle\uparrow|$. The third term in the r.h.s in Eq. (1.1) describes the interaction between up spins, where $V_{\ell m}$ is a power-law decaying function of the distance,

$$V_{\ell m} = \frac{C_p}{|\mathbf{x}_l - \mathbf{x}_m|^p}, \tag{1.2}$$

where C_p is the dispersion coefficient [21] and $\mathbf{x}_l$ is the position of the lth site. Note that p characterizes the interaction [21]; $p = 3$ for the dipole interaction associated

with the *d*-orbital excitation, and 6 for the van der Waals interaction with the *s*-orbital excitation. For the case of $p = 6$ in Eq. (1.2), the interaction is fast decaying in distance so that the dynamics is effectively dominated by the nearest-neighbor interaction [22].

In the limit of $\Delta \gg \Omega, |V_{\ell m}|$, the Rabi oscillation is suppressed due to the large energy gap between up and down spin states, implying that a spin configuration, for an example $|a\rangle = |\cdots \downarrow\downarrow\uparrow \cdots\rangle$ may be approximately an eigenstate of H_R. Therefore, given an initial spin configuration, there is no fluctuation in time. However, if $V_{\ell m} = -\Delta$ for the nearest-neighbor pair ℓ and m and the ℓth spin is up, the mth spin can fluctuate with Ω. This is a so-called antiblockade mechanism in which an excited atom facilitates Rabi oscillation at the nearest-neighbor atom. This is reminiscent of the branching process in the CP. In fact, there is an additional process called the co-agulation process in which an excited atom facilitates the nearest-neighbor atom from up spin to down spin. Although this process do not belong to the CP model, this is not a problem to realize the DP class because the coagulation process is irrelevant, i.e. it does not affect the universal behavior. The effective Hamiltonian can be described in one dimension:

$$\hat{H}_{\text{eff}} = \Omega \sum_{\ell} \hat{P}_{\ell} \hat{\sigma}_{\ell}^{x}, \tag{1.3}$$

where the projection operator is given by $\hat{P} = \hat{n}_{\ell-1} + \hat{n}_{\ell+1} - 2\hat{n}_{\ell-1}\hat{n}_{\ell+1}$. We are interested near the critical point, where the low-density limit leads to $\hat{P} \approx \hat{n}_{\ell-1} + \hat{n}_{\ell+1}$. In order to realize the classical contact process, the coherence should be suppressed. This is achieved via the strong dephasing rate denoted as Γ. Additionally, the decay in the classical contact process is implemented by the radiative decay from $|\uparrow\rangle$ to $|\downarrow\rangle$ with zero-temperature heat bath with a rate γ. In the strong dephasing limit, it was revealed that the coherent dynamics can be neglected so that the effective Hamiltonian in Eq. (1.3) is effectively classicalized and reduces as the following two Lindblad

operators [23].

$$\hat{L}_\ell^{(b)} = \sqrt{\kappa}\hat{P}_\ell\hat{\sigma}_\ell^+ \, , \qquad \hat{L}_\ell^{(c)} = \sqrt{\kappa}\hat{P}_\ell\hat{\sigma}_\ell^- \, , \quad \hat{L}_\ell^{(d)} = \sqrt{\gamma}\hat{\sigma}_\ell^- \qquad (1.4)$$

where $\kappa = 4\Omega^2/\Gamma$. The derivation of the strong dephasing limit is described using superoperator formalism in Appendix A.1. Thus the classical contact process is theoretically derived as well as experimentally realized [24].

Motivated by this experimental set-up, the classical contact process in Eq. (1.4) can be generalized by adding the coherent branching and coagulation Eq. (1.3). Then, this model is called the quantum contact process [25, 26], which offers the simple model exhibiting nonequilibrium phase transitions in open quantum systems.

1.3 Quantum contact process

We consider a one-dimensional quantum spin chain with a periodic boundary condition, where each state of a site (active or inactive) represents the up or down spin state, denoted as $|\uparrow\rangle$ or $|\downarrow\rangle$. The time evolution of the density matrix $\hat{\rho}$ is described by the Lindblad equation, which consists of the Hamiltonian and dissipative terms [27]:

$$\partial_t\hat{\rho} = -\mathrm{i}\left[\hat{H}_S, \hat{\rho}\right] + \sum_{a=d,b,c}\sum_{\ell=1}^{N}\left[\hat{L}_\ell^{(a)}\hat{\rho}\hat{L}_\ell^{(a)\dagger} - \frac{1}{2}\left\{\hat{L}_\ell^{(a)\dagger}\hat{L}_\ell^{(a)}, \hat{\rho}\right\}\right]. \qquad (1.5)$$

The Hamiltonian $\hat{H}_S$, which governs the branching and coagulation processes and represents coherent interactions, is expressed as

$$\hat{H}_S = \omega\sum_{\ell=1}^{N}\left[\left(\hat{n}_{\ell-1} + \hat{n}_{\ell+1}\right)\hat{\sigma}_\ell^x\right]. \qquad (1.6)$$

The Lindblad decay, branching, and coagulation operators are given by

$$\hat{L}_\ell^{(d)} = \sqrt{\gamma}\,\hat{\sigma}_\ell^- \,, \tag{1.7}$$

$$\hat{L}_\ell^{(b)} = \sqrt{\kappa}\,(\hat{n}_{\ell-1} + \hat{n}_{\ell+1})\hat{\sigma}_\ell^+ \,, \tag{1.8}$$

$$\hat{L}_\ell^{(c)} = \sqrt{\kappa}\,(\hat{n}_{\ell-1} + \hat{n}_{\ell+1})\hat{\sigma}_\ell^- \,, \tag{1.9}$$

respectively.

Quantum branching and coagulation occur at a rate of ω, and the corresponding classical processes occur at a rate of κ. When $\omega \to 0$, the model is reduced to the classical CP, which belongs to the DP class. When ω is small, inactive particles become more abundant with time, and eventually, the system is fully occupied by inactive particles. Thus, the system is no longer dynamic and falls into an absorbing state, which is represented by $\hat{\rho}_{ab} = |\downarrow \cdots \downarrow\rangle\langle\downarrow \cdots \downarrow|$. When ω is large, the system remains in an active state with a finite density of active particles. Thus, the QCP exhibits a phase transition from an active to an absorbing state as ω is decreased.

1.4 Overview of thesis

This thesis presents recent studies of the critical behavior of the open quantum many-body systems. It focuses on the analytical and numerical methods to investigate the universality class in open quantum many-body systems. Specifically, we deal with the quantum contact process by semi-classical field-theoretic calculations, classical and quantum Monte-Carlo simulation, and machine learning methods. Furthermore, we cover the numerical technique to investigate the mean-field beahvior in large qubit size.

In chapter 2, we provide background physics of preliminary knowledge in the classical field theory [28–30]. The readers already familiar with the classical field theory may skip this chapter without any loss in continuity. The absorbing state phase transition of the classical contact process is presented with the microscopic rules. More-

over, the MSRJD field-theoretical approach is presented from the classical Langevin equation. Then, mean-field critical exponents by scaling theory are obtained. Next, the renormalization group approach to obtain the critical exponents below the upper critical dimension will be introduced. Finally, we apply the field-theoretic approach to the long-range contact process model and the tricritical contact process model. We hope this is helpful to understand the chapter 3.

In chapter 3, we consider a quantum spin model with a long-range QCP [31], where the branching and coagulation processes are allowed not only for the nearest-neighbor pairs but also for long-distance pairs, coherently and incoherently. Using the semi-classical approach, we show that the mean-field phase diagram of our long-range model is similar to that of the nearest-neighbor QCP [25, 26], where the continuous (discontinuous) transition is found in the weak (strong) quantum regime. However, at the tricritical point, we find a new universality class, which was neither that of the QCP at the tricritical point nor that of the classical directed percolation model with long-range interactions. Implementation of the long-range QCP using interacting cold gases is discussed.

In chapter 4, we deeply study the new universality class obtained in chapter 3. To this end, we extend the tricritical CP model to one with long-range interaction [32]. In particular, we investigate the properties of the long-range tricritical DP (LTDP) class below the upper critical dimension. We numerically obtain a set of critical exponents in the LTDP class. Finally, we construct a diagram of universality classes.

In chapter 5, we present the quantum simulation methods. Firstly, the exact numerical method for open quantum systems called quantum jump Monte Carlo simulation [33] is introduced. This approach is able to simulate up to the system size $N \sim 25$. Secondly, the tensor network approach [34, 35] based on the matrix product state and the time-evolving block decimation is presented. This method approximately considers the low-entangled state so that it is able to simulate up to the system size $N \sim 100$. These methods will be used in the next chapter.

In chapter 6, we investigate one and two-dimensional quantum contact process using quantum simulations [36]. We find the crossover from a quantum to a classical absorbing phase transition arising in the one-dimensional quantum contact process. We find that in one dimension, when the QCP starts from a homogeneous state with all active sites, there exists a critical line in the region $0 \leq \kappa < \kappa_*$, along which the exponent α associated with the density of active sites decreases continuously from a quantum to the classical directed percolation (DP) value. This behavior implies that the quantum coherent effect still remains to some extent in the region near $\kappa = 0$. This anomalous crossover behavior allows us to measure the display between the quantum DP and classical DP effect using the Rydberg atom experiment. However, when the QCP starts from a heterogeneous state with all inactive sites but one active site in one dimension, all critical exponents have the classical DP values for $\kappa \geq 0$. In two dimensions, the anomalous crossover behavior does not occur and the classical DP behavior appears in the entire region of $\kappa \geq 0$ regardless of initial configurations. The neural network machine learning technique is used to identify the critical line and to determine the correlation length exponent. Numerical simulations using the quantum jump Monte Carlo technique and the tensor network method are performed to determine all the other critical exponents of the QCP.

In chapter 8, we investigate the mean-field behavior of dissipative quantum systems using the permutational symmetry of fully-connected graph [37]. Recently, the phase transitions and critical phenomena of the dissipative quantum systems were analytically investigated via various theoretical approaches. Numerical verifications are crucial for the phenomena, because sometimes theoretical make predictions that are contradictory to each other. However, numerical verifications are still missing due to the exponential computational complexity of the quantum systems. Here, we use the exact numerical solution to unveil the mean-field (MF) behavior of the dissipative transverse Ising (DTI) model, driven-dissipative XY model, and quantum contact process (QCP). We find that the DTI model exhibits a continuous phase transition for the

9

entire parameter space, and the driven-dissipative XY model shows a discontinuous phase transition, contrary to the results from Keldysh formalism. Instead, those correspond to the fluctuationless MF approach. The phase transitions of QCP shows that the transition line and universality class correspond to the semi-classical approach; however, we discover a crossover region analogous to the one-dimensional QCP, which is not predicted by theoretical methods. Finally, we identify various advantages of the exact numerical method and compare it with quantum jump Monte Carlo simulation.

Conclusions are followed in Chapter 8.

Chapter 2

Nonequilibrium phase transitions in classical systems

In this chapter, we briefly provide the classical field theory, and the readers already familiar with the concept may skip this chapter. For the classical field theory, we recommend the excellent review article [28] and books [29, 30].

2.1 Introduction

Field-theoretic approaches and the *renormalization group* (RG) method have had a huge contribution in our understanding of the universal critical behaviors that emerge near critical points. In this chapter, we describe the collective behaviors of systems, which undergoes a continuous *nonequilibrium phase transition* with displaying generic scale invariance. We then deal with capturing the stochastic dynamics of the long-wavelength ($q \to 0$) modes of the order parameter, any conserved quantities, and additional relevant variables.

Specifically, we describe how a representation in terms of a field-theoretic action can be obtained for general non-linear Langevin stochastic differential equations. We will then demonstrate how the perturbative RG can be employed to derive the asymptotic scaling laws in classical stochastic systems. Moreover, we obtain the upper critical dimension d_c (for dimensions $d \leq d_c$, low-dimensional fluctuations strongly affect the universal properties) and systematically compute the critical exponents.

In case of the real-space RG, the *RG transformation* consists of the elimination of

microscopic degrees of freedom (*coarse-graining*) and *rescaling*. This transformation changes the system's properties away from the critical point, where the system exhibits only finite characteristic length scales. However, at critical point there are no finite correlation lengths and thus the properties of the system remain unaffected by the rescaling procedure (i.e. we look the system larger and larger). In this way, critical point corresponds to a fixed point of the renormalization transformation.

The *universality* does not depend on the microscopic details but specified by the three factors: the *symmetry*, *range of the interactions*, and its spatial dimension. In Sec. 2.2, we review the well-established Martin–Siggia–Rose–Janssen–de Dominicis (MSRJD) approach, and then we apply this theory into some systems such as the contact process (CP) [Sec. 2.3], the CP with *long-range interactions* [Sec. 3.4], and the *tricritical* CP [Sec. 2.5]. Apparently, those three models have different universality classes with CP since long-ranged CP (tricritical CP) is different the range of the interactions (symmetry) from CP.

2.2 MSRJD field theory

In this section, we consider Martin–Siggia–Rose–Janssen–de Dominicis (MSRJD) approach, which is the field-theoretic representation of Langevin equations. Let us begin our discussion by constructing a path integral reformulation of Langevin equations. Equations of motion of nonequilibrium system are represented by Langevin equation, which is given by

$$\partial_t n = F[n] + \xi \,, \tag{2.1}$$

where $n = n(\boldsymbol{x},t)$ is a time-dependent random variable, $F[n] = F[n(\boldsymbol{x},t)]$ a function, and $\xi = \xi(\boldsymbol{x},t)$ a noise term. Gaussian noise field $\xi(\boldsymbol{x},t)$, which is defined by its cor-

relations

$$\langle \xi(\boldsymbol{x},t)\xi(\boldsymbol{x}',t')\rangle = \Gamma N[n(\boldsymbol{x},t)]\delta^d(\boldsymbol{x}-\boldsymbol{x}')\delta(t-t'). \tag{2.2}$$

$N[n(\boldsymbol{x},t)]$ can be a constant for Brownian motion or $n(\boldsymbol{x},t)$ for directed percolation. Generally, $N[n] \propto \mathcal{O}(n)$ is termed the multiplicative noise. Partition function is defined as the functional integral over all realizations of field $n(\boldsymbol{x},t)$ and the noise $\xi(\boldsymbol{x},t)$ which satisfy the Langevin equation. Then, partition function may then be formally represented as

$$Z = \int Dn \langle \delta(\partial_t n - F[n] - \xi)\rangle_\xi = \int Dn \int D\xi P(\xi)\delta(\partial_t n - F[n] - \xi), \tag{2.3}$$

where Jacobian is a constant in Ito discretization (see Appendix B.1). Representing the δ-function in Eq. (2.3) in terms of a Fourier integral

$$\begin{aligned}
Z &= \int Dn \int D\xi \exp\left(-\int dt \int d^d x \frac{\xi^2}{2\Gamma N[n]}\right) \\
&\quad \times \int D\tilde{n} \exp\left(-\int dt \int d^d x \left[\tilde{n}(\partial_t n - F[n] - \xi)\right]\right) \\
&= \int Dn \int D\tilde{n} \exp\left(-\int dt \int d^d x \left[\tilde{n}(\partial_t n - F[n] - \frac{\Gamma}{2}\tilde{n}N[n])\right]\right), \tag{2.4}
\end{aligned}$$

where $\tilde{n}$ is the auxiliary field. The partition function with a statistical weight determined by the action

$$S = \int dt \int d^d x \left[\tilde{n}(\partial_t n - F[n] - \frac{\Gamma}{2}\tilde{n}N[n])\right]. \tag{2.5}$$

Next sections will be devoted to different universality classes such as DP universality, long-ranged DP universality, and TDP universality.

2.3 Contact process

The microscopic rules of the (classical) contact process presented in Sec. 1.1. The mean-field Langevin equation of the density of active sites n is given by

$$\partial_t n_i(t) = -\gamma n_i(t) + \frac{\kappa}{z} \sum_{\langle i,j \rangle} n_j(t)(1 - n_i(t)) + \xi_i(t),$$ (2.6)

where $z = 2d$ is a number of the nearest-neighbors and $\langle i, j \rangle$ stands for the nearest neighbor of i. The noise $\xi_i(t)$ is a multiplicative Gaussian random variable with zero mean and whose correlation [Appendix B.2] is

$$\langle \xi_i(t)\xi_j(t') \rangle = \Gamma n \delta_{i,j} \delta(t - t').$$ (2.7)

It is convenient to adopt a continuum description (see Appendix B.3), in which n represents the local particle density. Rescaling the time $t \to \gamma t$ or equivalently $\gamma = 1$, Eq. (2.6) is given as follows.

$$\partial_t n = D\nabla^2 n - (1 - \kappa)n - \kappa n^2 + \xi,$$ (2.8)

where D is a diffusion constant.

Using the Martin–Siggia–Rose–Janssen–Dominicis (MSRJD) formalism presented in previous section, we obtain the action as follows:

$$S = \int dt \int d^d x \left[\tilde{n} \left(\partial_t n - D\nabla^2 n - (\kappa - 1)n + \kappa n^2 - \frac{\Gamma}{2}\tilde{n}n \right) \right].$$ (2.9)

2.3.1 Upper critical dimension and mean-field critical exponents

We obtained the action of CP by MSRJD field-theoretic approach, which is rewritten as

$$S = \int dt \int d^d x \left[\tilde{n} \left(\tau \partial_t n - D \nabla^2 n + u_2 n + u_3 n^2 - \frac{\Gamma}{2} \tilde{n} n \right) \right],$$ (2.10)

where $\tau = 1$, $u_2 \equiv 1 - \kappa$, and $u_3 \equiv \kappa$. To symmetrize the cubic terms, rescaling $n \to \sqrt{\frac{\Gamma}{2u_3}} n$, $\tilde{n} \to \sqrt{\frac{2u_3}{\Gamma}} \tilde{n}$, and $\sqrt{\frac{\Gamma u_3}{2}} \to u_3$, the action is written as

$$S = \int dt \int d^d x \left[\tilde{n} \left(\tau \partial_t - D \nabla^2 + u_2 \right) n + u_3 \tilde{n} (n - \tilde{n}) n \right].$$ (2.11)

Physical properties remain the same if we change the spatio-temporal coordinates scale by a constant factor. Under the scaling transformations, which are given by

$$x \to x' = \frac{x}{s}, \ t \to t' = \frac{t}{s^z}, \ n \to n' = s^\chi n, \ \tilde{n} \to \tilde{n}' = s^{\tilde{\chi}} \tilde{n},$$ (2.12)

where $s > 1$. The action Eq. (2.10) has the rapidity-reversal symmetry (see Appendix B.4) which implies that the $\chi = \beta / \nu_\perp$ and $\tilde{\chi} = \tilde{\beta} / \nu_\perp$ have to be identical. Under the transformation given by Eq. (2.34), $S[n, \tilde{n}] \to S'[n', \tilde{n}']$ is given by

$$S' = \int dt' \int d^d x' \, s^{d+z} \left[\tilde{n}' \left(\tau s^{-z-2\chi} \partial_{t'} - D s^{-2-2\chi} \nabla'^2 + u_2 s^{-2\chi} \right) n' + u_3 s^{-3\chi} \tilde{n}' (n' - \tilde{n}') n' \right].$$ (2.13)

Therefore, we obtain the following relations of the parameters under the scaling transformation:

$$\tau \to \tau' = s^{d-2\chi} \tau, \qquad D \to D' = s^{d+z-2-2\chi} D, \qquad u_2 \to u_2' = s^{d+z-2\chi} u_2,$$

$$u_3 \to u_3' = s^{d+z-3\chi} u_3.$$ (2.14)

15

To make the fluctuations scale invariant at the critical point $u_2 = 0$, we must ensure that the action stays fixed. Thus we choose $\chi = d/2$ in order to be invariant of temporal fluctuations scale and then choose $z = 2$ in order to be invariant of spatial fluctuations scale. The cubic term is rescaled as $u'_3 = s^{2-d/2}u_3$. Thus for $d > d_c = 4$ where d_c is the upper critical dimension, u_3 is irrelevant, which means that the action becomes the Guassian (quadratic) function in Eq. (2.13). For this reason, the fixed point above the upper critical dimension is called the Gaussian fixed point. For $d < 4$, u_3 becomes relevant. In this case, the Gaussian fixed point is shifted due to the higher-order terms, leading to the Wilson-Fisher fixed point, which will be discussed in next subsection.

Finally, we can compute the mean-field critical exponents. Homogeneous mean-field solution gives the critical exponent $\beta = 1$ [Appendix B.5]. Thus, we can obtain $\nu_\perp = \beta/\chi = 0.5$ and $z = 2$. The independent critical exponents of DP universality is three, and thus critical exponents other than $\{\beta, \nu_\perp, z\}$ are computed using the scaling relations.

2.3.2   Below the upper critical dimension: the ε-expansion

We obtained the upper critical dimension and the mean-field critical exponents in previous subsection. Whereas the mean-field exponents are valid above the upper critical dimension, below the upper critical dimension, the low-dimensional fluctuations make the relevant effects and violate mean-field picture. Slightly below the upper critical dimension, say $d = d_c - \varepsilon$, we could compute the critical exponents by using the perturbation expansion (ε-expansion). Similarly to equilibrium phase transition, we can define the elements of the graphical ε-expansion. In RG transformation, we use the Wick's theorem [Appendix B.6] and the following cumulant expansion.

Cumulant expansion: In the presence of the interaction term, the expectation of

any observable $\mathcal{O}$ is given by

$$\langle\mathcal{O}\rangle = \frac{\int Dn\,\mathcal{O}e^{-S_0-S_{int}}}{\int Dn\,e^{-S_0-S_{int}}} = \frac{\int Dn\,\mathcal{O}e^{-S_0}[1-S_{int}+S_{int}^2/2-\cdots]}{\int Dn\,e^{-S_0}[1-S_{int}+S_{int}^2/2-\cdots]}$$
$$= \frac{Z_0[\langle\mathcal{O}\rangle_0 - \langle\mathcal{O}S_{int}\rangle_0 + \langle\mathcal{O}S_{int}^2\rangle_0/2 - \cdots]}{Z_0[1-\langle S_{int}\rangle_0 + \langle S_{int}^2\rangle_0/2 - \cdots]}, \tag{2.15}$$

where S_0 is the free quadratic action and $S_{int} = S - S_0$ is the interacting action as follows:

$$S_0 = \int dt \int d^dx \left[\tilde{n}\left(\tau\partial_t - D\nabla^2 + u_2\right)n\right], \qquad S_{int} = \int dt \int d^dx \left[u_3\tilde{n}(n-\tilde{n})n\right]. \tag{2.16}$$

Expanding the denominator gives

$$\langle\mathcal{O}\rangle = \left[\langle\mathcal{O}\rangle_0 - \langle\mathcal{O}S_{int}\rangle_0 + \frac{\langle\mathcal{O}S_{int}^2\rangle_0}{2} - \cdots\right] \times \left[1 + \langle S_{int}\rangle_0 + \langle S_{int}\rangle_0^2 - \frac{\langle S_{int}^2\rangle_0}{2} - \cdots\right]$$
$$= \langle\mathcal{O}\rangle_0 - \left(\langle\mathcal{O}S_{int}\rangle_0 - \langle\mathcal{O}\rangle_0\langle S_{int}\rangle_0\right)$$
$$+ \frac{1}{2}\left(\langle\mathcal{O}S_{int}^2\rangle_0 - 2\langle\mathcal{O}S_{int}\rangle_0\langle S_{int}\rangle_0 + 2\langle\mathcal{O}\rangle_0\langle S_{int}\rangle_0^2 - \langle\mathcal{O}\rangle_0\langle S_{int}^2\rangle_0\right) + \cdots$$
$$\equiv \sum_{n=0}^{\infty} \frac{(-1)^n}{n!}\langle\mathcal{O}S_{int}^n\rangle_0^c. \tag{2.17}$$

The connected averages (cumulants) are defined as the combination of unperturbed expectation values appearing at various orders in the expansion. As you already know, the terms in the perturbation series get complicated. Feynman developed a useful Feynman diagram which has the one-to-one correspondence to a term in perturbation series.

Now, let us consider the renormalization group transformation: rescaling and coarse graining.

1) Rescaling : We already conducted this process in Eq. (2.14), expanding $s = 1 + l$
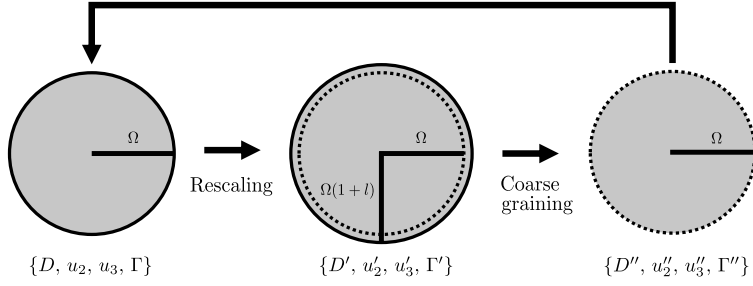
Figure 2.1: RG transformation regularized with a hard cutoff Ω: rescaling and coarse-graining.
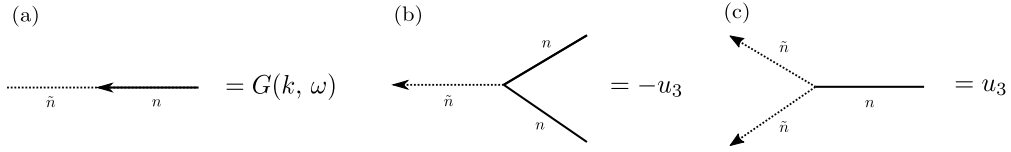
Figure 2.2: Elements of the graphical perturbation expansion of DP: (a) bare propagator; (b) bare three-point vertex function.
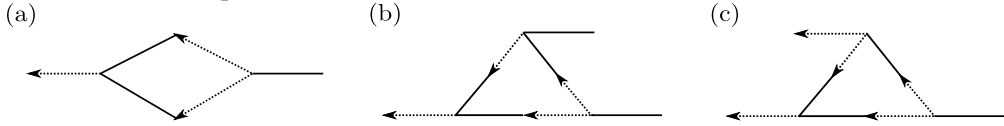
Figure 2.3: One-loop Feynman diagrams for DP: (a) two-point green function; (b) two-point vertex function; (b) three-point non-linear function; (c) three-point noise vertex.

for ($l \ll 1$).

$$D' = [1 + l(d + z - 2 - 2\chi)]D, \qquad \tau' = [1 + l(d - 2\chi)]\tau,$$

$$u_2' = [1 + l(d + z - 2\chi)]u_2, \qquad u_3' = [1 + l(d + z - 3\chi)]u_3. \quad (2.18)$$

2) Coarse-graining : Integrating out degrees of freedom. The graphical loops are depicted in Fig. 2.1 where an arrow marks a $\tilde{n}$-leg represented as dotted lines. We draw diagrams with the arrows always directed to the left (ascending time ordering from right to left). The bare propagator [Appendix B.7] and vertex functions are shown in Fig. 2.2. One-loop diagrams are shown in Fig. 2.3. From the cumulant expansion, one can obtain the propagator $-G''^{-1}(k, \omega) = -G'^{-1}(k, \omega) +$

Fig. 3(a) with $G^{-1}(k, \omega) = Dk^2 - i\omega\tau - u_2$ and the vertex $-u_3'' = -u_3' + $Fig. 3(b).

$$\text{Fig. 3(a)} = -2(\frac{u_3}{2})^2 \int \frac{d^d k' d\omega'}{(2\pi)^{d+1}} G(\frac{k}{2} + k', \frac{\omega}{2} + \omega') G(\frac{k}{2} - k', \frac{\omega}{2} - \omega')$$

$$= -2(\frac{u_3}{2})^2 \int \frac{d^d k'}{(2\pi)^d} \int_{-\infty}^{\infty} \frac{d\omega'}{2\pi} \frac{1}{D(k/2 + k')^2 - u_2 - i(\omega/2 + \omega')\tau}$$

$$\frac{1}{D(k/2 - k')^2 - u_2 - i(\omega/2 - \omega')\tau}$$

$$= -(\frac{u_3}{2})^2 \int \frac{d^d k'}{(2\pi)^d} \frac{1}{\tau(Dk^2/4 + Dk'^2 - u_2 - i\omega\tau/2)}, \qquad (2.19)$$

$$\text{Fig. 3(b)} = 16(\frac{u_3}{2})^3 \int \frac{d^d k d\omega}{(2\pi)^{d+1}} G^2(k, \omega) G(-k, -\omega)$$

$$= 16(\frac{u_3}{2})^3 \int \frac{d^d k}{(2\pi)^d} \int_{-\infty}^{\infty} \frac{d\omega}{2\pi} \frac{1}{(Dk^2 - u_2 - i\omega\tau)^2} \frac{1}{Dk^2 - u_2 + i\omega\tau}$$

$$= 4(\frac{u_3}{2})^3 \int \frac{d^d k}{(2\pi)^d} \frac{1}{\tau(Dk^2 - u_2)^2}. \qquad (2.20)$$

This is when regularization comes into play. Here, we use the hard cutoff regularization scheme in which we integrate out up to Ω [Fig. 2.1]. We remark that dimensional regularization with $\Omega \to \infty$ can also be used with minimal subtraction (see Section 10 of Ref. [11]). With the hard cutoff regularization scheme, Eq. (2.19) and Eq. (2.20) can be calculated as

$$\text{Fig. 3(a)} = -(\frac{u_3}{2})^2 \int \frac{d^d k'}{(2\pi)^d} \frac{1}{\tau(Dk^2/4 + Dk'^2 - u_2 - i\omega\tau/2)}$$

$$= -\frac{u_3^2}{4(2\pi)^d \tau} \int_{\Omega}^{\Omega(1+l)} dk' \frac{k'^{d-1} S_d}{Dk^2/4 + Dk'^2 - u_2 - i\omega\tau/2}$$

$$= -\frac{u_3^2 S_d \Omega^d l}{4\tau(2\pi)^d} \frac{1}{Dk^2/4 + D\Omega^2 - u_2 - i\omega\tau/2}$$

$$= -\frac{u_3^2 S_d \Omega^d l}{4\tau(2\pi)^d} \left(\frac{1}{D\Omega^2 - u_2} - \frac{D}{4(D\Omega^2 - u_2)^2} k^2 + \frac{i\tau}{2(D\Omega^2 - u_2)^2} \omega + \cdots \right),$$

$$(2.21)$$

$$\text{Fig. 3(b)} = 4\left(\frac{u_3}{2}\right)^3 \int \frac{d^d k}{(2\pi)^d} \frac{1}{\tau (Dk^2 - u_2)^2} = \frac{u_3^3 S_d \Omega^d l}{2\tau (2\pi)^d (D\Omega^2 - u_2)^2}. \quad (2.22)$$

The coupling constants are changed in coarse-graining as following:

$$D'' = D' - \frac{u_3^2 l S_d \Omega^d}{16\tau (2\pi)^d (D\Omega^2 - u_2)^2}, \qquad \tau'' = \tau' - \frac{u_3^2 l S_d \Omega^d}{8(2\pi)^d (D\Omega^2 - u_2)^2},$$

$$u_2'' = u_2' - \frac{u_3^2 l S_d \Omega^d}{4\tau (2\pi)^d (D\Omega^2 - u_2)}, \qquad u_3'' = u_3' - \frac{u_3^3 S_d \Omega^d l}{2\tau (2\pi)^d (D\Omega^2 - u_2)^2}.$$

$$(2.23)$$

Finally, enumerating the rescaling [Eq. (2.18)] and coarse-graining [Eq. (2.23)], we obtain the RG flow equations

$$\partial_l D = D(d + 2\chi + z - 2 - S_1), \qquad \partial_l \tau = \tau (d + 2\chi - 2S_1),$$

$$\partial_l u_2 = u_2 (d + 2\chi + z - S_2), \qquad \partial_l u_3 = u_3 (d + 3\chi + z - 8S_1), \quad (2.24)$$

where $S_1 = \frac{u_3^2 l S_d \Omega^d}{16\tau (2\pi)^d (D\Omega^2 - u_2)^2}$ and $S_2 = \frac{u_3^2 l S_d \Omega^d}{4\tau u_2 (2\pi)^d (D\Omega^2 - u_2)}$. In order to make the fluctuations scale invariant, we set $\partial_l D = 0$ and $\partial_l \tau = 0$. Then Eq. (2.24) becomes

$$\partial_l u_2 = u_2 (S_1 - S_2 + 2), \qquad \partial_l u_3 = u_3 \left(\frac{\varepsilon}{2} - 6S_1\right), \quad (2.25)$$

where $d = 4 - \varepsilon$. In the (u_2, u_3)-plane, fixed points are given by

$$u_2^* = \frac{4D^* \Omega^{*2} \varepsilon}{24 + 5\varepsilon} \simeq \frac{D^* \Omega^{*2}}{6} \varepsilon + \mathscr{O}(\varepsilon^2),$$

$$u_3^* = \left(\frac{2D^*(\varepsilon + 24)}{24 + 5\varepsilon} \sqrt{\frac{\tau \varepsilon (2\pi)^4}{3S_4}}\right)^2 \simeq \frac{4D^* \Omega^{*2} \tau^* (2\pi)^4}{3S_4} \varepsilon + \mathscr{O}(\varepsilon^2). \quad (2.26)$$

The non-trivial fixed point is called the Wilson-Fisher fixed point. The linearized RG

flow is governed by the matrix

$$M = \begin{pmatrix} \left.\frac{\partial(\partial_l u_2)}{\partial u_2}\right|_{u_2^*, u_3^*} & \left.\frac{\partial(\partial_l u_2)}{\partial u_3}\right|_{u_2^*, u_3^*} \\ \left.\frac{\partial(\partial_l u_3)}{\partial u_2}\right|_{u_2^*, u_3^*} & \left.\frac{\partial(\partial_l u_3)}{\partial u_3}\right|_{u_2^*, u_3^*} \end{pmatrix} = \begin{pmatrix} 2 - \frac{\varepsilon}{4} & -\sqrt{\frac{S_d \Omega^4}{3\tau(2pi)^4}}\varepsilon \\ 0 & -\varepsilon \end{pmatrix}. \quad (2.27)$$

The eigenvalues of this matrix are $\lambda_1 = 2 - \varepsilon/4$ and $\lambda_2 = -\varepsilon$. Here the first eigenvalue is positive and represents the repulsive line of the renormalization group flow, meaning that u_2 diverges as e^{λ_1} the fixed point is approached. Since u_2 plays the role of the reduced percolation probability (mass gap), we may identify $v_\perp^{-1} = 2 - \varepsilon/4$. From $\partial_l D = 0$ and $\partial_l \tau = 0$, $\chi = \beta/v_\perp = 2 - 7\varepsilon/12$ and $z = 2 - \varepsilon/12$, which gives the critical exponents as follows:

$$v_\perp = \frac{1}{2} + \frac{\varepsilon}{16} + \mathcal{O}(\varepsilon^2), \qquad \beta = 1 - \frac{\varepsilon}{6} + \mathcal{O}(\varepsilon^2), \qquad v_\parallel = 1 + \frac{\varepsilon}{12} + \mathcal{O}(\varepsilon^2). \quad (2.28)$$

2.4 Contact process with long-range interaction

According to the DP conjecture, nonequilbrium phase transitions with short-range interaction generally falls into DP class. In many realistic spreading processes, however, interactions are long-ranged described by Lèvy flights $P(r) \sim r^{-d-\sigma}$. In the presence of the long-range interaction, the rules of CP are modified as follows.

i) Decay : an active particle becomes inactive at a rate γ.

ii) Branching : an inactive particle becomes active at a rate $\kappa P(r)$ when it contacts a distant active particle.

The mean-field Langevin equation of the density of active sites n is given by

$$\partial_t n_i(t) = -\gamma n_i(t) + \kappa \sum_{j \neq i} P(|\boldsymbol{r}_i - \boldsymbol{r}_j|) n_j(t)(1 - n_i(t)) + \xi_i(t). \quad (2.29)$$

It is convenient to adopt a continuum description (see Appendix B.8), in which n represents the local particle density. Rescaling the time $t \to \gamma t$ or equivalently $\gamma = 1$,

Eq. (2.29) is given as follows.

$$\partial_t n = D\nabla^2 n + D_\sigma \nabla^\sigma n - (1-\kappa)n - \kappa n^2 + \xi, \tag{2.30}$$

where D and D_σ are a diffusion constant.

Using the Martin–Siggia–Rose–Janssen–Dominicis (MSRJD) formalism presented in previous section, we obtain the action as follows:

$$S = \int dt \int d^d x \left[\tilde{n} \left(\partial_t n - D\nabla^2 n - D_\sigma \nabla^\sigma n + (1-\kappa)n + \kappa n^2 - \frac{\Gamma}{2}\tilde{n}n \right) \right]. \tag{2.31}$$

2.4.1 Upper critical dimension and mean-field critical exponents

We obtained the action of long-ranged CP by MSRJD field-theoretic approach, which is rewritten as

$$S = \int dt \int d^d x \left[\tilde{n} \left(\tau\partial_t n - D\nabla^2 n - D_\sigma \nabla^\sigma n + u_2 n + u_3 n^2 - \frac{\Gamma}{2}\tilde{n}n \right) \right], \tag{2.32}$$

where $\tau = 1$, $u_2 \equiv 1 - \kappa$, and $u_3 \equiv \kappa$. To symmetrize the cubic terms, rescaling $n \rightarrow \sqrt{\frac{\Gamma}{2u_3}}n$, $\tilde{n} \rightarrow \sqrt{\frac{2u_3}{\Gamma}}\tilde{n}$, and $\sqrt{\frac{\Gamma u_3}{2}} \rightarrow u_3$, the action is written as

$$S = \int dt \int d^d x \left[\tilde{n} \left(\tau\partial_t - D\nabla^2 - D_\sigma \nabla^\sigma + u_2 \right) n + u_3 \tilde{n}(n - \tilde{n})n \right]. \tag{2.33}$$

By the scale invariance, action should be invariant if we change the spatio-temporal coordinates scale by a constant factor. Under the scaling transformations, which are given by

$$x \rightarrow x' = \frac{x}{s}, \; t \rightarrow t' = \frac{t}{s^z}, \; n \rightarrow n' = s^\chi n, \; \tilde{n} \rightarrow \tilde{n}' = s^{\tilde{\chi}}\tilde{n}, \tag{2.34}$$

where $s > 1$. The action Eq. (2.32) has the rapidity-reversal symmetry (see Appendix B.2) which implies that the $\chi = \beta/\nu_\perp$ and $\tilde{\chi} = \tilde{\beta}/\nu_\perp$ have to be identical. Under the trans-

formation given by Eq. (2.34), $S[n, \tilde{n}] \rightarrow S'[n', \tilde{n}']$ is given by

$$S' = \int dt' \int d^d x' \, s^{d+z} \left[\tilde{n}' \left(\tau s^{-z-2\chi} \partial_{t'} - D s^{-2-2\chi} \nabla'^2 - D_\sigma s^{-\sigma-2\chi} \nabla'^\sigma + u_2 s^{-2\chi} \right) n' \right.$$
$$\left. + u_3 s^{-3\chi} \tilde{n}' (n' - \tilde{n}') n' \right]. \tag{2.35}$$

Therefore, we obtain the following relations of the parameters under the scaling transformation:

$$\tau \rightarrow \tau' = s^{d-2\chi} \, \tau, \qquad D \rightarrow D' = s^{d+z-2-2\chi} \, D, \qquad D_\sigma \rightarrow D'_\sigma = s^{d+z-\sigma-2\chi} \, D_\sigma,$$
$$u_2 \rightarrow u'_2 = s^{d+z-2\chi} \, u_2, \qquad u_3 \rightarrow u'_3 = s^{d+z-3\chi} \, u_3. \tag{2.36}$$

To make the fluctuations scale invariant at the critical point $u_2 = 0$, we must ensure that the action stays fixed. For $\sigma > 2$, D_σ is irrelevant; however, D is relevant, where the universality belongs to DP class (see Sec. 2.3). On the other hand, for $\sigma < 2$, D becomes irrelevant; however, D_σ becomes relevant. From now on, we focus on the region where D_σ is relevant for $\sigma < 2$. Thus we choose $\chi = d/2$ in order to be invariant of temporal fluctuations scale. Similarly, by choosing $z = \sigma$, spatial fluctuations become scale invariant. The cubic term is rescaled as $u'_3 = s^{\sigma-d/2} u_3$. Thus for $d > d_c = 2\sigma$ where d_c is the upper critical dimension, u_3 is irrelevant, which means that the action becomes the Guassian (quadratic) function in Eq. (2.35). For this reason, the fixed point above the upper critical dimension is called the Gaussian fixed point. For $d < 2\sigma$, u_3 becomes relevant. In this case, the Gaussian fixed point is shifted due to the higher-order terms, leading to the Wilson-Fisher fixed point, which will be discussed in next subsection.

Finally, we can compute the mean-field critical exponents. Homogeneous mean-field solution gives the critical exponent $\beta = 1$ [Appendix B.4]. Thus, we can obtain $\nu_\perp = \beta/\chi = 1/\sigma$ and $z = \sigma$.

2.4.2 Below the upper critical dimension: the ε-expansion

Comparing with the action of DP class, long-range DP has the fractional Laplacian in quadratic term. Thus, the only difference is the Green's function. The Green function is changed from $G(k, \omega) = (Dk^2 - i\omega\tau + u_2)^{-1}$ (see Appendix B.7) to $G(k, \omega) = (D_\sigma k^\sigma - i\omega\tau + u_2)^{-1}$. Since the cubic terms remain the same, one-loop Feynman diagrams is not changed (see Fig. 2.2 and Fig. 2.3). Here, we shall calculate the one-loop propagator and show that one-loop diagram does not contribute to the coefficient D_σ.

1) Rescaling : We already conducted this process in Eq. (2.36), expanding $s = 1 + l$ for $(l \ll 1)$.

$$D'_\sigma = [1 + l(d + z - \sigma - 2\chi)]D_\sigma, \qquad \tau' = [1 + l(d - 2\chi)]\tau,$$

$$u'_2 = [1 + l(d + z - 2\chi)]u_2, \qquad u'_3 = [1 + l(d + z - 3\chi)]u_3. \quad (2.37)$$

2) Coarse-graining : Integrating out degrees of freedom. The bare propagator and vertex functions are shown in Fig. 2.2. One-loop diagrams are shown in Fig. 2.3. From the cumulant expansion, one can obtain the propagator $-G''^{-1}(k, \omega) = -G'^{-1}(k, \omega) + $ Fig. 3(a) with $G(k, \omega) = (D_\sigma k^\sigma - i\omega\tau + u_2)^{-1}$.

$$
\begin{aligned}
\text{Fig. 3(a)} &= -2(\frac{u_3}{2})^2 \int \frac{d^d\mathbf{k}' d\omega'}{(2\pi)^{d+1}} G(\frac{\mathbf{k}}{2} + \mathbf{k}', \frac{\omega}{2} + \omega') G(\frac{\mathbf{k}}{2} - \mathbf{k}', \frac{\omega}{2} - \omega') \\
&= -2(\frac{u_3}{2})^2 \int \frac{d^d\mathbf{k}'}{(2\pi)^d} \int_{-\infty}^{\infty} \frac{d\omega'}{2\pi} \frac{1}{D_\sigma|\mathbf{k}/2 + \mathbf{k}'|^\sigma - u_2 - i(\omega/2 + \omega')\tau} \\
&\quad \frac{1}{D_\sigma|\mathbf{k}/2 - \mathbf{k}'|^\sigma - u_2 - i(\omega/2 - \omega')\tau} \\
&= -2(\frac{u_3}{2})^2 \int \frac{d^d\mathbf{k}'}{(2\pi)^d} \frac{1}{\tau(D_\sigma|\mathbf{k}/2 + \mathbf{k}'|^\sigma + D_\sigma|\mathbf{k}/2 - \mathbf{k}'|^\sigma - 2u_2 - i\omega\tau)}.
\end{aligned}
$$
$$(2.38)$$

Since k is very small in long-wavelength limit, we may expand the denominator

$$
\begin{aligned}
|\boldsymbol{k}/2 + \boldsymbol{k}'|^\sigma &= k'^\sigma \left| 1 + \frac{k\cos\theta}{k'} + \frac{k^2}{4k'^2} \right|^{\sigma/2} \\
&= k'^\sigma + \frac{\sigma\cos\theta}{2} k'^{\sigma-1} k + \left(\frac{\sigma}{8} + \frac{\sigma(\sigma-2)}{8}\cos^2\theta \right) k'^{\sigma-2} k^2 + \mathcal{O}(k^3),
\end{aligned}
\tag{2.39}
$$

where $\mathcal{O}(k^\sigma)$ vanishes during the expansion. Therefore Eq. (2.38) becomes

$$
\begin{aligned}
\text{Fig. 3(a)} &= -2\left(\frac{u_3}{2}\right)^2 \int \frac{d^d \boldsymbol{k}'}{(2\pi)^d \tau} \left[2D_\sigma k'^\sigma + \frac{D_\sigma \sigma}{4} k'^{\sigma-2} k^2 \right. \\
&\quad + \frac{D_\sigma \sigma(\sigma-2)}{4}\cos^2\theta k'^{\sigma-2} k^2 - 2u_2 - i\omega\tau \Big]^{-1} \\
&= -\frac{l\Omega^d S_{d-1} u_3^2}{2\tau(2\pi)^d} \int_0^\pi d\theta \sin^{d-2}\theta \left[2D_\sigma \Omega^\sigma - 2u_2 - i\omega\tau + \frac{D_\sigma \sigma}{4} \Omega^{\sigma-2} k^2 \right. \\
&\quad + \frac{D_\sigma \sigma(\sigma-2)}{4}\cos^2\theta \Omega^{\sigma-2} k^2 \Big)\Big]^{-1},
\end{aligned}
\tag{2.40}
$$

where $S_d = 2\pi^{d/2}/\Gamma(d/2)$ is the solid angle. Let us expand the last term in Eq. (2.40) with respect to k and ω.

$$
\begin{aligned}
\text{Fig. 3(a)} &\simeq -\frac{l\Omega^d S_{d-1} u_3^2}{2\tau(2\pi)^d} \int_0^\pi d\theta \sin^{d-2}\theta \left[\frac{1}{2D_\sigma \Omega^\sigma - 2u_2} + \frac{i\tau}{(2D_\sigma \Omega^\sigma - 2u_2)^2}\omega \right. \\
&\quad - \frac{D_\sigma \sigma \Omega^{\sigma-2} + D_\sigma \sigma(\sigma-2)\cos^2\theta \Omega^{\sigma-2}}{4(2D_\sigma \Omega^\sigma - 2u_2)^2} k^2 \bigg].
\end{aligned}
\tag{2.41}
$$

Using the relation $\int_0^\pi \sin^{d-2}\theta = S_d/S_{d-1}$, $\int_0^\pi \sin^{d-2}\theta \cos^2\theta = S_d/dS_{d-1}$, we finally obtain

$$
\begin{aligned}
\text{Fig. 3(a)} &= -\frac{l\Omega^d S_d u_3^2}{4\tau(2\pi)^d} \left[\frac{1}{D_\sigma \Omega^\sigma - u_2} + \frac{i\tau}{2(D_\sigma \Omega^\sigma - u_2)^2}\omega \right. \\
&\quad - \frac{D_\sigma \sigma \Omega^{\sigma-2} + D_\sigma \sigma(\sigma-2)\Omega^{\sigma-2}/d}{8(D_\sigma \Omega^\sigma - u_2)^2} k^2 \bigg].
\end{aligned}
\tag{2.42}
$$

Clearly, $\mathcal{O}(k^\sigma)$ does not exist in Eq. (2.42), which means that coarse graining does not contribute to D'_σ, i.e. $D''_\sigma = D'_\sigma$.

Thus, plugging this relation into Eq. (2.37), $D''_\sigma = D'_\sigma = [1 + l(d + z - \sigma - 2\chi)]D_\sigma$ or equivalently $\partial_l D_\sigma = d + z - \sigma - 2\chi$. Similarly to Sec. 2.3, in order to make the fluctuations scale invariant, we set $\partial_l D_\sigma = 0$, which gives the hyperscaling relation

$$d + z - \sigma - 2\chi = 0. \tag{2.43}$$
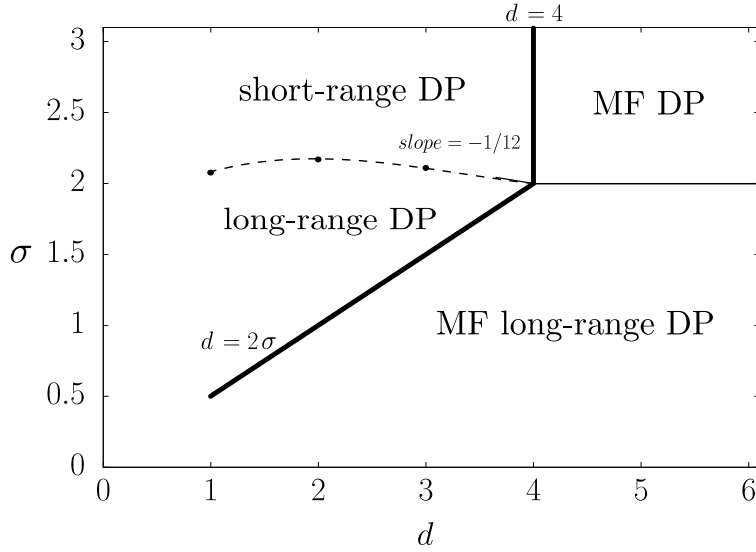
Figure 2.4: Universality class diagram of long-range DP in the parameter space (d, σ).

Now, let us consider the universality class diagram for (d, σ). We obtained the upper critical dimension $d_c = \min(2\sigma, 4)$ and the hyperscaling relation $d + z - \sigma - 2\chi = 0$ which is valid for $d < d_c$ and the region that fractional Laplacian is relevant. In Fig. 2.4, the upper critical dimension is represented as the bold line. Since the hyperscaling relation is valid for long-range DP regime and the critical exponents of long-range DP are changed continuously to short-range DP, the dots in Fig. 2.4 are obtained the hyperscaling relation $\sigma^* = d + z_{SR} - 2\chi_{SR}$, where z_{SR} and χ_{SR} are the numerical values of the short-range DP.

2.5 Tricritical contact process

As we discussed in Sec. 2.1, the universality class may be changed when symmetry is broken. The symmetry of DP class is the rapidity-reversal symmetry, which implies that the critical exponent of n and $\tilde{n}$ should be the same. In this section, we shall deal with the tricritical contact process (TCP) whose rapidity-reversal symmetry of CP is broken due to the higher-order interaction. In the presence of the higher-order interaction, the rules of CP are modified as follows.

   i) Decay : an active particle becomes inactive at a rate γ.

   ii) Branching : an inactive particle becomes active at a rate κ when it contacts a neighboring active particle.

   iii) **Pair branching** : an inactive particle becomes active at a rate ω when it contacts a pair of the active particles.

The mean-field Langevin equation of the density of active sites n is given by

$$\partial_t n_i(t) = -\gamma n_i(t) + \frac{\kappa}{z} \sum_{\langle i,j \rangle} n_j(t)(1-n_i(t)) + \frac{\omega}{2(z-1)} \sum_{\langle i,j \rangle} \sum_{\langle i,j,k \rangle} n_k n_j(1-n_i(t)) + \xi_i(t) \,,$$

$$(2.44)$$

where $z = 2d$ is a number of the nearest-neighbors and $\langle i,j,k \rangle$ stands for the nearest neighbor of a pair of i and j. The noise $\xi_i(t)$ is a multiplicative Gaussian random variable with zero mean and whose correlation [Appendix B.2] is

$$\langle \xi_i(t) \xi_j(t') \rangle = \Gamma n \delta_{i,j} \delta(t-t') \,. \tag{2.45}$$

It is convenient to adopt a continuum description (see Appendix B.3), in which n represents the local particle density. Rescaling the time $t \to \gamma t$ or equivalently $\gamma = 1$,

Eq. (2.44) is given as follows.

$$\partial_t n = D\nabla^2 n - (1-\kappa)n - (\kappa-\omega)n^2 - \omega n^3 + \xi, \tag{2.46}$$

where D is a diffusion constant.

2.5.1 Phase diagram

In this subsection, we shall deal with the phase diagram of the TCP. Firstly, let us consider the homogeneous mean-field equation give by

$$\partial_t n = D\nabla^2 n - u_2 n - u_3 n^2 - u_4 n^3 + \xi, \tag{2.47}$$

where $u_2 = 1-\kappa$, $u_3 = \kappa-\omega$, and $u_4 = \omega$. In steady-state [$\partial_t n = 0$], we obtain solutions as

$$n^* = 0 \quad \text{and} \quad n^* = n^*_\pm \equiv \frac{-u_3 \pm \sqrt{u_3^2 - 4u_2 u_4}}{2u_4}. \tag{2.48}$$

Performing the linear stability analysis, we find that the first solution $n = 0$ is stable for $u_2 > 0$ and unstable for $u_2 < 0$. Thus, $u_2 = 1-\kappa = 0$ is the boundary of the stable solution at the fixed point $n = 0$, equivalent to the boundary of active phase in Fig. 2.5.

For the second solution $n^*_{a,\pm}$, we perform the linear stability analysis as

$$\delta\dot{n}^*_\pm = -(u_2 + 2u_3 n^*_\pm + 3u_4 n^{*2}_\pm)\delta n_\pm \tag{2.49}$$

$$= n^*_\pm(-u_3 - 2u_4 n^*_\pm)\delta n_\pm = \mp n^*_\pm\sqrt{u_3^2 - 4u_2 u_4}\,\delta n_\pm. \tag{2.50}$$

Thus, n^*_+ and n^*_- are stable for $n^*_+ > 0$ and $n^*_- < 0$, respectively. Because the negative density is not physically acceptable, n^*_- is ignored. For $n = n^*_+$, the phase boundary is

obtained by the conditions $u_3^2 - 4u_2u_4 = 0$ and $u_3 \leq 0$. These conditions lead to

$$(\kappa + \omega)^2 - 4\omega = 0 \text{ for } \kappa < \omega, \qquad (2.51)$$

where $n_+^* \geq 0$. This phase boundary is drawn by white dashed curve in Fig. 2.5.
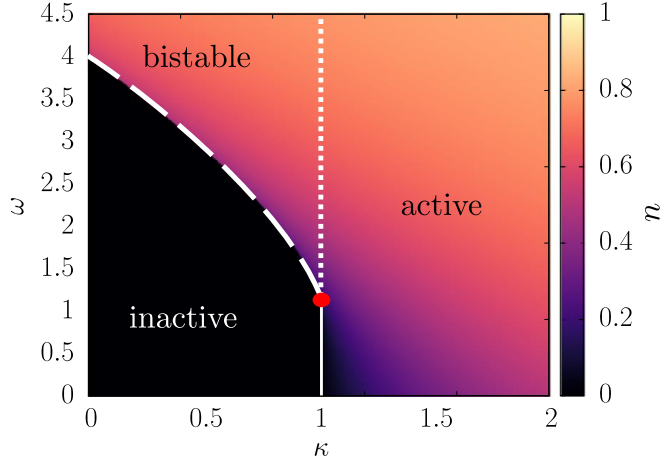
Figure 2.5: Phase diagram of TCP in the parameter space (κ, ω).

2.5.2 Upper critical dimension and mean-field critical exponents

Using the Martin–Siggia–Rose–Janssen–Dominicis (MSRJD) formalism presented in previous section, we obtain the action as follows:

$$S = \int dt \int d^d x \left[\tilde{n} \left(\partial_t n - D\nabla^2 n + u_2 n + u_3 n^2 + u_4 n^3 - \frac{\Gamma}{2} \tilde{n} n \right) \right]. \qquad (2.52)$$

This action will be found in the next chapter from the quantum model with different microscopic rules.

Chapter 3

Nonequilibrium phase transition in open quantum systems

A large part of this chapter is published in Ref. [31].

3.1 Introduction

Nonequilibrium phase transitions into an absorbing state have been extensively studied [20,28,29,38–45]. However, in recent years, they have attracted a significant amount of attention because some of these transitions have been experimentally realized in turbulence [46] and dissipative Rydberg atom quantum systems [24]. One of the most robust classes of absorbing transitions is the directed percolation (DP) class [28, 29, 42–44], in which the dynamics spreads by a contact process (CP). An active particle becomes inactive at a rate γ, whereas an inactive particle becomes active at a rate κ when it contacts a neighboring active particle. If κ/γ is small, the system falls into an absorbing state. Otherwise, it is in an active state. The CP model can be used for modeling the epidemic spread of infectious disease and the reaction–diffusion process of interacting particles. On the other hand, the Reggeon field theory reveals the universal properties of the DP class [47,48].

The CP can be generalized in various ways. Here, we introduce two cases associated with the main topic of this paper. One is the long-range CP. This process was inspired by disease contagion by long-distance insect flight. We recall a simple lattice model associated with the long-range CP [49–52], in which the activation process is

modified as follows. At a rate $\kappa P(\mathbf{x})$, each active particle activates an inactive particle at distance $|\mathbf{x}|$ in a random direction. $P(\mathbf{x})$ is thought to follow the power law $P(\mathbf{x}) \sim 1/|\mathbf{x}|^{d+p}$, where d is the spatial dimension, and $p > 0$ is a control parameter. Owing to the long-range interaction, the transition property of the DP class can be changed when $p < p_c$, where p_c depends on the dimension d [50]. When $p > p_c$, the long-range interaction is irrelevant. The other variant is the so-called tricritical CP [53–57]. In this modification, in addition to the ordinary CP, an inactive particle becomes active at a rate ω when it contacts two consecutive active particles. This tricritical CP exhibits a first-order transition for $\kappa < \omega$ and a second-order transition for $\kappa > \omega$. Thus, a tricritical point occurs at $\kappa = \omega$ with the tricritical directed percolation (TDP) class.

Although the DP class is theoretically well established, experimental realization of DP behavior has been elusive. It was only recently that two experiments associated with this DP class were implemented [24, 46]. We are particularly interested in the experiment in dissipative quantum systems of Rydberg atoms. An essential factor for realizing the DP class in Rydberg atoms is the antiblockade effect. An inactive spin is activated by detuning the excitation energy so that it is comparable to the energy of interaction with the active spin of the nearest neighbor [58, 59]. This is reminiscent of the branching process in the CP. We remark that the antiblockade dynamics can be implemented incoherently when strong dephasing noise is applied. Then, quantum coherence becomes negligible, and the dynamics is reduced to the classical DP process. When quantum coherence is effective, this case is called the quantum contact process (QCP), and coherent and incoherent CPs can be realized simultaneously [25,26]. Competition between the two types of process leads to the TDP class at the tricritical point. This resembles the behavior of spin glass systems, in which competing interactions between spins generate a negative cubic term of the Landau free energy and a tricritical point. In the strong quantum regime, the system undergoes a discontinuous transition.

When Rydberg atoms interact via the dipole–dipole interaction, it is natural to

consider cold atomic systems with long-range interaction. Similar studies of dipole–dipole interactions were performed in quantum systems associated with several phenomena, for instance, quantum magnetism [60–62], Anderson localization [63–65], Rydberg energy transport [66], and Rydberg blockade [67]. However, the long-range Rydberg atom system under the antiblockade condition has not been investigated yet, even though the results are expected to contribute to theoretical development of the QCP. In this paper, we consider the long-range QCP in the open quantum spin system. We set up the Lindblad equation for the density matrix in terms of the Hamiltonian with long-range interaction and the dissipators for decay and long-range branching and coagulation. Using mean-field (MF) theory, we obtain a phase diagram including absorbing and active states, and discontinuous and continuous transition curves with a tricritical point. This diagram is similar to that of the classical TDP model. However, the continuous transition changes from the ordinary DP to the long-range DP class [49, 52]. The TDP transition at the tricritical point also changes. We expect it to be in a long-range TDP class corresponding to the TDP; however, it has not been explored yet. Using the scaling argument, we determine the critical exponents of the long-range TDP in the MF limit. Moreover, we determine the upper critical dimension.

The remainder of this paper is organized as follows. In Sec. 3.2.2, we derive the quantum Langevin equation of the long-range QCP. The MF equation and its phase diagram are presented in Sec. 3.3, and the scaling behavior and upper critical dimension are presented in Sec. 3.4. Finally, we conclude our work and discuss the relationship between our model and the behavior of interacting cold gases in Sec. 3.5.

3.2 Equations of motion for the long-range quantum contact process

3.2.1 Lindblad equation

The Lindblad equation describes a quantum system coupled to the environment in the context of the Born–Markov approximation [27]. We consider a quantum spin model on a d-dimensional lattice, where each spin state denotes the state of a single atom at a site with $|\uparrow\rangle$, that is, an active state, and $|\downarrow\rangle$, that is, an inactive state. Interactions between atoms and between atoms and the baths may result in the dynamics of the QCP, which are described by the Lindblad equation. The equation is generally composed of the Hamiltonian and dissipative terms. Our equation also contains the coherent terms for branching and coagulation and incoherent ones for not only branching and coagulation, but also decay of active states (see Fig. 1), and is given by

$$
\begin{aligned}
\partial_t \hat{\rho} &= -i\left[\hat{H}_S, \hat{\rho}\right] + \sum_l \left[\hat{L}_l^{(d)} \hat{\rho} \hat{L}_l^{(d)\dagger} - \frac{1}{2}\left\{\hat{L}_l^{(d)\dagger} \hat{L}_l^{(d)}, \hat{\rho}\right\}\right] \\
&\quad + \sum_{i=b,c} \sum_{l,m} \left[\hat{L}_{ml}^{(i)} \hat{\rho} \hat{L}_{ml}^{(i)\dagger} - \frac{1}{2}\left\{\hat{L}_{ml}^{(i)\dagger} \hat{L}_{ml}^{(i)}, \hat{\rho}\right\}\right],
\end{aligned} \tag{3.1}
$$

where the Hamiltonian $\hat{H}_S$ is defined as

$$
\hat{H}_S = \omega \sum_{l,m} P(|\mathbf{x}_m - \mathbf{x}_l|)\left(\hat{n}_m \hat{\sigma}_l^+ + \hat{n}_m \hat{\sigma}_l^-\right), \tag{3.2}
$$

and the Lindblad jump operators of decay, branching, and coagulation are given by

$$
\hat{L}_l^{(d)} = \sqrt{\gamma}\hat{\sigma}_l^-, \tag{3.3}
$$

$$
\hat{L}_{ml}^{(b)} = \left[\kappa P(|\mathbf{x}_m - \mathbf{x}_l|)\right]^{1/2} \hat{n}_m \hat{\sigma}_l^+, \tag{3.4}
$$

$$
\hat{L}_{ml}^{(c)} = \left[\kappa P(|\mathbf{x}_m - \mathbf{x}_l|)\right]^{1/2} \hat{n}_m \hat{\sigma}_l^-, \tag{3.5}
$$
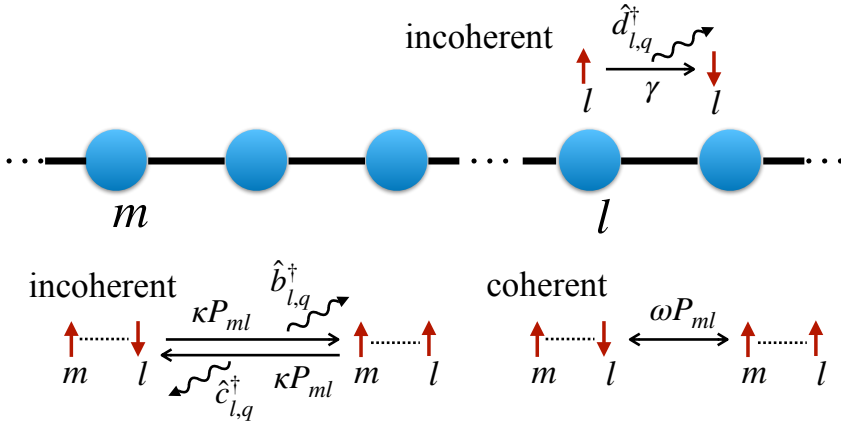
Figure 3.1: Schematic of QCP with long-range interaction in one dimension. In this model, there are two incoherent processes and one coherent process, which are represented by the total Hamiltonian in Eq. (3.7). The incoherent processes are induced by interaction with harmonic baths. The first incoherent process decays each site (denoted as l) by raising the harmonic bath's state at the rate γ, given by the second summation term in Eq. (3.8). The second incoherent process consists of branching and coagulation. Specifically, if site m is in an active state, site l branches (coagulates) at a rate κP_{ml} via directional links (denoted as ml) by raising the bath's state, which is given by the second summation term in Eqs. (3.9) and (3.10). The rate decreases algebraically as the distance increases. Similarly, the coherent process, which consists of quantum long-range branching and coagulation and involves the off-diagonal elements of the density matrix during the dynamics, is induced by the system Hamiltonian [Eq. (3.2)].

respectively. Here, $\hat{\sigma}_l^+$ and $\hat{\sigma}_l^+$ are the raising and lowering operators of the spin at site l, respectively, which are defined in terms of the spin basis as $\hat{\sigma}^+ = |\uparrow\rangle\langle\downarrow|$ and $\hat{\sigma}^- = |\downarrow\rangle\langle\uparrow|$.

Because $\hat{n}_l$ is the number operator of the active state, $\hat{n} = |\uparrow\rangle\langle\uparrow|$, the composite operator $\hat{n}_m\hat{\sigma}_l^+$ or $\hat{n}_m\hat{\sigma}_l^-$ with $l \neq m$ means that the active state at site m activates or deactivates the state at l, representing the branching and coagulation processes, as seen in Eqs. (3.2), (3.4), and (3.5). Instead, $\hat{L}_l^{(d)}$ denotes the decay dynamics of the active state at l. Therefore, if there is no active state, no further dynamics occurs, implying an absorbing state. Note that m and l need not be a nearest-neighbor pair in the interaction. Indeed, $P(|\mathbf{x}_m - \mathbf{x}_l|)$ in the dynamic equation [Eq. (6.1)] represents the

Lévy distribution, which decays as

$$P(|\mathbf{x}_m - \mathbf{x}_l|) \sim 1/|\mathbf{x}_m - \mathbf{x}_l|^{p+d}, \tag{3.6}$$

and which determines the amplitude of the long-range interaction. Here, we set $P(|\mathbf{x}_m - \mathbf{x}_l|) = 0$ when $m = l$. In addition, the distribution satisfies the normalization condition,

$$\sum_m P(|\mathbf{x}_m - \mathbf{x}_l|) = \sum_l P(|\mathbf{x}_m - \mathbf{x}_l|) = 1.$$

It is obvious that the dynamics of populations (the diagonal elements of $\hat{\rho}$) in Eq. (6.1) in the absence of coherent dynamics is equivalent to the ordinary long-range contact process. Consequently, depending on parameters such as κ and γ, the steady state for $\omega = 0$ shows the active or inactive phase, and the transition between them belongs to the long-range DP universality class. If ω is increased, the coherence may change the nature of the transition in the system. Note that in the limit $p \to \infty$, our model becomes equivalent to the nearest-neighbor QCP in previous works [25, 26].

3.2.2 Total Hamiltonian

By solving the Lindblad equation, Eq. (6.1), one may find the phase diagram of the system; however, this is not easy when system size N becomes large, $N \gg 1$. Instead, in this work we take the semiclassical approach starting with the quantum Langevin equation, as seen in previous works for the nearest-neighbor QCP [25, 26].

To derive the Langevin equations, we first set the equivalent Hamiltonian for a system with N spins, N_b harmonic baths, and their interactions, where N_b is given by $N_b = 2N^2 - N$, as follows. The total Hamiltonian should be given by

$$\hat{H}_{\text{tot}} = \hat{H}_S + \sum_l \hat{H}_d(l) + \sum_{m,l} \left[\hat{H}_b(m,l) + \hat{H}_c(m,l) \right], \tag{3.7}$$

where $\hat{H}_S$ is the same as in Eq. (3.2). There are three types of Hamiltonians for the

baths and interactions (see Fig. 1). First, the Hamiltonian $\hat{H}_d$, which corresponds to the decay process, is assigned to each spin, and $\hat{H}_d(l)$ defined on spin l is then given by

$$\hat{H}_d(l) = \sum_q \theta_q \hat{d}^\dagger_{l,q} \hat{d}_{l,q} + \sum_q \left[\lambda_q \hat{d}^\dagger_{l,q} \hat{\sigma}^-_l + h.c. \right] , \tag{3.8}$$

where θ_q denotes the energy of bath particles with momentum q, and $h.c.$ stands for the Hermitian conjugate. Here, $\hat{d}^\dagger_{l,q}$ and $\hat{d}_{l,q}$ are the creation and annihilation operators, respectively, of particles of the bath associated with spin l, and λ_q is the coupling strength of the decay process of the active state accompanied by emission of a single bath particle. Note that baths having different site indices are mutually independent, which is represented in the commutation relation for $\hat{d}^\dagger_{l,q}$ and $\hat{d}_{l,q}$, that is, $[\hat{d}_{l,q}, \hat{d}^\dagger_{m,q'}] = \delta_{l,m} \delta_{q,q'}$.

The other Hamiltonians, for branching ($\hat{H}_b$) and coagulation ($\hat{H}_c$), are defined at each link (l,m) with direction, which means $\hat{H}_{b(c)}(m,l) \neq \hat{H}_{b(c)}(l,m)$. The branching and coagulation Hamiltonians are also given by the bath energy and interactions, similar to that of the decay process. Because branching and coagulation are allowed between long-distance spins, the interaction between the system and bath particles contains the distribution $P(|\mathbf{x}_m - \mathbf{x}_l|)$, so the Hamiltonians are given by

$$\hat{H}_b(m,l) = \sum_q \phi_q \hat{b}^\dagger_{ml,q} \hat{b}_{ml,q} + \sum_q \left[\chi_q \sqrt{P_{ml}} \hat{b}^\dagger_{ml,q} \hat{n}_m \hat{\sigma}^+_l + h.c. \right] ,$$
$$\tag{3.9}$$

$$\hat{H}_c(m,l) = \sum_q \phi_q \hat{c}^\dagger_{ml,q} \hat{c}_{ml,q} + \sum_q \left[\chi_q \sqrt{P_{ml}} \hat{c}^\dagger_{ml,q} \hat{n}_m \hat{\sigma}^-_l + h.c. \right] ,$$
$$\tag{3.10}$$

where P_{ml} is shorthand notation for the Lévy distribution. Further, $\hat{b}_{ml,q}$ and $\hat{c}_{ml,q}$ are also operators of the harmonic baths defined on the directional link, which satisfy the commutation relation, $[\hat{b}_{ml,q}, \hat{b}^\dagger_{m'l',q}] = \delta_{l,l'} \delta_{m,m'}$ (the relations for $\hat{c}_{lm,q}$ and $\hat{c}^\dagger_{lm,q}$ are obtained by replacing $\hat{b}$ and $\hat{b}^\dagger$ with $\hat{c}$ and $\hat{c}^\dagger$, respectively). Further, ϕ_q and χ_q are the

energy function and coupling between the system and baths, respectively, where the branching and coagulation Hamiltonians share the same functions. Note that we have thus used N_b independent baths, including N decay, $N(N-1)$ branching, and $N(N-1)$ coagulation baths.

To obtain Eq. (6.1) for the density operator, we consider that the bath is in a pure state $|0\rangle_B$ with zero temperature such that $\hat{d}|0\rangle_B = \hat{b}|0\rangle_B = \hat{c}|0\rangle_B = 0$. Following the Born–Markov approximation, where the density operator of the total system can be given approximately by the product state, $\hat{\rho}(t) \otimes \hat{\rho}_B$, with the stationary bath density $\hat{\rho}_B = |0\rangle\langle 0|_B$ [27], the density operator $\hat{\rho}(t+dt)$ is given by

$$\hat{\rho}(t+dt) = \text{tr}_B \left\{ e^{-idt\hat{H}_{\text{tot}}} \hat{\rho}(t) \otimes |0\rangle\langle 0|_B e^{idt\hat{H}_{\text{tot}}} \right\}. \tag{3.11}$$

Expanding the evolution operators up to the second order of dt and using $\langle \hat{H}_I \rangle_B$, where $\hat{H}_I$ is the part of Eq. (3.7) representing the interaction between the system and bath, and $\langle \cdot \rangle_B$ denotes $\langle 0| \cdot |0\rangle_B$ with the bath state, we write Eq. (3.11) up to the order of dt^2:

$$\begin{aligned}
\hat{\rho}(t+dt) &= \hat{\rho}(t) - idt\left[\hat{H}_S, \hat{\rho}(t)\right] \\
&\quad + dt^2 \left(\hat{H}_S \hat{\rho}(t) \hat{H}_S - \frac{1}{2}\left\{\hat{H}_S^2, \hat{\rho}(t)\right\} \right) \\
&\quad + dt^2 \left(\langle \hat{H}_I \hat{\rho}(t) \otimes |0\rangle\langle 0|_B \hat{H}_I \rangle_B - \frac{1}{2}\left\{\langle \hat{H}_I^2 \rangle_B, \hat{\rho}(t)\right\} \right).
\end{aligned} \tag{3.12}$$

Because $\langle \hat{d}_q \hat{d}_q^\dagger \rangle_B = 1$, $\langle \hat{b}_q \hat{b}_q^\dagger \rangle_B = 1$, and $\langle \hat{c}_q \hat{c}_q^\dagger \rangle_B = 1$, and otherwise the correlators of

bath particles are zero, the third line in Eq. (3.12) can be written as

$$dt^2 \sum_l \sum_q \lambda_q^2 \left[\hat{\sigma}_l^- \hat{\rho} \left(\hat{\sigma}_l^- \right)^\dagger - \frac{1}{2} \left\{ \left(\hat{\sigma}_l^- \right)^\dagger \hat{\sigma}_l^- , \hat{\rho} \right\} \right]$$

$$+ dt^2 \sum_{l,m} \sum_q \chi_q^2 P_{ml} \left[\hat{n}_m \hat{\sigma}_l^+ \hat{\rho} \left(\hat{n}_m \hat{\sigma}_l^+ \right)^\dagger - \frac{1}{2} \left\{ \left(\hat{n}_m \hat{\sigma}_l^+ \right)^\dagger \hat{n}_m \hat{\sigma}_l^+ , \hat{\rho} \right\} \right]$$

$$+ dt^2 \sum_{l,m} \sum_q \chi_q^2 P_{ml} \left[\hat{n}_m \hat{\sigma}_l^- \hat{\rho} \left(\hat{n}_m \hat{\sigma}_l^- \right)^\dagger - \frac{1}{2} \left\{ \left(\hat{n}_m \hat{\sigma}_l^- \right)^\dagger \hat{n}_m \hat{\sigma}_l^- , \hat{\rho} \right\} \right] .$$

In accordance with the Weisskopf–Wigner theory [68], we extract the slow mode of bath particles around $q = 0$ by setting $\lambda_q \approx \lambda_{q=0}$ and $\chi_q \approx \chi_{q=0}$. Then, the summations over q become $\sum_q \lambda_q^2 \approx \lambda_0^2 \sum_q$ and $\sum_q \chi_q^2 \approx \chi_0^2 \sum_q$. To evaluate $\sum_q$, we use the definition of the Dirac delta function, $(2\pi)^{-1} \sum_q \exp(-i\omega_q \tau) = \delta(\tau)$, with a linear function ω_q of q. Inserting $\tau = 0$ in both $\exp(-i\omega_q \tau)$ and $\delta(\tau)$, one can see

$$dt^2 \lambda_0^2 \sum_q \to dt \, 2\pi \lambda_0^2 , \quad dt^2 \chi_0^2 \sum_q \to dt \, 2\pi \chi_0^2 ,$$

where we have used the fact that $\delta(0) \to 1/dt$ as $dt \to 0$. Therefore, we can reduce dt^2 to dt in the third line of Eq. (3.12). Defining $\gamma = 2\pi \lambda_0^2$ and $\kappa = 2\pi \chi_0^2$, and retaining the order of dt, we arrive at the Lindblad equation [Eq. (6.1)] from Eq. (3.12).

3.2.3 Quantum Langevin equation

Now, we derive the equations of motion for the system degrees of freedom from the Heisenberg equation in the total Hilbert space. During the procedure, noise and the influence of heat baths will be defined so that the quantum Langevin equation, which is the starting point for the semiclassical theory of the long-range QCP, can be obtained.

For the system operators $\hat{a}_l = \hat{\sigma}_l^x, \hat{\sigma}_l^y, \hat{n}_l$, which are Hermitian operators, the Heisen-

berg equation is given by $\partial_t \hat{a}_l(t) = i[\hat{H}, \hat{a}_l(t)]$; then

$$\partial_t \hat{a}_l = i \left\{ [\hat{H}_S, \hat{a}_l] + [\hat{H}_d(l), \hat{a}_l] + \sum_{m,j=b,c} [\hat{H}_j(m,l) + \hat{H}_j(l,m), \hat{a}_l] \right\}. \qquad (3.13)$$

The first term in Eq. (3.13) consists only of system operators:

$$i[\hat{H}_S, \hat{a}_l] = i\omega \sum_m P_{ml} \left([\hat{n}_m \hat{\sigma}_l^+, \hat{a}_l] + [\hat{n}_l \hat{\sigma}_m^+, \hat{a}_l] + h.c. \right), \qquad (3.14)$$

and the other terms, which are obtained from commutation with the interaction terms, are mixtures of the system and bath operators, as shown below. The commutation with the decay Hamiltonian reads

$$i[\hat{H}_d(l), \hat{a}_l] = \sum_q \lambda_q \left(i\hat{d}_{l,q}^\dagger [\hat{\sigma}_l^-, \hat{a}_l] - i[\hat{a}_l, \hat{\sigma}_l^+] \hat{d}_{l,q} \right), \qquad (3.15)$$

that with the branching Hamiltonian is

$$i[\hat{H}_b(m,l), \hat{a}_l] = \sum_q \chi_q \sqrt{P_{ml}} \left(i\hat{b}_{ml,q}^\dagger [\hat{n}_m \hat{\sigma}_l^+, \hat{a}_l] + h.c. \right), \qquad (3.16)$$

and finally, that with the coagulation Hamiltonian is

$$i[\hat{H}_c(m,l), \hat{a}_l] = \sum_q \chi_q \sqrt{P_{ml}} \left(i\hat{c}_{ml,q}^\dagger [\hat{n}_m \hat{\sigma}_l^-, \hat{a}_l] + h.c. \right). \qquad (3.17)$$

Note that $i[\hat{H}_{b(c)}(l,m), \hat{a}_l]$ can be obtained by replacing l and m with each other, except for $\hat{a}_l$, in Eqs. (3.16) and (3.17). Here, the Heisenberg picture has been used for all operators such that $\hat{a}_l \equiv \hat{a}_l(t) = e^{i\hat{H}t} \hat{a}_l(0) e^{-i\hat{H}t}$, where $\hat{a}_l(0)$ denotes the Schrödinger operator. Henceforth, an operator without an explicit time represents the Heisenberg operator at time t.

To proceed a step further, we need functional forms of $\hat{b}_{ml,q}$, $\hat{c}_{ml,q}$, and $\hat{d}_{l,q}$, whose equations of motion are also obtained from the Heisenberg equations, $\partial_t \hat{d}_{l,q} = i[\hat{H}_d(l), \hat{d}_{l,q}]$,

$\partial_t \hat{b}_{ml,q} = i[\hat{H}_b(m,l), \hat{b}_{ml,q}]$, and $\partial_t \hat{c}_{ml,q} = i[\hat{H}_c(m,l), \hat{c}_{ml,q}]$, respectively. It is easy to show that the solutions are given by

$$
\begin{aligned}
\hat{d}_{l,q} &= \hat{d}_{l,q}(0)e^{-i\theta_q t} - i\lambda_q \int_0^t d\tau \, \hat{\sigma}_l^-(\tau)e^{-i\theta_q(t-\tau)}, & (3.18) \\
\hat{b}_{ml,q} &= \hat{b}_{ml,q}(0)e^{-i\phi_q t} \\
& \quad - i\chi_q\sqrt{P_{ml}} \int_0^t d\tau \, \hat{n}_m(\tau)\hat{\sigma}_l^+(\tau)e^{-i\phi_q(t-\tau)}, & (3.19) \\
\hat{c}_{ml,q} &= \hat{c}_{ml,q}(0)e^{-i\phi_q t} \\
& \quad - i\chi_q\sqrt{P_{ml}} \int_0^t d\tau \, \hat{n}_m(\tau)\hat{\sigma}_l^-(\tau)e^{-i\phi_q(t-\tau)}. & (3.20)
\end{aligned}
$$

Plugging Eqs. (3.18)–(3.20) into Eqs. (3.15)–(3.17) reveals that the equation of motion for $\hat{a}_l$ can be divided into two parts, where one part is composed only of the system operators, and the other contains both system and bath operators. For example, inserting Eq. (3.18) into Eq. (3.15), we get

$$
\begin{aligned}
i\left[\hat{H}_d(l), \hat{a}_l\right] &= \sum_q \lambda_q \left(i\hat{d}_{l,q}^\dagger(0) \left[\hat{\sigma}_l^-, \hat{a}_l\right] e^{i\theta_q t} + h.c. \right) & (3.21) \\
& \quad - \sum_q \lambda_q^2 \int_0^t d\tau \left(\hat{\sigma}_l^+(\tau) \left[\hat{\sigma}_l^-, \hat{a}_l\right] e^{i\theta_q(t-\tau)} + h.c. \right),
\end{aligned}
$$

where the first line gives the quantum noise from the bath, and the second line is the dissipative term. Employing the Weisskopf-Wigner theory as shown in the previous section (3.2.2), we let λ_q be constant in Eq. (3.21), which leads to $\lambda_0^2 \sum_q e^{i\theta_q(t-\tau)} \approx 2\pi\lambda_0^2 \delta(t-\tau)$. Therefore, Eq. (3.21) reads

$$
\begin{aligned}
& \sqrt{\frac{\gamma}{2\pi}} \sum_q \left(i\hat{d}_{l,q}^\dagger(0)e^{i\theta_q t} \left[\hat{\sigma}_l^-, \hat{a}_l\right] - i\left[\hat{a}_l, \hat{\sigma}_l^+\right] \hat{d}_{l,q}(0)e^{-i\theta_q t} \right) \\
& \quad - \frac{\gamma}{2}\left(\hat{\sigma}_l^+ \left[\hat{\sigma}_l^-, \hat{a}_l\right] + \left[\hat{a}_l, \hat{\sigma}_l^+\right] \hat{\sigma}_l^- \right), & (3.22)
\end{aligned}
$$

because $\int_0^t d\tau \delta(t-\tau) = 1/2$, and $\gamma = 2\pi\lambda_0^2$. For Eqs. (3.16) and (3.17), one can also obtain similar expressions with $\kappa = 2\pi\chi_0^2$.

Because the second line in Eq. (3.22) can be rewritten as

$$\left(\sqrt{\gamma}\hat{\sigma}_l^-\right)^\dagger \hat{a}_l \sqrt{\gamma}\hat{\sigma}_l^- - \frac{1}{2}\left\{\left(\sqrt{\gamma}\hat{\sigma}_l^-\right)^\dagger \sqrt{\gamma}\hat{\sigma}_l^-, \hat{a}_l\right\} \equiv \hat{F}(\hat{a}_l, \sqrt{\gamma}\hat{\sigma}_l^-),$$

by combining Eqs. (3.14)–(3.17) with the Weisskopf–Wigner theory, we obtain the equations of motion for $\hat{a}_l$, which are given by

$$
\begin{aligned}
\partial_t \hat{a}_l &= i\omega \sum_m P_{ml}\left([\hat{n}_m\hat{\sigma}_l^+, \hat{a}_l] + [\hat{n}_l\hat{\sigma}_m^+, \hat{a}_l] + h.c.\right)\\
&\quad + \sum_{\alpha,m} \hat{F}\left(\hat{a}_l, \hat{I}_{lm}^\alpha\right) + \hat{\eta}(\hat{a}_l),
\end{aligned}
\tag{3.23}
$$

where for convenience we defined the interaction operators $\hat{I}_{lm}^\alpha$ as

$$
\begin{aligned}
\hat{I}_{lm}^1 &= \sqrt{\gamma}\hat{\sigma}_l^-\delta_{l,m},\\
\hat{I}_{lm}^2 &= \sqrt{\kappa P_{ml}}\,\hat{n}_m\hat{\sigma}_l^+,\quad \hat{I}_{lm}^3 = \sqrt{\kappa P_{ml}}\,\hat{n}_l\hat{\sigma}_m^+,\\
\hat{I}_{lm}^4 &= \sqrt{\kappa P_{ml}}\,\hat{n}_m\hat{\sigma}_l^-,\quad \hat{I}_{lm}^5 = \sqrt{\kappa P_{ml}}\,\hat{n}_l\hat{\sigma}_m^-.
\end{aligned}
\tag{3.24}
$$

The Kronecker delta function $\delta_{lm} = 1$ for $l = m$ and is zero otherwise. Although $\hat{I}_{lm}^\alpha$ has the same form as the Lindblad jump operators in Eqs. (3.3)–(3.5), it is composed of the Heisenberg operators defined at time t, which are different from the Lindblad operators. Finally, the *noise* operator $\hat{\eta}(\hat{a}_l, t)$ is also written in terms of $\hat{I}_{lm}^\alpha$ and the corresponding bath operators. We redefine the bath operators $\hat{B}_{lm,q}^\alpha(t)$ with the original operators as

$$
\begin{aligned}
\hat{B}_{lm,q}^1(t) &= \hat{d}_{l,q}(0)\,\delta_{l,m}e^{-i\theta_q t},\\
\hat{B}_{lm,q}^2(t) &= \hat{b}_{ml,q}(0)e^{-i\phi_q t},\quad \hat{B}_{lm,q}^3(t) = \hat{b}_{lm,q}(0)e^{-i\phi_q t},\\
\hat{B}_{lm,q}^4(t) &= \hat{c}_{ml,q}(0)e^{-i\phi_q t},\quad \hat{B}_{lm,q}^5(t) = \hat{c}_{lm,q}(0)e^{-i\phi_q t}.
\end{aligned}
\tag{3.25}
$$

Then, one can write the noise operator in the compact form

$$\hat{\eta}(\hat{a}_l) = \frac{i}{\sqrt{2\pi}} \sum_{\alpha} \sum_{m,q} \left(\hat{B}^{\alpha}_{lm,q}(t) \right)^{\dagger} \left[\hat{I}^{\alpha}_{lm}, \hat{a}_l \right] + h.c. \tag{3.26}$$

Obviously, the quantum average of the noise operators becomes zero: $\langle \hat{\eta}(\hat{a}_l) \rangle_B = 0$.

3.3 Mean-field result

3.3.1 Mean-field equations

To explore the MF phase transition of the QCP, we extract the MF equation from the quantum Langevin equation, Eq. (3.23), by taking the trace of the equations of the operators with the initial density operator given by $\hat{\rho}(0) \otimes \hat{\rho}_B$. By defining

$$a_l(t) \equiv \langle \hat{a}_l(t) \rangle = \operatorname{tr} \hat{a}_l(t) \hat{\rho}(0) \otimes \hat{\rho}_B, \tag{3.27}$$

the equations of the fields can be obtained; for example, the equation of motion for n_l is given by

$$\dot{n}_l = \omega \sum_m P_{ml} \langle \hat{n}_m \hat{\sigma}^y_l \rangle - \gamma n_l + \kappa \sum_m P_{ml} \left(n_m - 2 \langle \hat{n}_m \hat{n}_l \rangle \right). \tag{3.28}$$

One can also derive similar equations for $\sigma^x_l(t)$ and $\sigma^y_l(t)$. Ignoring correlations such as $\langle \hat{n}_m \hat{\sigma}^y_l \rangle \to n_m(t) \sigma^y_l(t)$ and taking uniform fields, $n_l(t) \to n(t)$, $\sigma^x_l(t) \to \sigma^x(t)$, and $\sigma^y_l(t) \to \sigma^y(t)$, we arrive at the MF equations, which are given by

$$
\begin{aligned}
\dot{n} &= \omega n \sigma^y + (\kappa - 1)n - 2\kappa n^2, \\
\dot{\sigma}^x &= -\omega \sigma^x \sigma^y - \frac{1+\kappa}{2} \sigma^x - \kappa n \sigma^x, \\
\dot{\sigma}^y &= \omega \left\{ 2n + (\sigma^x)^2 - 4n^2 \right\} - \frac{1+\kappa}{2} \sigma^y - \kappa n \sigma^y,
\end{aligned} \tag{3.29}
$$

where we rescale time, $t\gamma \to t$, $\omega/\gamma \to \omega$, and $\kappa/\gamma \to \kappa$. Note that the above equations are equivalent to the MF equation used in previous studies for the nearest-neighbor QCP model [25,26].

3.3.2 Phase diagram

In this section, we review the previous MF result, which is also similar to those in previous studies of TDP [29,47,54,55]. It is found that the steady-state solutions or fixed points, n_0, σ_0^x, and σ_0^y, satisfying $\dot{a} = 0$ in Eq. (3.29), form two groups as follows. One is given by

$$\sigma_0^x = 0, \qquad \sigma_0^y = \frac{4\omega n_0(1 - 2n_0)}{1 + \kappa + 2\kappa n_0},$$

$$n_0 = 0, \frac{\omega^2 - \kappa \pm \sqrt{(\omega^2 - \kappa)^2 + (\kappa^2 + 2\omega^2)(\kappa^2 - 1)}}{4\omega^2 + 2\kappa^2}, \tag{3.30}$$

and the other is given by

$$\sigma_0^x = \pm\sqrt{4n_0^2 - 2n_0 - (1 + \kappa + 2\kappa n_0)^2/(2\omega)^2}, \tag{3.31}$$

$$\sigma_0^y = -\frac{1 + \kappa + 2\kappa n_0}{2\omega}, \qquad n_0 = 0, \frac{1}{6} - \frac{1}{2\kappa}.$$

Note that if only real solutions are required, the latter should be ruled out because solutions n_0 do not give real values of σ_0^x in Eq. (3.31). Moreover, the nonzero solutions $n_0 = n_0^+ \equiv \frac{\omega^2 - \kappa + \sqrt{(\omega^2 - \kappa)^2 + (\kappa^2 + 2\omega^2)(\kappa^2 - 1)}}{4\omega^2 + 2\kappa^2}$ and $n_0 = n_0^- \equiv \frac{\omega^2 - \kappa - \sqrt{(\omega^2 - \kappa)^2 + (\kappa^2 + 2\omega^2)(\kappa^2 - 1)}}{4\omega^2 + 2\kappa^2}$ in Eq. (3.30) does not exist when $(\omega^2 - \kappa)^2 < (\kappa^2 + 2\omega^2)(1 - \kappa^2)$, which is inside the (blue) dashed curve and lower (black) dotted curve in Fig. 3.2.

Now, we check the stability of Eq. (3.30) through linearization of Eq. (3.29) around the fixed points. Inserting $n = n_0 + \delta n$, $\sigma^y = \sigma_0^y + \delta\sigma^y$, and $\sigma^x = \sigma_0^x + \delta\sigma^x$ into Eq. (3.29), and expanding up to the linear order of perturbations, we then obtain the
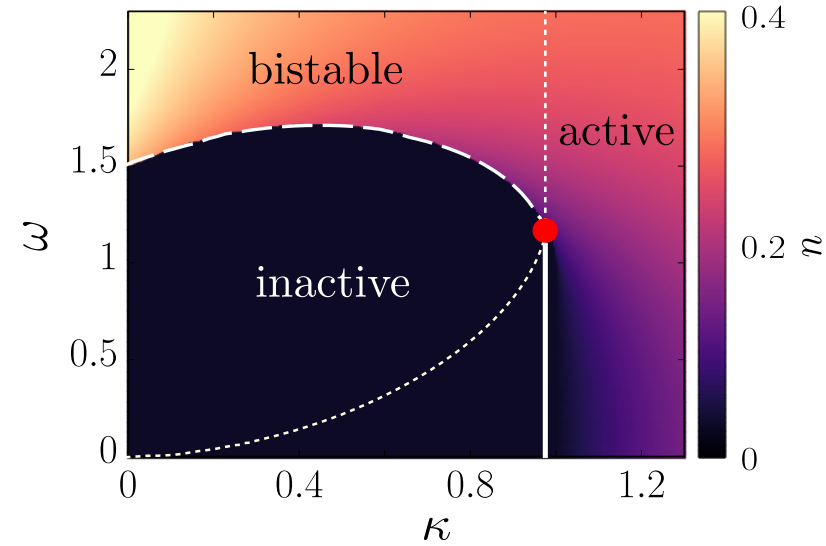
Figure 3.2: Phase diagram of QCP. This diagram is represented as a plot of the classical rate κ and the quantum rate ω. In the weak quantum regime, the second-order transition is observed [(red) solid vertical line and (red) filled circle; Eq. (E.9)]. In contrast, in the strong quantum regime, the absorbing transition is found to be of the first-order type [upper dashed (blue) curve between bistable and inactive states; Eq. (E.10)]. The (red) filled circle, at which the two transitions intersect, is the tricritical point. (Black) dotted vertical line represents the boundary of the number of the stable solutions and (black) lower dotted curve inside the inactive region represents the boundary between the existence and nonexistence of multiple solutions.

linear equation $\dot{\delta\mathbf{a}} = \mathbf{M}\delta\mathbf{a}$, where

$$\delta\mathbf{a} = (\delta n, \delta\sigma^y, \delta\sigma^x)^{\mathsf{T}}, \tag{3.32}$$

and the matrix $\mathbf{M}$ is

$$\mathbf{M} = \begin{pmatrix} \omega\sigma_0^y - 4\kappa n_0 + \kappa - 1 & \omega n_0 & 0 \\ -8\omega n_0 - \kappa\sigma_0^y + 2\omega & -\frac{2\kappa n_0 + \kappa + 1}{2} & 0 \\ 0 & 0 & -\frac{2\omega\sigma_0^y + 2\kappa n_0 + \kappa + 1}{2} \end{pmatrix}. \tag{3.33}$$

For $n_0 = \sigma_0^y = \sigma_0^x = 0$, all the eigenvalues of $\mathbf{M}$ are negative at $\kappa < 1$, meaning that the fixed point is stable, whereas one of the eigenvalues becomes positive when $\kappa > 1$. Thus, $\kappa = 1$ is the boundary for the fixed point, $n_0 = \sigma_0^y = \sigma_0^x = 0$.

For the nonzero solutions $n_0 = n_0^{+(-)}$ in Eq. (3.30), by investigating the eigenvalues of Eq. (3.33), one can note that $n_0 = n_0^+$ and $n_0 = n_0^-$ are stable when $n_0^+ > 0$ and $n_0^- < 0$, respectively. More precisely, $n_0 = n_0^+, \sigma_0^y = \sigma_0^y(n_0^+), \sigma_0^x = 0$ is the stable fixed point when $n_0^+ > 0$ and $n_0^+ > \frac{1}{6} - \frac{1}{2\kappa}$. Because negative density, $n < 0$, is not physically allowed, the fixed point $n_0 = n_0^- < 0$ should be ruled out in this analysis. To find the stable region of n_0^+, first we note that $n_0^+ \geq 0$ becomes marginal along two curves. One is the (red) solid vertical line including a (red) filled circle in Fig. 3.2,

$$\kappa = 1, \omega \leq 1, \tag{3.34}$$

where $n_0^+ = n_0 = 0$, and the other is the dashed (blue) curve, given by

$$\omega = \left(1 + \kappa - \kappa^2 + \sqrt{(1 + \kappa - \kappa^2)^2 - \kappa^4}\right)^{1/2} \text{ at } \kappa \leq 1, \tag{3.35}$$

where $n_0^+ = n_0^- \geq 0$. n_0^+ is found to be stable outside of the region enclosed by the two curves, Eqs. (E.9) and (E.10). Thus, the stability analysis yields the phase diagram shown in Fig. 3.2. With the boundaries described by Eqs. (E.9) and (E.10), there are

45

three regions: (i) the inactive phase, $n_0 = 0$, (ii) the active phase, $n_0 = n_0^+$, divided by Eq. (E.9) with a single stable fixed point, and (iii) a bistable phase possessing two stable fixed points, $n_0 = 0$ and $n_0 = n_0^+$, with the boundary curves of Eq. (E.10) and $\kappa = \kappa_c$ with $\omega > 1$. The solutions of Eq. (3.30) show that between (i) and (ii) there exist second-order phase transitions with the order parameter exponent $\beta = 1$ for $\omega < 1$ and $\beta = 1/2$ at $\omega = 1$. Moreover, one can observe that the first-order transition may occur between (i) and (iii), implying that $(\kappa, \omega) = (\kappa_c, 1)$ where the boundaries meet at the tricritical point.

By substituting the expression for σ_0^y in Eq. (3.30) into the equation for n [Eq. (3.29)], one may expand the equation with small n_0 near the critical line Eq. (E.9) as

$$\dot{n} = 0 = -u_2 n_0 - u_3 n_0^2 - u_4 n_0^3 + \mathcal{O}(n_0^4), \tag{3.36}$$

where $u_2 = (\kappa_c - \kappa)$, and u_3 and u_4 are given by

$$u_3 = \frac{2\kappa(1+\kappa) - 4\omega^2}{1+\kappa}, \qquad u_4 = \frac{8\omega^2(1+2\kappa)}{(1+\kappa)^2}, \tag{3.37}$$

respectively. Note that Eq. (3.36) implies an effective MF potential defined as

$$U_{MF} = \sum_{k=2} \frac{u_k}{k} n^k, \tag{3.38}$$

where u_k is defined in Eq. (3.36). Then, the solution n_0 satisfying Eq. (3.36) is also the steady-state solution of the single effective equation of the order parameter, which is given by

$$\dot{n} = -\partial U_{MF}/\partial n. \tag{3.39}$$

By expanding U_{MF} up to the fourth order, it is found that when $\omega < 1$, u_3 and u_4 are positive near $\kappa = \kappa_c$. Consequently, $n_0 = 0$ becomes unstable, and the stable fixed point is given by $n_0 \approx (\kappa - \kappa_c)/u_3$ at $\kappa > \kappa_c$; consequently, the DP critical exponent $\beta = 1$. On the other hand, at $\omega = 1$, it is found that $u_3 = 0$ at $\kappa = \kappa_c$ yields a different

universality, called the TDP class, where the fixed point is given by $n_0 \approx \sqrt{(\kappa - \kappa_c)/u_4}$ with $\beta = 1/2$. We conclude that the effective single equation Eq. (3.39) well describes the critical behavior in the steady state, which is consistent with the linear stability analysis based on the MF equations of all the system variables in Eq. (3.29).

We also observe that the effective equation Eq. (3.39) captures a change in the nature of the transition at the tricritical point $(\kappa, \omega) = (\kappa_c, 1)$. Expanding U_{MF} up to the fourth order again, as shown in Eq. (3.36), one can see that all the positive coefficients u_k yield the single fixed point $n_0 = 0$, but given negative u_3, an additional positive and stable fixed point can exist as

$$n_0 = \frac{-u_3 + \sqrt{u_3^2 - 4u_2 u_4}}{2u_4}, \tag{3.40}$$

where $u_3^2 \geq 4u_2 u_4$ is also satisfied. Because we consider only the limits $\kappa \to \kappa_c$ and $\omega \to 1$, the discriminant $u_3^2 = 4u_2 u_4$ may give the curve near the tricritical point,

$$\omega = 1 + \sqrt{3(\kappa_c - \kappa)/2}, \tag{3.41}$$

which is also obtainable by expanding Eq. (E.10) at $\kappa = \kappa_c$. Of course, there is another solution, $\omega = 1 - \sqrt{3(\kappa_c - \kappa)/2}$, but it does not satisfy $u_3 < 0$. If $\omega > 1 + \sqrt{3(\kappa_c - \kappa)/2}$ at $\kappa < \kappa_c$, there are two stable fixed points, $n_0 = 0$ and Eq. (3.40), which is consistent with the previous discussion of the linear stability analysis. Because the fixed point of Eq. (3.40) disappears abruptly, and $n_0 = 0$ becomes the only fixed point crossing the curve of Eq. (3.41) from right to left, one may observe the first-order phase transition in this regime. Although the analysis of the MF potential for the first-order transition is valid near the tricritical point, the entire analysis of linear stability with Eq. (3.32) implies a first-order transition with the transition line described by Eq. (E.10).

3.4 Scaling behavior

3.4.1 Phenomenological equation

To investigate the low-dimensional QCP, one may add spatiotemporal fluctuations to the MF equations, Eq. (3.29), as seen in previous works [25,26], where the action for n, σ^x, and σ^y is obtained by the so-called Martin–Siggia–Rose–Janssen–de Dominicis (MSRJD) field theory [11,69-71]. In this work, instead we start with the effective MF equation of n, Eq. (3.39), which is a plausible assumption near the critical line in Eq. (E.9) because σ^x and σ^y may arrive quickly in the steady state [Eq. (3.30)] owing to the finite gap energy, as seen in Eq. (3.29). Near the critical line, by plugging $n_0 \approx \sigma_0^y \approx 0$ and $\sigma_0^x = 0$ into Eq. (3.29), one can see that the excitation gap for σ^x and σ^y is given by $(1 + \kappa_c)/2$. Then, the critical dynamics can be described by a single equation associated with n and based on Eq. (3.39) with fluctuations. Using the standard MSRJD theory and the scaling theory, we will show the critical exponents and upper critical dimensions of the long-range QCP.

The phenomenological Langevin description has been regarded as a very useful method to study the critical phenomena of DP-type models [28,29], where the strength of the white noise is proportional to the density of active states because stochasticity is induced by the active states. We also follow the phenomenological approach to obtain the Langevin-type effective equation. Note that the field n in the MF equations is the expectation value of the operator obtained by the trace over the density operator, as seen in Eq. (3.27), implying that n can also be thought of as an averaged field over the quantum noise manifested in the noise operator in Eq. (3.23). To describe the noise, one may start from the equations of operators. Instead of using the quantum noise operators [Eq. (3.26)] directly, we introduce a stochastic density field ξ satisfying $\overline{\xi} = n$, where the overbar denotes the average over a phenomenological noise η. We regard ξ as a coarse-grained field of the active sites measured in a single realization, and take η as the white Gaussian noise, which is plausible in thermodynamic limit. Near the critical

point, ξ may be governed by the effective Langevin equation keeping the low energy fluctuations, given by

$$\partial_t \xi_l = \kappa \sum_m P_{ml} \xi_m - \kappa \xi_l - \frac{\partial U_{MF}(\xi_l)}{\partial \xi_l} + \eta_l, \qquad (3.42)$$

where the first term is the lowest order contribution of Lévy flight, and the potential $U_{MF}(\xi)$ is defined as having the same form as in Eq. (3.38),

$$U_{MF}(\xi) = \sum_{k=2} \frac{u_k}{k} \xi^k. \qquad (3.43)$$

Setting $\overline{\eta} = 0$, taking the average of η in Eq. (3.42), and ignoring correlations such that $\overline{\xi^k} \approx n^k$ with $k \geq 2$ and fluctuations, one can obtain the same MF equation as Eq. (3.39) from the equation for ξ, Eq. (3.42).

The noise η should be invoked by the original quantum dynamics so that Eq. (3.42) reflects the original dynamics of $\hat{n}$. In the original dynamics, existing active states can generate stochastic processes such as decay and branching via interactions with the baths. Therefore, we require that the strength $\mathscr{D}$ defined in

$$\overline{\eta_l(t)\eta_m(t')} = \mathscr{D}_l \, \delta_{m,l} \, \delta(t-t') \qquad (3.44)$$

depends on the density ξ_l as $\mathscr{D}_l \propto \xi_l$, implying also that when $\xi = 0$, there is no fluctuation, so the absorbing state is achieved. Moreover, one may suspect that the original quantum noise itself also obeys the similar relation

$$\langle \hat{\eta}(\hat{n}_l(t)) \, \hat{\eta}(\hat{n}'_m(t')) \rangle_B \approx \hat{\mathscr{D}}_l \, \delta_{m,l} \, \delta(t-t'), \qquad (3.45)$$

with $\hat{\mathscr{D}}_l \propto \langle \hat{n}_l \rangle_B$, where $\hat{\mathscr{D}}$ is the strength of the quantum noise [68, 72]. Indeed, it has been revealed that the quantum noise strength in the nearest-neighbor QCP is proportional to $\langle \hat{n} \rangle_B$ [25, 26]. If this is also true in our case, we can assume that the phe-

nomenological noise η originates from the quantum noise operator $\hat{\eta}$ with a strength $\overline{\mathcal{D}} = \langle \hat{\mathcal{D}} \rangle$, at least up to the leading order.

Now, we check the strength of the quantum noise in the long-range QCP, which is given by the correlators of the noise operators in Eq. (3.26):

$$\langle \hat{\eta}(\hat{a}_l(t)) \hat{\eta}(\hat{a}'_k(t')) \rangle_B = \mathrm{tr}_B \frac{1}{2\pi} \sum_{\alpha,\beta} \sum_{m,q} \sum_{m',q'} \left[\hat{a}_l(t), \left(\hat{I}^{\alpha}_{lm}(t) \right)^{\dagger} \right] \qquad (3.46)$$
$$\times \hat{B}^{\alpha}_{lm,q}(t) \left(\hat{B}^{\beta}_{km',q'}(t') \right)^{\dagger} \left[\hat{I}^{\beta}_{km'}(t'), \hat{a}'_k(t') \right] \hat{\rho}_B,$$

where again $\hat{\rho}_B = |0\rangle\langle 0|_B$. By using the commutation relations of $\hat{B}^{\alpha}$, Eq. (3.46) can be divided into three parts:

$$\hat{\mathcal{D}}_1 \delta_{l,k} \delta(t - t') + \hat{\mathcal{D}}_2 \delta(t - t') + \hat{\mathcal{D}}_3 \delta_{t,t'}, \qquad (3.47)$$

where the first term is given by

$$\hat{\mathcal{D}}_1 = \mathrm{tr}_B \sum_{\alpha} \sum_{m} \left[\hat{a}_l, \left(\hat{I}^{\alpha}_{lm} \right)^{\dagger} \right] \left[\hat{I}^{\alpha}_{lm}, \hat{a}'_l \right] \hat{\rho}_B, \qquad (3.48)$$

the second term $\hat{\mathcal{D}}_2$ reads

$$\hat{\mathcal{D}}_2 = \mathrm{tr}_B \left\{ \left[\hat{a}_l, \left(\hat{I}^2_{lk} \right)^{\dagger} \right] \left[\hat{I}^3_{kl}, \hat{a}'_k \right] + \left[\hat{a}_l, \left(\hat{I}^3_{lk} \right)^{\dagger} \right] \left[\hat{I}^2_{kl}, \hat{a}'_k \right] \right.$$
$$\left. + \left[\hat{a}_l, \left(\hat{I}^4_{lk} \right)^{\dagger} \right] \left[\hat{I}^5_{kl}, \hat{a}'_k \right] + \left[\hat{a}_l, \left(\hat{I}^5_{lk} \right)^{\dagger} \right] \left[\hat{I}^4_{kl}, \hat{a}'_k \right] \right\} \hat{\rho}_B, \qquad (3.49)$$

and finally,

$$\hat{\mathcal{D}}_3 = \mathrm{tr}_B \frac{1}{4} \sum_{\alpha,\beta} \sum_{m,m'} \left[\left[\hat{a}_l, \left(\hat{I}^{\alpha}_{lm} \right)^{\dagger} \right], \left(\hat{I}^{\beta}_{km'} \right)^{\dagger} \right] \left[\hat{I}^{\alpha}_{lm}, \left[\hat{I}^{\beta}_{km'}, \hat{a}'_k \right] \right] \hat{\rho}_B, \qquad (3.50)$$

where we omitted the site indices in $\hat{\mathcal{D}}_{1,2,3}$. To obtain $\hat{\mathcal{D}}_3$, we used the fact that the system operators and bath operators commute when they are at the same time, for instance, $\hat{n}_l(t)\hat{d}_{l,q}(t) = \hat{d}_{l,q}(t)\hat{n}_l(t)$. Further, using the solutions of the bath particles,

Eqs. ([3.18](#))–([3.20](#)), with the Weisskopf–Wigner theory, one can obtain the above form of $\hat{\mathscr{D}}_3$.

In Eq. ([3.47](#)), the contribution of $\hat{\mathscr{D}}_3$ can be ignored because $\delta(t - t') \gg \delta_{t,t'}$ at $t = t'$. Moreover, $\hat{\mathscr{D}}_2$ contains the contributions of only the pair (l, k), whereas l-to-all coupling contributes to $\hat{\mathscr{D}}_1$. Therefore, the strength of the noise, including $\hat{\mathscr{D}}$ in Eq. ([3.45](#)), may be determined mainly by $\hat{\mathscr{D}}_1$. Because $\hat{\mathscr{D}}_1$ is not a Hermitian operator, to obtain a real value, we take

$$\mathrm{Re}\langle\hat{\mathscr{D}}_1\rangle \equiv \langle\hat{\mathscr{D}}_1 + \hat{\mathscr{D}}_1^\dagger\rangle/2. \tag{3.51}$$

Now, we can obtain the noise strength $\mathrm{Re}\langle\hat{\mathscr{D}}_l\rangle$ for $\hat{\eta}(\hat{n}_l)$ from Eq. ([3.51](#)) by setting $\hat{a}_l = \hat{a}'_l = \hat{n}_l$:

$$\mathrm{Re}\langle\hat{\mathscr{D}}_l\rangle = n_l + \kappa \sum_m P_{ml} n_m. \tag{3.52}$$

Because we are interested in the critical dynamics, where long-wavelength excitation is crucial, we use the approximation $n_m \approx n_l$ for all m in the summation term in Eq. ([3.52](#)), which leads to

$$\mathrm{Re}\langle\hat{\mathscr{D}}_l\rangle \approx (1 + \kappa)n_l. \tag{3.53}$$

This is what we expected, and now we take $\mathscr{D}_l = (1 + \kappa)\xi_l$ for the noise strength in our Langevin equation [Eq. ([3.42](#))].

We point out that the leading order of the noise strength for $\hat{\sigma}^x$ or $\hat{\sigma}^x$ is given by a constant; more precisely,

$$\mathrm{Re}\langle\hat{\eta}(\hat{\sigma}_l^x(t))\,\hat{\eta}(\hat{\sigma}_l^x(t'))\rangle \approx \mathrm{Re}\langle\hat{\eta}(\hat{\sigma}_l^y(t))\,\hat{\eta}(\hat{\sigma}_l^y(t'))\rangle \approx (1 + \kappa)\delta(t - t').$$

Moreover, the noise operator $\hat{\eta}(\hat{n})$ is correlated with $\hat{\eta}(\hat{\sigma}^x)$ and $\hat{\eta}(\hat{\sigma}^y)$ as follows:

$$\text{Re}\,\langle \hat{\eta}(\hat{n}_l(t))\,\hat{\eta}(\hat{\sigma}_l^x(t'))\rangle \quad \approx \quad \sigma_l^x \delta(t-t')/2\,,$$

$$\text{Re}\,\langle \hat{\eta}(\hat{n}_l(t))\,\hat{\eta}(\hat{\sigma}_l^y(t'))\rangle \quad \approx \quad \sigma_l^y \delta(t-t')/2\,.$$

Thus, even if there is no active state at some point, active states can be induced by fluctuations of $\hat{\sigma}^x$ and $\hat{\sigma}^y$, which implies that the absorbing state cannot be achieved. This is reminiscent of the quantum fluctuation induced by the uncertainty relations between the Pauli spin operators. Therefore, our semiclassical approach must be associated with a proper time scale, where the quantum fluctuation is negligible. At this stage, we assume the time scale without proof.

In short, we introduced the stochastic field ξ as the density field of active states and its phenomenological Langevin equation. To capture the critical dynamics of QCP, we took the lowest-order fluctuation in the long-range interaction to the MF equation of the order parameter n. Since the original dynamics shows the absorbing transition, we assumed that the strength of the white Gaussian noise is proportional to the density field. Indeed, we confirmed that the original quantum noise also has the multiplicative nature, so we adopted the functional form of the quantum-noise strength in the lowest order as one of our phenomenological noise η. Because the Langevin equation of ξ is the classical field equation, one can apply the classical field theory to the QCP effectively at least near the critical point. Finally, we remark that the quantum Langevin equation can be transformed to the *c*-number Langevin equation [72, 73]. One may apply the conversion method in this work and expect to obtain a similar equation to ours, Eq. (3.42). To check whether our assumptions are adequate and resolve the problem of time scale, it is worth studying the relationship between the phenomenological and Langevin equations.

Table 3.1: MF critical exponents. These critical exponents are obtained using the scaling transformation of Eq. (3.58). The universality classes are determined by the power of the long-range interaction (p) and the strength of the coherent dynamics (ω in $\hat{H}_s$). The long-range interaction is relevant (irrelevant) for $p \leq 2$ ($p > 2$). Depending on whether $u_3 = 0$ or $u_3 > 0$, d_c and β can vary.

		d_c	β	$\nu_\perp$	$\nu_\parallel$	z
$\kappa = \kappa_c, \omega = 1$	$p > 2$ (TDP)	3	$1/2$	$1/2$	1	2
($u_3 = 0$)	$p \leq 2$ (long-range TDP)	$3p/2$	$1/2$	$1/p$	1	p
$\kappa = \kappa_c, \omega < 1$	$p > 2$ (DP)	4	1	$1/2$	1	2
($u_3 > 0$)	$p \leq 2$ (long-range DP)	$2p$	1	$1/p$	1	p

3.4.2 Critical exponents and upper critical dimensions

To apply the scaling theory, the equation for continuous fields is more convenient than the discrete equation. Taking the continuum limit with an appropriate rescaling like $\partial_t \to \tau \partial_t$, where τ is a scaling parameter, and expanding the Lévy term up to two leading orders, as in previous works [49–52, 74], we write the Langevin equation of the continuous density field $\xi = \xi(\mathbf{r}, t)$ up to the u_4 term as

$$\tau \partial_t \xi = D \nabla^2 \xi + D_p \nabla^p \xi - u_2 \xi - u_3 \xi^2 - u_4 \xi^3 + \eta. \tag{3.54}$$

Here D and D_p are the diffusion constants, obtained from the expansion, given by $\kappa \int d\mathbf{r}' P(|\mathbf{r} - \mathbf{r}'|) \xi(\mathbf{r}') \approx \kappa \xi + D \nabla^2 \xi + D_p \nabla^p \xi$, and the noise $\eta(\mathbf{r}, t)$ in the continuum limit obeys

$$\overline{\eta(\mathbf{r}_1, t_1) \eta(\mathbf{r}_0, t_0)} = \Gamma \xi(\mathbf{r}_0, t_0) \delta(\mathbf{r}_1 - \mathbf{r}_0) \delta(t_1 - t_0), \tag{3.55}$$

where $\Gamma = (1 + \kappa)$. Note that u_k in Eq. (3.54) was also rescaled appropriately.

Setting $\Gamma = 0$, which yields $\xi = n$, one can obtain the MF exponents for the correlation length, $\nu_\perp$, and time, $\nu_\parallel = z \nu_\perp$. Under the scaling transformations, which are

given by

$$|\mathbf{r}| \to |\mathbf{r}'| = s|\mathbf{r}|, \, t \to t' = s^z t, \, \xi \to \xi', \tag{3.56}$$

where $s > 1$, the transformed equation is written as

$$\tau s^{-z} \partial_t \xi' = D s^{-2} \nabla^2 \xi' + D_p s^{-p} \nabla^p \xi' - u_2 \xi' - u_3 \xi'^2 - u_4 \xi'^3. \tag{3.57}$$

Because near the critical point the order parameter obeys the scaling form of $\xi'(\mathbf{r}') = s^{-\beta/\nu_\perp} \xi(\mathbf{r})$ [28, 29], we rewrite Eq. (3.57) in terms of ξ as

$$\tau \partial_t \xi = D s^{z-2} \nabla^2 \xi + D_p s^{z-p} \nabla^p \xi - u_2 s^z \xi - u_3 s^{z-\beta/\nu_\perp} \xi^2 - u_4 s^{z-2\beta/\nu_\perp} \xi^3.$$

When $p > 2$ and $u_3 > 0$, one may set $z = 2$ and $\beta/\nu_\perp = z = 2$; then, at the critical point where $u_2 = 0$, the equation given by

$$\tau \partial_t \xi = D \nabla^2 \xi - u_3 \xi^2$$

is invariant under the scaling transformation because $D_p s^{z-p} \nabla^p \xi$ and $u_4 s^{z-2\beta/\nu_\perp} \xi^3$ vanish by repeated transformations. Using the value $\beta = 1$, we obtain the exponents, $\nu_\perp = 1/2$, and thus $\nu_\parallel = 1$. These exponents belong to the DP class.

For $p > 2$ and $u_3 = 0$, however, the relevant equation is given by

$$\tau \partial_t \xi = D \nabla^2 \xi - u_4 \xi^3,$$

so $\beta/\nu_\perp = z/2 = 1$. Using $\beta = 1/2$ at the tricritical point corresponding to $u_3 = 0$, we obtain the exponents $\nu_\perp = 1/2$ and $\nu_\parallel = 1$, which correspond to the TDP universality. Therefore, if $p > 2$, the long-range term becomes irrelevant for both $u_3 > 0$ and $u_3 = 0$, so the universality is equal to that in the short-range model. On the other hand, if $p < 2$, one can see that the relevant term becomes $D_p s^{z-p} \nabla^p \xi$ instead of $D s^{z-2} \nabla^2 \xi$, leading to the dynamic exponent $z = p$. Consequently, $\beta/\nu_\perp = z = p$ for $u_3 > 0$, whereas

$\beta/\nu_\perp = z/2 = p/2$ for $u_3 = 0$, yielding $\nu_\perp = 1/p$ for both cases. The MF exponents for the short-range and long-range cases are summarized in Table 3.1.

To check the relevance of the noise, we employ the path integral formalism including the noise term in Eq. (3.54). Using the MSRJD theory for the Langevin equation, we obtain the action $S = S[\xi, \tilde{\xi}]$ for Eq. (3.54), where $\tilde{\xi}$ is the response field, as follows:

$$S = \int d\mathbf{x}\, \tilde{\xi} \left[\tau \partial_t - D\nabla^2 - D_p \nabla^p + u_2 + u_3 \xi + u_4 \xi^2 - \frac{\Gamma}{2} \tilde{\xi} \right] \xi, \qquad (3.58)$$

where $\mathbf{x} = (\mathbf{r}, t)$. Under the transformation given by Eq. (3.56), $S[\xi, \tilde{\xi}] \to S'[\xi', \tilde{\xi}']$, where S' can be written in terms of ξ and $\tilde{\xi}$ using the relations $\xi' = s^{-b}\xi$ and $\tilde{\xi}' = s^{-\tilde{b}}\tilde{\xi}$, and is given by

$$
\begin{aligned}
S' \;=\; & \int d\mathbf{x}\, s^{d+z} \tilde{\xi} \left[\tau s^{-z-b-\tilde{b}} \partial_t - D s^{-2-b-\tilde{b}} \nabla^2 - D_p s^{-p-b-\tilde{b}} \nabla^p \right. \\
& \left. + u_2 s^{-b-\tilde{b}} + u_3 s^{-2b-\tilde{b}} \xi + u_4 s^{-3b-\tilde{b}} \xi^2 - \frac{\Gamma}{2} s^{-b-2\tilde{b}} \tilde{\xi} \right] \xi.
\end{aligned}
\qquad (3.59)
$$

Therefore, we obtain the following relations of the parameters under the scaling transformation:

$$
\begin{aligned}
\tau &\;\to\; \tau' = s^{d-b-\tilde{b}} \tau, \\
D &\;\to\; D' = s^{d+z-2-b-\tilde{b}} D, \\
D_p &\;\to\; D_p' = s^{d+z-p-b-\tilde{b}} D_p, \\
u_2 &\;\to\; u_2' = s^{d+z-b-\tilde{b}} u_2, \\
u_3 &\;\to\; u_3' = s^{d+z-2b-\tilde{b}} u_3, \\
u_4 &\;\to\; u_4' = s^{d+z-3b-\tilde{b}} u_4, \\
\Gamma &\;\to\; \Gamma' = s^{d+z-b-2\tilde{b}} \Gamma.
\end{aligned}
\qquad (3.60)
$$

Note that the transformations of the parameters in Eq. (3.60) correspond to the Wilson renormalization group (RG) procedure [3, 28].

One can choose $b + \tilde{b} = d$ so that τ is invariant under the transformation in Eq. (3.60). Moreover, the relations for D and D_p suggest that the dynamic exponent $z = 2$ for $p > 2$ and $z = p$ for $p < 2$. If $z = 2$ at $p > 2$, the long-range term with D_p becomes irrelevant, whereas the short-range term with D is relevant, and vice versa for $p < 2$ with $z = p$. Above the upper critical dimension, $d > d_c$, the higher-order potential terms and noise term are irrelevant, so the Gaussian fixed point is stable. Therefore, the relevance of u_3, u_4, and Γ determines the upper critical dimension. The case of finite u_3 is well-known, as follows [49–52]. If u_3 is finite, u_4 is automatically irrelevant at d_c, which implies that at $d \lesssim d_c$, u_3 and Γ are relevant. Thus, one may infer that at $d = d_c$, $b = \tilde{b} = z$, leading to $b = d_c/2 = z$. Because $z = 2$ or $z = p$, the upper critical dimensions of the short-range and long-range QCPs are given by $d_c = 4$ and $d_c = 2p$, respectively. Note that by using $b = \beta/\nu_\perp$ with $\beta = 1$, one can obtain the MF exponents obtained in the noiseless equation, Eq. (3.57).

Finally, we discuss the TDP universality with the long-range interaction. In this case, $u_3 = 0$; thus, u_4 and Γ become relevant terms at $d \lesssim d_c$. Similar to the case of DP, at $d = d_c$, the invariance of u_4 and Γ in Eq. (3.60) yields $b = z/2$ and $\tilde{b} = z$. Because $b + \tilde{b} = d_c$, the upper critical dimension of TDP is given by $d_c = 3z/2$. Therefore, for short-range TDP, it is found that $d_c = 3$, as shown in previous works [47, 54, 55], and for long-range TDP with $p < 2$, it is found that $d_c = 3p/2$, which is similar to the long-range DP case, but the constant differs from 2 for the DP class. Again, with $b = \beta/\nu_\perp$ and $\beta = 1/2$, we obtain the MF exponents for the TDP universality. Because it is well known that the tricritical point does not exist in the one-dimensional DP-type model in the absence of the long-range interaction [28], one may ask whether the tricritical point is sustained when $d = 1$ is below the upper critical dimension or $p > 2/3$. To answer that, numerical studies and RG approaches to long-range TDP are needed.

3.5 Discussion and Conclusion

Now, we discuss how the long-range QCP can emerge from the cold atomic system. We start with the Hamiltonian of Rydberg atoms under the antiblockade effect [23]:

$$\hat{H}_R = \Omega \sum_l^N \hat{\sigma}_l^x + \Delta \sum_l^N \hat{n}_l + \sum_{l \neq m} \frac{V_{lm}}{2} \hat{n}_l \hat{n}_m, \qquad (3.61)$$

where Ω is the Rabi oscillation frequency, Δ denotes the detuning energy, and V_{lm} is the long-range interaction between excited atoms. Because Δ is very large, Rabi oscillation is suppressed, but if we set $V_{lm} = -\Delta$ for the nearest-neighbor pairs, the excitation can be enhanced by the interaction. This mechanism leads to coherent and incoherent CPs, where the long-range nature of V_{lm} is usually neglected to realize the absorbing state on long time scales [23,25,26]. However, these approaches are based on the low-density limit; therefore, one spin can interact with approximately only one particle. As pointed out in a previous work [23], when one spin simultaneously interacts with not only the nearest-neighbor spins, but also long-distance spins, the long-range effect may change the universality of the system.

We investigated the critical behavior of the quantum long-range CP, which is realized by coherently and incoherently driven interacting cold atomic systems. We derived the Heisenberg equations from the total Hamiltonian consisting of the system, the baths, and their interaction. Using the semiclassical approach, we obtained the MF equation for the long-range QCP, where branching and coagulation are realized as Lévy flight. Then we obtained a phase diagram similar to that for the short-range QCP. Next, we set up the phenomenological Langevin equation and built the Martin–Siggia–Rose–Janssen–de Dominicis action. Using scaling theory, we determined the critical exponents in the MF limit. Depending on the model parameters, the DP-type and TDP-type transitions occur. For the DP-type case, the critical exponents were obtained as those of the long-range DP [49,52]. For the TDP-type case at the tricritical

point, new critical exponents were obtained, the universality class of which we identify as the long-range TDP class. Moreover, we determined the upper critical dimension for the long-range TDP, $d_c = 3p/2$, which is different from that of the long-range DP class, $d_c = 2p$. The critical exponents for the ordinary DP and TDP and the long-range DP and TDP classes are compared in Table 3.1. Recently a similar result that a first and second-order phase transition coexist has been reported in the quantum epidemic model, realizable in a dissipative atomic system with long-range interaction [75]. We expect that our semi-classical approach is also applicable to the epidemic model using a three-state quantum spin system. Also, we remark that we considered here the homogeneous mean-field behavior, and it would be interesting how the heterogeneous structure affects on the universal behavior [76].

In this study, we focused on the long-range nonequilibrium absorbing phase transition in the dissipative quantum spin system. We obtained the phase diagram and determined the transition properties within the analytic theoretical framework in the MF limit. However, the transition behavior below the upper critical dimension has not been determined yet. The renormalization group approach to this problem seems to be challenging, yet numerical simulation studies remain as the next problem.

Chapter 4

Numerical simulation of long-range TDP in low dimensions

Major contents of this chapter is published in Ref. [32].

4.1 Introduction

In statistical physics, nonequilibrium phase transitions into an absorbing state are a well-known phenomenon and have been widely studied [20,28,29,38–45]. One of the most popular models is a contact process (CP). In the CP model, the system contains either an active or an inactive particle at each site of a d-dimensional lattice. An active particle activates an inactive particle at the nearest-neighbor site with probability κ; otherwise, it becomes inactive itself with probability $1 - \kappa$. By contrast, an inactive particle cannot recover to an active particle alone. When κ is small, inactive particles become more abundant with time, and eventually the system is fully occupied by inactive particles. Then, the system is no longer dynamic and falls into an absorbing state. When κ is large, the system remains in an active state with a finite density of active particles. Thus, the CP model exhibits a phase transition from an active to an absorbing state as the control parameter κ is decreased in any spatial dimension. This absorbing transition is second-order and belongs to the so-called directed percolation (DP) universality class [28,29,42–44,47,48]. In the DP class, the mean-field solution is valid above the upper critical dimension $d_c = 4$. The CP model can be applied to diverse phenomena such as the epidemic spread of infectious disease and the reaction-

diffusion process of interacting particles.

The CP model has been modified in various ways to describe different phenomena. For instance, Lübeck introduced the so-called tricritical CP (TCP) model as follows. In addition to the ordinary CP, a pair of consecutive active particles can activate an inactive particle at a nearest-neighbor site with probability ω [53–57, 77]. The TCP model exhibits an absorbing transition, which is either first-order or second-order depending on the parameters (κ, ω). The two types of phase boundaries meet at a tricritical point. The absorbing transition at the tricritical point is second-order, and its critical behavior, which is denoted as tricritical DP (TDP), is distinct from that of the DP class. The TDP class has been extensively studied, and various features have been identified. Using the field theoretical approach [53], the critical exponents of the TDP class were determined, together with the upper critical dimension, $d_c = 3$ [53, 77, 78]. Moreover, extensive numerical simulations were performed in two dimensions in Refs. [54, 55, 57] using slightly different models. However, the simulations yielded critical exponents that were inconsistent with each other, which was attributed to the inaccuracy of the numerical value of the tricritical point [45]. It was also argued that the first-order transition does not occur in the one-dimensional DP-type model [79]. Thus, the lower critical dimension seems to be two.

Recently, the TDP class has attracted considerable attention from the physics community after the quantum contact process (QCP), which belongs to the TDP universality class in the mean-field semi-classical limit, was investigated and realized experimentally in a dissipative quantum system of Rydberg atoms in the presence of the strong dephasing [24]. An active (inactive) particle is represented by a Rydberg atom in an excited state (the ground state). An inactive particle is activated by detuning the excitation energy of an active particle, in a process called antiblockade [58, 59]. This antiblockade dynamics can be implemented incoherently when strong dephasing noise is applied. In this case, the quantum coherence becomes negligible, and the dynamics is reduced to the classical CP process, which generates a second-order transition. How-

ever, when quantum coherence is essential, this case is called the QCP, and it yields second-order and first-order transitions [25,26]. Competition between the two types of processes leads to a tricritical point, which yields another second-order transition that belongs to the TDP class.

We remark that if an atom is excited to the *s*-state by the QCP, then quantum coherence would occur locally, so the short-range TCP (STCP) model [Fig. 4.1(a)] would be relevant, which is equivalent to ordinary TCP. On the other hand, if excitation to the *d*-state occurs, dipole–dipole interactions become effective, and a long-range TCP (LTCP) model [Fig. 4.1(b), (c), and (d)] would be relevant. Although the STCP model has been extensively investigated not only in the mean-field limit but also for low-dimensional cases, the LTCP model has only a mean-field solution [31].

In phase transitions, the interaction range is an essential factor determining the universality class of phase transitions in both equilibrium [80–85] and nonequilibrium systems [49–52, 86]. Thus, the classical CP model with long-range interactions was introduced, motivated by the fact that epidemic diseases can be spread by, for instance, Lévy flight. In this model, the activation process is realized by assigning the probability $\kappa P_I(r)$ that each active particle activates an inactive particle at distance r. Thus, $P_I(r)$ represents the probability that a particle at distance r is chosen. $P_I(r)$, which follows the power-law $\sim 1/r^{d+\sigma}$, is non-trivial, where $\sigma > 0$ is a control parameter.

This long-range CP (LCP) exhibits σ-dependent critical behavior, which is relevant within the interval denoted as $[\sigma_{c1}, \sigma_{c2}]$. Below σ_{c1}, the critical behavior is consistent with the mean-field solution. Using the field-theoretical approach, d_c is determined as $\min(4, 2\sigma)$ [49, 50]. Thus, for $\sigma < 2$ or $d < 4$, $d_c = 2\sigma$, and $\sigma_{c1} = d/2$ for $d < 4$. Above σ_{c2}, it belongs to the ordinary DP class. Field-theoretical analysis revealed that $\sigma_{c2} = d + z(1 - 2\delta)$, where z is a dynamic exponent, and δ is the critical exponent for the density of active particles $\rho_a(t) \sim t^{-\delta}$ of the ordinary DP class. When z and δ were replaced with their DP values, σ_{c2} was found to be 2.0766 in one dimension, 2.1725 in two dimensions, and 2.126 in three dimensions. However, direct simulation data in

one dimension could not reproduce the value $\sigma_{c2} \approx 2.08$, so further investigation is needed in future work to resolve this inconsistency [49]. For $d > 4$, there exists one threshold, $\sigma_c = 2$, such that for $\sigma < 2$, the mean-field solution of the long-range DP is valid, whereas for $\sigma > 2$, the mean-field solution of the ordinary DP is valid.

We focus on the LTCP model. In our previous work, we constructed a phase diagram based on the mean-field solution, which is valid for $d > d_c = \min(3, 1.5\sigma)$ [31]. In this case, there exists a characteristic value $\sigma_c = 2$ such that for $\sigma < \sigma_c$, the mean-field solution of the LTCP is relevant, and for $\sigma > \sigma_c$, the LTCP model behaves like the STCP model. We will show later that when $d < 3$, the LTCP model exhibits distinctive behavior (characterized as that of the LTCP class) in the interval $[\sigma_{c1}, \sigma_{c2}]$, where $\sigma_{c1} = 2d/3$ because $d_c = 1.5\sigma$, and σ_{c2} is determined by the hyperscaling relation $\sigma_{c2} = d + z(1 - \delta - \delta')$, where δ' is the critical exponent for the survival probability $P(t) \sim t^{-\delta'}$. We need to replace z, δ, and δ' in the formula with the numerical values of the short-range TDP (STDP) to obtain σ_{c2}. For $\sigma < \sigma_{c1}$ shown in Fig. 4.1(d), the mean-field behavior of the LTDP class appears, and for $\sigma > \sigma_{c2}$ shown in Fig. 4.1(a), the behavior of the STDP class appears. The universality class diagram will be shown later. As in the LCP model, the value of σ_{c2} is obtained from the hyperscaling relation; however, it is not consistent with the value obtained directly from numerical simulations. Finally, we determine the critical exponents of the LTCP model in the interval $[\sigma_{c1}, \sigma_{c2}]$, which vary continuously with σ.

The remainder of this paper is organized as follows. In Sec. 4.2, we present the rules of the long-range TCP in detail. In Sec. 4.3, the critical behavior of the absorbing transition is determined. In Sec. 4.4, we set up the Langevin equation to derive the scaling relation. In Sec. 4.5, we report numerical results for the long-range TCP. In the final section, a summary and discussion are presented.
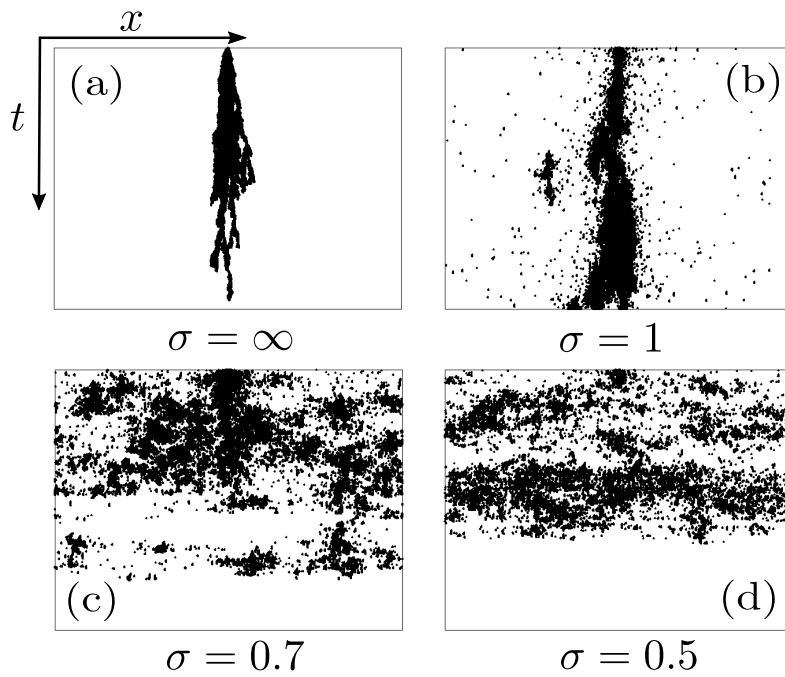
Figure 4.1: Snapshot of active sites of the LTCP model in one dimension at a critical point $(\kappa_c(\omega), \omega)$ at a fixed $\omega = 0.5 < \omega_c$ (a) and (b) and at the tricritical point (κ_t, ω_t) (c) and (d). For $\sigma > 1$, the tricritical point does not exist.

Table 4.1: Reaction schemes of the CP, TCP, and LTCP. A (0) represents the active (inactive) state. TCP* denotes the TCP model. When the Lévy exponent $\sigma \to \infty$ in the LTCP, the LTCP model is reduced to the m-TCP used in Sec. 4.5.1. The last column indicates the processes explained in Sec. 4.2. The notation $\cdots$ in the LTCP column represents long-range interactions. $P_I(|\boldsymbol{r} - \boldsymbol{r}'|) \sim 1/|\boldsymbol{r} - \boldsymbol{r}'|^{d+\sigma}$.

CP		TCP*		LTCP		
Reaction	Probability	Reaction	Probability	Reaction	Probability	Process
$\underline{A} \to 0$	$1 - \kappa$	$\underline{A} \to 0$	$(1-\omega)(1-\kappa)$	$\underline{A} \to 0$	$(1-\omega)(1-\kappa)$	i-a
$\underline{A}0 \to AA$	κ	$\underline{A}0 \to AA$	$(1-\omega)\kappa$	$\underline{A}\cdots 0 \to A \cdots A$	$(1-\omega)\kappa P_I(|\boldsymbol{r} - \boldsymbol{r}'|)$	i-b
		$\underline{A}0 \to 00$	$\omega(1-\kappa)$	$\underline{A}0 \to 00$	$\omega(1-\kappa)$	ii-a
		$\underline{A}0 \to AA$	$\omega\kappa$	$\underline{AA}\cdots 0 \to AA \cdots A$	$\omega\kappa P_I(|\boldsymbol{r} - \boldsymbol{r}'|)$	ii-b
		$\underline{AA}0 \to AAA$	ω			

4.2 LTCP model

We perform numerical simulations by extending the algorithm used in Ref. [55] for the STCP model to the long-range case. Specifically, the model is set up on a d-dimensional lattice composed of L^d sites, where L is the lateral size of the system, and each site is in either the active state (denoted as A) or the inactive state (denoted as 0). We use two different initial configurations: i) one site is active, and the others are all inactive, and ii) all sites are active. Each case will be used for different purposes. We use the periodic boundary condition in the simulations. At each time step, the following rules are applied.

i) An active site is chosen randomly from the list of active sites. Its position is denoted as $\boldsymbol{r}_0$. With probability $1 - \omega$, a long-range CP is performed as follows:

   i-a) With probability $1 - \kappa$, the active site chosen in step i) is inactivated.

   i-b) With probability κ, a site at a distance r from the position $\boldsymbol{r}_0$ is selected with probability $P_I(x)$. If this target site is inactive (0), its state is changed to active (A).

ii) An active site is chosen randomly from the list of active sites. Its position is denoted as r_0. The state of a nearest-neighbor site is checked with probability ω.

    ii-a) If the neighbor is inactive, then the active site at r_0 is inactivated with probability $1 - \kappa$.

    ii-b) If the neighbor is active, then a third site is selected at a distance r from r_0 with probability $P_I(r)$. If this target is inactive, it is activated with probability κ.

iii) If the number of active sites is zero, the simulation ends. Otherwise, the time t is advanced by $1/N_a$, where $N_a(t)$ is the total number of active sites in the system at time t, and the simulation returns to step i).

In this rule, $P_I(r)$ is given as $\sim 1/r^{d+\sigma}$. This model is controlled by three parameters: i) the Lévy exponent $\sigma > 0$ controlling the long-range interaction, ii) the probability ω of checking the nearest-neighbor site before the reaction, and iii) the probability of the branching process κ. The reactions are summarized in Table 4.1.

4.3 Critical behavior of the absorbing transition

Here we introduce the basic physical quantities used to characterize the critical behavior of the absorbing transition. To proceed, we first consider a system in which a single active site is located at $r = 0$ at time $t = 0$, and the remaining sites are inactive. The LTCP begins in this configuration. We measure the following quantities to characterize the criticality of the LTCP: i) the survival probability $P(t)$ (i.e., the probability that the system has not entered in the absorbing state), ii) the number of active sites $N_a(t)$, and iii) the mean square of the distance from the origin $R^2(t)$. That is, $R^2(t) = (1/N_a(t)) \sum_{j=1}^{N_a} r_j^2$, where r_j is the position of the j-th active site. When sufficiently long-range interactions are considered, the arithmetic average of

$R^2(t) \equiv \langle |r(t)|^2 \rangle$ may be difficult to obtain numerically [49, 50]. The geometric average $R^2(t) = \exp[\langle \ln |r(t)|^2 \rangle]$ may be a suitable alternative. Second, one may take as the initial configuration that occupied entirely by active sites. Using this initial configuration, iv) the density $\rho_a(t)$ of active sites at time t is measured.

At the critical point, these quantities exhibit power-law behavior as follows:

$$P(t) \propto t^{-\delta'}, \quad N_a(t) \propto t^{\eta}, \quad R^2(t) \propto t^{2/z}, \quad \rho_a(t) \sim t^{-\delta}. \tag{4.1}$$

The mean density of surviving active sites behaves as $\rho_a(t)P(t) = N_a(t)/R^d(t)$. Thus, the exponent δ is related to the other exponents as $\delta = d/z - \eta - \delta'$. In particular, at the tricritical point, these exponents are denoted as δ'_t, η_t, z_t, and δ_t. Hereafter, we drop the subscript t indicating the tricritical case for brevity unless it is necessary for clarity.

In the supercritical region, $\kappa > \kappa_c$ for each given $\omega < \omega_t$, and $P(t)$ reaches P_s in the steady state, where $P_s \sim (\kappa - \kappa_c)^{\beta'}$. $\rho_a(t)$ behaves similarly to $\rho_a(t) \to \rho_{a,s} \sim (\kappa - \kappa_c)^{\beta}$. The exponents β' and β are related to $\delta' = \beta'/\nu_\parallel$ and $\delta = \beta/\nu_\parallel$, where the exponent $\nu_\parallel$ is the mean survival time exponent defined in terms of the mean survival time $\tau \sim (\kappa - \kappa_c)^{-\nu_\parallel}$. At the tricritical point, $\beta \neq \beta'$ (equivalently, $\delta \neq \delta'$), whereas in the DP class, they are the same.

We characterize the critical behavior in finite systems using the finite-size scaling (FSS) theory. In this approach, the critical exponents are determined using the data collapse technique for scaling functions. Data collapse technique is achieved by scaling hypothesis in which the large-scale properties are invariant near the tricritical point $(\kappa_t = \kappa_c(\omega_t), \omega_t)$ under the following scale transformations.

$$\Delta\kappa \to s^{-1}\Delta\kappa, \quad \rho_a \to s^{-\beta}\rho_a, \quad N_a \to s^{\nu_\parallel \eta}N_a, \quad P \to s^{-\beta'}P,$$
$$\zeta \to s^{\nu_\perp}\zeta, \quad \tau \to s^{\nu_\parallel}\tau, \quad \Delta\omega \to s^{-\phi}\Delta\omega, \tag{4.2}$$

where $\Delta\kappa = \kappa - \kappa_t$, $\Delta\omega = \omega - \omega_t$, and s is a scale factor and $\nu_\perp$ is the spatial correlation

exponent defined in terms of the spatial correlation $\zeta \sim (\kappa - \kappa_c)^{-\nu_\perp}$. In addition, ϕ is a crossover exponent defined as the ratio of the scaling exponent of $\Delta\kappa$ and $\Delta\omega$. For instance, at the tricritical point (κ_t, ω_t), the average density $\rho_a(t)$ of active sites behaves as $\rho_a(t,N) = s^\beta \rho_a(s^{\nu_\parallel}t, s^{\bar{\nu}_\perp}N)$, where $\bar{\nu}_\perp \equiv d\nu_\perp$.

When $s^{\nu_\parallel}t = 1$ is chosen, $\rho_a(t) = t^{-\delta}f_n(tN^{-\bar{z}})$. Similarly, the other quantities are reduced as

$$P(t) = t^{-\delta'}f_p(tN^{-\bar{z}}), \quad N_a(t) = t^\eta f_N(tN^{-\bar{z}}), \tag{4.3}$$

where $\bar{z} = z/d$, $z = \nu_\parallel/\nu_\perp$, and f_n, f_p, and f_N are scaling functions.

Near the tricritical point, the number of active sites and the density of active sites scales as

$$N_a(t,\Delta\kappa,\Delta\omega) = s^{-\nu_\parallel\eta}N_a(s^{\nu_\parallel}t, s^{-1}\Delta\kappa, s^{-\phi}\Delta\omega), \tag{4.4}$$

$$\rho_a(t,\Delta\kappa,\Delta\omega) = s^\beta \rho_a(s^{\nu_\parallel}t, s^{-1}\Delta\kappa, s^{-\phi}\Delta\omega). \tag{4.5}$$

At $\Delta\omega = 0$, by choosing $s^{\nu_\parallel}t = 1$, we can reduce Eq. (4.4) to

$$N_a(t) = t^\eta f_1(t^{1/\nu_\parallel}\Delta\kappa), \tag{4.6}$$

where f_1 is a scaling function. Alternatively, in the steady state $t \to \infty$, by choosing $s^{-\phi}\Delta\omega = 1$, we can reduce Eq. (4.5) to

$$\rho_a(t) = \Delta\omega^{\beta/\phi}f_2((\Delta\omega)^{-1/\phi}\Delta\kappa), \tag{4.7}$$

where f_2 is a scaling function. In a steady-state simulation, the absorbing state can be reached because of finite-size effects [87,88]. To overcome this problem, when the system reaches the absorbing state, we perform a spontaneous creation, $0 \to A$.

In this section, we briefly reviewed the power-law behavior and FSS theory of the absorbing state phase transition. These context will be used in Sec. 4.5 to perform the
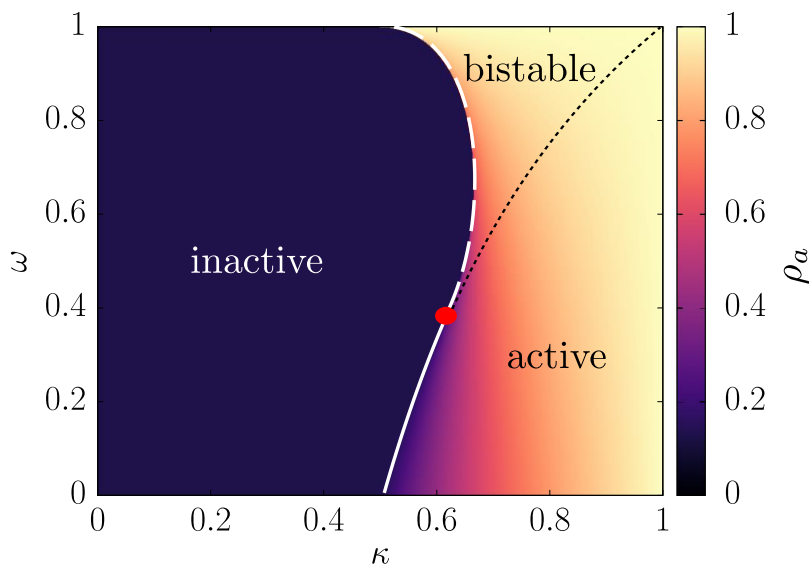
Figure 4.2: Phase diagram of the TCP model in the mean-field limit. A tricritical point (red dot) is located at $(0.6180, 0.3820)$. White solid (dashed) curve represents a continuous (discontinuous) transition.

numerical analysis of the critical exponents.

4.4 Analytic results

4.4.1 Phase diagram in the mean-field limit

In this section, we recall the analytic result based on the mean-field approach obtained in a previous work [31]. The density of active sites at time t averaged over the surviving sample is denoted as $\rho_a(t)$. In the mean-field limit, we ignore the effect of local density fluctuations and write the dynamic equation of the LTCP model as

$$\partial_t \rho_a(t) = -u_2 \rho_a - u_3 \rho_a^2 - u_4 \rho_a^3, \tag{4.8}$$

where $u_2 = \omega\kappa + 1 - 2\kappa$, $u_3 = \kappa - \omega - \omega\kappa$, and $u_4 = \omega\kappa$. These coefficients are derived on the basis of the reactions listed in Table I.

In the steady state, we set $\partial_t \rho_a = 0$ and obtain the solutions as

$$\rho_a^* \equiv 0 \;\; \text{and} \;\; \rho_{a,\pm}^* \equiv \frac{-u_3 \pm \sqrt{u_3^2 - 4u_2 u_4}}{2u_4}. \tag{4.9}$$

Linear stability analysis reveals that the first solution, $\rho_a^* = 0$, is stable for $u_2 > 0$ and unstable for $u_2 < 0$. Thus, $u_2 = \omega\kappa + 1 - 2\kappa = 0$ is the boundary of the stable solution at the fixed point $\rho_a^* = 0$, which is equivalent to the boundary of the active phase in Fig. 4.2.

For the second solution, $\rho_{a,\pm}^*$, we analyze the linear stability as

$$\delta\dot{\rho}_{a,\pm} = -(u_2 + 2u_3\rho_{a,\pm}^* + 3u_4\rho_{a,\pm}^{*2})\delta\rho_{a,\pm} \tag{4.10}$$

$$= \rho_{a,\pm}^*(-u_3 - 2u_4\rho_{a,\pm}^*)\delta\rho_{a,\pm} = \mp\rho_{a,\pm}^*\sqrt{u_3^2 - 4u_2 u_4}\,\delta\rho_{a,\pm}. \tag{4.11}$$

Thus, $\rho_{a,+}^*$ and $\rho_{a,-}^*$ are stable for $\rho_{a,+}^* > 0$ and $\rho_{a,-}^* < 0$, respectively. Because $\rho_a > 0$, $\rho_{a,-}^*$ is ignored. For $\rho_a = \rho_{a,+}^*$, we obtain two phase boundaries. The first is $u_2 = 0$ and $u_3 \geq 0$. Thus, $u_3^2 - 4u_2 u_4 \geq 0$. These conditions are rewritten in terms of (κ, ω) as follows:

$$\omega\kappa + 1 - 2\kappa = 0, \;\; \text{and} \;\; \omega \leq \omega_t \equiv \frac{3 - \sqrt{5}}{2}. \tag{4.12}$$

Thus, $\rho_{a,+}^* = 0$. The first equation and second inequality above were used to generate the white solid curve in Fig. 4.2, and the red dot indicates $\omega = \omega_t$.

The second phase boundary is obtained from the conditions $u_3^2 - 4u_2 u_4 = 0$ and $u_3 \leq 0$. These conditions lead to

$$(\kappa - \omega - \omega\kappa)^2 - 4\omega\kappa(1 - 2\kappa + \omega\kappa) = 0 \text{ for } \omega \geq \omega_t \text{ and } \kappa \geq 0.5, \tag{4.13}$$

where $\rho_{a,+}^* \geq 0$. This phase boundary is drawn as a white dashed curve in Fig. 4.2.

There exist three phases in the phase diagram (Fig. 4.2): i) the inactive (absorbing)

phase with $\rho_a = 0$, ii) the active phase with $\rho_a = \rho_{a,+}^* > 0$, and iii) the bistable phase with two stable fixed points, $\rho_a = 0$ and $\rho_a = \rho_{a,+}^* > 0$. The phase boundaries are determined by the conditions derived above. We will show later that the phase transition across the first boundary above (indicated by the white solid curve) is second-order, whereas that across the second boundary (indicated by the dashed curve) is first-order. Therefore, a tricritical point is formed at (κ_t, ω_t). The critical exponent of the order parameter defined as $\rho_a \sim (\kappa - \kappa_c)^\beta$ across the white solid curve is found to be $\beta = 1$ for $\omega < \omega_t$, and the exponent β_t for $\rho_a \sim (\kappa - \kappa_t)^{\beta_t}$ is found to be $\beta_t = 1/2$ at $\omega = \omega_t$.

To confirm our analytic result, we numerically verified the phase diagram on the fully connected lattice. Specifically, using the FSS theory, we obtained the tricritical point and critical exponents presented in the next subsection corresponding to the analytic results.

4.4.2 Hyperscaling relation for LTDP

In this section, we recall the field-theoretic analysis performed in the previous work [31] to obtain the exact scaling relation and mean-field exponents. To account for the spatial fluctuations and noise induced by active particles occupying active sites, we set up the Langevin equation as follows:

$$\partial_t \rho_a = D_\sigma \nabla^\sigma \rho_a + D \nabla^2 \rho_a - u_2 \rho_a - u_3 \rho_a^2 - u_4 \rho_a^3 + \xi, \qquad (4.14)$$

where D_σ and D are the diffusion constants obtained from a small momentum expansion, which are given by $(1 - \omega)\kappa \int d\mathbf{r}' P(|\mathbf{r} - \mathbf{r}'|)\rho_a(\mathbf{r}') \approx (1 - \omega)\kappa\rho_a + D_\sigma \nabla^\sigma \rho_a + D\nabla^2 \rho_a$. The noise $\xi(\mathbf{r},t)$ is a multiplicative Gaussian random variable with zero mean and a correlation of

$$\langle \xi(\mathbf{r},t)\xi(\mathbf{r},t)\rangle = \Gamma\rho_a(\mathbf{r},t)\delta^d(\mathbf{r} - \mathbf{r}')\delta(t - t'). \qquad (4.15)$$

Using the Martin–Siggia–Rose–Janssen–de Dominicis formalism [69–71, 89, 90] for the Langevin equation, we obtain the action as follows:

$$S = \int d\boldsymbol{x} \rho_a' \left[\partial_t - D\nabla^2 - D_\sigma \nabla^\sigma + u_2 + u_3 \rho_a + u_4 \rho_a^2 - \frac{\Gamma}{2} \rho_a \right] \rho_a, \qquad (4.16)$$

where ρ_a' is an auxiliary field, and $\boldsymbol{x} = (\boldsymbol{r}, t)$.

If u_3 is finite, u_4 is irrelevant at d_c, which implies that the action described by Eq. (4.16) belongs to the long-range DP (LDP) class. It is satisfied by the so-called rapidity-reversal (or duality) symmetry, which is invariant under the exchange $\rho_a(\boldsymbol{r}, t) \leftrightarrow -\rho_a'(\boldsymbol{r}, -t)$. Rapidity-reversal symmetry implies that the critical exponents β and β' must be identical. It was revealed that in the LDP class, D_σ is not renormalized [49, 50]. This means that D_σ is invariant under the scaling transformation; thus, one obtains the exact scaling relation $d + z - \sigma - 2z\delta = 0$ [49–52, 86].

At the tricritical point, $u_3 = 0$, the rapidity-reversal symmetry is broken, and $\beta \neq \beta'$. Crossover behavior occurs when more than one fixed point appears in the phase diagram. Scaling theory is used to obtain the mean-field critical exponents:

$$\beta = 0.5, \; \beta' = 1, \; \nu_\perp = 1/\sigma, \; \nu_\parallel = 1, \; z = p, \; \phi = 0.5, \qquad (4.17)$$

which are expected to be valid above the upper critical dimension $d_c = 1.5\sigma$. For the LDP class, loop corrections can be represented as an integer power series in momentum space [50]. This can be applied to LTDP as well, which means that the coefficient of the fractional Laplacian is not renormalized (see Appendix C.2). This implies that the coefficient of the fractional Laplacian must be invariant under the renormalization group (RG) transformation. Hence, one can obtain the so-called hyperscaling relation

$$d + z - \sigma - z(\delta + \delta') = 0, \qquad (4.18)$$

which is valid below the upper critical dimension, $d \leq d_c$.

Below d_c, the universal features of the LTCP model depend on σ, which is within the interval $[\sigma_{c1}, \sigma_{c2}]$. Thus, we consider the following three domains. First, below σ_{c1}, the interaction range can be superdiffusive; thus, mean-field critical behavior appears. In other words, above the upper critical dimension $d > d_c = 1.5\sigma$, mean-field behavior is expected. Thus, $\sigma_{c1} = 2d/3$. Second, σ_{c2} is determined to be 1.36067 using Eq. (4.18). Finally, in the regime $\sigma > \sigma_{c2}$, the exponents are reduced to those of the STDP class.

4.5 Numerical Results

4.5.1 STCP model in two dimensions
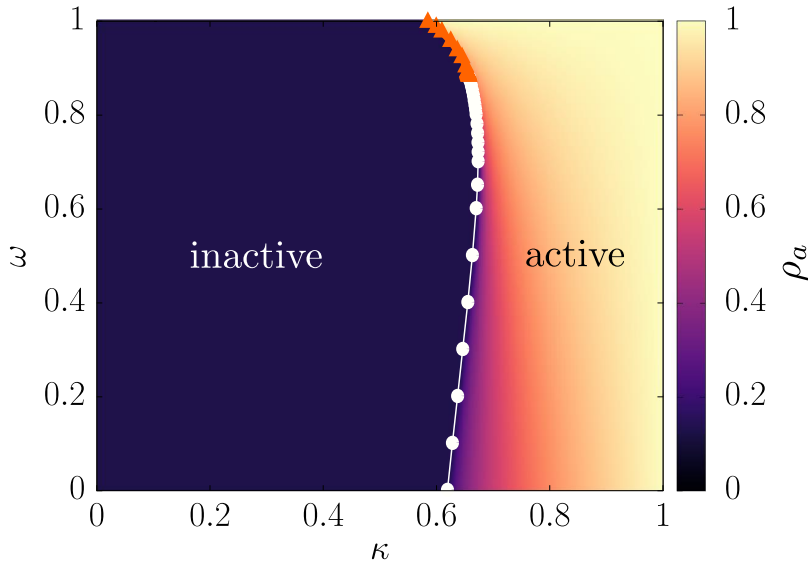
Figure 4.3: Phase diagram of the *m*-TCP model in two dimensions. A tricritical point is located at $(0.6606466, 0.879)$. White (Orange) curve represents a continuous (discontinuous) transition. At $\omega = 0$, the model is reduced to the CP model at $\kappa_c = 0.622466$. The data points (white circles and orange triangles) represent numerical results.

We consider an STCP model called the *m*-TCP model to distinguish it from other previous models designed as models of the STCP class. This model is a simple version of the LTCP model obtained by replacing the long-range interaction with short-range
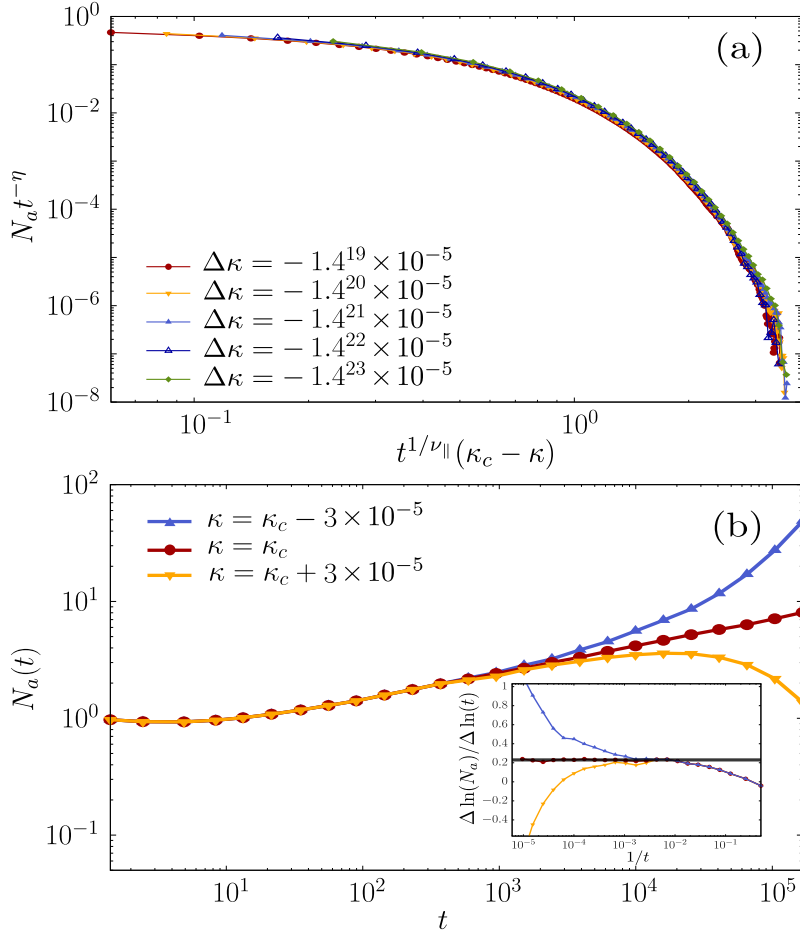
Figure 4.4: (a) Scaling plot of $N_a t^{-\eta}$ versus $t^{1/\nu_\parallel}(\kappa_c - \kappa)$ for different values of κ. Data points collapse well onto a single curve for $\eta = 0.230$ and $\nu_\parallel = 1.295$. (b) Plot of $N_a(t)$ versus t at and around κ_c. Inset: Local slopes of $N_a(t)$ versus $1/t$ for these data points obtained in (a). $\omega = 0.6$, and $\kappa_c = 0.67326$.

interaction, which we will consider next. In fact, the STCP model was explored in Refs. [54,55,57] using slightly different rules, but the numerical values of their critical exponents differed from each other. The origin of this difference will be discussed later. Here, we check the justification for our LTCP model using the simplified version, the *m*-TCP model, by comparing our simulation results with those obtained in Refs. [54, 55,57]. This *m*-TCP model contains two control parameters, κ and ω. In (κ, ω) space, there exist second-order and first-order phase transition curves and a tricritical point at
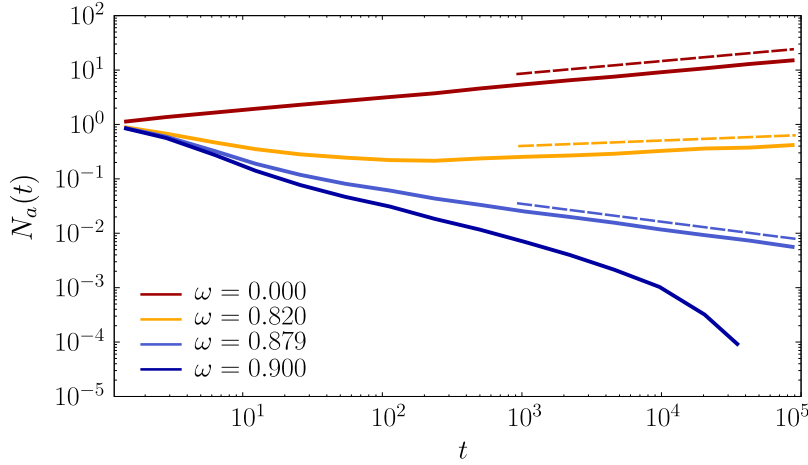
Figure 4.5: Plot of $N_a(t)$ for different values of ω: $\omega = 0$ at the DP point; $\omega = 0.879$ at the TDP point; $\omega = 0.82$ in the crossover region between these two points; and $\omega = 0.9$ in the first-order transition domain. Dashed lines are guidelines with slope $0.230, 0.102$, and -0.353, from the top. The system size is taken as $N = 10^8$.

Table 4.2: $2d$ TDP universality at tricritical point (κ_t, ω_t) for various models. Here, we determine the tricritical point of Lübeck's TCP model by finding the power-law behavior of the number of active sites $N_a(t)$.

Model	(κ_t, ω_t)	$\nu_\parallel$	z	δ	δ'	η
Generalized DK [54]	$(0.1813672, 2.795)$	$1.156(4)$	$2.110(6)$	$0.087(3)$	$1.218(7)$	$-0.353(9)$
Ordinary TCP [55]	$(0.286237, 0.919)$	1.15 ± 0.005	2.11 ± 0.01	0.09 ± 0.01	1.22 ± 0.008	-0.35 ± 0.008
Modified TCP	$(0.6606466, 0.879)$	1.15 ± 0.005	2.11 ± 0.01	0.09 ± 0.01	1.22 ± 0.008	-0.35 ± 0.008

which the two transition curves meet.

To determine the second-order curve, we find a critical point κ_c for each value of ω in the region $\omega < \omega_t$ as follows. First, we use the FSS method based on Eq. (4.6). We take the scale factor s as $s = \kappa_c - \kappa$ and plot $N_a(t)t^{-\eta}$ versus $(\kappa_c - \kappa)t^{1/\nu_\parallel}$. If we choose κ_c correctly, then the data points for different κ values would collapse onto a single curve. Indeed, we obtain this result, for instance, for $\omega = 0.6$ with $\kappa_c = 0.67326$ [Fig. 4.4(a)]. In the second method, we check the local slope of the curve of $N_a(t)$ as a
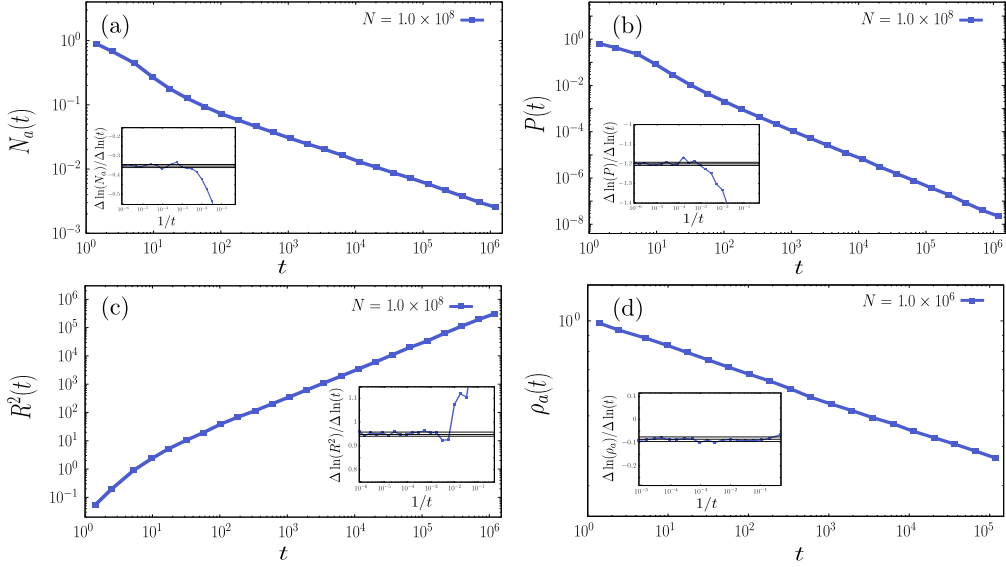
Figure 4.6: Plots of four physical quantities used to characterize the absorbing transition of the *m*-TCP model in two dimensions at a tricritical point: (a) $N_a(t)$ versus t, (b) $P(t)$ versus t, (c) $R^2(t)$ versus t, and (d) $\rho_a(t)$ versus t. The exponent values are estimated as follows: (a) $\eta = -0.35 \pm 0.008$, (b) $\delta' = 1.22 \pm 0.008$, (c) $2/z = 0.947 \pm 0.004$, and (d) $\delta = 0.09 \pm 0.01$. Insets: Local slopes of each quantity versus $1/t$ to confirm the estimated slopes.

function of t. If we choose κ_c correctly, then $N_a(t)$ would exhibit power-law behavior as a function of t with the exponent $\eta(\omega)$ [Fig. 4.4(b)]. Using these two methods, we determine the critical points κ_c for each value of ω.

We obtain the phase diagram shown in Fig. 4.3. When $\omega = 0$, the absorbing transition belongs to the DP class, and thus $\eta \approx 0.230$. We trace the value of the exponent η as a function of ω in Fig. 4.5. The ω values are chosen as follows: (i) $\omega = 0$ (DP class); (ii) $\omega = 0.82$ (in the crossover region from DP to TDP); (iii) $\omega = 0.879$ (TDP class); and (iv) $\omega = 0.9$ (in the region of the first-order transition). In Fig. 4.5, there are two generic power-law lines at $\omega = 0$ and $\omega = 0.879$. At the tricritical point, we obtain the tricritical exponents as $\eta = -0.35 \pm 0.008$, $\delta' = 1.22 \pm 0.008$, $z = 2.11 \pm 0.01$, and $\delta = 0.09 \pm 0.01$ in Fig. 4.6. When we perform the data collapse, the error bars are measured by controlling the exponents until the data collapse breaks down. The
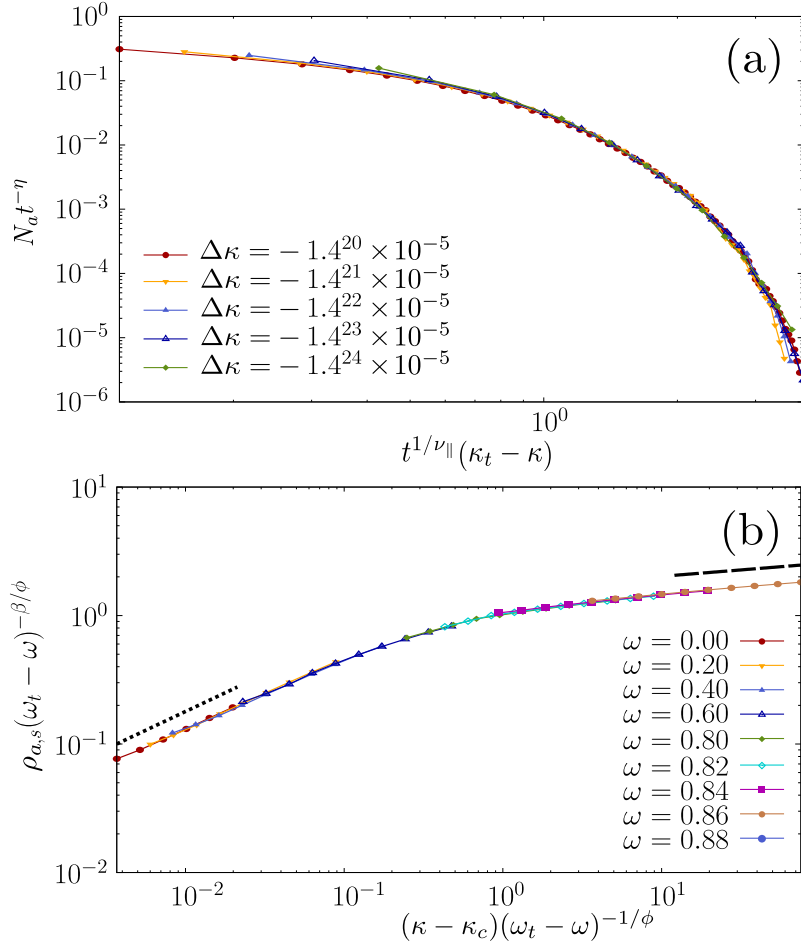
Figure 4.7: FSS analysis of the *m*-TCP model. (a) Scaling plot of $N_a t^{-\eta}$ versus $t^{1/\nu_\parallel}(\kappa_t - \kappa)$ for different values of κ. Data points collapse well onto a single curve for $\kappa_t = 0.6606466$, $\eta = -0.353$, and $\nu_\parallel = 1.16$. (b) Scaling plot of $\rho_{a,s}(\omega_t - \omega)^{-\beta/\phi}$ versus $(\kappa - \kappa_c)(\omega_t - \omega)^{-1/\phi}$ for different values of ω, where $\rho_{a,s}$ represents ρ_a in the steady state. Dotted (Dashed) line is a guideline with slope $\beta_{DP} = 0.584$ ($\beta_t = 0.101$). Data points collapse well onto a single curve for $\phi = 0.52$.

exponent $\nu_\parallel$ is obtained from the rescaling plot of $N_a(t)t^{-\eta}$ versus $t^{1/\nu_\parallel}(\kappa_t - \kappa)$ for different κ values in Fig. 4.7(a). In Fig. 4.7(b), the crossover exponent ϕ is obtained from the rescaling plot of $\rho_{a,s}(\omega_t - \omega)^{-\beta/\phi}$ versus $(\kappa - \kappa_c)(\omega_t - \omega)^{-1/\phi}$. In this case, $\phi = 0.52 \pm 0.02$ is obtained, in agreement with the result in Ref. [55]. We remark that the authors of Refs. [54,55,57] considered TCP models with slightly different reaction
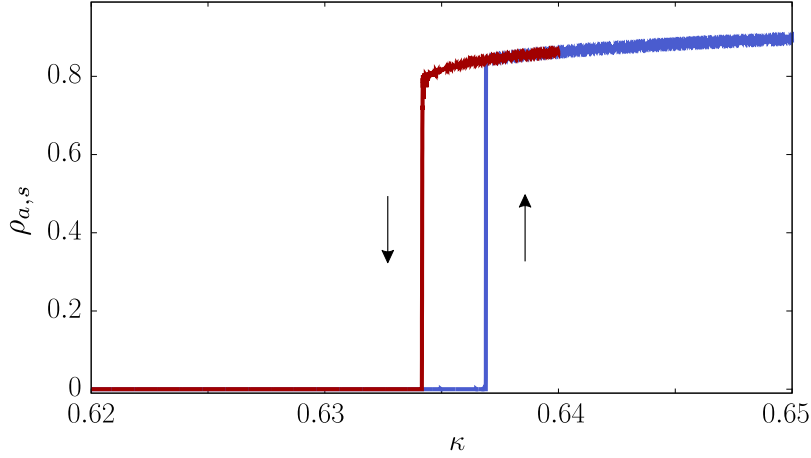
Figure 4.8: Plot of $\rho_{a,s}$ versus κ for the m-TCP model at a fixed $\omega = 0.95 > \omega_t$. A hysteresis curve is obtained. The system size is $N = 10^6$.

rules. Further, they obtained slightly different critical exponent values. It was argued that this discrepancy results from the different methodologies used to determine the tricritical point in Ref. [55]. The author of Ref. [55] used FSS of the order parameter in the steady state. It is difficult to find a tricritical point correctly using this method, because FSS in the steady state is not sensitive to κ_t. On the basis of our two criteria, we obtain $\omega_t = 0.9190$ instead of the value of 0.9055 in Ref. [55]. At our tricritical point, we obtain critical exponent values similar to those in Ref. [54]. In Table 4.2, we list the three sets of critical exponent values of the STCP model obtained using three different rules.

For $\omega > \omega_t$, as represented by the orange curve in Fig. 4.3, a first-order transition occurs. One of the features of the first-order transition is the presence of a hysteresis curve. Thus, we check whether a hysteresis curve is indeed generated. After taking an ω value larger than ω_t, say $\omega = 0.95$, we calculate the LTDP dynamics for a given κ and obtain $\rho_a(\kappa)$ in the steady state. Next, we increase κ slightly and simulate the LTDP dynamics again; we obtain ρ_a in the steady state. We repeat this process in the forward direction, in which κ is increased, and in the backward direction, in which κ is decreased. Indeed, we obtain a hysteresis curve, as shown for $\omega = 0.95$ in Fig. 4.8.

Here, we determine the critical point of the first-order transition following the method used in Refs. [55, 91]. For fixed ω and κ, we set up an initial configuration in which half of the sites are assigned to the active state and the remaining sites are assigned to the inactive state, and the LTDP dynamics is simulated. The system reaches either the absorbing state ($\rho_a = 0$) or the active state ($\rho_a > 0$) depending on initial configuration and given κ. We measure the fraction of initial configurations that reach the absorbing state as a function of κ. The transition point κ_c is determined as the one at which the fraction becomes half.

4.5.2 LTCP model in two dimensions

We perform numerical simulations of the LTCP model in two dimensions, in which the long-range interaction exponent σ is varied in the range $[0.1, 3.0]$ in steps of $\Delta\sigma = 0.1$. For each value of σ, we determine both the critical points (κ_c, ω_c) and the tricritical point (κ_t, ω_t) using the two methods employed in the previous subsection. As in the phase diagram of the m-TCP model, a second-order (first-order) transition occurs for $\omega < \omega_t(\sigma)$ ($\omega > \omega_t(\sigma)$). Thus, a tricritical point appears for each value of σ, as shown in Fig. 4.9(a). The second-order transition belongs to the long-range DP class when $\omega \ll \omega_t(\sigma)$ for the given σ values. However, as ω approaches ω_t, the critical exponents exhibit crossover behavior.

At the tricritical point, the critical exponent values of δ', η, z, and δ are obtained for each value of σ in the range $[0.1, 3]$ in steps of $\Delta\sigma = 0.1$, as shown in Fig. 4.9(b). The obtained critical values are listed in Table C.1. Each critical exponent value exhibits crossover behavior across σ_{c1} and σ_{c2}. The value of σ_{c1} is determined to be $4/3$ in two dimensions, because $d_c = 1.5\sigma_{c1}$. For $\sigma < \sigma_{c1}$, mean-field behavior occurs, whereas for $\sigma > \sigma_{c1}$, a significant low-dimensional fluctuation effect appears. The upper bound σ_{c2}, across which the universality class changes from the two-dimensional LTDP class to the two-dimensional STDP class, was determined using the hyperscaling relation (4.18). We remark that whereas in the regions $\sigma < \sigma_{c1}$ and $\sigma > \sigma_{c2}$, the
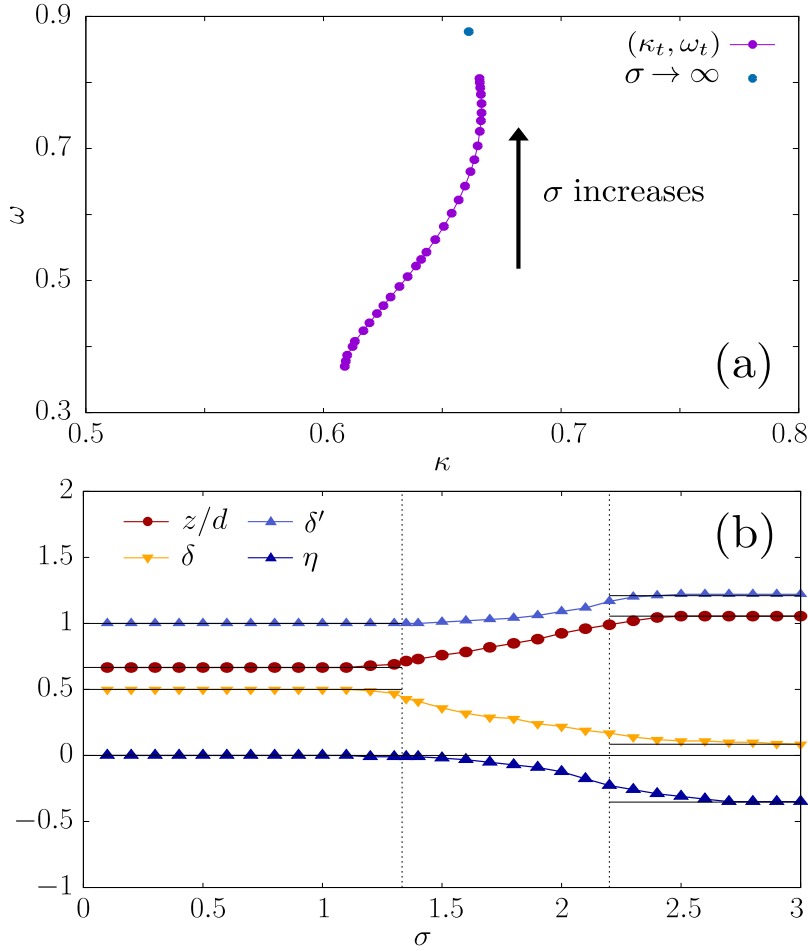
Figure 4.9: For the LTCP model in two dimensions, (a) plot of the tricritical points in (κ, ω) space for different σ values in $[0.1, 3.0]$. (b) Plots of the critical exponents z/d, δ, δ', and η as a function of σ. σ_{c1} and σ_{c2} are indicated by vertical dotted lines. The thin solid lines in the regions $\sigma < \sigma_{c1}$ and $\sigma > \sigma_{c2}$ are guidelines showing that the curves converge to constant values.

exponents are constant regardless of σ, in the interval $[\sigma_{c1}, \sigma_{c2}]$, the critical exponents vary constantly as a function of σ, which is a prototypical pattern that appears in the long-range CP model.

Indeed, we find numerically that the critical exponent values for σ between $[\sigma_{c1} = 4/3, \sigma_{c2} \approx 2.2]$ vary depending on σ, as listed in Table C.1. For instance, for $\sigma = 2.0$, we obtain the critical exponents directly by measuring the slopes as $\eta = -0.129 \pm$
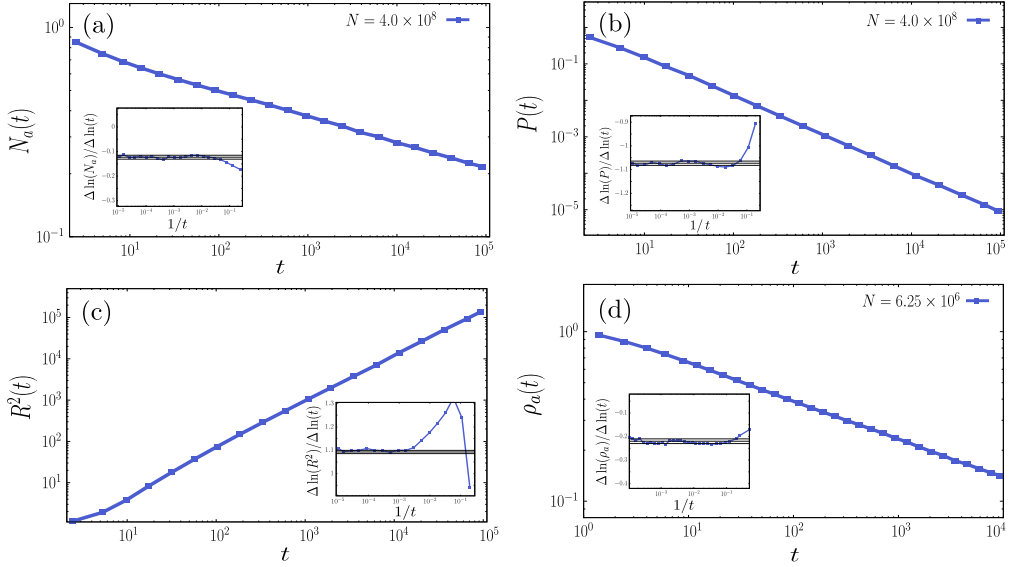
Figure 4.10: For the LTDP model with $\sigma = 2.0$ in two dimensions, plots of (a) $N_a(t)$, (b) $P(t)$, (c) $R^2(t)$, and (d) $\rho_a(t)$ versus t. We obtain the exponent values as $\eta = -0.129 \pm 0.010$, $\delta' = 1.073 \pm 0.010$, $2/z = 1.087 \pm 0.010$, and $\delta = 0.212 \pm 0.010$, respectively. Insets: local slopes of each quantity versus $1/t$.

0.010, $\delta' = 1.073 \pm 0.010$, $z = 1.840 \pm 0.015$, and $\delta = 0.212 \pm 0.010$, as shown in Fig. 4.10. We also obtain the critical exponents using the FSS method. We plot $N_a t^{-\eta}$ versus $tN^{-\bar{z}}$ for different system sizes N in Fig. 4.11(a), the rescaled quantity $P(t)t^{\delta'}$ versus $tN^{-\bar{z}}$ in Fig. 4.11(b). The exponent $\nu_\parallel$ is obtained from the scaling plot of $N_a(t)t^{-\eta}$ versus $t^{1/\nu_\parallel}(\kappa_t - \kappa)$ for different values of κ in Fig. 4.12(a). The data points for different κ values collapse well onto the curve for $\nu_\parallel = 1.07 \pm 0.005$. In Fig. 4.12(b), the crossover exponent ϕ is obtained from the scaling plot of $\rho_{a,s}(\omega_t - \omega)^{-\beta/\phi}$ versus $(\kappa - \kappa_c)(\omega_t - \omega)^{-1/\phi}$ for different values of ω. The data points for different values of ω also collapse well onto a curve for $\phi = 0.52 \pm 0.02$. The critical exponent values for other σ values are listed in Table C.1.

Using the field theory approach, the upper critical dimension was determined to be $d_c = 1.5\sigma$ [31]. Thus, when $\sigma < 4/3$, d_c is smaller than $d = 2$. In this case, when we perform dimensional analysis, we need to use d_c rather than $d = 2$. For instance, for hyperscaling analysis, we need to use $\bar{\nu} = d_c\nu$, i.e., $\bar{\nu} = (1.5\sigma)\nu$ for $\sigma < 4/3$ and $\bar{\nu} =$
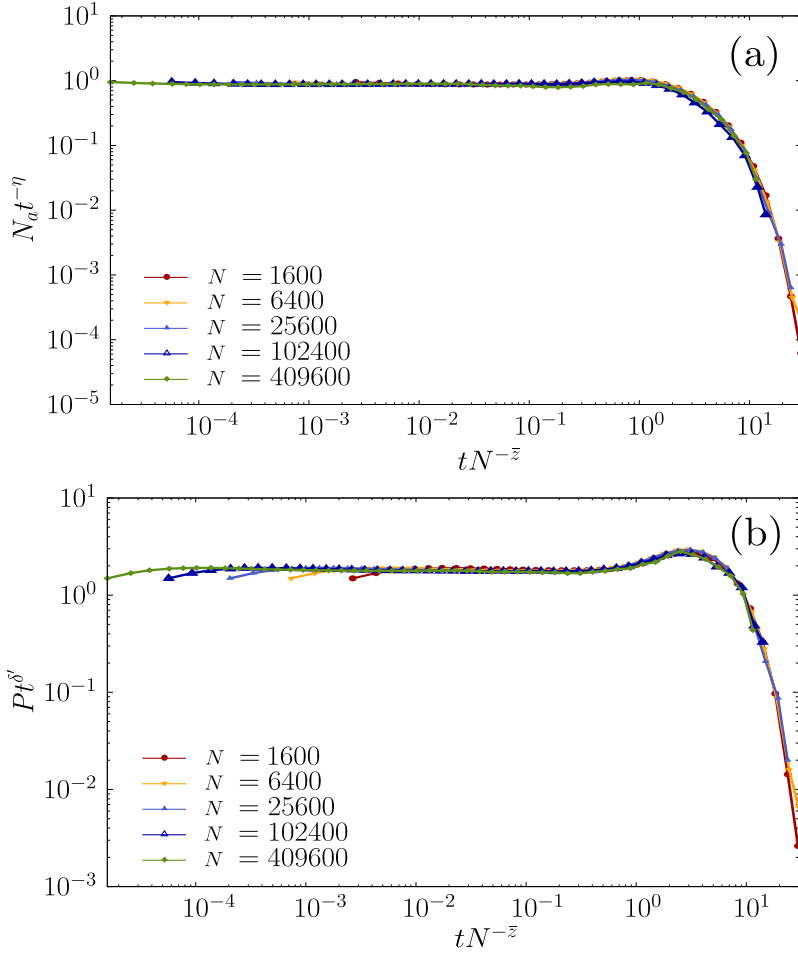
Figure 4.11: For the LTDP model with $\sigma = 2.0$ in two dimensions, (a) scaling plot of $N_a t^{-\eta}$ versus $tN^{-\bar{z}}$ for $\eta = -0.129$ and $\bar{z} = 0.922$. (b) Scaling plot of $P(t)t^{\delta'}$ versus $tN^{-\bar{z}}$ for $\delta' = 1.073$ and $\bar{z} = 0.922$.

2ν for $\sigma > 4/3$ in two dimensions. To confirm this scaling theory, for $\sigma = 2.0 > 4/3$, we obtain the dynamic exponent z by directly measuring the local slope of the plot of $R^2(t)$ versus t in Fig. 4.10(c) and the exponent $\bar{z}$ from the scaling plots in Figs. 4.11(a) and (b). For $\sigma < 4/3$, we also obtain the dynamic exponent z in Fig. 4.13(a) and the exponent $\bar{z}$ from the scaling plots in Fig. 4.13(b). Thus, we confirm that $z/\bar{z}$ is close to 2 for $\sigma = 2$ and 1.204 for $\sigma = 0.8$. The hysteresis of the first-order transition for $\omega > \omega_t$ is shown in Fig. 4.14.
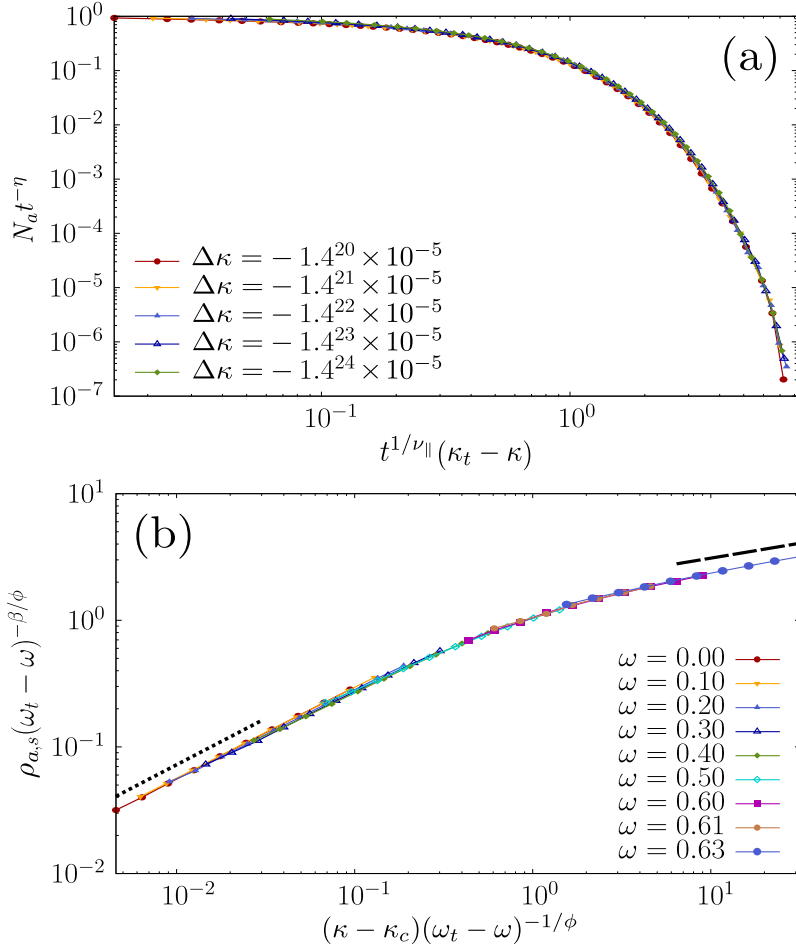
Figure 4.12: For the LTDP model with $\sigma = 2.0$ in two dimensions, (a) scaling plot of $N_a t^{-\eta}$ versus $t^{1/\nu_\parallel}(\kappa_t - \kappa)$ for different values of κ. Data points collapse well onto a single curve for $\kappa_t = 0.661663$, $\eta = -0.129$, and $\nu_\parallel = 1.07$. (b) Scaling plot of $\rho_{a,s}(\omega_t - \omega)^{-\beta/\phi}$ versus $(\kappa - \kappa_c)(\omega_t - \omega)^{-1/\phi}$ for different values of ω. Dotted (Dashed) line is a guideline with slope $\beta_{\mathrm{LDP}} = 0.7316$ ($\beta_t = 0.2236$). Data points collapse well onto a single curve for $\phi = 0.52$.

4.5.3 LTCP model in one dimension

We perform numerical simulations in one dimension, in which the exponent σ was taken from the interval $[0.1, 1.1]$ in steps of $\Delta\sigma = 0.1$. For each value of σ, we determine a critical point (κ_c, ω_c) and a tricritical point (κ_t, ω_t) using the same method as in the previous subsections. As in the phase diagram of the m-TCP model, a second-order
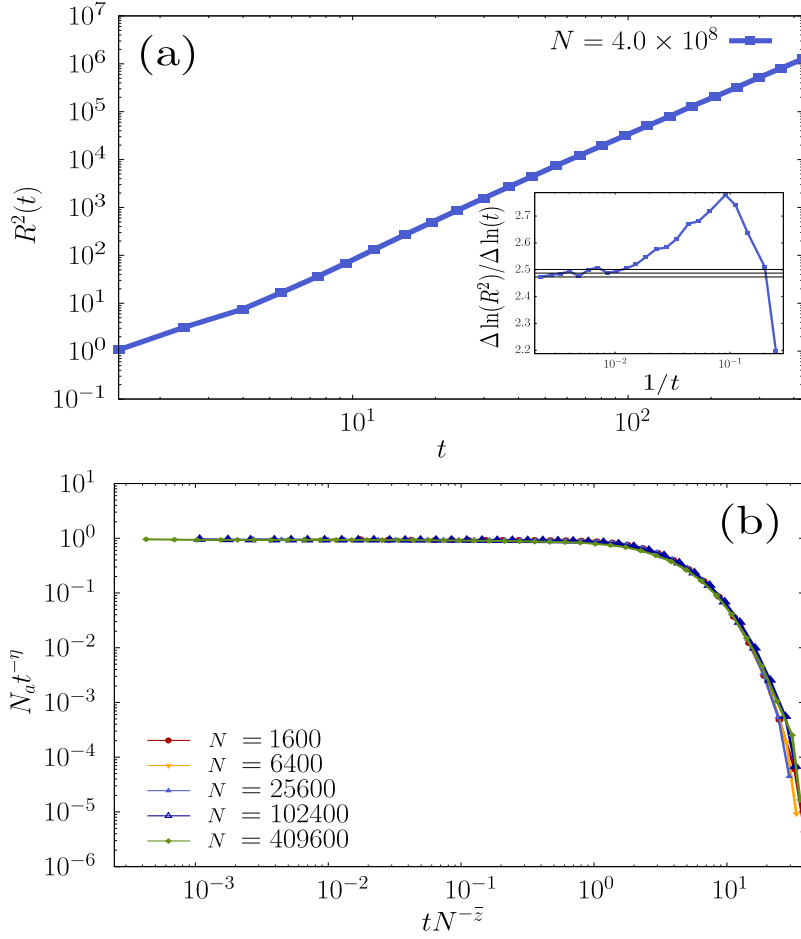
Figure 4.13: Plots of LTCP in two dimensions for $\sigma = 0.8$. (a) Plot of $R^2(t)$ versus t. Inset represents local slopes of each quantity versus $1/t$. (b) Scaling plot of $N_a t^{-\eta}$ versus $t N^{-\bar{z}}$ for $\eta = 0$ and $\bar{z} = 0.666$. We obtain the exponent values as (a) $2/z = 2.491 \pm 0.010$ and (b) $\bar{z} = 0.666 \pm 0.003$.

(first-order) transition occurs for $\omega < \omega_t(\sigma)$ ($\omega > \omega_t(\sigma)$).

Next, we determine an interval $[\sigma_{c1}, \sigma_{c2}]$ within which the dynamics of the LTCP model becomes nontrivial. We first determine that $\sigma_{c1} = 2/3$ using the criterion $d = 1.5\sigma_{c1}$ at $d = 1$. For $\sigma < \sigma_{c1}$, the mean-field solution is valid, and the upper critical dimension is determined as $d_c = (3/2)\sigma$. For $\sigma > \sigma_{c1}$, the upper critical dimension is larger than the dimension $d = 1$. Accordingly, when we use $\bar{\nu} = d\nu$, we need to take $\bar{\nu} = (1.5\sigma)\nu$ for $\sigma < 2/3$ and $\bar{\nu} = \nu$ for $\sigma > 2/3$ in one dimension. We confirm this
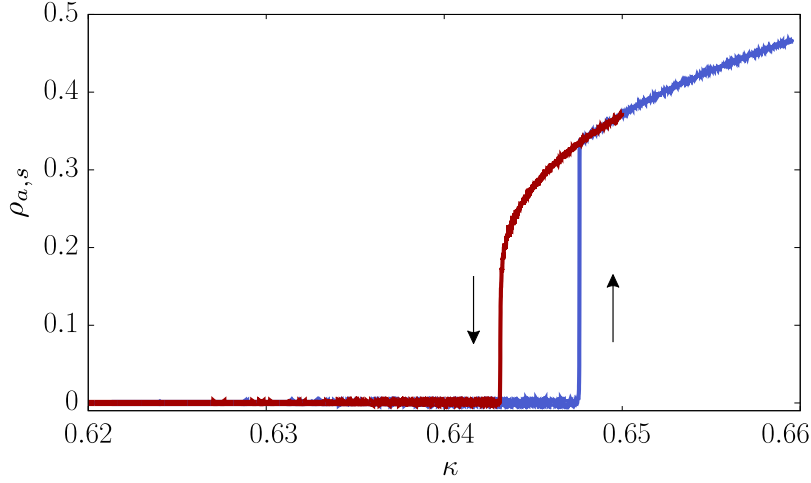
Figure 4.14: For the LTCP model with $\sigma = 1.0$ in two dimensions at $\omega = 0.55 > \omega_t$, plot of $\rho_{a,s}$ versus κ. A hysteresis curve is obtained. The system size is $N = 10^6$.

property by measuring the ratio $\bar{z}/z$ for different σ values smaller than and larger than σ_{c1}. To confirm this scaling theory, for $\sigma = 0.7 > 2/3$, we obtain the dynamic exponent z by directly measuring the local slope in the plot of $R^2(t)$ versus t in Fig. 4.16(c) and the exponent $\bar{z}$ from the scaling plots in Figs. 4.17(a) and (b). For $\sigma < 2/3$, we also obtain the dynamic exponent z in Fig. 4.19(a) and the exponent $\bar{z}$ from the scaling plots in Fig. 4.19(b). Thus, we confirm that $z/\bar{z}$ is close to 1 for $\sigma = 0.7$ and 0.749 for $\sigma = 0.5$.

To determine σ_{c2}, we recall the previous result that for a short-range DP-type CP model, a first-order transition does not occur in one dimension [79]. Thus, an STDP class does not appear in the region $\sigma > \sigma_{c2}$ [56]. On the basis of this background, we need to determine the σ range in which the LTCP universality class exists in one dimension. Thus, we need to check whether a tricritical point exists in the interval $\sigma_{c1} < \sigma < \sigma_{c2}$.

The numerical simulation results show that a tricritical point still exists in the region $\sigma > \sigma_{c1}$, but it disappears near $\sigma \simeq 1.0$, as a discontinuous transition does not occur (Fig. 4.20). Thus, we take $\sigma_{c2} \simeq 1.0$. The tricritical points for given σ values less
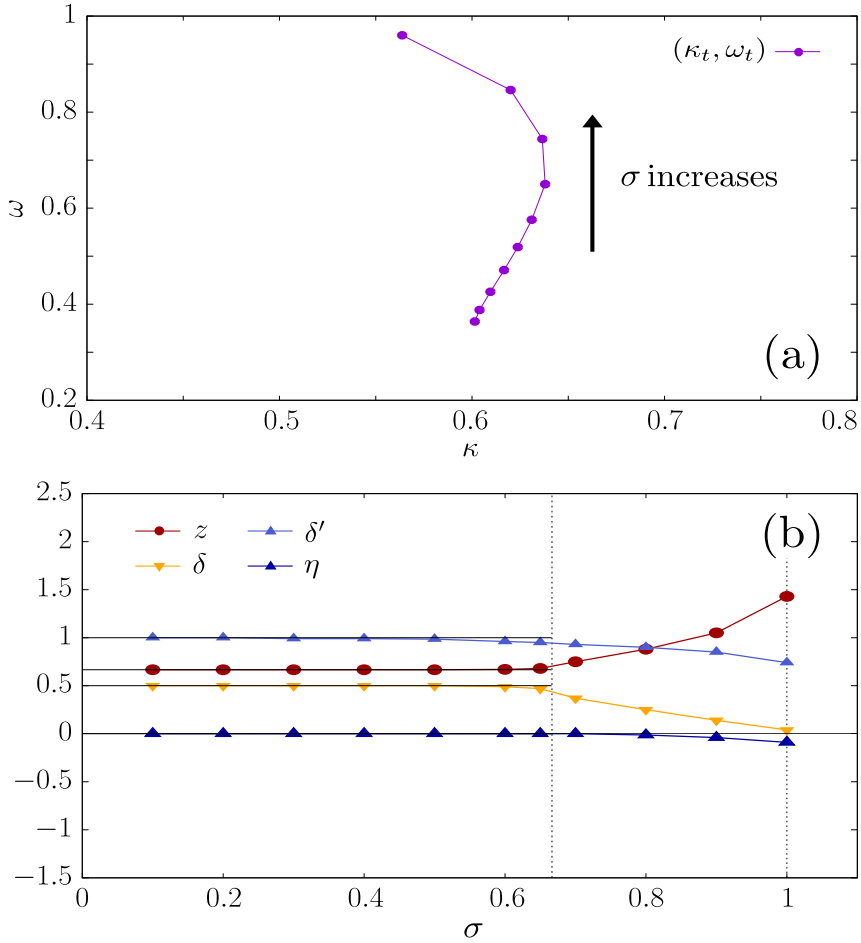
Figure 4.15: For the LTCP model in one dimension, (a) plot of the tricritical points in (κ, ω) space for different σ values in $[0.1, 1.0]$. (b) Plots of the critical exponent values z, δ, δ', and η as a function of σ at the tricritical point. σ_{c1} and σ_{c2} are indicated by vertical dotted lines.

than σ_{c2} are determined and shown in Fig. 4.15(a). As σ approaches 1.0 in the phase diagram, ω_t also approaches 1.0 [Fig. 4.15(a)]. By contrast, when $\omega = 1$, the LTDP dynamics is frozen because the absorbing state is reached immediately after the dynamics starts from an initial configuration in which either all the sites are fully active or only one site is active (see Table 4.1). Thus, the dynamics near $\sigma \approx 1.0$ is so sensitive that precise numerical measurement of the critical exponents is almost impossible.

At the tricritical point, the critical exponent values of δ', η, z, and δ are obtained
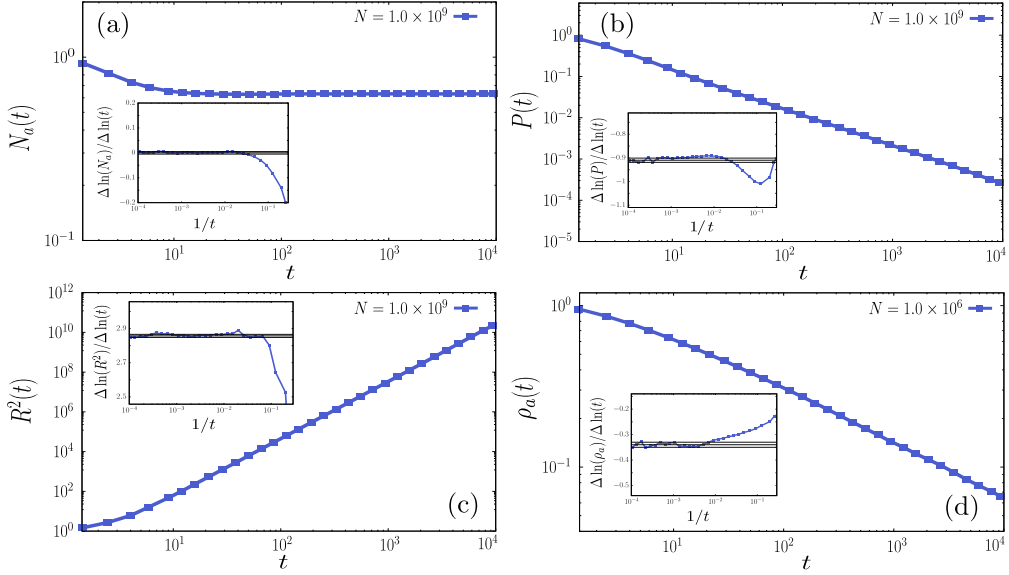
Figure 4.16: For the LTDP model with $\sigma = 0.7$ in one dimension at the tricritical point, plots of (a) $N_a(t)$, (b) $P(t)$, (c) $R^2(t)$, and (d) $\rho_a(t)$ versus t. We estimate the exponent values to be $\eta = 0.000 \pm 0.005$, $\delta' = 0.912 \pm 0.01$, $z = 0.701 \pm 0.01$, and $\delta = 0.34 \pm 0.01$, respectively. Insets: local slopes of each quantity versus $1/t$.

for each value of σ in the range $[0.1, 1.0]$ in steps of $\Delta\sigma = 0.1$, as shown in Fig. 4.15(b). The obtained critical values are listed in Table C.2. For $\sigma > \sigma_{c2}$, all the transition lines belongs to the DP class. We remark that whereas in the region $\sigma < \sigma_{c1}$, the exponents are constant regardless of σ, they vary constantly as a function of σ in the interval $[\sigma_{c1}, \sigma_{c2}]$, which is a prototypical pattern that appears in the long-range CP model. Indeed, we find numerically that the critical exponent values for σ between $[\sigma_{c1} = 2/3, \sigma_{c2} \approx 1.0]$ vary depending on σ, as shown in Table C.2. For instance, for $\sigma = 0.7$, we obtain the critical exponents directly by slope measurements as $\eta = 0.000 \pm 0.005$, $\delta' = 0.912 \pm 0.01$, $z = 0.701 \pm 0.01$, and $\delta = 0.34 \pm 0.01$, as shown in Fig. 4.16. We also obtain the critical exponents using the FSS method. We plot $N_a t^{-\eta}$ versus $tN^{-\bar{z}}$ for different system sizes N in Fig. 4.17(a), the rescaled quantity $P(t)t^{\delta'}$ versus $tN^{-\bar{z}}$ in Fig. 4.17(b). The exponent $\nu_{\parallel}$ is obtained from the scaling plot of $N_a(t)t^{-\eta}$ versus $t^{1/\nu_{\parallel}}(\kappa_t - \kappa)$ for different values of κ in Fig. 4.18(a). The data points
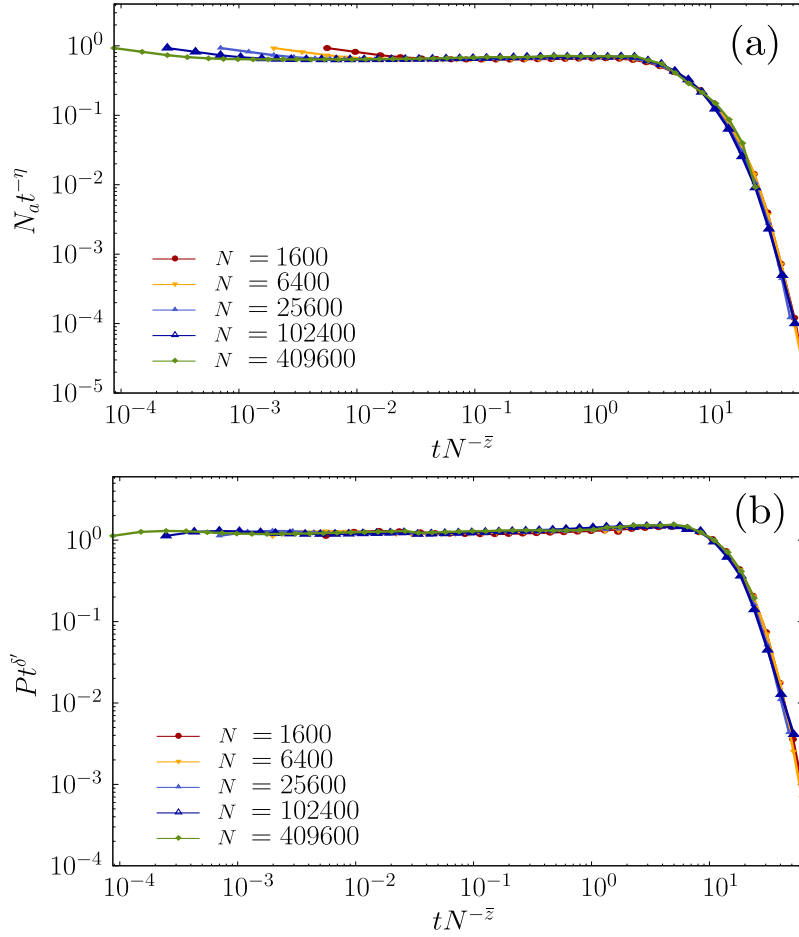
Figure 4.17: For the LTDP model with $\sigma = 0.7$ in one dimension, (a) scaling plot of $N_a t^{-\eta}$ versus $tN^{-\bar{z}}$ for $\eta = 0.000$ and $\bar{z} = 0.701$. (b) Scaling plot of $Pt^{\delta'}$ versus $tN^{-\bar{z}}$ for $\delta' = 0.912$ and $\bar{z} = 0.701$.

for different κ values collapse well onto a curve for $\nu_\parallel = 1.05 \pm 0.005$. In Fig. 4.18(b), the crossover exponent ϕ is obtained from the scaling plot of $\rho_{a,s}(\omega_t - \omega)^{-\beta/\phi}$ versus $(\kappa - \kappa_c)(\omega_t - \omega)^{-1/\phi}$ for different values of ω. The data points for different values of ω also collapse well onto a curve for $\phi = 0.52 \pm 0.02$. The critical exponent values for other σ values are listed in Table C.2. The hysteresis of the first-order transition for $\omega > \omega_t$ is shown in Fig. 4.20.
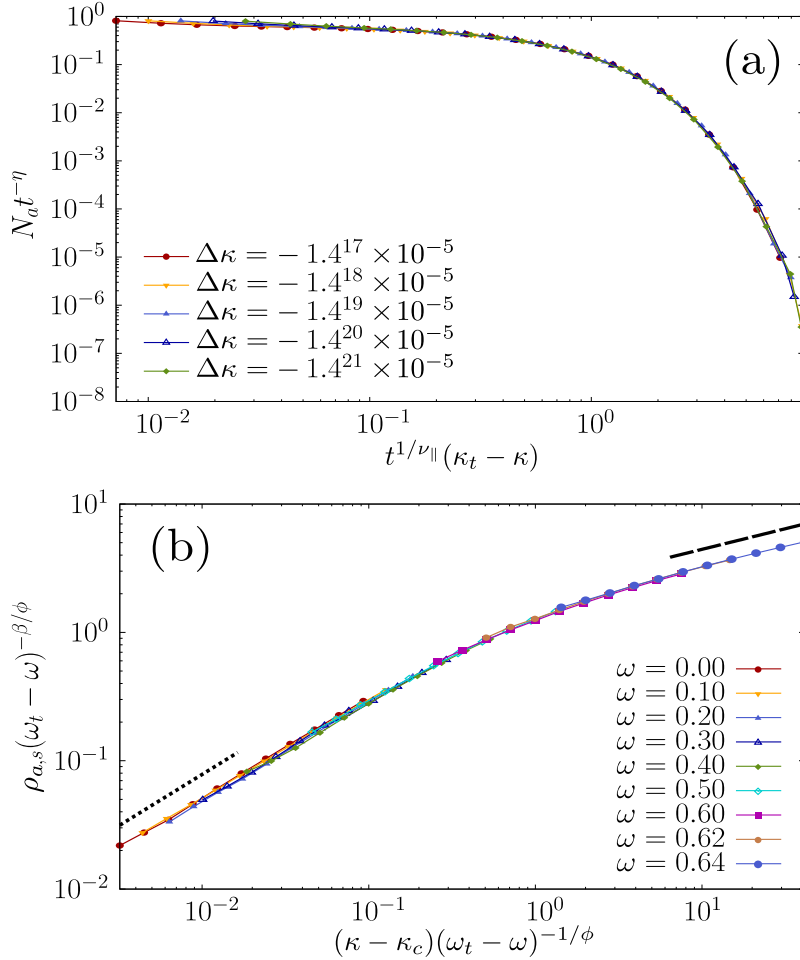
Figure 4.18: For the LTCP model with $\sigma = 0.7$ in one dimension, (a) scaling plot of $N_a t^{-\eta}$ versus $t^{1/\nu_\parallel}(\kappa_t - \kappa)$ for different values of κ. Data points collapse well onto a single curve for $\kappa_t = 0.637508$, $\eta = 0.00$, and $\nu_\parallel = 1.05$. (b) Scaling plot of $\rho_{a,s}(\omega_t - \omega)^{-\beta/\phi}$ versus $(\kappa - \kappa_c)(\omega_t - \omega)^{-1/\phi}$ for different values of ω. Dotted (Dashed) line is a guideline with slope $\beta_{\text{LDP}} = 0.800$ ($\beta_t = 0.321$). Data points collapse well onto a single curve with $\phi = 0.52$.

4.6 Conclusion and Discussion

In this paper, we investigated the critical behavior of the LTCP model, i.e., the TCP with long-range interaction in the form of $1/r^{d+\sigma}$ at a tricritical point, in one and two dimensions. First, we determined the domain of the LTDP universality class in the pa-
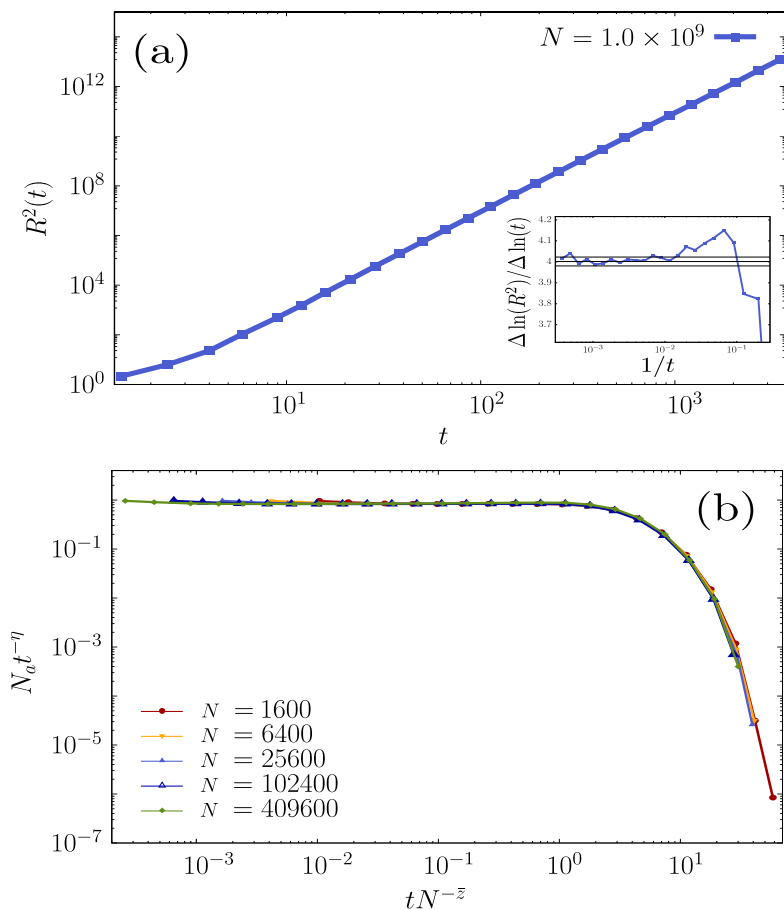
Figure 4.19: For the LTCP model with $\sigma = 0.5$ in one dimension, (a) plot of $R^2(t)$ versus t. We obtain the exponent $2/z = 4.004 \pm 0.010$. Inset represents local slopes at each t as a function of $1/t$. (b) Scaling plot of $N_a t^{-\eta}$ versus $tN^{-\bar{z}}$ for $\eta = 0$ and $\bar{z} = 0.666$.

rameter space (d, σ), as shown in Fig. 4.21. The domain is surrounded by the domains of the low-dimensional STDP class, the mean-field STDP class, and the mean-field LTDP class. These four domains meet at the point $(d, \sigma) = (3, 2)$. Below the upper critical dimension $d_c = 3$, the domain of the LTDP class is sandwiched between those of the low-dimensional STDP and the mean-field LTDP class, denoted as the shaded area bounded by $\sigma_{c1}(d) < \sigma < \sigma_{c2}(d)$ for each d. Analytically, $\sigma_{c1}(d)$ was determined using the formula $\sigma_{c1} = (2/3)d$, which was derived by dimensional analysis in
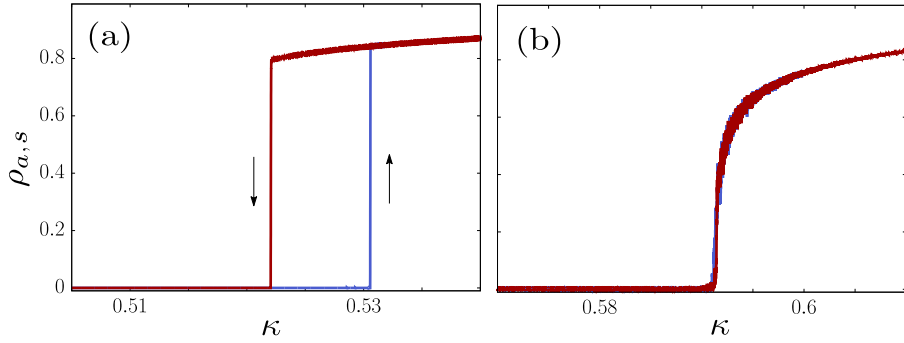
Figure 4.20: Plot of $\rho_{a,s}$ versus κ for the LTCP model in one dimension. (a) With $\sigma = 0.7$ at $\omega = 0.9 > \omega_t$, a hysteresis curve is obtained. (b) With $\sigma = 1.0$ at $\omega = 0.97$, a hysteresis curve does not occur. The system size is taken as $N = 10^6$.
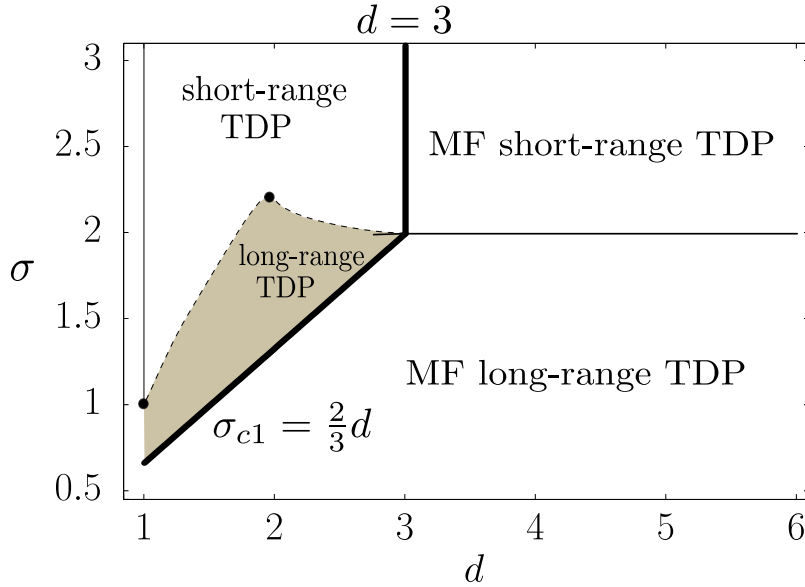
Figure 4.21: Diagram of universality classes of the LTCP model in the parameter space (d, σ). Mean-field solution is valid beyond the upper critical dimension line (bold line), $\min(3, 1.5\sigma)$. The slope of the dashed line near $(d, \sigma) = (3, 2)$ is 0.0304, according to Eq. (4.18), and is indicated by a short solid line. The dot at $(2, 2.2)$ indicates the σ_{c2} value obtained from numerical simulations of the LTCP model in two dimensions. The dot at $(1, 1.0)$ was numerically estimated for $d = 1$ and indicates σ_{c2}. The dashed curves connecting these three points separate the STDP region from the LTDP region. Along the thin solid line above the point $(1,1)$ in one dimension, a tricritical point is absent, so this thin line is excluded from the STDP region.

90

the mean-field limit. $\sigma_{c2}(d)$ was determined using $d + z(1 - \delta - \delta')$, where z, δ, and δ' are the exponents of the STDP class. Near the point $(3, 2)$, using the ε expansion of the RG approach for the STDP class [53,78], we obtained $\sigma = 2 - 0.0304\varepsilon + \mathcal{O}(\varepsilon^2)$ in $d = 3 - \varepsilon$ spatial dimensions. Therefore, we obtained the tangent of the phase boundary between the STDP and LTDP domains as $\Delta\sigma/\Delta d \approx 0.0304$ near the point $(3, 2)$ in Fig. 4.21.

Second, we numerically determined the critical exponent values at the tricritical point for $d = 1$ and $d = 2$. The numerical results showed that although the critical exponents are independent of the control parameter σ for $\sigma < \sigma_{c1}$ and $\sigma > \sigma_{c2}$, they vary continuously with σ between $[\sigma_{c1}, \sigma_{c2}]$. The numerical values of the critical exponents are listed in Tables C.1 and C.2 (Appendix C.3).

We unexpectedly obtained the following noteworthy behavior. First, in two dimensions, the numerically obtained value of σ_{c2} was not consistent with the theoretical value based on the STDP class; rather, it was close to the value obtained using the DP class. Second, in one dimension, the boundary σ_{c2} could not be determined from the STDP class, because the first-order transition does not occur in one dimension for the ordinary CP model. Thus, we determined σ_{c2} only numerically.

The LTCP model in one dimension is particularly notable. For each given σ in the range $[0.1, 1.0]$ in steps of $\Delta\sigma = 0.1$, as shown in Fig. 4.15(a), there exists a tricritical point (κ_t, ω_t). This figure shows that ω_t increases with increasing σ. We also found that the gap in the discontinuous transition near the tricritical point at $\sigma = 0.7$ (Fig. 4.20 (a)) is supposed to be decreasing as increasing σ and eventually the gap diminishes at a characteristic value of σ, denoted as σ_{c2} and estimated to be $\sigma_{c2} \approx 1.0$ (Fig. 4.20 (b)). This implies that ω_t approaches $\omega_t \to 1$, the upper bound of the pair-branching probability ω. In the semi-classical approach, the quantum coherence effect was regarded as the classical effect of a pair-branching process with the control parameter ω. Thus when $\omega = 1$, the LTCP model most highly reflects the quantum coherence effect. On the other hand, the previous studies [92–94] of QCP in one dimension revealed that

the tricritical point does not occur. This previous result seems to be associated with the current result that the tricritical point disappears beyond $\omega = 1$ as $\sigma > 1$. This is also consistent with another previous result that the STCP model, corresponding to the limit $\sigma \to \infty$ of the LTCP model, does not exhibit any discontinuous transition [79] in one dimension owing to strong fluctuation effect.

In this respect, although a discontinuous transition was not observed in short-range QCP in one dimension [92, 93], we guess that it could occur in long-range QCP in one dimension. In this case, a tricritical point and a new emerging behavior could be observed. An experiment of Rydberg atoms exciting to d-state is a potential candidate. Due to dipole interactions, long-range interaction is intrinsically generated.

Finally, we shall discuss the tricritical contact process in scale-free network. Recently, it was revealed that the homogeneous mean-field universality of the tricrticial contact process corresponds to that of the simplicial susceptibile-infected-susceptible model [95]. Moreover, it was shown that this model in scale-free network [96] exhibits the hybrid transition [97] (which contains natures of both first-order and second-order phase transitions).

In summary, we obtained the diagram of universality classes based on the analytical and numerical results in Tables C.1 and C.2 (Fig. 4.21). The local slope at $d = 3$ was determined by inserting the results of ε expansion for the STDP class [53, 78] into Eq. (4.18). The values of σ_{c2} in one and two dimensions were numerically obtained. In Ref. [98], the discrepancy between the simulated and field-theoretical σ_{c2} values is reported for other models such as the Ising [99, 100] and percolation models [101]. Here, although we obtained the Monte Carlo simulation results, the ε expansion of the LTCP model is still missing. Thus, further studies are needed from the perspective of RG theory.

Chapter 5

Simulation method of quantum systems

This chapter briefly covers the simulation method of open quantum systems: quantum jump Monte Carlo method [102, 103] and tensor network method [104]. The quantum jump Monte Carlo method is the exact simulation method to study the open quantum systems. However, this method is hard to perform the large systems size, due to the exponential complexity of Hilbert space as the system size increases. On the other hand, the tensor network methods have a advantage in efficiently compressing the memory, which enables to perform the large system size. Those two methods will be used for calculating the dynamics of open quantum many-body systems throughout the rest of the thesis.

5.1   Quantum jump Monte Carlo method

The quantum jump Monte Carlo (QJMC) (also known as Monte Carlo wavefunction) was derived in the 1990s. It is a numerical Monte-Carlo analysis used to solve the Lindblad equation describing the interaction between a quantum system and a Markovian environment. Open quantum systems are characterized by the presence of decoherence and dissipation. Decoherence makes the quantum objects behave classically (the emergence of classicality within quantum theory) and dissipation is induced by energy loss by the environment. Let us consider the one-dimensional spin-1/2 system with N sites. Dealing with the density matrix with the size $2^N \times 2^N$ is beyond the scope of the memory capacity even in modern computer. Thus instead of dealing with the
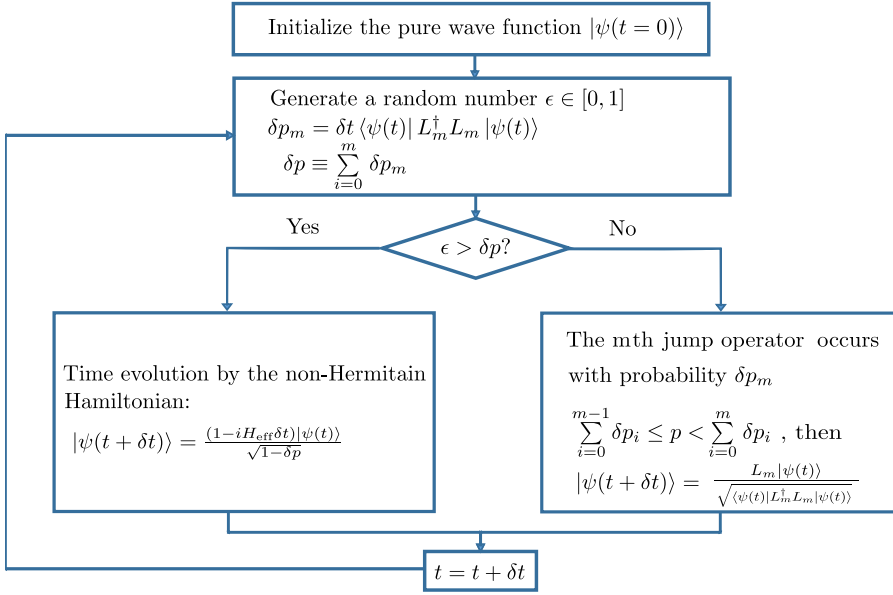
Figure 5.1: Flowchart of quantum jump Monte Carlo method. Repeat until $t = T_{\text{end}}$.

density matrix, it is more feasible to simulate a wave function with the size 2^N. Then pure states are propagated in time, with the dissipative process being described by a modification to the Hamiltonian, combined with quantum jumps.

5.1.1 Derivation

The Lindblad equation can be rewritten as

$$\partial_t \hat{\rho} = -i \left(\hat{H}_{\text{eff}} \hat{\rho} - \hat{\rho} \hat{H}_{\text{eff}}^\dagger \right) + \sum_k \hat{L}_m \hat{\rho} \hat{L}_m^\dagger, \text{ where } \hat{H}_{\text{eff}} = \hat{H} - \frac{i}{2} \sum_m \hat{L}_m^\dagger \hat{L}_m. \qquad (5.1)$$

This Hamiltonian is not the usual sense since it is not Hermitian, so its eigenvalues are not the energy. The first two terms in Eq. (5.1) can be interpreted as time evolution of this effective Hamiltonian

$$|\psi(t + \delta t)\rangle = e^{-iH_{\text{eff}}\delta t} |\psi(t)\rangle, \qquad (5.2)$$

94

where the time evolution operator is non-unitary. Thus, a normalization factor should be taken into account

$$\langle \psi(t+\delta t) | \psi(t+\delta t) \rangle = 1 - \delta p, \tag{5.3}$$

and δp is defined as

$$\delta p = \sum_m \delta p_m + \mathcal{O}(\delta t^2) = \delta t \sum_m \langle \psi(t) | \hat{L}_m^\dagger \hat{L}_m | \psi(t) \rangle + \mathcal{O}(\delta t^2). \tag{5.4}$$

Thus, the normalized wave function of non-Hermitian time evolution is given by

$$|\psi_{\text{evol}}(t+\delta t)\rangle = e^{-iH_{\text{eff}}\delta t} \frac{|\psi(t)\rangle}{\sqrt{1-\delta p}}. \tag{5.5}$$

Next, we can interpret the last term in Eq. (5.1) as the a quantum jump operator:

$$\left|\psi_{\text{jump}}(t+\delta t)\right\rangle = \frac{\hat{L}_m |\psi(t)\rangle}{\sqrt{\langle \psi(t) | \hat{L}_m^\dagger \hat{L}_m | \psi(t)\rangle}}, \tag{5.6}$$

with probability δp_m. Expanding the density matrix of an ensemble of pure states $\hat{\rho} = \sum_k p_k |\psi_k\rangle\langle\psi_k| = \mathcal{E}[|\psi\rangle\langle\psi|]$, Eq. (5.1) is written as

$$\hat{\rho}(t+\delta t) = \mathcal{E}\left[(1-\delta p)|\psi_{\text{evol}}(t+\delta t)\rangle\langle\psi_{\text{evol}}(t+\delta t)| + \sum_m \delta p_m |\psi_{\text{jump}}\rangle\langle\psi_{\text{jump}}|\right]. \tag{5.7}$$

This representation can be interpreted as two possible outcomes for random number $\varepsilon \in [0,1]$:

1. $\varepsilon > \delta p$: time evolution by the non-Hermitian Hamiltonian given by Eq. (5.5).

2. $\sum_{i=0}^{m-1} \delta p_i < \varepsilon < \sum_{i=0}^{m} \delta p_i$: the mth quantum jump operator occurs given by Eq. (5.6).

The flow chart in QJMC simulations is shown in Fig. 5.1. In the next section, we will present the tensor network method, which can be used to perform the simulation in

large system size.

5.2 Tensor network method

5.2.1 Matrix product state

The matrix product state (MPS) is popular technique to numerically calculate physical observables in one dimension. Let us consider the one-dimensional spin-1/2 system with N sites. Then the wave function is represented as

$$|\psi\rangle = \sum_{s_1,\cdots,s_N} c^{s_1,\cdots,s_N}|s_1,\cdots,s_N\rangle. \tag{5.8}$$

The exact description of the coefficient demands the exponential complexity as the system size increases. In this case, it is very challenging to simulate the quantum system above $N = 20$. Thus, to reduce the number of the coefficient, one uses the following expression:

$$c^{s_1,\cdots,s_N} \rightarrow c^{s_1}\cdots c^{s_N}. \tag{5.9}$$

However, this approximation cannot represent the entangled state, e.g. singlet state for $|\psi\rangle = 1/\sqrt{2}\,(|\uparrow\downarrow\rangle - |\downarrow\uparrow\rangle)$ due to $c^{\uparrow\downarrow} \neq c^{\downarrow\uparrow}$. To circumvent this problem, matrix product states is suggested by replacing the coefficient as the matrix

$$c^{s_1}\cdots c^{s_N} \rightarrow M^{s_1}\cdots M^{s_N}, \tag{5.10}$$

where the dimension of the matrix is called the bond dimension χ. This written form is called MPS and linearly proportional to the system size. Specifically, the number of coefficients for Eq. (5.8), Eq. (5.9), and Eq. (5.10) are given by $\mathcal{O}(2^N)$, $\mathcal{O}(2N)$, and $\mathcal{O}(2N\chi^2)$, respectively. The example of MPS of $1d$ systems is given as follows.

- Singlet state of 2-qubit: $|\psi\rangle = \frac{1}{\sqrt{2}}(|\uparrow\downarrow\rangle - |\downarrow\uparrow\rangle)$.

$$M_1^\uparrow = (\frac{1}{\sqrt{2}} \quad 0), \quad M_2^\uparrow = \begin{pmatrix} 0 \\ -1 \end{pmatrix}, \quad M_1^\downarrow = (0 \quad \frac{1}{\sqrt{2}}), \quad M_2^\downarrow = \begin{pmatrix} 1 \\ 0 \end{pmatrix}.$$

$$c^{\uparrow\downarrow} = M_1^\uparrow M_2^\downarrow = \frac{1}{\sqrt{2}}, \qquad c^{\downarrow\uparrow} = M_1^\downarrow M_2^\uparrow = -\frac{1}{\sqrt{2}}.$$

- W state of 3-qubit: $|\psi\rangle = \frac{1}{\sqrt{3}}(|\uparrow\downarrow\downarrow\rangle + |\downarrow\uparrow\downarrow\rangle + |\downarrow\downarrow\uparrow\rangle)$.

$$M_1^\uparrow = (\frac{1}{\sqrt{3}} \quad 0), \quad M_2^\uparrow = \begin{pmatrix} 0 & 0 \\ 1 & 0 \end{pmatrix}, \quad M_3^\uparrow = \begin{pmatrix} 0 \\ 1 \end{pmatrix},$$

$$M_1^\downarrow = (0 \quad \frac{1}{\sqrt{3}}), \quad M_2^\downarrow = \begin{pmatrix} 1 & 0 \\ 0 & 1 \end{pmatrix}, \quad M_3^\downarrow = \begin{pmatrix} 1 \\ 0 \end{pmatrix}.$$

$$c^{\uparrow\downarrow\downarrow} = M_1^\uparrow M_2^\downarrow M_3^\downarrow = \frac{1}{\sqrt{3}}, \quad c^{\downarrow\uparrow\downarrow} = M_1^\downarrow M_2^\uparrow M_3^\downarrow = \frac{1}{\sqrt{3}}, \quad c^{\downarrow\downarrow\uparrow} = M_1^\downarrow M_2^\downarrow M_3^\uparrow = \frac{1}{\sqrt{3}}.$$

Now, the question is how to make MPS for the given quantum state. To represent any quantum state, singular value decomposition (SVD) from linear algebra is used.

5.2.2 Time evolving block decimation

The time-evolving block decimation (TEBD) is a method to evolve the time dynamics using MPS. To this end, this method relies on a Trotter-Suzuki decomposition of a local Hamiltonian $H = \sum_j h_{j,j+1} = H_1 + H_2 + H_3 + \cdots$. For a small time step τ, the Trotter-Suzuki decomposition is represented as

$$|\psi(\tau)\rangle = e^{-\tau H} |\psi\rangle = e^{-\tau H_1/2} e^{-\tau H_2/2} e^{-\tau H_3/2} \cdots e^{-\tau H_3/2} e^{-\tau H_2/2} e^{-\tau H_1/2} |\psi\rangle + \mathcal{O}(\tau^3).$$

Then, combining the MPS and the TEBD, we can rewrite the flow chart in QJMC simulations in Fig. 5.2.
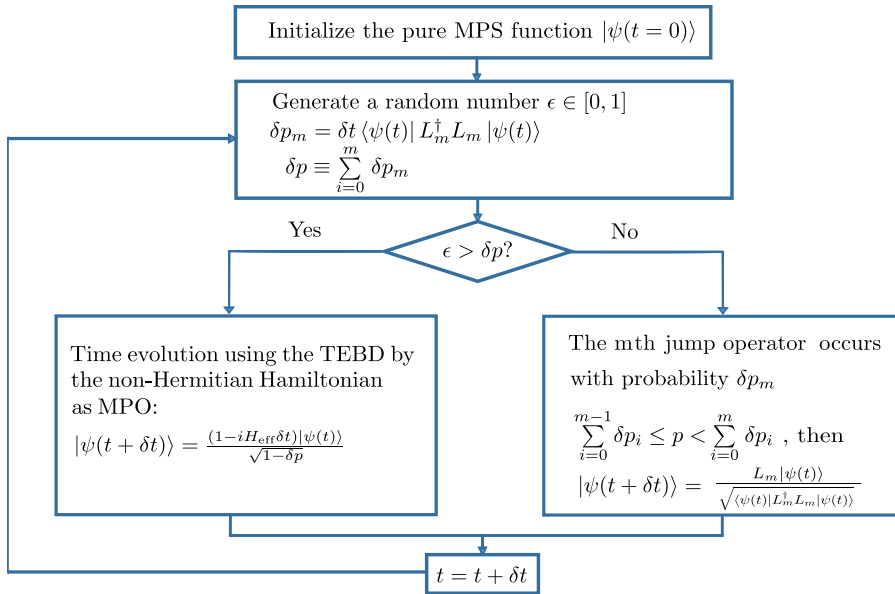
Figure 5.2: Flowchart of quantum jump Monte Carlo method with the MPS and TEBD. Repeat until $t = T_{\text{end}}$.

Chapter 6

Critical behaviors of 1d-QCP and 2d-QCP using quantum simulations

Major contents of this chapter is based on the preprint [36].

6.1 Introduction

Quantum critical phenomena in nonequilibrium systems have attracted considerable attention recently [75, 105–122] with the development of experimental techniques in cold atomic physics such as trapped ions [108] and lattices of ultracold ions [109–111]; driven circuit quantum electrodynamics systems [112]; and semiconductor microcavities [113]. The quantum criticality in the equilibrium state may be perturbed by the external environment, and thus the combined system is left in a non-equilibrium state. Here, we are interested in dissipative phase transitions arising from competition between the coherent Hamiltonian dynamics and incoherent dissipation process [5–17]. For these systems, questions arise as to whether the competition between quantum coherent and classical incoherent fluctuations produces another type of universal behavior [7, 17] and the conditions under which they exhibit classical critical behavior in terms of the loss rates to the environment [9, 10, 12].

Here, we aim to answer these questions by considering the quantum contact process [25, 26, 31, 92–94, 123, 124] in one dimension (1d-QCP). In the contact process (CP), each element of the system is in an active or inactive state, and its state changes according to given CP rules [20, 28, 29, 38, 40, 41, 45]. When all the elements are in
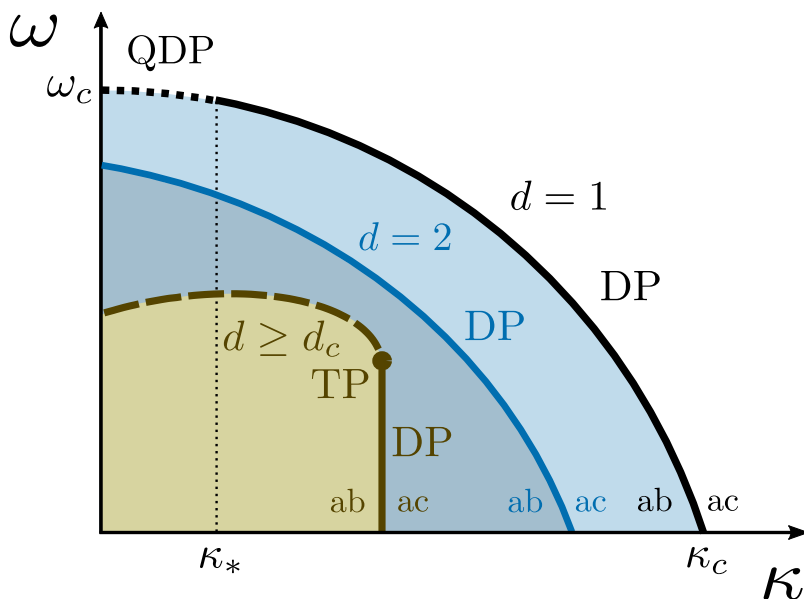
Figure 6.1: Schematic phase diagram of the QCP in the parameter space (κ, ω) in the mean-field limit (inside, $d \geq d_c$, where d is the spatial dimension and $d_c = 3$ is the upper critical dimension), in two dimensions (middle, $d = 2$), and one dimension (outside, $d = 1$). "ab" and "ac" represent absorbing phase and active phase, respectively. For $d \geq d_c$, discontinuous (dashed curve) and continuous transitions (solid line) occur, and they meet at a tricritical point. For $d = 2$, a continuous DP transition occurs over the entire region $[0, \kappa_c]$. For $d = 1$, a continuous DP transition occurs in the region $[\kappa_*, \kappa_c]$; however, in the interval $[0, \kappa_*]$, the exponent α of the density of active sites $n(t) \sim t^{-\alpha}$ from a homogeneous initial state decreases continuously as κ is increased with QDP values.

the inactive state, the system becomes trapped in a frozen configuration and no further dynamics proceeds. This absorbing phase transition of the classical CP that belongs to the directed percolation (DP) universality class. Meanwhile, the DP transition appears in diverse nonequilibrium systems; however, its experimental observation had been elusive but a couple of exceptions in turbulent liquid crystals [46] and Rydberg atoms [24]. Here, we focus on the recent observation of the $1d$-QCP in the dissipative quantum system of Rydberg atoms.

The dynamics of the 1D-QCP is described by the Lindblad equation, which consists of a Hamiltonian and dissipative terms. Their contributions to the overall dynam-

ics are adjusted by the model parameters ω (for the coherent quantum effect) and κ (for the incoherent classical dynamics). Thus, the system can exhibit a quantum or classical phase transition in extreme cases. A previous result based on the semiclassical mean-field solution [25] showed that the QCP exhibits a continuous (discontinuous) phase transition when κ is large (small). Thus, a tricritical point (TCP) exists, as shown in Fig. 6.1. The continuous transition belongs to the mean-field DP (MF-DP) universality class, and the TCP belongs to the mean-field tricritical DP (MF-TDP) class.

Using the functional renormalization approach, it was revealed that as dimension is decreased from the upper critical dimension $d_c = 3$, the tricritical point shifts toward the quantum axis with $\kappa = 0$ [94]. This indicates that a quantum phase transition would occur only for the case $\kappa = 0$. This behavior may be analogous to the fact that a quantum phase transition in equilibrium systems occurs only at zero temperature. Associated with this conjecture, a recent numerical study [123] of the $1d$-QCP with $\kappa = 0$ using the tensor network approach [92, 93, 123] revealed that the QCP exhibits a continuous transition in a quantum DP class: When the dynamics starts from a homogeneous state, i.e., all the sites are in the active state, the density of active sites at time t, denoted as $n(t)$, decays as $n(t) \sim t^{-\alpha}$ at a quantum critical point ω_c. The exponent $\alpha \approx 0.32$ obtained by the tensor network approach differs from the DP value $\alpha_{DP} \approx 0.16$. However, other exponents except the hyperscaling exponent $\nu_\perp$ for spatial correlation length have the DP values. In fact, the inconsistency of $\nu_\perp$ is inevitable, because the tensor network approach is not valid for strong entangled quantum systems. Using the quantum jump Monte Carlo approach, we obtain $\nu_\perp$ as the DP value, which will be presented later. On the other hand, when the QCP starts from a heterogeneous state, i.e., all the sites but one site are in the inactive state, all critical exponents have the classical DP values. Thus, the critical behavior of the $1d$-QCP with $\kappa = 0$ depends on the initial configurations.

In many dissipative quantum systems, quantum phase transitions would reduce to corresponding classical ones. This was expressed in terms of the quantum-to-classical

mapping [4]. This originates from that the quantum critical behavior in d spatial dimensions corresponds to the classical critical behavior in $d + z$ dimensions, where z is the dynamic critical exponent of the quantum system. This mapping was proposed based on the field theoretical argument that imaginary time in the quantum system acts as an additional dimension in the corresponding classical system.

For $1d$-QCP, here we are interested in how the quantum behavior responds to an external perturbation, that is, how the quantum behavior is changed to the classical DP behavior as the strength κ of classical fluctuations is increased from zero. We find that there exists an interval $[0, \kappa_*]$ in which the exponent α decreases continuously from the quantum value $\alpha \approx 0.32$ to the DP value ≈ 0.16 as κ is increased from $\kappa = 0$ to κ_*. The phase diagram for the $1d$-QCP is shown in Fig. 6.1. This result implies that the quantum effect still remains to some extent in the region $\kappa = [0, \kappa_*]$. This indicates that the crossover from the $1d$-QCP class to the classical DP class occurs in a soft-landing manner.

We extend our studies to two dimensional QCP ($2d$-QCP). Using the functional renormalization approach, it was conjectured that the $2d$-QCP exhibits a discontinuous transition at $\kappa = 0$ [26]. However, we find that the transition is continuous. Moreover, the continuous transition belongs to the classical DP class. The exponent α for the homogeneous initial condition has the DP value. Thus, the intermediate region $[0, \kappa_*]$ is absent. This implies that the strength of quantum fluctuations is weaker than that of classical fluctuations in two dimensions. For higher dimensions $d \geq d_c = 3$, a discontinuous transition occurs at $\kappa = 0$.

The critical behaviors of the $1d$-QCP and $2d$-QCP are obtained in the following ways. Once using the neural network (NN) machine learning algorithm, the transition point $\omega_c(\kappa)$ for each given κ is determined. Then at $\omega_c(\kappa)$, applying finite-size scaling (FSS) analysis for different system sizes, the exponent $\nu_\perp$ is determined [127–129]. At the transition point $\omega_c(\kappa)$, using the quantum jump Monte Carlo (QJMC) method [102, 103] as well as the tensor network method, to confirm in large system sizes, other

critical exponents are determined.

The 1d-QCP is experimentally realizable in the dissipative quantum system of Rydberg atoms. An essential factor in this experiment is so-called antiblockade: An inactive (active) spin is activated (inactivated) by detuning the excitation energy as much as the interaction energy to the active spin at the nearest neighbor. Moreover, when the strength of dephasing noise is sufficiently strong, the quantum coherences are suppressed and then the dynamics may be reduced to the classical CP process [23]. Otherwise, quantum coherence is effective, and a mixed of coherent and incoherent CPs can be realized [25,26]. Thus, by controlling the ratio between the Rabi frequency and the dephasing rate, one may find the crossover behavior from a quantum to a classical nonequilibrium phase transition. It was revealed that the classical parameter is related to $\kappa = 4\Omega^2/\Gamma$, where Ω is the Rabi frequency and Γ is the dephasing rate [23]. The derivation is shown in Appendix. Thus for $\Omega < \sqrt{\kappa_*\Gamma}/2$, the quatum-DP (QDP) behavior appears. This region is a quantum critical region where the quantum fluctuations play a role in universal behavior.

The paper is organized as follows: We first introduce the 1d-QCP model, and specify the classical and quantum limits in Sec. 6.2. The structure of our NN and optimization scheme are presented in Sec. 6.3.1. Finite-size scaling behaviors using the NN, QJMC and tensor network methods; the universality class; and the crossover behavior are presented in Sec. 6.3.3. Summary and final remarks are presented in Sec. 6.4. Additionally, technical details of QCP in the classical limit using the quantum Monte Carlo method, neural network approach with different training regions, and the derivation of the model parameter κ for the classical dynamics in terms of the experimental parameters of Rabi frequency Ω and dephasing rate Γ are presented in Appendices.

6.2 Model

We consider a one-dimensional quantum spin chain with a periodic boundary condition, where each state of a site (active or inactive) represents the up or down spin state,

103
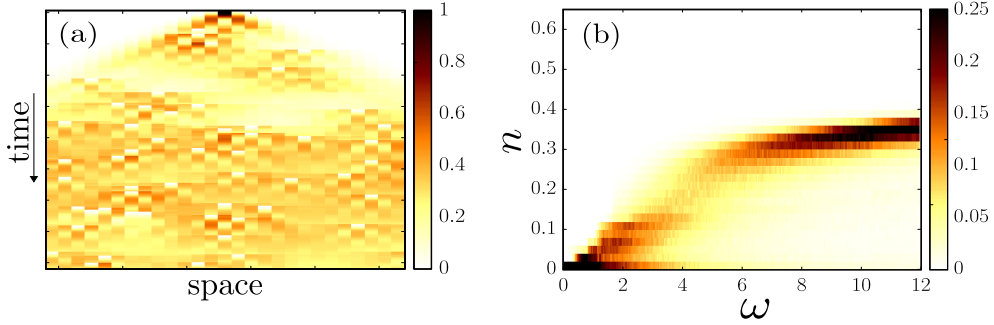
Figure 6.2: Plots using QJMC method. (a). Trajectory of the $1d$-QCP with $\kappa = 0$ and $\omega > \omega_c$ from a single active site at the center. (b). Histogram of the densities of active sites in steady states as a function of ω for system size $N = 20$. The data are obtained using QJMC simulations. Time t and the control parameter ω are given in units of $1/\gamma$ and γ, respectively.

denoted as $|\uparrow\rangle$ or $|\downarrow\rangle$. A QCP consists of three incoherent and two coherent processes: i) decay, in which an active site is incoherently inactivated spontaneously at a rate γ; ii) incoherent branching or coagulation, in which an active particle incoherently activates or inactivates an inactive particle at the nearest-neighbor site at a rate κ, respectively; and iii) coherent branching or coagulation, which is a quantum counterpart of process ii) driven by a Hamiltonian at a rate ω, respectively. The classical ii) and quantum iii) rules are in competition, which may change the transition behavior.

The time evolution of the density matrix $\hat{\rho}$ is described by the Lindblad equation, which consists of the Hamiltonian and dissipative terms [27]:

$$\partial_t \hat{\rho} = -\mathrm{i}\left[\hat{H}_S, \hat{\rho}\right] + \sum_{a=d,b,c} \sum_{\ell=1}^{N} \left[\hat{L}_\ell^{(a)} \hat{\rho} \hat{L}_\ell^{(a)\dagger} - \frac{1}{2}\left\{\hat{L}_\ell^{(a)\dagger} \hat{L}_\ell^{(a)}, \hat{\rho}\right\}\right]. \tag{6.1}$$

The Hamiltonian $\hat{H}_S$, which governs the branching and coagulation processes and represents coherent interactions, is expressed as

$$\hat{H}_S = \omega \sum_{\ell=1}^{N} \left[(\hat{n}_{\ell-1} + \hat{n}_{\ell+1})\,\hat{\sigma}_\ell^x\right]. \tag{6.2}$$
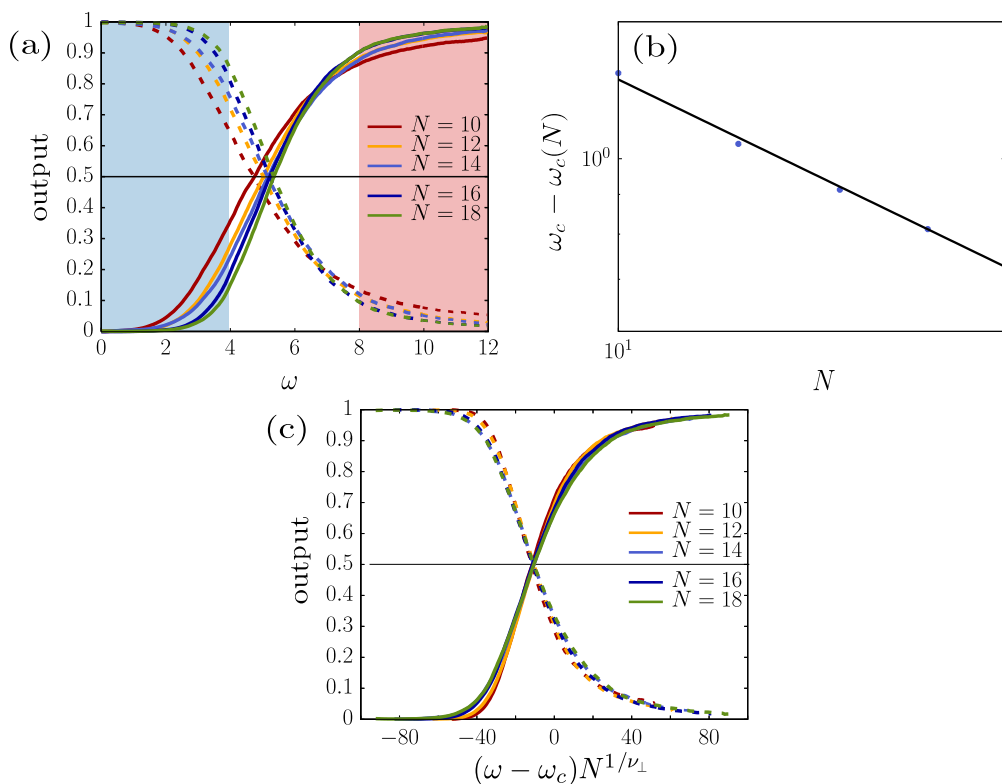
Figure 6.3: Plots using neural network method. (a) Plot of the output averaged over a test set as a function of ω for different system sizes. Solid (dashed) line represents the values of the first (second) output neuron. From this plot, we estimate the crossing point of the two outputs and regard it as the transition point $\omega_c(N)$ for a given system size N. (b) Plot of $\omega_c - \omega_c(N)$ versus N, where ω_c is chosen so as to yield power-law behavior and is regarded as the transition point in the thermodynamic limit. The slope represents the value of the critical exponent $-1/\nu_\perp$. (c) Scaling plot of the output versus $(\omega - \omega_c)N^{1/\nu_\perp}$. For the obtained numerical values of $\nu_\perp$ and ω_c, the data collapse well for system sizes $N = 10, 12, 14, 16$, and 18.

Here $\hat{\sigma}_l^i$ denotes the Pauli matrix, where the superscript and subscript stand for the spin axis and site index, respectively, and $\hat{n}_l$ means the number operator for a up spin at the

lth site. The Lindblad decay, branching, and coagulation operators are given by

$$\hat{L}_\ell^{(d)} = \sqrt{\gamma}\,\hat{\sigma}_\ell^- \,, \tag{6.3}$$

$$\hat{L}_\ell^{(b)} = \sqrt{\kappa}\,(\hat{n}_{\ell-1} + \hat{n}_{\ell+1})\hat{\sigma}_\ell^+ \,, \tag{6.4}$$

$$\hat{L}_\ell^{(c)} = \sqrt{\kappa}\,(\hat{n}_{\ell-1} + \hat{n}_{\ell+1})\hat{\sigma}_\ell^- \,, \tag{6.5}$$

respectively. $\hat{\sigma}_\ell^+$ and $\hat{\sigma}_\ell^-$ are the raising and lowering operators of the spin at site ℓ, respectively; they are defined in terms of the spin basis as $\hat{\sigma}^+ = |\!\uparrow\rangle\langle\downarrow\!|$ and $\hat{\sigma}^- = |\!\downarrow\rangle\langle\uparrow\!|$. In addition, $\hat{n} = \hat{\sigma}^+\hat{\sigma}^-$ and $\hat{\sigma}^x = \hat{\sigma}^+ + \hat{\sigma}^-$ are the number operator and spin flip operator, respectively. In addition, we rescale time and the quantum control parameters ω and κ in units of γ; therefore, we set $\gamma = 1$.

Quantum branching and coagulation occur at a rate ω, and the corresponding classical processes occur at a rate κ. When $\omega \to 0$, the model is reduced to the classical CP, which belongs to the DP class. Here, we first consider the pure quantum limit $\kappa \to 0$ but with finite ω. The opposite limit $\omega \to 0$ with finite κ, and the case of both ω and κ being finite are discussed in Appendix D.1.

When ω is small, inactive particles become more abundant with time, and eventually the system is fully occupied by inactive particles. Thus, the system is no longer dynamic and falls into an absorbing state, which is represented by $\hat{\rho}_{\mathrm{ab}} = |\!\downarrow \cdots \downarrow\rangle\langle\downarrow \cdots \downarrow\!|$. When ω is large, the system remains in an active state with a finite density of active particles [Fig. 6.2(a)]. Thus, the QCP exhibits a phase transition from an active to an absorbing state as ω is decreased.

6.3 Results

6.3.1 NN approach

The NN approach has recently served as a powerful tool [130, 131] for understanding phase transitions in classical systems [127], which exhibit patterns involving many
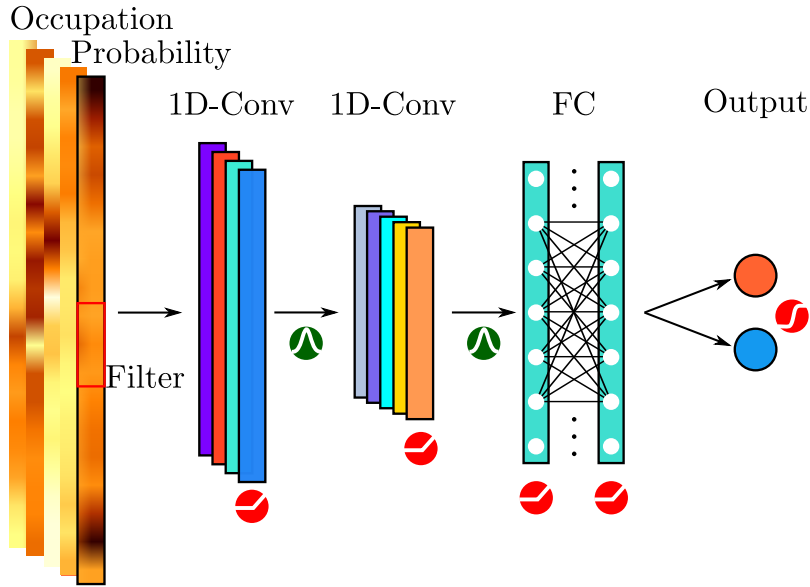
Figure 6.4: Schematic illustration of the convolutional neural network built in combination of a one-dimensional convolutional layer (1d-Conv) and a fully connected layer (FC). The red circles represent the activation function of each layer. The green circles below the arrows represent the batch normalization.

components. Each component has one of two values, for instance, the up and down spin states in ferromagnetic systems. By contrast, each component of a quantum system has a real value, and thus the patterns are much more complex. Nevertheless, the NN approach has reportedly been successfully used to determine the transition points of closed quantum systems on the basis of simulation data [132]–[134] and experimental images [135], [136]. On the other hand, for quantum dissipative systems, an unsupervised NN approach was used to generate the configurations in steady state [137]–[141]. This approach was efficient, because it spends less computing resources to generate configurations compared to conventional simulations. Meanwhile, in dissipative quantum systems, to determine a transition point accurately, large system sizes are necessary and thus a huge computing resources for simulations. Here, we use the NN approach as an alternative way and obtain an accurate transition point enough to investigate the critical behavior of 1d-QCP at the transition point.

For classical systems, the transition point of a continuous absorbing transition is normally indicated by the presence of power-law behavior of the order parameter with respect to time [32, 38]. Consequently, a large system size is required to identify the transition point. Accurately identifying the transition point using QJMC simulations of the QCP is even more difficult and is thus a challenging problem. To overcome this difficulty, we notice that the system is in the absorbing state for $\omega \ll \omega_c$ and in the active state for $\omega \gg \omega_c$. Combining this observation with a recently proposed NN supervised learning concept, we identify the transition point as follows.

To implement the NN approach, we first organize a dataset of the occupation probability of site ℓ, which is denoted as $p_\ell(t) = \text{Tr}[\hat{\rho}(t)\hat{n}_\ell]$. Using the QJMC method, we generate a steady-state configuration and obtain the occupation probabilities of each site, $\{p_\ell\}$. We collect 5×10^3 configurations in $\omega \in [0, 12]$ at $\Delta\omega = 0.04$ intervals. To prepare the training dataset for supervised learning, we label the configurations using one-hot encoding [142], where the absorbing state ($\omega \in [0, 4]$) is encoded as $(0, 1)$, and the active state ($\omega \in [8, 12]$) is encoded as $(1, 0)$ [see shaded regions in Fig. 6.3(a)].

After we collected the snapshots, we tried to train the NN. The objective of the learning procedure is to optimize the neural network to adjust the weights of connections between neural units to achieve a variational minimization of a properly defined cost function. To this end, we construct the hidden layers of the NN, including one-dimensional convolutional layers, batch normalization layers [143], and fully connected layers, as shown in Fig. 6.4. We employ the framework of TENSORFLOW [144] and use ReLU and tanh for the activation function in the hidden layer. Two neurons in the output layer are used, and a softmax function is used as the activation function in the output layer. We employ the cross-entropy or the mean-square error function as the cost (error) function of the NN, which is then optimized using Adam [145] or RMSProp. We change the architecture and optimization algorithms in various ways. Regardless of these changes, the well-trained machines produce consistent results. To check the sensitivity of the positions of the left and right boundaries, the NN ap-

proach with different training regions is described and its results are presented in Appendix D.3. Once the NN is well-trained with the labeled training dataset in the two regions, we obtain the outputs for the entire ω region.

Next, using the obtained transition points $\omega_c(N)$ for given system sizes, we perform FSS analysis and identify the transition point in the thermodynamic limit ω_c. We also determine the correlation length exponent $\nu_\perp$. Next, we determine the other critical exponents by performing extensive QJMC simulations up to system size $N = 20$ and tensor network method of a large system $N = 80$ at ω_c. Specifically, tensor network method is implemented by the QJMC method with the matrix product states and time-evolving block decimation.

6.3.2 Finite-size scaling analysis for 1d-QCP

In Fig. 6.3(a), the two outputs of the NN indicate the predictabilities that the system will fall into the absorbing state and remain in the active state, respectively. The crossing point of these outputs indicates a transition point $\omega_c(N)$ for a given system size N [Fig. 6.3(a)]. Several studies [127–129] showed that the predictability exhibits FSS behavior. Using the obtained $\omega_c(N)$ for different system sizes, we determine ω_c in the thermodynamic limit by plotting $\omega_c - \omega_c(N)$ versus N [Fig. 6.3(b)], which is expected to behave as $\omega_c - \omega_c(N) \sim N^{-1/\nu_\perp}$. Indeed, the plot exhibits power-law behavior when an appropriate value of ω_c is chosen, and the critical exponent $\nu_\perp$ is obtained from the slope of the power-law curve. We obtain $\omega_c \approx 6.04$ and $\nu_\perp = 1.06 \pm 0.04$; the latter is in agreement with the value of $\nu_\perp \approx 1.096$ for the DP class in one dimension, but differs from the value of $\nu_\perp \approx 0.5 \pm 0.2$ obtained using the tensor network approach. The scaling plot is drawn in the form of the output versus $(\omega - \omega_c)N^{1/\nu_\perp}$ for different N values [Fig. 6.3(c)]. The data for different system sizes seem to collapse.

Next, we measure the values of the other critical exponents using the quantum jump Monte Carlo (QJMC) method in the critical region around ω_c and the tensor network method for larger system sizes. First, we take an initial state in which a sin-

gle active seed is present at $\ell = 0$, and the remaining sites are inactive. This configuration is expressed as $\hat{\rho}(0) = \hat{\sigma}_0^+ \hat{\rho}_{ab} \hat{\sigma}_0^-$. We measure the following quantities: i) the survival probability, that is, the probability that the system does not fall into an absorbing state, $P(t) = 1 - \text{Tr}[\hat{\rho}(t)\hat{\rho}_{ab}]$; ii) the number of active sites, $N_a(t) = \sum_\ell \text{Tr}[\hat{\rho}(t)\hat{n}_\ell]$; iii) the mean square distance of the active sites from the origin, $R^2(t) = \sum_\ell \text{Tr}[\ell^2 \hat{\rho}(t)\hat{n}_\ell]/N_a(t)$; iv) the density of seed-site over all runs, $\rho_d(t) = \text{Tr}[\hat{\rho}(t)\hat{n}_{\ell=0}] \sim N_a(t)/R(t)$; and v) the density of seed-site over surviving runs, $\rho_{d,s}(t) = \rho_d/P(t)$. At the transition point, these quantities exhibit the following power-law behaviors: $P(t) \propto t^{-\delta'}$, $N_a(t) \propto t^\eta$, $R^2(t) \propto t^{2/z}$, $\rho_d(t) \propto t^{\eta - 1/z}$, and $\rho_{d,s}(t) \propto t^{-\delta}$. For the relation $\rho_d(t) = \rho_{d,s}(t)P(t) \sim t^{-\delta - \delta'}$, the scaling relation $\eta - 1/z = -(\delta + \delta')$ holds. We estimate the exponents $\delta + \delta'$, η, δ', z, and δ by direct measurement of the slopes in the double-logarithmic plots, as shown in Fig. 6.5. We estimate the exponent z using the data collapse technique. For instance, for the survival probability $P(t)$, we plot $P(t)t^{\delta'}$ versus tN^{-z} for different system sizes N. We determine z as the value at which the data for different system sizes collapse onto a single curve. The values of critical exponents are in good agreement with the DP values within the error bars (Table I).

Table 6.1: Critical point and critical exponents for the $1d$-QCP.

	$1d$-QCP from CNN+QJMC	$1d$-QCP from tensor network [92,93]	$1d$-DP
ω_c	6.04	6.0 ± 0.05	—
δ'	0.16 ± 0.05	0.26 ± 0.04	0.159
z	1.55 ± 0.06	1.61 ± 0.16	1.581
η	0.30 ± 0.05	0.26 ± 0.05	0.313
$\delta + \delta'$	0.32 ± 0.01	0.36 ± 0.12	0.318
α	0.32 ± 0.01	0.36 ± 0.08	0.159
$\nu_\perp$	1.06 ± 0.04	0.5 ± 0.2	1.096

Second, we take a homogeneous initial state in which the entire system is occupied by active sites at $t = 0$, which is expressed as $\hat{\rho}(0) = |\uparrow \cdots \uparrow\rangle\langle\uparrow \cdots \uparrow|$. From this initial state, we measure vi) the density $n(t)$ of active sites at time t averaged over all
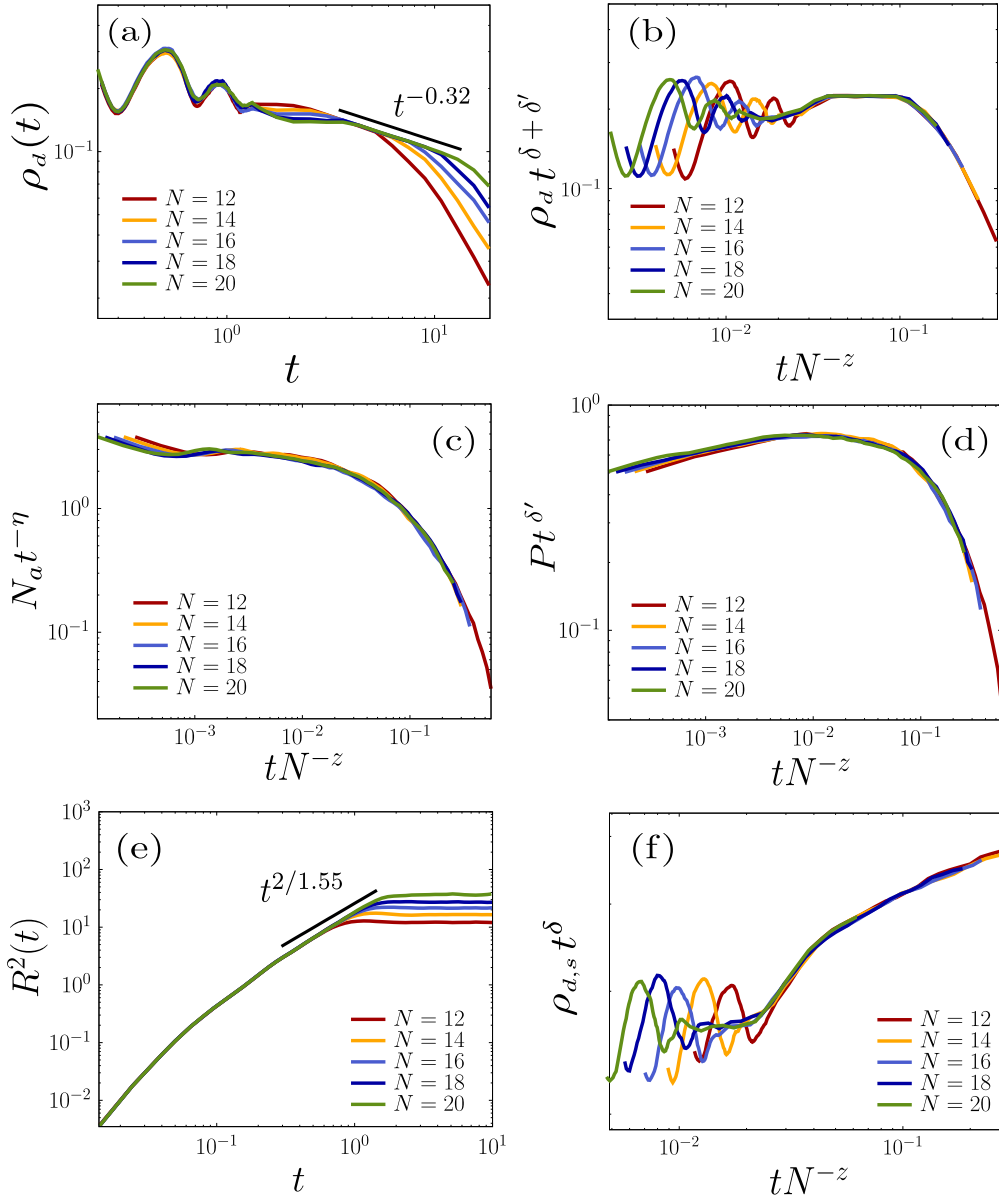
Figure 6.5: Estimates of the critical exponents of the $1d$-QCP starting from a single active site. (a) Plot of $\rho_d(t)$ versus t, which behaves as $\rho_d(t) \sim t^{-\delta-\delta'}$. (b) Scaling plot of $\rho_d(t)t^{\delta+\delta'}$ versus tN^{-z} for $\delta + \delta' = 0.32$ and $z = 1.55$. (c) Scaling plot of $N_a(t)t^{-\eta}$ versus tN^{-z} for $\eta = 0.30$ and $z = 1.55$. (d) Scaling plot of $P(t)t^{\delta'}$ versus tN^{-z} for $\delta' = 0.16$ and $z = 1.55$. (e) Plot of $R^2(t)$ as a function of t. (f) Scaling plot of $\rho_{d,s}(t)t^{\delta}$ versus tN^{-z} for $\delta = 0.16$ and $z = 1.55$.

111
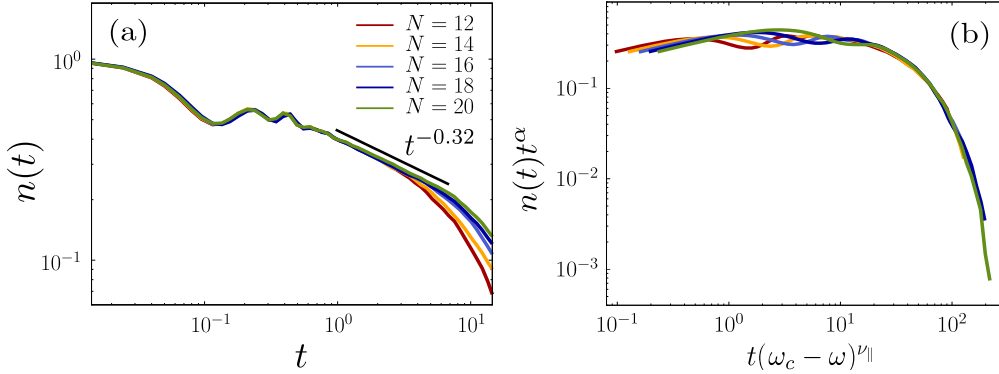
Figure 6.6: Estimates of the critical exponent α and $\nu_\parallel$ from the homogeneous state. (a) Plot of $n(t)$ as a function of t for different system sizes when $\kappa = 0$, which shows that $n(t) \sim t^{-\alpha}$, with $\alpha = 0.32$. (b) Data points collapse well onto a single curve for $\omega_c = 6.04$, $\alpha = 0.32$, and $\nu_\parallel = 1.73$. The units of control parameter is given as γ.

runs. This quantity is formulated as $n(t) = (\sum_\ell \text{Tr}[\hat{\rho}(t)\hat{n}_\ell])/N$. We find that $n(t)$ exhibits power-law decay as $n(t) \sim t^{-\alpha}$ with the exponent $\alpha = 0.32 \pm 0.01$, as shown in Fig. 6.6(a). This value is consistent with the result obtained by applying the tensor network approach; however, it is not consistent with the corresponding DP value, which was estimated as $\alpha_{\text{DP}} = 0.16$. Therefore, the $1d$-QCP for $\kappa = 0$ creates another universal behavior.

In Fig. 6.6(b), the exponent $\nu_\parallel$ is obtained from the rescaling plot of $n(t)t^\alpha$ versus $t(\omega_c - \omega)^{\nu_\parallel}$ for different ω values. The ω values are taken from the region used in classical contact process [Fig. D.2(b)]. We obtain $\nu_\parallel = 1.73$ and thus $\nu_\perp = \nu_\parallel/z \simeq 1.095$. This value is consistent with the one from the NN approach.

We note that $\rho_d(t)$ and $n(t)$ are actually the same quantity even though they emerge from different initial states [146]. They exhibit the same critical behaviors in the CP class (see Appendix D.2), but they exhibit different critical behaviors for the $1d$-QCP. This behavior is unusual, because the universality class is independent of the initial state according to the theory of critical phenomena. To understand the underlying mechanism, we increase the control parameter κ from zero to $\kappa = 0.6$ in steps of 0.2 and explore the behavior of $n(t)$ at each $\omega_c(\kappa)$ [Fig. 6.7(a)]. We find that the value

of α decreases continuously from 0.32 for $\kappa = 0$ to $\alpha = 0.16$ for $\kappa = 0.6$. Furthermore, we perform the tensor network method based on the matrix product states and time-evolving block decimation to confirm in large system size [Fig. 6.7(b)]. Using the FSS analysis, we determine the exponent z for each given κ [Fig. 6.7(c)−(f)]. These results suggest that α decreases continuously as κ is increased and reaches the DP value at $\kappa_* \approx 0.58$. (Table 6.2)

6.3.3 Finite-size scaling analysis for 2d-QCP

We investigate the critical behavior of QCP in two dimensions (2d-QCP). At $\kappa = 0$, we find that the 2d-QCP exhibits the continuous absorbing state phase transition. Taking a similar steps of the 1d-QCP, we obtain the critical exponents of 2d-QCP using the QJMC simulations. For $\kappa = 0$, we obtain $\omega_c \approx 0.94$. At this ω_c, we find that $n(t)$ exhibits power-law decay as $n(t) \sim t^{-\alpha}$ with $\alpha = 0.45 \pm 0.03$, as shown in Fig. 6.8(a). This value is in agreement with the corresponding DP value in two dimensions. In Fig. 6.8(b), the exponent $\nu_\parallel$ is determined by rescaling plot of $n(t)t^{\alpha}$ versus $t(\omega_c - \omega)^{\nu_\parallel}$ for different ω as $\nu_\parallel = 1.30$. Thus, the critical exponents obtained from the homogeneous initial state are good agreement with the DP values within the error bars.

Next, we estimate the exponents η and δ' by direct measurement of the slopes in the double-logarithmic plots, as shown in Fig. 6.9. We estimate the exponent z using the data collapse technique. For instance, for the survival probability $P(t)$, we plot $P(t)t^{\delta'}$ versus tN^{-z} for different system sizes N. We determine z as the value at which the data for different system sizes collapse onto a single curve. For the 2d-QCP, we find that the rapidity-reversal symmetry holds because $\alpha = \delta'$. The values of critical exponents are in good agreement with the DP values within the error bars. Therefore, the 2d-QCP for $\kappa = 0$ belongs to the DP class. We conclude that the quantum coherent effect is irrelevant in two dimensions.

Table 6.2: Critical exponent α for different κ values.

κ	α
0.0	0.32 ± 0.01
0.1	0.28 ± 0.01
0.2	0.24 ± 0.01
0.3	0.22 ± 0.01
0.4	0.20 ± 0.01
0.5	0.18 ± 0.01
≥ 0.58	$1d$ DP values

6.4 Discussion

We investigated $1d$-QCP and $2d$-QCP as prototypical examples of nonequilibrium absorbing phase transitions in dissipative quantum systems. The phase diagram was obtained (Fig. 6.1) in the parameter space (κ, ω), which represent the contributions of the classical and quantum effects, respectively. When the $1d$-QCP starts from the homogeneous state, the transition curve between the absorbing and active phases is composed of two parts: a quantum region $[0, \kappa_*]$ and the classical DP region $[\kappa_*, \kappa_c]$. In the quantum region, the critical exponent α, which is associated with the density of active sites $n(t)$, decreases continuously as κ is increased from the quantum value to the classical DP value as presented in Table II. Thus, the crossover from a quantum to a classical behavior proceeds gradually. When the $1d$-QCP starts from the heterogeneous state, such an anomalous crossover does not occur. We find a continuous transition at $\kappa = 0$ in the DP class. For the $2d$-QCP, a similar continuous transition occurs, which is in contrast to the expectation from the functional renormalization group approach [26]. It is interesting to note that in the mean-field solution, the transition in the region near $\kappa = 0$ is discontinuous. This discontinuous transition is changed to a continuous transition with a continuously varying exponent, provided that the $1d$-QCP starts from the

homogeneous state.

Based on our result, the 1D-QDP universality class has the same critical exponents with the classical DP class except for the critical exponent α, with the relation $\alpha_{TDP} = 2\alpha_{DP}$, and the rapidity-reversal symmetry of DP class is broken. This is reminiscent of the mean-field picture that MF-DP class and MF-TDP class have the only difference in the critical exponent α, with the relation $\alpha_{TDP} = 2\alpha_{DP}$. Thus we shall compare the low-dimensional TDP and DP classes. In one dimension, the 1D-QDP class is different with the 1D-TDP class, which does not exist because the tricritical point vanishes. On the other hand, in two dimensions, the 2D-QCP class does not exist, and the 2D-TDP class exists.

The quantum coherent effect for mean-field limit seems to be irrelevant as in the $2d$-QCP because the quantum fluctuations are stronger at the lower dimensions. If this scenario is valid, the continuous transition with DP class should appear for all transition line in mean-field limit. Hence the mean-field critical behavior using Keldysh formalism [147] may be examined.

The NN approach we used was applied to the dataset obtained by the QJMC simulations. We think that this approach can be applied directly to snapshots obtained in the cold Rydberg experiments. Furthermore, our approach will be used in near future for other dissipative systems where a transition point is hardly determined. Examples include dissipative transverse-field Ising model, dissipative XYZ model, and dissipative anisotropic Heisenberg model.
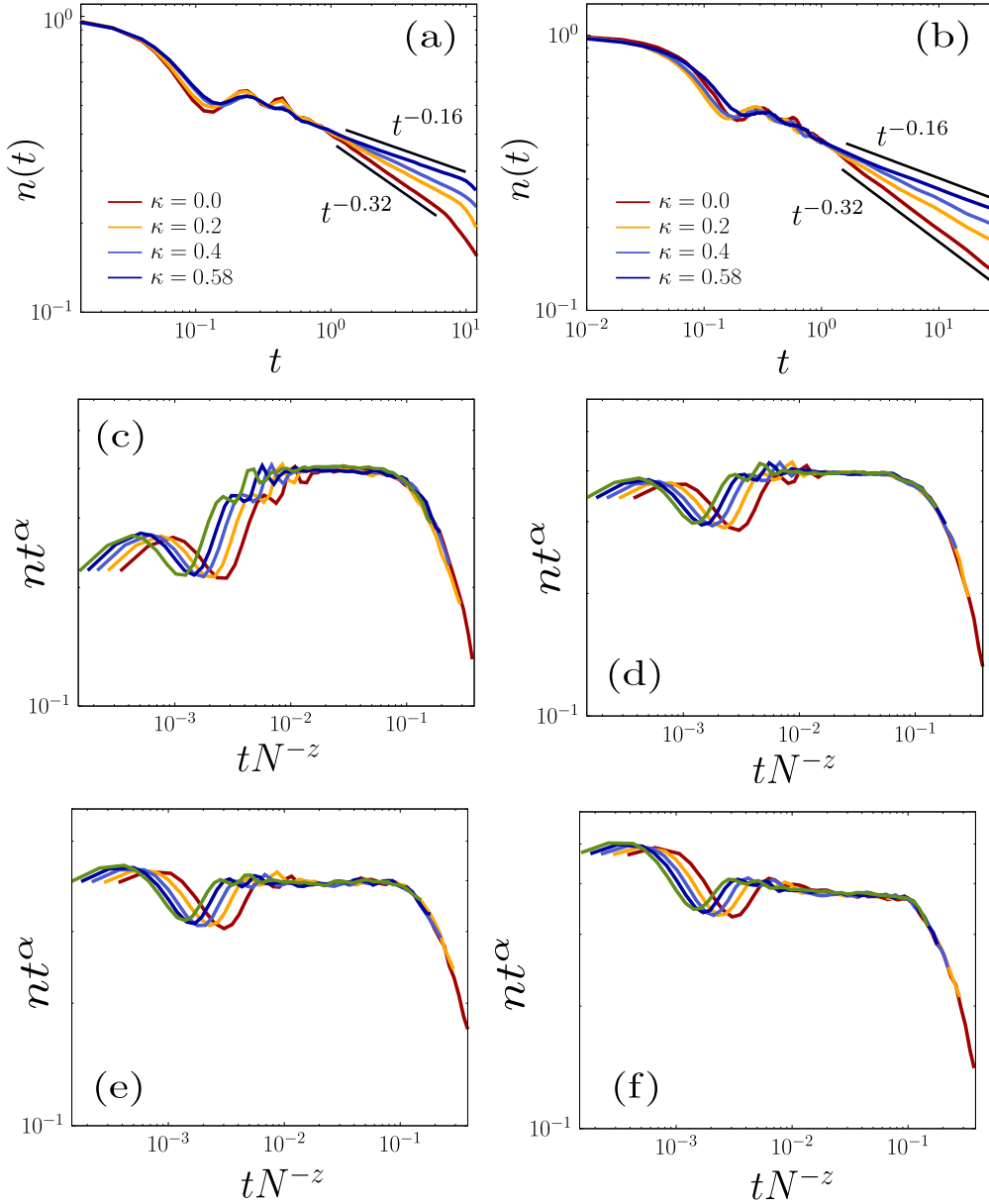
Figure 6.7: Estimates of the critical exponent α from the homogeneous state for $\kappa \geq 0$. Plot of $n(t)$ as a function of t for different κ in the range $\kappa \in [0, 0.6]$ in steps of 0.2 using the QJMC with $N = 20$ for (a) and tensor network method with $N = 80$ and bond dimension $\chi = 1024$ for (b). The lower (upper) solid line is a guideline with slope -0.32 (-0.16). Scaling plots of $n(t)t^{\alpha}$ versus tN^{-z} with the classical parameter (c) $\kappa = 0.0$, (d) $\kappa = 0.2$, (e) $\kappa = 0.4$, and (f) $\kappa = 0.58$. The critical exponents are taken as $z = 1.55$ and $\alpha = 0.32$ for (c), $\alpha = 0.24$ for (d), $\alpha = 0.20$ for (e), and $\alpha = 0.16$ for (f).
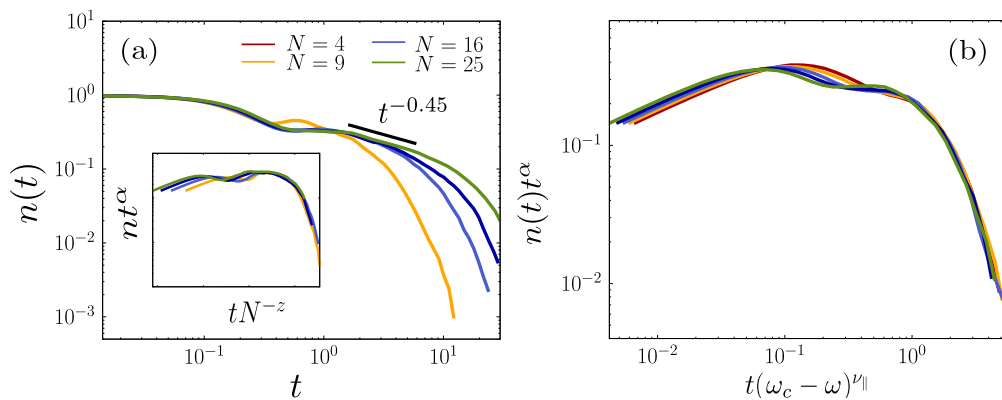
Figure 6.8: Estimates of the critical exponent α and $\nu_\parallel$ for the 2d-QCP. Initial state starts from the homogeneous state. (a) Plot of $n(t)$ as a function of t for different system sizes when $\kappa = 0$, which shows that $n(t) \sim t^{-\alpha}$, with $\alpha = 0.45$. The inset shows the scaling plot of $n(t)t^\alpha$ versus tN^{-z} for $\alpha = 0.32$ and $z = 1.76$. Caption: Data points collapse well onto a single curve for $\omega_c = 0.94$, $\alpha = 0.45$, and $\nu_\parallel = 1.30$. The units of control parameter is given as γ.
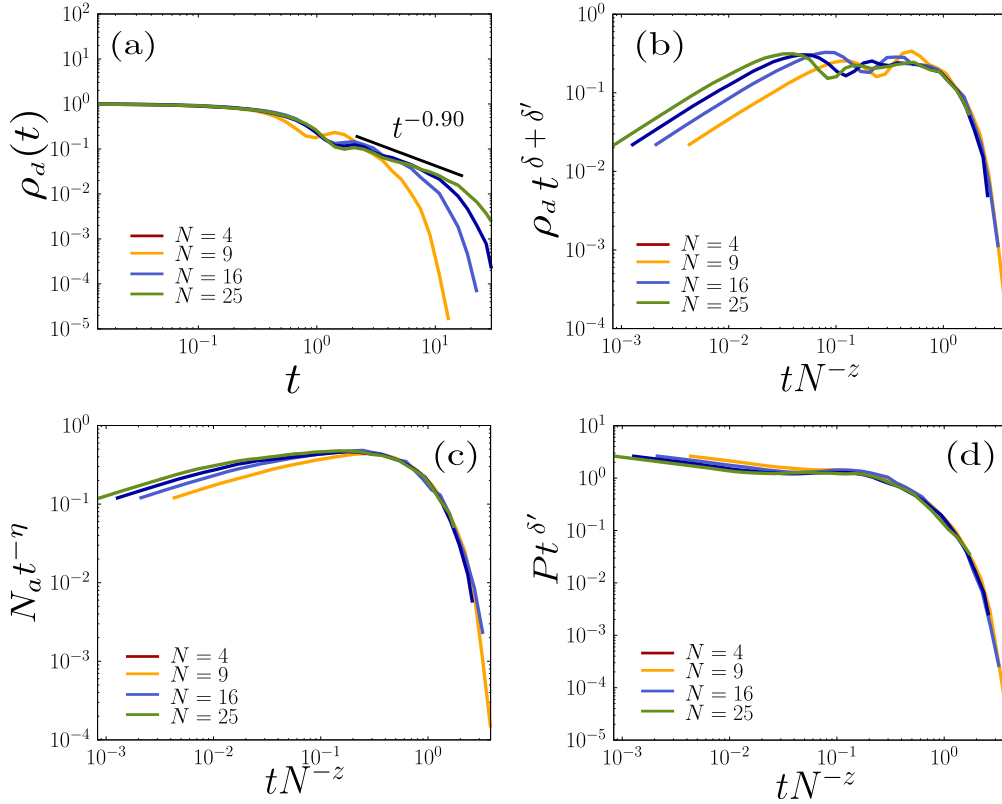
Figure 6.9: Estimates of the critical exponents of the $2d$-QCP starting from a single active site. (a) Plot of $\rho_d(t)$ versus t, which behaves as $\rho_d(t) \sim t^{-\delta-\delta'}$. (b) Scaling plot of $\rho_d(t)t^{\delta+\delta'}$ versus tN^{-z} for $\delta + \delta' = 0.90$ and $z = 1.76$. (a) Scaling plot of $N_a(t)t^{-\eta}$ versus tN^{-z} for $\eta = 0.23$ and $z = 1.76$. (b) Scaling plot of $P(t)t^{\delta'}$ versus tN^{-z} for $\delta' = 0.45$ and $z = 1.76$.

Chapter 7

Phase transitions in the infinite dimensional dissipative quantum systems

Major contents of this chapter are largely based on Ref. [37].

7.1 Introduction

The study of collective behavior of dissipative quantum many-body systems has been an active field in both theoretically and experimentally [75, 105–107, 109–122]. The mutual competition between coherent Hamiltonian and incoherent dissipation dynamics can make a novel physical phenomena, such as time crystals [148, 149], zero-entropy entangled states [150, 151], driven-dissipative strong correlations [152, 153], and dissipative phase transitions in the nonequilibrium steady-state [5, 6, 8–11] including novel universal behavior [17, 36]. However, the solid understanding of the analytical approaches to these systems is still limited due to the lack of a concept analogous to the partition function in equilibrium systems.

Nevertheless, the various theoretical approaches have been developed, including the fluctuationless mean-field theory, semi-classical approach, and Keldysh formalism. Furthermore, the field-theoretical approaches including the semi-classical approach and Keldysh formalism are used to obtain the low-dimensional physics using ε-expansion or functional renormalization group [6, 26, 147]. However, the theoretical predictions from each approach are qualitatively different [154]. For instance, in the dissipative transverse Ising (DTI) model, one difference is that the second-order

transition is replaced by a first-order transition for large dissipation using Keldysh formalism instead of fluctuationless mean-field theory [154]. Thus, one should perform the higher dimensional simulations to check the validity of the mean-field theory; however, numerical methods including quantum jump Monte Carlo simulation [33], tensor network [34,35] and its variants [155–157] are not viable in higher (above two) dimensions because of the computational complexity, with the exponential growth of Hilbert space as system size increases.

Here, we implement a method [158] exploiting site-permutational symmetry of fully-connected graph to obtain the exact numerical solution in the infinite-dimensional dissipative quantum systems. By reducing the computational complexity to $\mathcal{O}(N^3)$ from the usual $\mathcal{O}(2^{2N})$, we perform the simulation of system size up to $N \sim 1000$ and resolve some of the unsolved disputes in dissipative quantum systems. We consider the the DTI model, driven-dissipative XY model, and quantum contact process (QCP), which have attracted much interest due to the relevance to the Rydberg atomic experiments [24, 159, 160]. When analytical approaches such as fluctuationless mean-field theory, semi-classical mean-field theory, and Keldysh formalism are implemented in these models, they result in predictions that are contradictory to each other. We obtain the phase diagram and discuss the types of transitions. Furthermore, we perform the finite-size scaling, which hasn't been viable due to the the complexity of the infinite-dimensional quantum system, and obtain critical exponents. We find that the transition lines and the types of the phase transitions correspond to the fluctuationless mean-field in each models. The DTI model exhibits a continuous phase transition for the entire parameter space, and the driven-dissipative XY model shows a discontinuous phase transition, contrary to the results from Keldysh formalism. The phase transitions of QCP shows that the transition line and universality class correspond to the semi-classical approach. However, we observe a crossover region where critical exponents continuously vary, which is not predicted by existing theoretical methods. Similar phenomenon was observed in the one-dimensional QCP [36].

7.2 Method

The time evolution of the open quantum system is described by the Lindblad equation, which consists of the Hamiltonian and dissipative terms:

$$\partial_t \hat{\rho} = -i \left[\hat{H}_S, \hat{\rho} \right] + \sum_{\ell=1}^{N} \left[\hat{L}_\ell \hat{\rho} \hat{L}_\ell^\dagger - \frac{1}{2} \left\{ \hat{L}_\ell^\dagger \hat{L}_\ell, \hat{\rho} \right\} \right]. \tag{7.1}$$

Qubit systems with fully-connected lattice are symmetric under any permutational of site indices; that is, the elements of the density matrix $\rho_{vw} = \rho_{P_\alpha(v) P_\alpha(w)}$ where v and w denote one of the 2^N configurations of N spins, and P denotes a permutation operator. If the dynamical equation and the initial density matrix both have site-permutation symmetry, the density matrix remains site-permutation symmetric. Here, we implement a method [158] to exploit this property to efficiently obtain solutions to the Lindblad equations of fully-connected qubit systems. Using the symmetry in two-level systems in the fully-connected lattice, the elements $|v\rangle \langle w|$ of the density matrix can be classified by (n_1, n_2, s), where n_1 is the number of ones in v, n_2 is the number of ones in w, and s is the number of sites where v and w are both one. Then, $0 \leq n_1, n_2, s \leq N$, and we can write the density matrix as

$$\hat{\rho} = \sum_{n_1, n_2, s} A_{n_1, n_2, s} |n_1, s\rangle \langle n_2, s|, \tag{7.2}$$

where $A_{n_1, n_2, s} = \langle n_1, s | \hat{\rho} | n_2, s \rangle$ is the 3-rank tensor whose components are a sum of elements of $\hat{\rho}$. For convenience, we introduce the Liouvillian superoperator $\mathscr{L}$ because the Lindblad equation in Eq. (7.1) is linear in ρ:

$$\partial_t \hat{\rho} = \mathscr{L} \hat{\rho}. \tag{7.3}$$
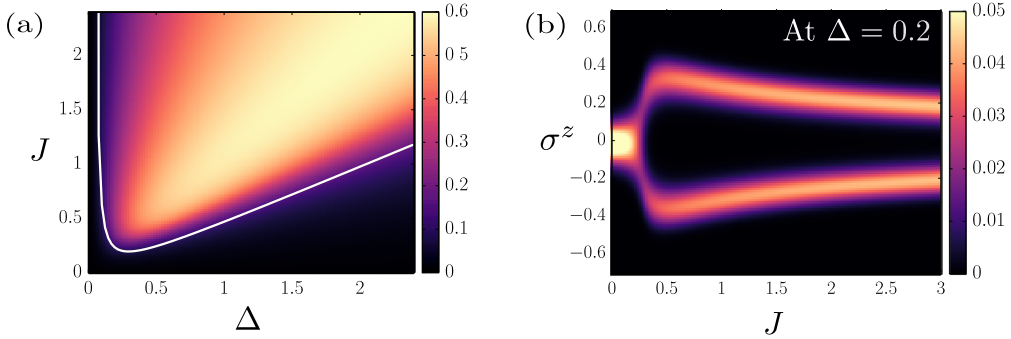
Figure 7.1: (a) Phase diagram of the fully-connected DTI in the parameter space (Δ, J). Continuous transitions (solid line) occur in entire parameter regime. (b) Histogram of order parameter in steady states as a function of J at $\Delta = 0.2$. Continuous transition occurs with Z_2 symmetry. System size is taken as $N = 128$.

Then, the time dynamics of Eq. (7.2) can be represented as the Liouvillian superoperator, given by

$$\sum_{n_1,n_2,s} \partial_t A_{n_1,n_2,s} |n_1,s\rangle \langle n_2,s| = \sum_{n_1,n_2,s} \mathscr{L} A_{n_1,n_2,s} |n_1,s\rangle \langle n_2,s|. \tag{7.4}$$

Thus, the computational complexity of $\mathscr{O}(N^3)$ suffices instead of the usual complexity of $\mathscr{O}(2^{2N})$. Furthermore, we can exploit the hermiticity of the density matrix and reduce the computational cost by half. This approach enables us to obtain the numerical solution in the systems beyond the scale otherwise viable.

7.3 Results

7.3.1 Dissipative transverse Ising model

We now consider the dissipative transverse Ising model [161]–[164], which has received considerable interest because of its experimental realization with ultracold Rydberg
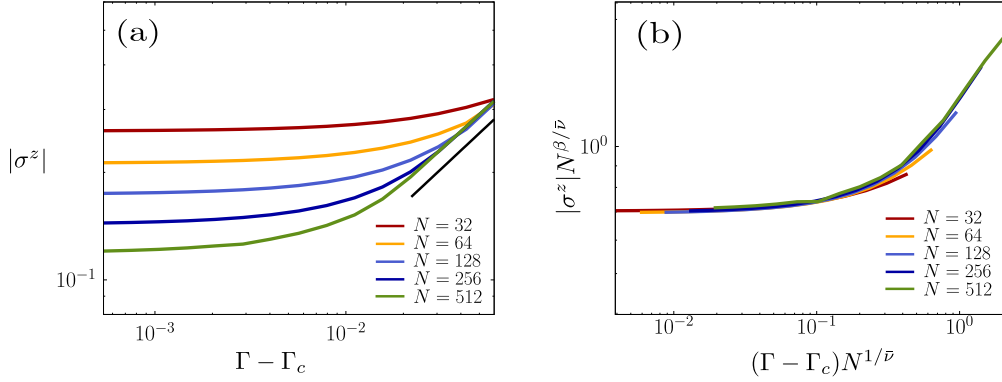
Figure 7.2: (a) Plot of $|\sigma^z|$ as a function of $J - J_c$ at $\Delta = 0.2$ for different system sizes, which shows that $|\sigma^z| \sim (J - J_c)^\beta$ for $\beta = 0.5$. (b) Scaling plot of the rescaled order parameter $|\sigma^z| N^{\beta/\bar{\nu}}$ versus $(J - J_c) N^{1/\bar{\nu}}$. The data are well collapsed onto a single curve with $\beta = 0.5$ and $\bar{\nu} = 1.75$.

atoms [159, 160]. The Hamiltonian $\hat{H}_S$ is expressed as

$$\hat{H}_S = -\frac{J}{N-1} \sum_{\ell \neq m} \hat{\sigma}_\ell^z \hat{\sigma}_m^z + \Delta \sum_\ell \hat{\sigma}_\ell^x, \tag{7.5}$$

where J denotes the interaction strength of ferromagnetic Ising interaction and Δ indicates strength of a transverse field. The Lindblad operators of decay is given by $\hat{L}_\ell = \sqrt{\Gamma} \hat{\sigma}_\ell^{x-} = \sqrt{\Gamma} \frac{\hat{\sigma}_\ell^y - i \hat{\sigma}_\ell^z}{2}$, with the decay rate Γ. In the absence of the Lindblad operator, the ground state of Eq. (7.5) was thoroughly investigated to exhibit to a quantum phase transition [165] from a ferromagnetic phase ($J \gg \Delta$) to a paramagnetic phase ($J \ll \Delta$). Note that the Hamiltonian exhibits Z_2, which is symmetric under the transformation $\hat{\sigma}^z \to -\hat{\sigma}^z$. For the open quantum systems, Z_2 symmetry can be broken if the Lindblad operator is given by $\hat{L}_\ell \sim \hat{\sigma}_\ell^-$, which can be seen in previous studies of dissipative Rydberg gases [161, 166, 167]. Here, the model still exhibits a Z_2 symmetry, which is symmetric under the transformation $(\hat{\sigma}^x, \hat{\sigma}^y, \hat{\sigma}^z) \to (\hat{\sigma}^x, -\hat{\sigma}^y, -\hat{\sigma}^z)$.

Recently, it was conjectured that the continuous transition can break down, and discontinuous transition can occur for strong dissipation regime both analytically [154] based on the Keldysh formalism and numerically [168] using a variational approach.

Specifically, the discontinuous transition occurs for $\Delta/\Gamma < 0.5$ [154] and for $\Delta/J < 0.22$ [168]. Here, we consider the former case by setting $\Gamma = 1$ and the latter case will be presented in the Appendix.

To verify the mean-field behavior, we use our exact numerical solution approach to DTI model. The phase diagram in the parameter space (Δ, J) is shown in Fig. 7.1(a), and the order parameter curve at $\Delta = 0.2$ is shown in Fig. 7.1(b). It seems to be continuous, and we perform the finite-size scaling for various Δ. When the transition type is continuous, then the critical behavior is shown and the critical exponent can be measured. In Fig. 7.2, we perform the finite-size scaling at $\Delta = 0.2$ and obtain the critical exponents $\beta = 0.50 \pm 0.01$ and $\bar{v} = d_c v = 1.75 \pm 0.01$. Thus, we conclude that the transition type of DTI model in all parameter spaces is continuous. Furthermore, we find that the transition type and line are exactly the same as the result of the fluctuation-less mean-field approach instead of Keldysh formalism. The fluctuationless mean-field equation and the corresponding transition line are shown in the Appendix.

Even though the dissipative transverse Ising model has the Z_2 symmetry, its universality class does not belong to the quantum Ising universality, where $\beta = 0.5$, $v = 0.5$, and $d_c = 3$. It is unconventional, so further investigation is needed in future work to resolve this inconsistency.

7.3.2 Driven-dissipative XY model

The Hamiltonian H_S of the driven-dissipative XY model is expressed as

$$\hat{H}_S = -\frac{J}{N-1}\sum_{\ell \neq m}\frac{\hat{\sigma}_\ell^x \hat{\sigma}_m^x + \hat{\sigma}_\ell^y \hat{\sigma}_m^y}{2} + \Omega \sum_\ell \hat{\sigma}_\ell^x + \Delta \sum_\ell \hat{\sigma}_\ell^z,$$

where J denotes the interaction strength, and Ω and Δ denotes the field in x- and z-axis respectively. The dissipative dynamics at each site is given by the Lindblad operator $\hat{L}_\ell = \sqrt{\Gamma}\hat{\sigma}_\ell^-$. Without coherent drive denoted by Ω in the Hamiltonian, the system approaches trivial state where all spins are in $|\downarrow\rangle$.
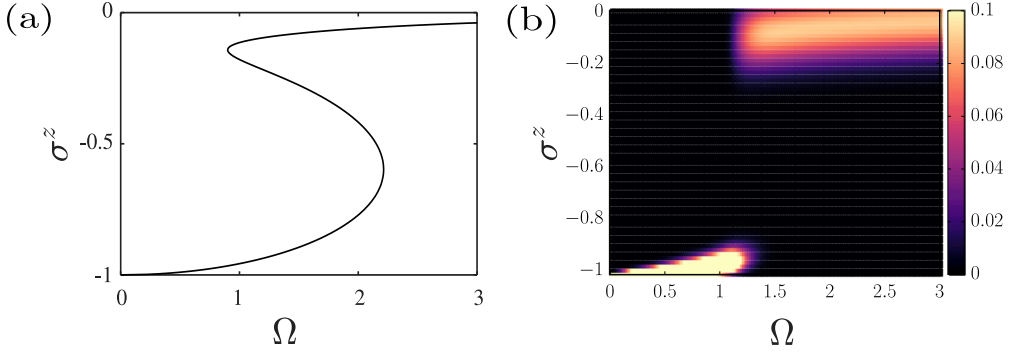
Figure 7.3: (a) The fluctuationless mean-field theoretical prediction of the order parameter $\sum_\ell \hat{\sigma}_\ell^z$ along the Ω-axis with $(J, \Delta) = (4, 0.5)$. (b) Probability distribution of the observable $\sum_\ell \hat{\sigma}_\ell^z$ of the driven-dissipative XY model with $N = 128$ and $(J, \Delta) = (4, 0.5)$. The diagram shows a discontinuous phase transition with bistability at $\Omega/\Gamma \simeq 1.4$ as expected by the fluctuationless mean-field theory.

The fluctuationless mean-field theory predicts a first-order phase transition in certain region. The full mean-field phase diagram has a rich structure, we are particularly interested in the vicinity of the first-order phase transition predicted by the theory. When parameters are fixed $(J, \Delta)/\Gamma = (4, 0.5)$, the theory predicts a first-order phase transition with bistable interval along the Ω-axis. The fluctuationless mean-field theoretical predictions are illustrated in Fig. 7.3(a) (See the Appendix for detailed calculations). However, the Keldysh formalism indicates the absence of phase transition [154].

To resolve the disparity between the two predictions, we use our method to the model along the Ω-axis with $(J, \Delta)/\Gamma = (4, 0.5)$. We illustrate the probability distribution of the observable $\sum_\ell \hat{\sigma}_\ell^z$ in Fig. 7.3. A first-order phase transition clearly manifests itself near $\Omega = 1.4$ with bistability in the vicinity of the phase transition.

7.3.3 Quantum contact process

We shall here consider the QCP [25,26,31,92,93,123,124], which is the paradigmatic model showing absorbing state phase transitions in open quantum systems. Recently,

QCP has received considerable interest because of its potential realization with ultra-cold Rydberg atoms based on the antiblocakde effect [24], and the universal behavior of one dimensional QCP [36,92,93,123] was revealed that the quantum coherent effect changes DP universality to quantum DP universality. The Hamiltonian $\hat{H}_S$ contains the coherent terms for branching and coagulation, which is given by

$$\hat{H}_S = \frac{\omega}{N-1} \sum_{m \neq \ell} \hat{n}_m (\hat{\sigma}_\ell^+ + \hat{\sigma}_\ell^-),
\tag{7.6}$$

and the Lindblad operators of decay, branching, and coagulation are given by

$$\hat{L}_\ell^{(d)} = \sqrt{\gamma} \hat{\sigma}_\ell^-, \quad \hat{L}_{m\ell}^{(b)} = \sqrt{\kappa} \hat{n}_m \hat{\sigma}_\ell^+, \quad \hat{L}_{m\ell}^{(c)} = \sqrt{\kappa} \hat{n}_m \hat{\sigma}_\ell^-,
\tag{7.7}$$

respectively. Here, $\hat{\sigma}_\ell^{\pm} = (\hat{\sigma}_\ell^x \pm i\hat{\sigma}_\ell^y)/2$. Because $\hat{n}_\ell$ is the number operator of the active state, $\hat{n} = |\uparrow\rangle\langle\uparrow|$, the composite operator $\hat{n}_m \hat{\sigma}_\ell^+$ or $\hat{n}_m \hat{\sigma}_\ell^-$ with $\ell \neq m$ means that the active state at site m activates or deactivates the state at ℓ, representing the branching and coagulation processes, as seen in Eq. (7.6) and $\hat{L}_\ell^{(b)}$ and $\hat{L}_\ell^{(c)}$ in Eq. (7.7). Instead, $\hat{L}_\ell^{(d)}$ in Eq. (7.7) denotes the decay dynamics of the active state at ℓ. Therefore, if there is no active state, no further dynamics occurs, implying an absorbing state.

A recent result based on the semi-classical mean-field solution [26, 31] showed that the QCP exhibits a continuous (discontinuous) phase transition when κ is large (small). Thus, a tricritical point (TCP) exists, as shown in Fig. 7.4(a). The continuous transition belongs to the DP universality class, and the TCP belongs to the tricritical DP class [32,54,55]. Two results are based on the Martin-Siggia-Rose-Janssen-de Dominicis field theory; however, transition lines are slightly different. The transition line of Ref. [31] corresponds to the flucutationless mean-field theory, while the transition line of Ref. [26] bends due to the fluctuation.

Using the permutational symmetry, we can obtain the exact numerical solution of the Lindblad master equation up to $N \sim 1000$. We obtain the phase diagram of the mean-field QCP in the parameter space (κ, ω). Along the transition line, we measure
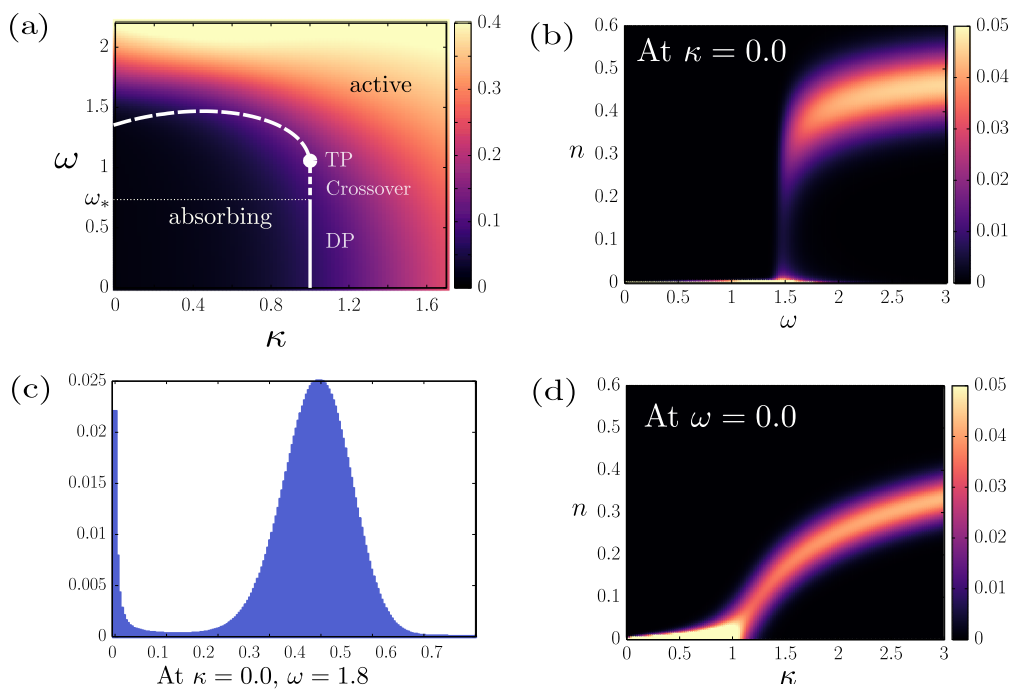
Figure 7.4: (a) Phase diagram of the fully-connected QCP in the parameter space (κ, ω). Discontinuous (dashed curve) and continuous transitions (solid and dotted line) occur, and they meet at a tricritical point. Continuous transitions in the region $[\kappa_*, \kappa_c]$; however, in the interval $[0, \omega_*]$, the exponents α and z varies continuously as ω is increased for the TDP values. (b) Histogram of the densities of active sites in steady states as a function of ω at $\kappa = 0.0$. (c) Histogram at $\omega = 1.8$ of (b), which shows the bimodal distribution. (d) Histogram of the densities of active sites in steady states as a function of κ at $\omega = 1.0$. System size is taken as $N = 256$.
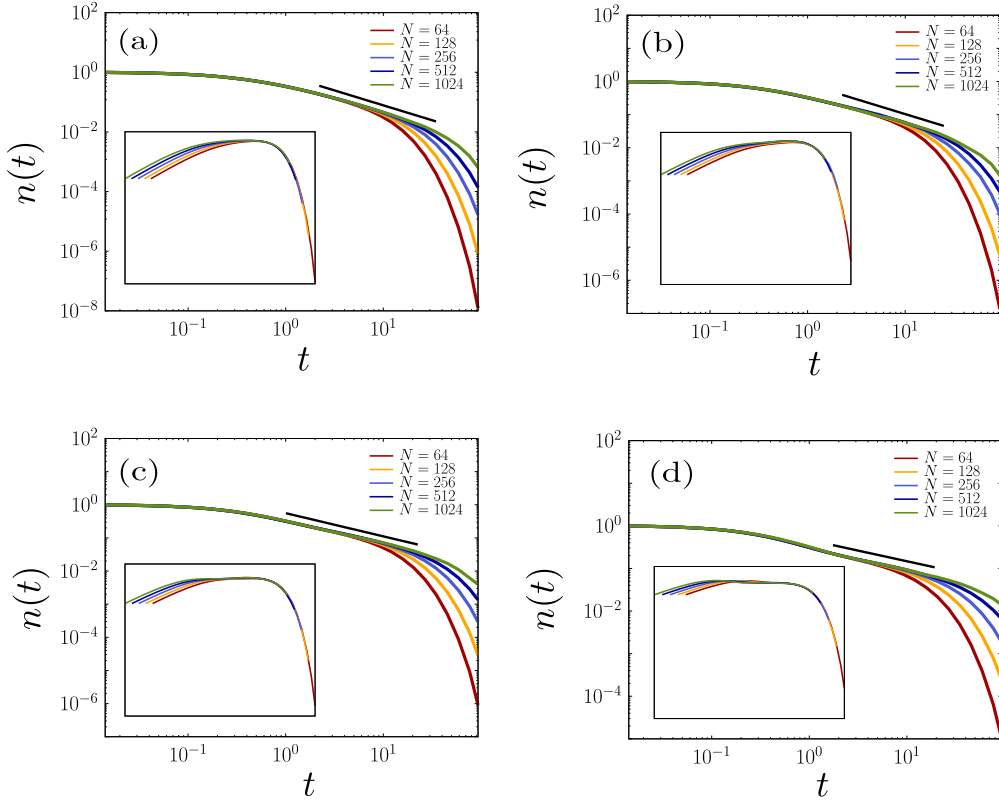
Figure 7.5: Estimates of the critical exponents of the MF-QCP using the exact numerical solution of Lindblad equation. Plot of $n(t)$ as a function of t for different ω in the range $\omega \in [0, 1.0]$. Plot of $n(t)$ as a function of t for different system sizes, which shows that $n(t) \sim t^{-\alpha}$, (a) for $\omega = 0$ with $\alpha = 1.0$, (b) for $\omega = 0.6$ with $\alpha = 0.92$, (c) for $\omega = 0.8$ with $\alpha = 0.70$, and (d) for $\omega = 1.0$ with $\alpha = 0.50$. Inset: Scaling plots of $n(t)t^{\alpha}$ versus tN^{-z}.

the various observables depending on the initial conditions. Here, we consider a homogeneous initial state in which the entire system is occupied by active sites at $t = 0$, which is expressed as $\hat{\rho}(0) = |\uparrow \cdots \uparrow\rangle\langle\uparrow \cdots \uparrow|$. The observables related an initial state in which a single active seed is present at $\ell = 0$ (and the remaining sites are inactive) will be presented in detail in the Appendix. From the homogeneous initial state, we measure the density $n(t)$ of active sites at time t. This quantity is formulated as $n(t) = (\sum_{\ell} \text{Tr}[\hat{\rho}(t)\hat{n}_{\ell}])/N$. We find that $n(t)$ exhibits power-law decay as $n(t) \sim t^{-\alpha}$ with exponent $\alpha = 1.00 \pm 0.02$ at $\omega = 0.0$ [Fig. 7.5(a)] and $\alpha = 0.50 \pm 0.02$ at $\omega = 1.0$

Table 7.1: Critical exponent α for different κ values.

ω	α (Exact numerical solution)
1.0	0.50 ± 0.02
0.9	0.61 ± 0.02
0.8	0.70 ± 0.02
0.7	0.81 ± 0.02
0.6	0.92 ± 0.02
≤ 0.53	MF DP values
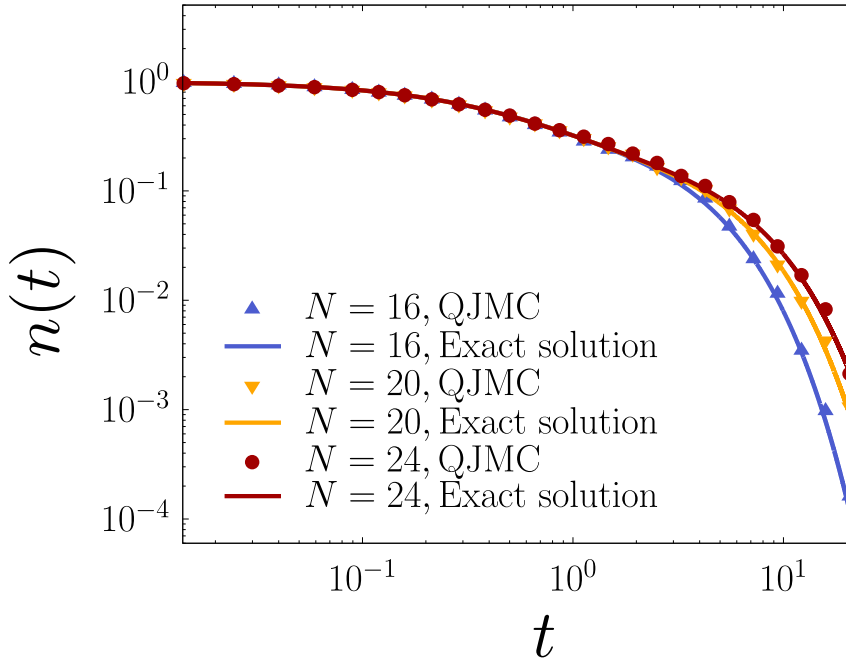
Figure 7.6: Comparison between exact numerical solution and quantum jump Monte Carlo simulation for the QCP model for $N = 16$, 20, and 24. The lines show the results of an exact numerical solution of the Lindblad equation and the symbols show the results of quantum jump Monte Carlo simulations.

[Fig. 7.5(d)]. This value is consistent with the result obtained by applying the semi-classical approach; however, we find there exists the crossover region where the exponent α is continuously varying. To be concrete, we find that the value of α decreases

continuously from 1.0 for $\omega = 0.53$ to $\alpha = 0.5$ for $\omega = 1.00$ (Table E.1). These results suggest that α increases continuously as ω is decreased and reaches the DP value at $\kappa_* \approx 0.53$.

7.4 Comparison with quantum jump Monte Carlo simulation

We perform the quantum jump Monte Carlo simulation to compare the results with our exact numerical approach for system size $N = 16, 20$, and 24 for QCP. Here, we focus on the power-law behavior at a tricritical point $(\kappa, \omega) = (1, 1)$. In Fig. 7.6, we compare the exact numerical solution for the QCP model for $N = 16, 20$, and 24 with quantum jump Monte Carlo simulation. We find the two methods are in good agreement.

7.5 Summary and Conclusions

We have implemented an exact numerical method in infinite-dimensional qubit systems, in some of which various theoretical methods make predictions that are contradictory to each other. In addition, we observe a crossover region which all the existing theoretical methods fail to predict. Using the FSS, which hasn't been viable due to the complexity of the numerical approach to infinite-dimensional systems, we confirm that the universality class and verify the universality class obtained from the analytical approach including Keldysh formalism, semi-classical approach, and fluctuationless mean-field approach. In addition, we compare the results obtained from the quantum jump Monte Carlo simulation in small qubit sizes.

For the DTI model, we find that the discontinuous phase transition does not occur in all transition line. In Keldysh formalism, it was conjectured that the discontinuous transition occurs for the strong dissipation regime [154]. Instead, the transition line and type of the transition corresponds to the flucutationless mean-field results. However, our result shows that the universality class does not belong to the quantum

Ising universality class, so further investigation is needed in future work to resolve this inconsistency. For driven-dissipative XY model, we find that a discontinuous phase transition occurs near the parameter predicted by the fluctuationless mean-field theory, as opposed to the prediction of the Keldysh formalism that there is no phase transition in the model. When one applies to the Keldysh formalism on those systems, it is necessary to map spins to hard-core boson; for instance, a hard-core bosonization via a large on-site potential, which might not result in a valid qubit system in the infinite potential limit.

For the QCP model, a previous result based on the semi-classical mean-field solution showed that the continuous transition belongs to the DP universality class, and the TCP belongs to the tricritical DP class (See Fig. 7.4). According to our approach, we find that transition lines are exactly the same with Ref. [31], and there is a crossover region along which the exponent α (which is associated with the density of active sites) decreases continuously from a tricritical directed percolation (DP) to the DP value, which is reminiscent of the one-dimensional QCP. In this regard, we shall compare the universal behavior between MF-QCP and one-dimensional QCP. Based on the exact numerical approach, we find there exists a crossover region of MF-QCP from the DP class to the TDP class with a tricritical point. The only different value of critical exponent between MF-TDP and MF-DP is the exponent α, and the scaling relation $\alpha = 2\delta'$ holds. This is analogous to the one-dimensional case between at quantum DP class at quantum axis and DP class. Hence we conclude that the tricritical point at $(1, 1)$ at MF limit moves on the quantum axis with $\kappa = 0$ in one dimension.

Chapter 8

Conclusion

In this dissertation, we have studied the nonequilibrium phase transitions in open quantum systems. The dissipative phase transition is one of the most interesting phenomena because it originates from competition between the quantum and classical fluctuations. Among these models, the quantum contact process (QCP) is the prototypical model to capture these physics because the DP class of its classical limit is well-studied and of the relevance of ultracold Rydberg experiments.

This dissertation has covered the QCP with long-range interactions and ordinary QCP. We shall conclude by discussing the each model focused on the question raised in Introduction that the novel universality class can be identified in open quantum many-body systems. Firstly, we considered the long-range QCP, where the branching and coagulation processes are allowed not only for the nearest-neighbor pairs but also for long-distance pairs, coherently and incoherently. Using the semi-classical field-theoretic approach to the quantum Langevin equations, we found a new universality class called "long-range tricritical DP (LTDP) class", which was found to be the classical universality. Thus, the quantum process is effectively reduced as the classical higher-order interaction in mean-field theory. Since it had not been studied yet, we deeply studied the low-dimensional physics of this universality class. Considering the long-range tricritical contact process belonging to the LTDP class, we numerically obtained a set of critical exponents in the LTDP class and determine the interval of σ for the LTDP class. Finally, we constructed a diagram of universality classes in the space (d, σ).

Since we analytically determine the mean-field universality class, interest naturally turned to lower-dimensional cases. Thus, we considered $1d$-QCP and $2d$-QCP using quantum simulations such as the quantum jump Monte Carlo (QJMC) simulation and the tensor network methods. For $1d$, we found an quantum critical region $[0, \kappa_*]$ where the quantum fluctuations play a role in universal behavior. Specifically, when the QCP starts from a homogeneous state with all active sites, there exists a critical line in the region $0 \leq \kappa < \kappa_*$, along which the exponent α associated with the density of active sites decreases continuously from a quantum to the classical directed percolation (DP) value. This behavior implies that the quantum coherent effect still remains to some extent in the region near $\kappa = 0$. This anomalous crossover behavior allows us to measure the display between the quantum DP and classical DP effect using the Rydberg atom experiment. For $2d$, the anomalous crossover behavior does not occur and the classical DP behavior appears in the entire region of $\kappa \geq 0$ regardless of initial configurations. The neural network machine learning technique is used to identify the critical line and to determine the correlation length exponent. Numerical simulations using the quantum jump Monte Carlo technique and the tensor network method are performed to determine all the other critical exponents of the QCP. Thus, we found the novel universality class called "quantum directed percolation (QDP) universality" in one dimension.

Lastly, we investigate the mean-field dissipative quantum systems using the permutational symmetry of fully-connected graph. It is based on the permutational symmetry, which is symmetric under any exchange of site indices. Crucially, our approach allows us to perform the simulation with the complexity $\mathcal{O}(N^3)$. Using this method, we unveil the mean-field behavior of the dissipative transverse Ising (DTI) model, driven-dissipative XY model, and quantum contact process. We find that the transition line and type of phase transition correspond to the fluctuationless mean-field for all models. Specifically, we find that the DTI model exhibits a continuous phase transition for the entire parameter space, and the driven-dissipative XY model shows a discontinuous

phase transition, contrary to the results from Keldysh formalism. Instead, those correspond to the fluctuationless MF approach. The phase transitions of QCP shows that the transition line and universality class correspond to the semi-classical approach; however, we discover a crossover region analogous to the one-dimensional QCP, which is not predicted by theoretical methods.

In conclusion, we have revealed that the novel universality class and crossover phenomena in open quantum many-body systems, which originates from the quantum fluctuations. However, there are many works to do such as the theoretical approach to the QDP and experimental realization. Furthermore, it would be interesting that the open quantum many-body systems are simulated using the quantum computers. We hope further experiments and simulations could confirm the universality class whose quantum coherent process is relevant.

Appendices

Appendix A

Appendix of chapter 1

A.1 Realization of classical contact process by Rydberg atomic experiment

The critical behavior of classical CP can be realized using Rydberg atomic experiment. Here we show that the transition rate κ of branching and coagulation processes in classical limit can be obtained in terms of the experimental parameters used in Rydberg atomic system.

A.1.1 Lindblad equation for Rydberg gases

To describe the Rydberg gases in open quantum systems, we employ the Lindblad equation as follows:

$$\partial_t \hat{\rho} = -\mathrm{i} \left[\hat{H}_0 + \hat{H}_\Omega, \hat{\rho} \right] + \sum_{i=1}^{2} D^{(i)}(\hat{\rho}),$$ (A.1)

where we have split H_{R} into two parts as

$$\hat{H}_0 = \Delta \sum_{\ell}^{N} \hat{n}_\ell + \sum_{\ell \neq m} \frac{V_{\ell m}}{2} \hat{n}_\ell \hat{n}_m, \quad \text{and} \quad \hat{H}_\Omega = \Omega \sum_{\ell}^{N} \hat{\sigma}_\ell^x,$$

and the Lindblad dissipator $D^{(i)}$ is given by

$$D^{(i)}(\hat{\rho}) = \sum_{\ell} \left(\hat{L}_{\ell}^{(i)} \hat{\rho} \hat{L}_{\ell}^{(i)\dagger} - \frac{1}{2} \left\{ \hat{L}_{\ell}^{(i)\dagger} \hat{L}_{\ell}^{(i)}, \hat{\rho} \right\} \right). \tag{A.2}$$

Here, the Lindblad operators defined on each site $\hat{L}_{\ell}^{(1)}$ and $\hat{L}_{\ell}^{(2)}$ stand for the decaying from $|\uparrow\rangle$ to $|\downarrow\rangle$ with zero-temperature heat bath and the dephasing processes, respectively, where the detail forms are given by

$$\hat{L}_{\ell}^{(1)} = \sqrt{\gamma} \hat{\sigma}_{\ell}^{-} \quad \text{and} \quad \hat{L}_{\ell}^{(2)} = \sqrt{\Gamma} \hat{n}_{\ell}. \tag{A.3}$$

Using the representation of operator with the spin configurations as basis such as $\rho_{ab} \equiv \langle a|\hat{\rho}|b\rangle$, where a and b denote the one of 2^N configurations of N spins, i.e., $|a\rangle = |\downarrow\uparrow \cdots \downarrow\rangle$, one can evaluate each term in the r.h.s. of Eq. (A.1) as follows: Since $\hat{H}_0$ is the diagonal matrix for the basis, the first term reads

$$\langle a|[\hat{H}_0, \hat{\rho}]|b\rangle = \left[\Delta \sum_{\ell} \left(\langle a|\hat{n}_{\ell}|a\rangle - \langle b|\hat{n}_{\ell}|b\rangle \right) \right.$$
$$\left. + \sum_{\ell \neq m} \frac{V_{\ell m}}{2} \left(\langle a|\hat{n}_{\ell}\hat{n}_m|a\rangle - \langle b|\hat{n}_{\ell}\hat{n}_m|b\rangle \right) \right] \rho_{ab},$$
$$= \left(\langle a|\hat{H}_0|a\rangle - \langle b|\hat{H}_0|b\rangle \right) \rho_{ab}, \tag{A.4}$$

which becomes zero when $a = b$. On the other hand, $\hat{H}_{\Omega}$ yields the transition between the states by flipping a single spin, then the second term in Eq. (A.1) can be written as

$$\langle a|[\hat{H}_{\Omega}, \hat{\rho}]|b\rangle = \Omega \sum_{\ell} \sum_{a'} \left[\langle a|\hat{\sigma}_{\ell}^{x}|a'\rangle \rho_{a'b} - \langle a'|\hat{\sigma}_{\ell}^{x}|b\rangle \rho_{aa'} \right], \tag{A.5}$$

where the diagonal term $a = b$ is given by

$$\langle a|[\hat{H}_{\Omega}, \hat{\rho}]|a\rangle = \Omega \sum_{\ell} \sum_{a'} \left[\langle a|\hat{\sigma}_{\ell}^{x}|a'\rangle \rho_{a'a} - \langle a'|\hat{\sigma}_{\ell}^{x}|a\rangle \rho_{aa'} \right]. \tag{A.6}$$

Note that the diagonal part Eq. (A.6) contains only off-diagonal contributions of density matrix because $\langle a|\hat{\sigma}_\ell^\pm|a\rangle = 0$, which will be used for deriving the rate equation. Similarly, we get the representations of Lindblad operators; for the decay operator

$$\langle a|D^{(1)}(\hat{\rho})|b\rangle = \gamma \sum_\ell \sum_{a'b'} \langle a|\hat{\sigma}_\ell^-|a'\rangle \langle b|\hat{\sigma}_\ell^-|b'\rangle^* \rho_{a'b'}$$
$$- \frac{\gamma}{2} \sum_\ell \left(\langle a|\hat{n}_\ell|a\rangle + \langle b|\hat{n}_\ell|b\rangle \right) \rho_{ab}, \tag{A.7}$$

where the diagonal term $a = b$ is given by

$$\langle a|D^{(1)}(\hat{\rho})|a\rangle = \gamma \sum_\ell \sum_{a'} \left[|\langle a|\hat{\sigma}_\ell^-|a'\rangle|^2 \rho_{a'a'} - |\langle a'|\hat{\sigma}_\ell^-|a\rangle|^2 \rho_{aa} \right]. \tag{A.8}$$

For the dephasing operator,

$$\langle a|D^{(2)}(\hat{\rho})|b\rangle = \Gamma \sum_\ell \left(\langle a|\hat{n}_\ell|a\rangle \langle b|\hat{n}_\ell|b\rangle - \frac{\langle a|\hat{n}_\ell|a\rangle}{2} - \frac{\langle b|\hat{n}_\ell|b\rangle}{2} \right) \rho_{ab},$$
$$= -\frac{\Gamma}{2} \sum_\ell |\langle a|\hat{n}_\ell|a\rangle - \langle b|\hat{n}_\ell|b\rangle| \rho_{ab}, \tag{A.9}$$

which becomes zero when $a = b$. If the Lindblad equation consists of only this dephasing dissipator, the density operator ρ_{ab} in long time limit becomes the diagonal matrix, which is why the $D^{(2)}$ is called the dephasing operator. In the limit of $\Gamma \gg \Omega, \gamma$, it is known that the coherent dynamics can be neglected so that the Lindblad equation Eq. (A.1) is effectively reduced to the classical rate equation [23]. In what follows, we will briefly show the procedure.

A.1.2 Derivation of transition rate in classical limit

For convenience, we introduce the super operator [169], by mapping the density operator to the density vector, $\rho_{ab} \to \rho_\alpha$, where a and b mean the one of spin configurations as defined before, and α is the corresponding vector index. Then we rewrite the Lind-

blad equation Eq. (A.1) in terms of the vectorized density operator $\vec{\rho}$

$$\partial_t \vec{\rho} = -i\hat{\mathscr{H}}\vec{\rho}, \tag{A.10}$$

where the super operator $\hat{\mathscr{H}}$ defined in the $4^N \times 4^N$ complex space is given by

$$\mathscr{H}_{\alpha\beta} \equiv i\frac{\partial\left(\partial_t\rho_\alpha\right)}{\partial\rho_\beta} \tag{A.11}$$

because Eq. (A.1) is the linear equation of ρ_α. We decompose the density vector to two parts as $\vec{\rho} = \vec{\mu} \oplus \vec{v}$, where $\vec{\mu}$ (belongs to the 2^N dimensional space $\mathscr{M}$) and $\vec{v}$ (belongs to the $4^N - 2^N$ dimensional space $\mathscr{N}$) are defined by arranging the ρ_{ab} as below:

$$\vec{\mu} = \underbrace{(\rho_0, \rho_1, \cdots, \rho_\alpha, \cdots, \rho_{2^N-1})}_{\rho_\alpha = \rho_{aa}}^T \in \mathscr{M},$$

$$\vec{v} = \underbrace{(\rho_{2^N}, \rho_{2^N+1}, \cdots, \rho_\alpha, \cdots \rho_{4^N-1})}_{\rho_\alpha = \rho_{a \neq b}}^T \in \mathscr{N}. \tag{A.12}$$

Here, the first 2^N components of vectors correspond to the diagonal components of density matrix, and the remainders are the off-diagonal terms of density matrix. From these decomposed vectors and Eqs (A.4)-(A.9), $\hat{\mathscr{H}}$ can be decomposed using the block matrix

$$\hat{\mathscr{H}} = \left(\begin{array}{c|c} \hat{\mathscr{H}}_1^{(1)} & \hat{\mathscr{H}}_1^{\Omega} \\ \hline \hat{\mathscr{H}}_2^{\Omega} & \hat{\mathscr{H}}^0 + \hat{\mathscr{H}}_3^{\Omega} + \hat{\mathscr{H}}_2^{(1)} + \hat{\mathscr{H}}^{(2)} \end{array}\right), \tag{A.13}$$

where the upper left (lower right) part of the matrix is mapping to $\mathscr{M} \to \mathscr{M}$ ($\mathscr{N} \to \mathscr{N}$), and the upper right (lower left) is mapping to $\mathscr{M} \to \mathscr{N}$ ($\mathscr{N} \to \mathscr{M}$). In addition, $\hat{\mathscr{H}}^{(1)} = \hat{\mathscr{H}}_1^{(1)} + \hat{\mathscr{H}}_2^{(1)}$ is separable as the two parts $\hat{\mathscr{H}}_1^{(1)} : \mathscr{M} \to \mathscr{M}$ and $\hat{\mathscr{H}}_2^{(1)} : \mathscr{N} \to \mathscr{N}$. Likewise, $\hat{\mathscr{H}}^{\Omega}$ is separable as the three parts as $\hat{\mathscr{H}}_1^{\Omega} : \mathscr{M} \to \mathscr{N}$, $\hat{\mathscr{H}}_2^{\Omega} : \mathscr{N} \to \mathscr{M}$, and $\hat{\mathscr{H}}_3^{\Omega} : \mathscr{N} \to \mathscr{N}$. $\hat{\mathscr{H}}_1^{\Omega}$ and $\hat{\mathscr{H}}_2^{\Omega}$ are a switching operator between spaces of $\mathscr{M}$ and $\mathscr{N}$ by flipping one single spin. The components for $\alpha = ab$ of the block matrix in

Eq. (A.13) are defined as below.

$$\mathscr{H}^0_{\alpha\alpha} = \frac{\partial \left([\hat{H}_\Omega, \hat{\rho}]\right)_\alpha}{\partial \rho_\alpha} = \langle a|\hat{H}_0|a\rangle - \langle b|\hat{H}_0|b\rangle, \tag{A.14}$$

$$\mathscr{H}^{(2)}_{\alpha\alpha} = i\frac{\partial \left(D^{(2)}(\hat{\rho})\right)_\alpha}{\partial \rho_\alpha} = -\frac{i\Gamma}{2}\sum_\ell |\langle a|\hat{n}_\ell|a\rangle - \langle b|\hat{n}_\ell|b\rangle|, \tag{A.15}$$

$$\mathscr{H}^\Omega_{1\,\alpha\beta} = \frac{\partial \left([\hat{H}_\Omega, \hat{\rho}]\right)_\alpha}{\partial \rho_\beta}$$
$$= \Omega\sum_\ell\sum_{a'}\left[\langle a|\hat{\sigma}^x_\ell|a'\rangle\delta_{\beta,a'a} - \langle a'|\hat{\sigma}^x_\ell|a\rangle\delta_{\beta,aa'}\right], \tag{A.16}$$

$$\mathscr{H}^\Omega_{2\,\alpha\beta} = \frac{\partial \left([\hat{H}_\Omega, \hat{\rho}]\right)_\alpha}{\partial \rho_\beta}$$
$$= \Omega\sum_\ell\left[\langle a|\hat{\sigma}^x_\ell|b\rangle\delta_{\beta,bb} - \langle a|\hat{\sigma}^x_\ell|b\rangle\delta_{\beta,aa}\right], \tag{A.17}$$

$$\mathscr{H}^{(1)}_{1\,\alpha\beta} = i\frac{\partial \left(D^{(1)}(\hat{\rho})\right)_\alpha}{\partial \rho_\beta}$$
$$= i\gamma\sum_\ell\sum_{a'}\left[|\langle a|\hat{\sigma}^-_\ell|a'\rangle|^2\delta_{\beta,a'a'} - |\langle a'|\hat{\sigma}^-_\ell|a\rangle|^2\delta_{\beta,aa}\right], \tag{A.18}$$

where each $(\cdot)_\alpha$ stands for the matrix element defined in Eqs. (A.4)-(A.9), corresponding to the vector index α.

Consequently, one can rewrite Eq. (A.10) in terms of $\vec{\mu}$ and $\vec{v}$,

$$\partial_t\vec{\mu} = -i\hat{\mathscr{H}}^{(1)}_1\vec{\mu} - i\hat{\mathscr{H}}^\Omega_1\vec{v}, \tag{A.19}$$

$$\partial_t\vec{v} = -i\hat{\mathscr{H}}^\Omega_2\vec{\mu} - i\left(\hat{\mathscr{H}}^0 + \hat{\mathscr{H}}^\Omega_3 + \hat{\mathscr{H}}^{(1)}_2 + \hat{\mathscr{H}}^{(2)}\right)\vec{v}. \tag{A.20}$$

In the limit of the strong dephasing, where $\hat{\mathscr{H}}^{(2)}$ may dominate the off-diagonal dynamics in Eq. (A.20), approximately the solution of Eq. (A.20) becomes an exponentially decaying function in time with a time scale of $1/\Gamma$ (Δ is also the large parameter, but $\hat{\mathscr{H}}^0$ just induces oscillation). Therefore, the full dynamics can be reduced to the diagonal dynamics of $\vec{\mu}$ effectively in the slower time scale than $1/\Gamma$. Inserting the

solution of Eq. (A.20), given by

$$\vec{v}(t) = e^{-i\left(\hat{\mathscr{H}}^0 + \hat{\mathscr{H}}_3^\Omega + \hat{\mathscr{H}}_2^{(1)} + \hat{\mathscr{H}}^{(2)}\right)t} \vec{v}(0)$$

$$- i \int_0^t dt' \, e^{-i\left(\hat{\mathscr{H}}^0 + \hat{\mathscr{H}}_3^\Omega + \hat{\mathscr{H}}_2^{(1)} + \hat{\mathscr{H}}^{(2)}\right)(t-t')} \hat{\mathscr{H}}_2^\Omega \vec{\mu}(t'), \qquad \text{(A.21)}$$

into the Eq. (A.19) with $\vec{v}(0) = 0$, we obtain

$$\partial_t \vec{\mu} = -i\hat{\mathscr{H}}_1^{(1)} \vec{\mu}(t)$$

$$- \int_0^t dt' \, \hat{\mathscr{H}}_1^\Omega e^{-i\left(\hat{\mathscr{H}}^0 + \hat{\mathscr{H}}_3^\Omega + \hat{\mathscr{H}}_2^{(1)} + \hat{\mathscr{H}}^{(2)}\right)(t-t')} \hat{\mathscr{H}}_2^\Omega \vec{\mu}(t'), \qquad \text{(A.22)}$$

Using the fact $\Gamma, \Delta \gg \gamma, \Omega$, we can expand the exponential function about the small parameter using the Zassenhaus formula [170], which then becomes

$$\partial_t \vec{\mu} = -i\hat{\mathscr{H}}_1^{(1)} \vec{\mu}(t) - \int_0^t dt' \, \hat{\mathscr{H}}_1^\Omega e^{-i\left(\hat{\mathscr{H}}^0 + \hat{\mathscr{H}}^{(2)}\right)(t-t')} \hat{\mathscr{H}}_2^\Omega \vec{\mu}(t')$$

$$+ \mathscr{O}(\Omega^2 \gamma, \Omega^3), \qquad \text{(A.23)}$$

We remark again that the time scale for dynamics of $\vec{\mu}$ is much larger than $1/\Gamma$, which leads to the replacement $\vec{\mu}(t') \rightarrow \vec{\mu}(t)$ in the integrand of Eq. (A.23), similarly to the Markov approximation [27]. Also, let the lower limit of the integral go to negative infinity due to the fast decaying of the exponential function. Then, rearranging the time integral of Eq. (A.23) as $(t - t') \rightarrow t'$, we obtain

$$\partial_t \vec{\mu} \approx -i\hat{\mathscr{H}}_1^{(1)} \vec{\mu}(t) - \int_0^\infty dt' \, \hat{\mathscr{H}}_1^\Omega e^{-i\left(\hat{\mathscr{H}}^0 + \hat{\mathscr{H}}^{(2)}\right)t'} \hat{\mathscr{H}}_2^\Omega \vec{\mu}(t). \qquad \text{(A.24)}$$

Now, one can see that the slow dynamics Eq. (A.24) is given only in terms of μ_α, meaning that it can be rewritten with the diagonal elements ρ_{aa} of the density operator. The first term in the r.h.s. of Eq. (A.24) is given by the diagonal element of Eq. (A.18),

which is only composed of diagonal elements μ_α or ρ_{aa} as below.

$$\left(-i\hat{\mathscr{H}}_1^{(1)}\vec{\mu}(t)\right)_\alpha = \gamma\sum_\ell\sum_b\left[|\langle a|\hat{\sigma}_\ell^-|b\rangle|^2\rho_{bb} - |\langle b|\hat{\sigma}_\ell^-|a\rangle|^2\rho_{aa}\right],$$

Next, since $\hat{\mathscr{H}}^0$ and $\hat{\mathscr{H}}^{(2)}$ are diagonal matrices, the αth component of second term is given by

$$\left(-\int_0^\infty dt'\, \hat{\mathscr{H}}_1^\Omega e^{-i\left(\hat{\mathscr{H}}^0+\hat{\mathscr{H}}^{(2)}\right)t'}\hat{\mathscr{H}}_2^\Omega\vec{\mu}\right)_\alpha$$
$$= -\sum_{\beta,\alpha'}\mathscr{H}_{1\,\alpha\beta}^\Omega\mathscr{H}_{2\,\beta\alpha'}^\Omega\mu_{\alpha'}\times\int_0^\infty dt'e^{-i\left(\mathscr{H}_{\beta\beta}^0+\mathscr{H}_{\beta\beta}^{(2)}\right)t'}. \tag{A.25}$$

Using Eqs. (A.16) and (A.17), one can rewrite Eq. (A.25) by changing $\alpha\to aa$

$$\Omega^2\sum_b(\rho_{bb}-\rho_{aa})\sum_\ell|\langle a|\hat{\sigma}_\ell^x|b\rangle|^2$$
$$\times\int_0^\infty dt'\left(e^{-i\left(\mathscr{H}_{ab,ab}^0+\mathscr{H}_{ab,ab}^{(2)}\right)t'}+e^{-i\left(\mathscr{H}_{ba,ba}^0+\mathscr{H}_{ba,ba}^{(2)}\right)t'}\right)$$
$$\equiv\sum_b\left(\Lambda_{a,b}\rho_{bb}-\Lambda_{b,a}\rho_{aa}\right). \tag{A.26}$$

where we have used $\sum_{\ell,\ell'}\left(\langle a|\hat{\sigma}_\ell^x|b\rangle\right)\left(\langle b|\hat{\sigma}_{\ell'}^x|a\rangle\right) = \sum_\ell\left|\langle a|\hat{\sigma}_\ell^x|b\rangle\right|^2$ which becomes zero when ℓ, ℓ' are different. Note that the transition rate $\Lambda_{a,b} = \Lambda_{b,a}$ induced by interaction is non-zero only when the spin configuration b is given by $|b\rangle = |a_1\rangle$, where $\{|a_1\rangle\}$ is generated from $|a\rangle$ by flipping a single spin: for example, if $|a\rangle = |\uparrow\downarrow\downarrow\rangle$ is given for $N = 3$, a set $\{|a_1\rangle\}$ can be defined as $\{|\downarrow\downarrow\downarrow\rangle, |\uparrow\uparrow\downarrow\rangle, |\uparrow\downarrow\uparrow\rangle\}$. Now, using $\mathscr{H}_{aa_1,aa_1}^{(2)} = -i\Gamma/2$ for any a_1, and $\mathscr{H}_{aa_1,aa_1}^0 = \langle a|\hat{H}_0|a\rangle - \langle a_1|\hat{H}_0|a_1\rangle$ we obtain the non-zero transition rate Λ_{a,a_1} in Eq. (A.26) as

$$\Lambda_{a,a_1} = \Omega^2\int_0^\infty dt'2e^{-\frac{\Gamma}{2}t'}\cos\left(\left\{\langle a|\hat{H}_0|a\rangle - \langle a_1|\hat{H}_0|a_1\rangle\right\}t'\right)$$
$$= \frac{\Gamma\Omega^2}{(\Gamma/2)^2 + \left(\langle a|\hat{H}_0|a\rangle - \langle a_1|\hat{H}_0|a_1\rangle\right)^2}. \tag{A.27}$$

From Eq. (A.7) and (A.26), therefore, one can see that the rate equation Eq. (A.24) up to the second order is written as

$$\partial_t \rho_{aa} = \sum_b \left(W_{a,b} \rho_{bb} - W_{b,a} \rho_{aa} \right),$$ (A.28)

where the transition rate $W_{a,b}$ reads

$$W_{a,b} = \gamma \sum_\ell |\langle a | \hat{\sigma}_\ell^- | b \rangle|^2 + \Lambda_{a,b}$$ (A.29)

A.1.3 Derivation of $\kappa = 4\Omega^2/\Gamma$

First, we consider only the nearest neighbor interaction, $V_{\ell m} = V_0$ for the nearest neighbor pair (ℓ, m), otherwise $V_{\ell m} = 0$. Defining a_ℓ as $|a_{1\ell}\rangle = \hat{\sigma}_\ell^x |a\rangle$, we obtain the transition rate Λ_{a,a_ℓ} in Eq. (A.27) as

$$\Lambda_{a,a_{1\ell}} = \frac{4\Omega^2}{\Gamma} \frac{1}{1 + \frac{4}{\Gamma^2} \left(\Delta + \langle a | \hat{P}_\ell | a \rangle V_0 \right)^2},$$ (A.30)

where $\hat{P}_\ell$ denotes the number of the nearest neighbor having the up state of the site ℓ, that is, $\hat{P}_\ell \equiv \sum_{m \in \text{n.n.}(\ell)} \hat{n}_m$. Setting $V_0 = -\Delta$ and $\Delta \gg \Gamma$, one can see that Eq. (A.30) is approximately zero, except for the case of $\langle a | \hat{P}_l | a \rangle = 1$. In the low density limit, where the number of up spins per site is vanishingly small, $n = \text{tr} \left[\hat{\rho} \sum_\ell \hat{n}_\ell \right] / N \ll 1$, configurations having small number of up spins yield a major contribution in $\hat{\rho}$. Then one can assume that $\langle a | \hat{P}_\ell | a \rangle$ for the major configuration is mostly zero or 1, leading to the following approximation:

$$\Lambda_{a,a_\ell} \approx \frac{4\Omega^2}{\Gamma} \langle a | \hat{P}_\ell | a \rangle = \sum_{m \in \text{n.n}(\ell)} \frac{4\Omega^2}{\Gamma} \langle a | \hat{n}_m | a \rangle.$$ (A.31)

Using $|a\rangle = \hat{\sigma}_\ell^x|a_{1\ell}\rangle$ and expanding to general configurations b, the transition rate $\Lambda_{a,b}$ becomes

$$\Lambda_{a,b} = \frac{4\Omega^2}{\Gamma}\sum_\ell \sum_{m \in \text{n.n.}(\ell)} \left(\left|\langle a|\hat{n}_m\hat{\sigma}_\ell^+|b\rangle\right|^2 + \left|\langle a|\hat{n}_m\hat{\sigma}_\ell^-|b\rangle\right|^2 \right), \qquad \text{(A.32)}$$

which is equivalent to the branching and coagulation processes in the ordinary CP model. Here we have used that $\langle a|\hat{n}_m\hat{\sigma}_\ell^+|b\rangle + \langle a|\hat{n}_m\hat{\sigma}_\ell^-|b\rangle = |\langle a|\hat{n}_m\hat{\sigma}_\ell^+|b\rangle|^2 + |\langle a|\hat{n}_m\hat{\sigma}_\ell^-|b\rangle|^2$ in Eq. (A.32). We expect that this approximation made in the limit of low density may be valid near the absorbing transition point, where the order parameter n is small.

Finally, we briefly present the diagonal component of the Lindblad equation with Lindblad operator $\hat{L}_\ell$ corresponding to Eq. (A.28).

$$\partial \rho_{aa} = \langle a|\sum_\ell \left(\hat{L}_\ell \hat{\rho}\hat{L}_\ell^\dagger - \frac{1}{2}\left\{\hat{L}_\ell^\dagger \hat{L}_\ell, \hat{\rho}\right\} \right)|a\rangle$$
$$= \sum_b \left(\sum_\ell |\langle a|\hat{L}_\ell|b\rangle|^2 \rho_{bb} - \sum_\ell |\langle b|\hat{L}_\ell|a\rangle|^2 \rho_{aa} \right), \qquad \text{(A.33)}$$

where the transition rate is given by $W_{a,b} = \sum_\ell |\langle a|\hat{L}_\ell|b\rangle|^2$. Thus, by Eqs. (A.29) and (A.32), the three Lindblad operators are obtained in Eqs. (6.3)-(6.5) with $\kappa = 4\Omega^2/\Gamma$.

Appendix B

Appendix of chapter 2

B.1 Jacobian

As a first step towards the construction of a path integral representation, we discretize time, $n(\boldsymbol{x},t) \to n_i$, $i = 1, \cdots, N$, according to Ito discretization, where Δt is the temporal discretization interval. Delta function may be formally represented as

$$1 = \int DX\, \delta(X) = \int Dn \left| \frac{\delta X}{\delta n} \right| \delta(X)\,, \tag{B.1}$$

where $DX = \prod_i dX_i$ is the functional measure and $\delta(X) = \prod_i \delta(X_i)$ with $X_i \equiv n_i - n_{i-1} + \Delta t \left[f(n_{i-1}) - \xi_{i-1} \right] = 0$ in Ito discretization scheme. Then the Jacobian $|\delta X/\delta n|$ may expressed as

$$\left| \frac{\delta X}{\delta n} \right| = \begin{vmatrix} 1 & 0 & 0 & \cdots & 0 & 0 \\ x & 1 & 0 & \cdots & 0 & 0 \\ 0 & x & 1 & \cdots & 0 & 0 \\ \vdots & \vdots & \vdots & \ddots & \vdots & \vdots \\ 0 & 0 & 0 & \cdots & 1 & 0 \\ 0 & 0 & 0 & \cdots & x & 1 \end{vmatrix} = 1\,, \tag{B.2}$$

where is a triangular matrix with unit diagonal. Thus, the functional determinant equals to unity.

B.2   Correlation of noise variables

B.2.1   Kramers-Moyal expansion

The dynamics in the lattice is described by the master equation.

$$\partial_t P(x,t) = \int dx' \left[W(x|x')P(x') - W(x'|x)P(x) \right] .$$

In the master equation, we substitute x' by $y = x - x'$ in the first term, $y = x' - x$ in the second term and then defining $t(y,x) \equiv W(x+y|x)$.

The master equation becomes

$$\begin{aligned}
\partial_t P(x) &= \int dy \left[W(x|x-y)P(x-y) - W(x+y|x)P(x) \right] \\
&= \int dy \left[t(y,x-y)P(x-y) - t(y,x)P(x) \right] \\
&= \int dy \left[\sum_{n=0}^{\infty} \frac{(-y)^n}{n!} \frac{\partial^n}{\partial x^n} \left(t(y,x)P(x) \right) - t(y,x)P(x) \right] \\
&= \sum_{n=1}^{\infty} \frac{(-1)^n}{n!} \frac{\partial^n}{\partial x^n} \left(\int dy\, y^n t(y,x)P(x) \right) \\
&= \sum_{n=1}^{\infty} \frac{(-1)^n}{n!} \frac{\partial^n}{\partial x^n} \left(\alpha_n(x)P(x) \right) ,
\end{aligned}$$

where $\alpha_n(x) = \int dy\, y^n t(y,x) = \int dx' (x' - x)^n W(x'|x)$. By terminating the series at the second term, we obtain Fokker-Planck equation.

$$\partial_t P = -\frac{\partial}{\partial x} \left(\alpha_1(x)P(x) \right) + \frac{1}{2} \frac{\partial^2}{\partial x^2} \left(\alpha_2(x)P(x) \right) . \tag{B.3}$$

B.2.2   Equivalence between Fokker-Planck equation and Langevin equation

We shall derive the equivalence between Fokker-Planck equation and Langevin equation. Consider an arbitrary function $f[x(t)]$. Then, we expand the stochastic equation

of $f[x(t)]$:

$$
\begin{aligned}
df[x(t)] &= f[x(t) + dx(t)] - f[x(t)] \\
&= f'[x(t)]dx(t) + \frac{1}{2}f''[x(t)]dx(t)^2 + \cdots - f[x(t)] \\
&= f'[x(t)](a(x,t)dt + b(x,t)dW) + \frac{1}{2}f''[x(t)](a(x,t)dt + b(x,t)dW)^2 + \cdots \\
&= \left(a[x(t),t]f'[x(t)] + \frac{1}{2}b[x(t),t]^2 f''[x(t)] \right) dt + b[x(t),t]f'[x(t)]dW(t).
\end{aligned}
$$
(B.4)

The result Eq. (B.4) is known as *Ito's formula*.

Next, Langevin equation in Ito scheme is as follows. (dW is the Wiener process. $dW = \xi dt$)

$$
dx = \alpha_1[x(t),t]dt + \alpha_2[x(t),t]dW.
$$

We now consider the dynamics of an arbitrary function $f(x(t))$.

$$
\frac{d\langle f[x(t)]\rangle}{dt} = \frac{d}{dt}\int dx P(x,t)f[x(t)] = \int dx\, \partial_t P(x,t)f[x(t)].
$$
(B.5)

On the other hand, the left hand side with Ito's formula Eq. (B.4) can be represented by probability $P(x,t)$

$$
\begin{aligned}
\frac{d\langle f[x(t)]\rangle}{dt} = \frac{\langle df\rangle}{dt} &= \int dx P(x,t)\left(\alpha_1[x(t),t]\frac{\partial f}{\partial x} + \frac{1}{2}(\alpha_2[x(t),t])^2\frac{\partial^2 f}{\partial x^2} \right) \\
&= \int dx \left(-\partial_x(\alpha_1(x,t)P) + \frac{1}{2}\partial_x^2(\alpha_2(x,t)^2 P) \right) f[x(t)].
\end{aligned}
$$
(B.6)

Comparing the right hand side of Eqs. (B.5) and (B.6), we can find connection between Fokker-Plank equation and Langevin equation following relation.

$$
\begin{aligned}
\frac{dx}{dt} &= \alpha_1(x,t) + \alpha_2(x,t)\zeta, \\
\partial_t P &= -\partial_x(\alpha_1(x,t)P) + \frac{1}{2}\partial_x^2(\alpha_2(x,t)^2 P).
\end{aligned}
$$
(B.7)

In summary, we obtained the Fokker-Planck equation [Eq. (B.3)] from the master equation by Kramers-Moyal expansion, and then using the Ito's formula we obtain the Langevin equation [Eq. (B.7)] from Fokker-Planck equation [Eq. (B.3)].

B.2.3 Application to contact process

Now we shall deal with the derivation of the correlation of noise in the contact process. The contact process has a reaction scheme such that branching $A + \phi \xrightarrow{\kappa} A + A$ and decay $A \xrightarrow{\gamma} \phi$. Let us consider the notation:

$$I = \text{number of active sites} = \text{extensive variable} \propto \text{system size } N,$$

$$n = \text{density of active sites } (I/N) = \text{intensive variable},$$

$$W(\Delta I|I) = \text{the size of jump is expressed in terms of the extensive variable } \Delta I.$$

Thus, the transition rates are as follows:

$$W(I+1|I) = N\kappa n(1-n) \qquad \text{for branching},$$

$$W(I-1|I) = N\gamma n \qquad \qquad \text{for decay}.$$

Then the master equation for the probability $P(n,t)$ reads

$$\partial_t P(n,t) = \int dn' \left[W(n|n')P(n',t) - W(n'|n)P(n,t) \right]$$

$$= F\left(n - \frac{1}{N}\right)P\left(n - \frac{1}{N}\right) - F(n)P(n) + G\left(n + \frac{1}{N}\right)P\left(n + \frac{1}{N}\right) - G(n)P(n),$$

$$(B.8)$$

where $F(n) = N\kappa n(1-n)$ and $G(n) = N\gamma n$. Expanding the inverse system size $F(n \pm 1/N)P(n \pm 1/N) = F(n)P(n) \pm N^{-1}\partial_n[F(n)P(n)] + (1/2)N^{-2}\partial_n^2[F(n)P(n)]$, the mas-

ter equation becomes

$$\partial_t P(n,t) \simeq -\frac{\partial}{\partial n}\left[(\kappa n(1-n) - \gamma n)P(n)\right] + \frac{\partial^2}{\partial n^2}\left[\frac{\kappa n(1-n) + \gamma n}{2N}P(n)\right], \quad \text{(B.9)}$$

which is equivalent to the Kramers-Moyal expansion up to second order.

The Fokker-Planck equation in Eq. (B.9) is equivalent to the following set of Langevin equation:

$$\partial_t n = (\kappa(1-n)n - \gamma n) + \underbrace{\sqrt{\frac{\kappa(1-n)n + \gamma n}{N}}\zeta}_{\equiv \xi}$$

Hereby, the ζ denotes Gaussian white noise terms. Therefore, the noise correlation shows the multiplicative nature such that $\langle \xi(\mathbf{x},t)\xi(\mathbf{x}',t)\rangle = (\kappa(1-n)n + \gamma n)/N \, \delta(\mathbf{x} - \mathbf{x}')\delta(t - t') \sim n\delta(\mathbf{x} - \mathbf{x}')\delta(t - t')$.

B.3 Continuum limit

For example in one dimension, the second term in Eq. (2.6) is written as

$$\frac{\kappa}{2}\sum_{i,j} n_j(t)(1 - n_i(t)) = \frac{\kappa}{2}\sum_i (1 - n_i)(n_{i-1} + n_{i+1})$$

$$\simeq \sum_i \frac{\kappa}{2}(1 - n_i)\left(n_i - \nabla n_i + \frac{\nabla^2 n_i}{2} + n_i + \nabla n_i + \frac{\nabla^2 n_i}{2}\right)$$

$$= \sum_i \frac{\kappa}{2}(1 - n_i)(2n_i + \nabla^2 n_i) \qquad \text{(B.10)}$$

In the mean-field, Eq. (B.10) is represented as

$$\frac{\kappa}{2d}(1 - n)(2dn + d\nabla^2 n) = \frac{\kappa}{2}\nabla^2 n + \kappa(1 - n)n - \frac{\kappa}{2}n\nabla^2 n.$$

The last term $[\sim n_i \nabla^2 n_{i+1}]$ is irrelevant (we can easily check in MSRJD action).

B.4 Rapidity-reversal symmetry

DP has a rapidity-reversal symmetry in which Eq. (2.11) is invariant under the transformation such that $n(\boldsymbol{r},t) \leftrightarrow -\tilde{n}(\boldsymbol{r},-t)$. This leads to the relation that two exponents β and $\tilde{\beta}$ are identical. In this appendix, we derive the dynamic equation of the phase boundary of active state of the DP class. Rescaling $n \to \sqrt{\frac{\Gamma}{2u_3}}n$, $\tilde{n} \to \sqrt{\frac{2u_3}{\Gamma}}\tilde{n}$, and $\sqrt{\frac{\Gamma u_3}{2}} \to u_3$ [28], the action is written as

$$S = \int d\boldsymbol{x} \left[\tilde{n} \left(\tau \partial_t - D\nabla^2 - D_\sigma \nabla^\sigma + u_2 \right) n + u_3 (n - \tilde{n}) n\tilde{n} \right]. \tag{B.11}$$

If the system is near a critical point, the saddle-point approximation may be valid. The dynamic equations for n and $\tilde{n}$ are obtained from the effective action, by the saddle point approximation $\frac{\delta S}{\delta n} = 0$ and $\frac{\delta S}{\delta \tilde{n}} = 0$, which is given by

$$\frac{\delta S}{\delta \tilde{n}} = (\tau \partial_t - D\nabla^2 - D_\sigma \nabla^\sigma + u_2)n + u_3 n^2 - 2u_3 \tilde{n} n = 0. \tag{B.12}$$

$$\frac{\delta S}{\delta n} = (-\tau \partial_t - D\nabla^2 - D_\sigma \nabla^\sigma + u_2)\tilde{n} - u_3 \tilde{n}^2 + 2u_3 \tilde{n} n = 0. \tag{B.13}$$

According to the definition of the rapidity-reversal symmetry, we rewrite Eq. (B.12) under the transformation $n(\boldsymbol{r},t) \leftrightarrow -\tilde{n}(\boldsymbol{r},-t)$ as

$$\partial_t \tilde{n} = -D\nabla^2 \tilde{n} - D_\sigma \nabla^\sigma \tilde{n} + u_2 \tilde{n} - u_3 \tilde{n}^2 + 2u_3 \tilde{n} n. \tag{B.14}$$

This corresponds to Eq. (B.13) and hence the rapidity-reversal symmetry holds.

B.5   Homogeneous mean-field equation of the CP

Inhomogeneous mean-field equation was give as Eq. (2.8). Assume that spatially homogeneous, then the diffusive term is ignored, which is given by

$$\partial_t n = (\kappa - 1)n - \kappa n^2. \tag{B.15}$$

In steady state $\partial_t n = 0$, $n = (\kappa - 1)^\beta / \kappa$ with $\beta = 1$.

B.6   Wick's theorem

Wick's theorem : The subscript 0 is used to indicate that the expectation values are taken with respect to the unperturbed Gaussian (quadratic) action.

$$\langle \prod_{i=1}^{l} n_i \rangle_0 = \begin{cases} 0 & \text{for } l \text{ odd} \\ \text{sum over all connected components} & \text{for } l \text{ even} \end{cases} \tag{B.16}$$

B.7   Momentum space representation and bare propagator (Green's function)

To compute momentum RG, we shall represent in momentum space using Fourier transform given by

$$\tilde{n}(\boldsymbol{x},t) = \int dq \, \tilde{n}_q \, e^{i(\boldsymbol{k}\cdot\boldsymbol{x} - \omega t)}, \qquad n(\boldsymbol{x},t) = \int dq \, n_q \, e^{i(\boldsymbol{k}\cdot\boldsymbol{x} - \omega t)}, \tag{B.17}$$

where $q \equiv (\mathbf{k}, \omega)$ and $dq = d^d k \, d\omega/(2\pi)^{d+1}$. Then, action given in Eq. (2.16) in momentum space becomes

$$
\begin{aligned}
S_0 &= \int dq \int dq' \int dt \int d^d x \left[e^{i(\mathbf{k}+\mathbf{k}')\cdot\mathbf{x}} e^{-i(\omega+\omega')t} \tilde{n}_{q'} \left(-i\tau\omega + Dk^2 - u_2 \right) n_q \right] \\
&= \int dq \left[\tilde{n}_{-q} (-i\tau\omega + Dk^2 - u_2) n_q \right], \\
S_{int} &= \int dq \int dq' \int dq'' \int dt \int d^d x \left[u_3 e^{i(\mathbf{k}+\mathbf{k}'+\mathbf{k}'')\cdot\mathbf{x}} e^{-i(\omega+\omega'+\omega'')t} \tilde{n}_q (n_{q''} - \tilde{n}_{q''}) n_{q'} \right] \\
&= \int dq \int dq' \left[u_3 \tilde{n}_q (n_{-q-q'} - \tilde{n}_{-q-q'}) n_{q'} \right].
\end{aligned} \tag{B.18}
$$

The quadratic free action may be expressed as

$$
S_0 = \frac{1}{2} \int dq \begin{pmatrix} n_{-q} & \tilde{n}_{-q} \end{pmatrix} \begin{pmatrix} 0 & Dk^2 - u_2 + i\tau\omega \\ Dk^2 - u_2 - i\tau\omega & 0 \end{pmatrix} \begin{pmatrix} n_q \\ \tilde{n}_q \end{pmatrix}. \tag{B.19}
$$

Then partition function with respect to the external fields $(j, \tilde{j})$ is given by

$$
\begin{aligned}
Z_0[j, \tilde{j}] &= \frac{\int Dn \int D\tilde{n} \exp\left[-S_0 + \int dq(\tilde{j}\tilde{n} + jn) \right]}{\int Dn \int D\tilde{n} \exp\left[-S_0 \right]} \\
&= \exp\left[\frac{1}{2} \int dq \begin{pmatrix} j_{-q} & \tilde{j}_{-q} \end{pmatrix} \begin{pmatrix} 0 & Dk^2 - u_2 + i\tau\omega \\ Dk^2 - u_2 - i\tau\omega & 0 \end{pmatrix}^{-1} \begin{pmatrix} j_q \\ \tilde{j}_q \end{pmatrix} \right].
\end{aligned} \tag{B.20}
$$

We now directly compute the matrix of two-point correlation functions

$$
\begin{pmatrix} \langle n_{-q} n_q \rangle & \langle n_{-q} \tilde{n}_q \rangle \\ \langle \tilde{n}_{-q} n_q \rangle & \langle \tilde{n}_{-q} \tilde{n}_q \rangle \end{pmatrix} = \begin{pmatrix} \frac{\delta^2 Z[j,\tilde{j}]}{\delta j_{-q} \delta j_q} & \frac{\delta^2 Z[j,\tilde{j}]}{\delta j_{-q} \delta \tilde{j}_q} \\ \frac{\delta^2 Z[j,\tilde{j}]}{\delta \tilde{j}_{-q} \delta j_q} & \frac{\delta^2 Z[j,\tilde{j}]}{\delta \tilde{j}_{-q} \delta \tilde{j}_q} \end{pmatrix}
$$

$$
= \begin{pmatrix} 0 & Dk^2 - u_2 + i\tau\omega \\ Dk^2 - u_2 - i\tau\omega & 0 \end{pmatrix}^{-1}
$$

$$
= \begin{pmatrix} 0 & (Dk^2 - u_2 - i\tau\omega)^{-1} \\ (Dk^2 - u_2 + i\tau\omega)^{-1} & 0 \end{pmatrix}.
$$

$$(B.21)$$

Thus, $G(k, \omega) = (Dk^2 - u_2 - i\tau\omega)^{-1}$ and $G(-k, -\omega) = (Dk^2 - u_2 + i\tau\omega)^{-1}$.

B.8 Derivation of the fractional Laplacian in continuum limit

In this appendix, we shall derive the fractional Laplacian of long-range interaction in continuum limit of Langevin equation. The second term in Eq. (2.29) is rewritten as

$$
\kappa \sum_j P(|\mathbf{r}_i - \mathbf{r}_j|) n_j (1 - n_i) = \kappa \sum_j P(|\mathbf{r}_i - \mathbf{r}_j|)(n_j - n_i + n_i)(1 - n_i)
$$

$$
= \kappa n_i (1 - n_i) + \kappa \sum_j P(|\mathbf{r}_i - \mathbf{r}_j|)(n_j - n_i)
$$

$$
+ \kappa \sum_j P(|\mathbf{r}_i - \mathbf{r}_j|)(n_j - n_i) n_i, \qquad (B.22)
$$

where the last term in Eq. (B.22) is higher order in spatial fluctuation. Thus, we ignore the last term and let us consider the second term in the continuum limit. As the lattice spacing goes to zero, a summation would be interpreted as the following integral

$$
\sum_{\mathbf{r}'} P(|\mathbf{r} - \mathbf{r}'|)(n(\mathbf{r}',t) - n(\mathbf{r},t)) \rightarrow \int d^d r' P(|\mathbf{r} - \mathbf{r}'|)(n(\mathbf{r}',t) - n(\mathbf{r},t)). \quad (B.23)
$$

The Levy-flight distribution $P(|\mathbf{r} - \mathbf{r}'|) \sim 1/|\mathbf{r} - \mathbf{r}'|^{d+\sigma}$ is normalized as $\int d\mathbf{r}' P(\mathbf{r} - \mathbf{r}') = 1$. Fourier transformation leads to

$$
\begin{aligned}
\int d^d r' \, &P(|\mathbf{r} - \mathbf{r}'|)(n(\mathbf{r}',t) - n(\mathbf{r},t)) \\
&= \int \frac{d^d k}{(2\pi)^d} P(k) n(k) e^{i\mathbf{k}\cdot\mathbf{r}} \\
&= \int d^d r' \int \frac{d^d k}{(2\pi)^d} \int \frac{d^d k'}{(2\pi)^d} P(k') \Big(n(k) e^{i(\mathbf{k}-\mathbf{k}')\cdot\mathbf{r}'} e^{i\mathbf{k}\cdot\mathbf{r}} \\
&\quad - n(k) e^{i(\mathbf{k}-\mathbf{k}')\cdot\mathbf{r}} e^{-i\mathbf{k}'\cdot\mathbf{r}} \Big) \\
&= \int \frac{d^d k}{(2\pi)^d} \Big(P(k) - P(0) \Big) n(k) e^{i\mathbf{k}\cdot\mathbf{r}} \\
&\simeq \int \frac{d^d k}{(2\pi)^d} \left(a_2 \nabla^2 + a_\sigma \nabla^\sigma \right) n(k) e^{i\mathbf{k}\cdot\mathbf{r}} \\
&= \left(a_2 \nabla^2 + a_\sigma \nabla^\sigma \right) n(r) \quad \text{where} \quad
\begin{cases}
a_\sigma > 0 & \text{if} \quad \sigma < 2 \\
a_2 > 0 & \text{if} \quad \sigma > 2
\end{cases}
\end{aligned} \tag{B.24}
$$

Here, the anomalous diffusive operator ∇^σ describes the long-range interaction and it is defined $\nabla^\sigma e^{i\mathbf{k}\cdot\mathbf{r}} = -|\mathbf{k}|^\sigma e^{i\mathbf{k}\cdot\mathbf{r}}$. The normalization condition is satisfied when we consider the lower cutoff part of the Levy distribution $P(\mathbf{r}) = P_L(\mathbf{r}) + P_S(\mathbf{r})$ where $P_L(\mathbf{r}) \propto 1/(r^2 + a^2)^{(d+\sigma)/2}$ is a Levy-flight part and $P_S(\mathbf{r}) \propto e^{-r^2/a^2}$ is a short-range contribution with the lower cutoff length scale a. Fourier transformation leads to $P_L(k) \propto (k/a)^{\sigma/2} K_{\sigma/2}(ak)$ and $P_S(k) \propto e^{-(ak)^2/4}$ where $K_{\sigma/2}$ is the modified Bessel function of the second kind. Therefore, we used $P(k) = P(0) - \frac{B}{2-\sigma}(ak)^\sigma - (A - \frac{B}{2-\sigma})(ak)^2 + \mathcal{O}(k^4, k^{2+\sigma}) \equiv P(0) - a_\sigma k^\sigma - a_2 k^2 + \mathcal{O}(k^4, k^{2+\sigma})$ using long-wavelength expansion with positive, non-singular constant A and B. Therefore, when we solve the Langevin equation with long-range interactions in continuum limit, the term of the long-range interaction leads to

$$
\kappa \sum_j P(|\mathbf{r}_i - \mathbf{r}_j|)(n_j - n_i) \to (D\nabla^2 + D_\sigma \nabla^\sigma) n(r), \tag{B.25}
$$

where $D = a_2\kappa$ and $D_\sigma = a_\sigma\kappa$.

Appendix C

Appendix of chapter 4

C.1 Coarse-grained variables

Here, we represent the critical points along the transition line as $\kappa_c(\omega)$ for each given ω and the tricritical point as (κ_t, ω_t). Note that $\kappa_c(\omega_t) = \kappa_t$. In numerical simulations, these physical quantities are measured as a function of κ for each value of ω. The relations of u_2 and u_3 as a function of κ and ω are determined as follows. Sufficiently close to the tricritical point, we can expand $u_2 = u_2(\kappa, \omega)$ for fixed $\omega = \omega_t$ and $u_3 = u_3(\kappa, \omega)$ along the transition line $(\kappa_c(\omega), \omega)$ using chain rules:

$$u_2(\kappa, \omega_t) = u_2(\kappa_t + \Delta\kappa, \omega_t) = \partial_\kappa u_2|_{\kappa_t} \Delta\kappa + \mathcal{O}((\Delta\kappa)^2),$$

$$u_3(\kappa, \omega) = u_3(\kappa_c(\omega) + \Delta\kappa, \omega_t - \Delta\omega)$$

$$= \partial_\kappa u_3|_{\kappa_t, \omega_t} \Delta\kappa + (\partial_\kappa u_3 \partial_\omega \kappa|_{\kappa_t, \omega_t} + \partial_\omega u_3)\Delta\omega + \mathcal{O}(\Delta\kappa\Delta\omega). \qquad \text{(C.1)}$$

If we perform a simulation at $(\kappa_c(\omega), \omega)$, $\delta\omega \gg \delta\kappa$, we can reduce $u_2 \simeq \Delta\kappa$ at a fixed ω_t in Eq. (4.6) and $u_3 \simeq \Delta\omega$ along the transition line in Eq. (4.7). We first obtain $\nu_\parallel$ using Eq. (4.6), and then the crossover exponent ϕ is obtained using Eq. (4.7). The exponents and relations are characterized by four independent exponents: δ, δ', z, and $\nu_\parallel$.

C.2 Calculation of propagator

Let us evaluate the propagator loop integral to determine why the fractional Laplacian is not renormalized. This can be done using the propagator loop integral in Ref. [53]. The only difference between the ordinary TDP and the LTDP lies in the Green function, which changes slightly from $G(\mathbf{k}, \omega) = (Dk^2 - i\omega\tau + u_2)^{-1}$ to $G(\mathbf{k}, \omega) = (D_\sigma k^\sigma - i\omega\tau + u_2)^{-1}$. Because the cubic terms remain the same, the relevant diagrams do not change, as shown in Ref. [53]. $I_0(k, \omega)$ is given by

$$
\begin{aligned}
I_0(k, \omega) &= \!\!\!\!\!\!\!\!\!\!\!\! \\
&= \int \frac{d^d q_1}{(2\pi)^d} \int \frac{d^d q_2}{(2\pi)^d} \int \frac{d\omega_1}{(2\pi)} \int \frac{d\omega_2}{(2\pi)} G(-\mathbf{k} - \mathbf{q}_1, -\omega - \omega_1) \\
&\quad \times G(\mathbf{q}_1, \omega_1) G(\mathbf{q}_1 + \mathbf{q}_2, \omega_1 + \omega_2) G(-\mathbf{q}_2, -\omega_2) \\
&= \int \frac{d^d q_1}{(2\pi)^d} \int \frac{d^d q_2}{(2\pi)^d} \int \frac{d\omega_1}{(2\pi)} \frac{1}{D_\sigma |\mathbf{k} + \mathbf{q}_1|^\sigma + i(\omega + \omega_1)\tau + u_2} \\
&\quad \times \frac{1}{D_\sigma q_1^\sigma - i\omega_1\tau + u_2} \frac{1}{D_\sigma q^\sigma + D_\sigma |\mathbf{q}_1 + \mathbf{q}_2|^\sigma - i\omega_1\tau + 2u_2} \\
&= \int \frac{d^d q_1}{(2\pi)^d} \int \frac{d^d q_2}{(2\pi)^d} \frac{1}{(i\omega + D_\sigma q_1^\sigma + D_\sigma |\mathbf{q}_1 + \mathbf{k}|^\sigma + 2u_2)} \\
&\quad \times \frac{1}{(i\omega + D_\sigma |\mathbf{q}_1 + \mathbf{q}_2|^\sigma + D_\sigma q^\sigma + D_\sigma |\mathbf{q}_1 + \mathbf{k}|^\sigma + 3u_2)},
\end{aligned}
\tag{C.2}
$$

where we set $\tau = 1$ and $D = 1$ without loss of generality. After ω_1 and ω_2 in Eq. (C.2) are integrated out using the Cauchy integral, I_0 is given by

$$
\begin{aligned}
I_0(k, \omega) &= \int \frac{d^d q_1}{(2\pi)^d} \int \frac{d^d q_2}{(2\pi)^d} \frac{1}{(i\omega + q_1^\sigma + |\boldsymbol{q}_1 + \boldsymbol{k}|^\sigma + 2u_2)} \\
&\quad \times \frac{1}{(i\omega + |\boldsymbol{q}_1 + \boldsymbol{q}_2|^\sigma + q_2^\sigma + |\boldsymbol{q}_1 + \boldsymbol{k}|^\sigma + 3u_2)} \\
&= \int \frac{d^d q_1}{(2\pi)^d} \int \frac{d^d q_2}{(2\pi)^d} \frac{1}{i\omega + q_1^\sigma + |\boldsymbol{q}_1 + \boldsymbol{k}|^\sigma + 2u_2} \\
&\quad \times \int_{-i\infty}^{i\infty} dz_1 \Gamma(1 + z_1) \Gamma(-z_1) \frac{\left(i\omega + q_2^\sigma + |\boldsymbol{q}_1 + \boldsymbol{k}|^\sigma + 3u_2\right)^{z_1}}{|\boldsymbol{q}_1 + \boldsymbol{q}_2|^{\sigma(1+z_1)}} \\
&= \int \frac{d^d q_1}{(2\pi)^d} \int \frac{d^d q_2}{(2\pi)^d} \frac{1}{i\omega + q_1^\sigma + |\boldsymbol{q}_1 + \boldsymbol{k}|^\sigma + 2u_2} \int_{-i\infty}^{i\infty} dz_1 \\
&\quad \times \int_{-i\infty}^{i\infty} dz_2 \Gamma(1 + z_1) \Gamma(-z_1) \Gamma(z_2 - z_1) \Gamma(-z_2) \frac{\left(i\omega + |\boldsymbol{q}_1 + \boldsymbol{k}|^\sigma + 3u_2\right)^{z_2}}{|\boldsymbol{q}_1 + \boldsymbol{q}_2|^{\sigma(1+z_1)} q_2^{\sigma(z_2 - z_1)}},
\end{aligned}
$$
(C.3)

where we used the Mellin–Barnes representation

$$
\frac{1}{(X + Y)^\lambda} = \int_{-i\infty}^{i\infty} dz \frac{Y^z}{X^{\lambda + z}} \frac{\Gamma(\lambda + z)\Gamma(-z)}{\Gamma(\lambda)}.
$$

Now, the integral over q_2 in Eq. (C.3) becomes

$$
\int \frac{d^d q_2}{(2\pi)^d} \frac{1}{q_2^a |\boldsymbol{q}_1 + \boldsymbol{q}_2|^b} = \frac{q_1^{d-(a+b)} \Gamma(\frac{a+b-d}{2}) \Gamma(\frac{d-a}{2}) \Gamma(\frac{d-b}{2})}{(4\pi)^{d/2} \Gamma(\frac{a}{2}) \Gamma(\frac{b}{2}) \Gamma(d - \frac{a+b}{2})}.
$$
(C.4)

After Eq. (C.4) is inserted into Eq. (C.3), I_0 is given by

$$
\begin{aligned}
I_0 &= \int \frac{d^d q_1}{(16\pi^3)^{d/2}} \int_{-i\infty}^{i\infty} dz_1 \int_{-i\infty}^{i\infty} dz_2 \Gamma(1 + z_1) \Gamma(-z_1) \Gamma(z_2 - z_1) \Gamma(-z_2) \\
&\quad \times \frac{\Gamma(\frac{\sigma}{2}(z_2 + 1) - \frac{d}{2}) \Gamma(\frac{d}{2} - \frac{\sigma}{2}(z_1 + 1)) \Gamma(\frac{d}{2} - \frac{\sigma}{2}(z_2 - z_1))}{\Gamma(\frac{\sigma}{2}(1 + z_1)) \Gamma(\frac{\sigma}{2}(z_2 - z_1)) \Gamma(d - \frac{\sigma}{2}(1 + z_2))} \\
&\quad \times \frac{q_1^{d - \sigma(z_2 + 1)} \left(i\omega + |\boldsymbol{q}_1 + \boldsymbol{k}|^\sigma + 3u_2\right)^{z_2}}{i\omega + q_1^\sigma + |\boldsymbol{q}_1 + \boldsymbol{k}|^\sigma + 2u_2}.
\end{aligned}
$$
(C.5)

Then, let us expand the last term in Eq. (C.5) with respect to k and ω.

$$\int \frac{d^d q_1}{(16\pi^3)^{d/2}} \frac{q_1^{d-\sigma(z_2+1)} \left(i\omega + |\boldsymbol{q}_1 + \boldsymbol{k}|^\sigma + 3u_2 \right)^{z_2}}{i\omega + q_1^\sigma + |\boldsymbol{q}_1 + \boldsymbol{k}|^\sigma + 2u_2}$$

$$= \int \frac{d^d q_1}{(16\pi^3)^{d/2}} q_1^{d-\sigma(z_2+1)}$$

$$\times \frac{\left(q_1^\sigma + 3u_2 + i\omega + \sigma q_1^{\sigma-1} k \cos(\theta) + \frac{\sigma}{2}k^2 q_1^{\sigma-2} + \frac{\sigma}{4}(\frac{\sigma}{2}-1)q_1^{\sigma-2}k^2 \cos^2(\theta) + \mathscr{O}(k^3) \right)^{z_2}}{2q_1^\sigma + 2u_2 + i\omega + \sigma q_1^{\sigma-1}k\cos(\theta) + \frac{\sigma}{2}k^2 q_1^{\sigma-2} + \frac{\sigma}{4}(\frac{\sigma}{2}-1)q_1^{\sigma-2}k^2\cos^2(\theta) + \mathscr{O}(k^3)}$$

$$= \int \frac{d^d q_1}{(16\pi^3)^{d/2}} \frac{q_1^{d-\sigma(z_2+1)}(3u_2 + q_1^\sigma)^{z_2}}{2q_1^\sigma + 2u_2}$$

$$\left(1 + \frac{i\omega + \sigma q_1^{\sigma-1}k\cos(\theta) + \frac{\sigma}{2}k^2 q_1^{\sigma-2} + \frac{\sigma}{4}(\frac{\sigma}{2}-1)q_1^{\sigma-2}k^2\cos^2(\theta) + \mathscr{O}(k^3)}{3u_2 + q_1^\sigma} \right)^{z_2} \times$$

$$\left(1 + \frac{i\omega + \sigma q_1^{\sigma-1}k\cos(\theta) + \frac{\sigma}{2}k^2 q_1^{\sigma-2} + \frac{\sigma}{4}(\frac{\sigma}{2}-1)q_1^{\sigma-2}k^2\cos^2(\theta) + \mathscr{O}(k^3)}{2q_1^\sigma + 2u_2} \right)^{-1}$$

$$= \int \frac{d^d q_1}{(16\pi^3)^{d/2}} \frac{q_1^{d-\sigma(z_2+1)}(3u_2 + q_1^\sigma)^{z_2}}{2q_1^\sigma + 2u_2} \left[1 + i\omega \left(\frac{z_2}{3u_2 + q_1^\sigma} - \frac{1}{2u_2 + 2q_1^\sigma} \right) \right.$$

$$+ k \left(\frac{z_2 \sigma q_1^{\sigma-1}\cos(\theta)}{3u_2 + q_1^\sigma} - \frac{\sigma q_1^{\sigma-1}\cos(\theta)}{2u_2 + 2q_1^\sigma} \right) + k^2 \left(\frac{z_2 \left(\frac{\sigma}{2}q_1^{\sigma-2} + \frac{\sigma}{4}(\frac{\sigma}{2}-1)\cos^2(\theta) \right)}{3u_2 + q_1^\sigma} \right.$$

$$- \frac{\frac{\sigma}{2}q_1^{\sigma-2} + \frac{\sigma}{4}(\frac{\sigma}{2}-1)\cos^2(\theta)}{2u_2 + 2q_1^\sigma} + \frac{z_2(z_2-1)\sigma^2 q_1^{2\sigma-2}\cos^2(\theta)}{2(3u_2 + q_1^\sigma)^2}$$

$$\left. \left. + \frac{\sigma^2 q_1^{2\sigma-2}\cos^2(\theta)}{(2u_2 + 2q_1^\sigma)^2} + \frac{z_2 \sigma^2 q_1^{2\sigma-2}\cos^2(\theta)}{(3u_2 + q_1^\sigma)(2u_2 + 2q_1^\sigma)} \right) + \mathscr{O}(k^3, \omega^2, k\omega) \right]. \tag{C.6}$$

We used the following relation, because k is very small in the long-wavelength limit.

$$(\boldsymbol{q}_1 + \boldsymbol{k})^\sigma = ((\boldsymbol{q}_1 + \boldsymbol{k})^2)^{\sigma/2}$$

$$= q_1^\sigma + \sigma q_1^{\sigma-2}\boldsymbol{q}_1 \cdot \boldsymbol{k} + \frac{\sigma}{2}k^2 q_1^{\sigma-2} + \frac{\sigma}{4}(\frac{\sigma}{2}-1)q_1^{\sigma-4}(2\boldsymbol{q}_1 \cdot \boldsymbol{k})^2 + \mathscr{O}(k^3)$$

$$= q_1^\sigma + \sigma q_1^{\sigma-1}k\cos(\theta) + \frac{\sigma}{2}k^2 q_1^{\sigma-2} + \sigma(\frac{\sigma}{2}-1)q_1^{\sigma-2}k^2\cos^2(\theta) + \mathscr{O}(k^3), \tag{C.7}$$

159

where θ is the angle between $\boldsymbol{q}_1$ and $\boldsymbol{k}$. To evaluate Eq. (C.6), it is often helpful to use the formulas

$$
\begin{aligned}
\int \frac{d^d q_1}{(2\pi)^d} f(q_1) &= \frac{S_{d-1}}{(2\pi)^d} \int_0^\infty dq_1 \int_0^\pi d\theta f(q_1) \sin^{d-2}(\theta) \\
&= \frac{S_d}{(2\pi)^d} \int_0^\infty dq_1 f(q_1), \\
\int \frac{d^d q_1}{(2\pi)^d} f(q_1) \cos(\theta) &= \frac{S_{d-1}}{(2\pi)^d} \int_0^\infty dq_1 \int_0^\pi d\theta f(q_1) \sin^{d-2}(\theta) \cos(\theta) = 0, \\
\int \frac{d^d q_1}{(2\pi)^d} f(q_1) \cos^2(\theta) &= \frac{S_{d-1}}{(2\pi)^d} \int_0^\infty dq_1 \int_0^\pi d\theta f(q_1) \sin^{d-2}(\theta) \cos^2(\theta) \\
&= \frac{S_d}{d(2\pi)^d} \int_0^\infty dq_1 f(q_1), \quad\quad\quad \text{(C.8)}
\end{aligned}
$$

where the surface area is defined as $S_d = \frac{2\pi^{d/2}}{\Gamma(d/2)}$. Then, Eq. (C.5) is given as follows:

$$
\begin{aligned}
I_0(k,\omega) = &\int_{-i\infty}^{i\infty} dz_1 \int_{-i\infty}^{i\infty} dz_2 \Gamma(1+z_1)\Gamma(-z_1)\Gamma(z_2-z_1)\Gamma(-z_2) \times \\
&\frac{\Gamma(\frac{\sigma}{2}(z_2+1)-\frac{d}{2})\Gamma(\frac{d}{2}-\frac{\sigma}{2}(z_1+1))\Gamma(\frac{d}{2}-\frac{\sigma}{2}(z_2-z_1))}{\Gamma(\frac{\sigma}{2}(1+z_1))\Gamma(\frac{\sigma}{2}(z_2-z_1))\Gamma(d-\frac{\sigma}{2}(1+z_2))} S_d \\
&\times \int_0^\infty \frac{dq_1}{(16\pi^3)^{d/2}} \frac{q_1^{d-\sigma(z_2+1)}(3u_2+q_1^\sigma)^{z_2}}{2q_1^\sigma + 2u_2} \\
&\times \Bigg[1 + \frac{i\omega}{D_\sigma}\left(\frac{z_2}{3u_2+q_1^\sigma} - \frac{1}{2u_2+2q_1^\sigma}\right) + k^2\left(\frac{z_2\left(\frac{\sigma}{2}q_1^{\sigma-2}+\frac{\sigma}{4d}(\frac{\sigma}{2}-1)\right)}{3u_2+q_1^\sigma}\right. \\
&\left. - \frac{\frac{\sigma}{2}q_1^{\sigma-2}+\frac{\sigma}{4d}(\frac{\sigma}{2}-1)}{2u_2+2q_1^\sigma} + \frac{z_2(z_2-1)\sigma^2 q_1^{2\sigma-2}}{2d(3u_2+q_1^\sigma)^2}\right. \\
&\left.\left. + \frac{\sigma^2 q_1^{2\sigma-2}}{d(2u_2+2q_1^\sigma)^2} + \frac{z_2\sigma^2 q_1^{2\sigma-2}}{d(3u_2+q_1^\sigma)(2u_2+2q_1^\sigma)}\right)\right] + \mathcal{O}(k^3,\omega^2,k\omega) \\
=& \ N_0 + N_\omega \omega + N_{k^2} k^2 + \mathcal{O}(k^3,\omega^2,k\omega), \quad\quad\quad \text{(C.9)}
\end{aligned}
$$

where N_0, N_ω, and N_{k^2} are coefficients. Finally, because the derivative of Eq. (C.9) with respect to k^σ vanishes, the coefficient D_σ is not renormalized up to the first order in the ε expansion around the upper critical dimension. Although we showed that it is valid for up to $\mathcal{O}(\varepsilon)$, it is commonly believed that nonlocal terms of the dynamic

action are not renormalized at all [171]–[173].

C.3 Tables of numerical estimates

Table C.1: Critical exponents for the LTDP model in two dimensions. For $\sigma < 4/3$, the universality class belongs to the mean-field LTDP. For $4/3 < \sigma < 2.2$, the universality class belongs to the LTDP. Finally, for $\sigma > 2.2$, the universality class belongs to the STDP.

σ	(κ_t, ω_t)	δ	δ'	$\bar{z} \equiv z/d$	$\nu_\parallel$	η	ϕ
0.2	$(0.609401, 0.378)$	0.500 ± 0.005	1.00 ± 0.02	0.666 ± 0.01	1.00 ± 0.01	0.000 ± 0.005	0.50 ± 0.01
0.4	$(0.612271, 0.400)$	0.500 ± 0.005	1.00 ± 0.02	0.666 ± 0.01	1.00 ± 0.01	0.000 ± 0.005	0.50 ± 0.01
0.6	$(0.616819, 0.424)$	0.500 ± 0.005	1.00 ± 0.02	0.666 ± 0.01	1.00 ± 0.01	0.000 ± 0.005	0.50 ± 0.01
0.8	$(0.622538, 0.450)$	0.500 ± 0.005	1.00 ± 0.02	0.666 ± 0.01	1.00 ± 0.01	0.000 ± 0.005	0.50 ± 0.01
1.0	$(0.628244, 0.475)$	0.500 ± 0.01	0.99 ± 0.02	0.666 ± 0.01	1.00 ± 0.01	0.000 ± 0.005	0.50 ± 0.01
1.2	$(0.635410, 0.506)$	0.485 ± 0.01	1.00 ± 0.02	0.678 ± 0.01	1.02 ± 0.01	-0.010 ± 0.005	0.50 ± 0.01
1.4	$(0.643351, 0.543)$	0.397 ± 0.01	1.01 ± 0.02	0.725 ± 0.01	1.03 ± 0.01	-0.022 ± 0.005	0.50 ± 0.01
1.5	$(0.647071, 0.562)$	0.345 ± 0.01	1.013 ± 0.02	0.758 ± 0.01	1.03 ± 0.01	-0.029 ± 0.005	0.51 ± 0.01
1.6	$(0.650679, 0.582)$	0.309 ± 0.01	1.021 ± 0.02	0.784 ± 0.01	1.04 ± 0.01	-0.032 ± 0.005	0.51 ± 0.01
1.7	$(0.653822, 0.601)$	0.281 ± 0.01	1.031 ± 0.02	0.819 ± 0.01	1.04 ± 0.01	-0.052 ± 0.005	0.51 ± 0.01
1.8	$(0.656771, 0.621)$	0.253 ± 0.01	1.041 ± 0.02	0.849 ± 0.01	1.05 ± 0.01	-0.071 ± 0.01	0.51 ± 0.02
1.9	$(0.659371, 0.641)$	0.223 ± 0.01	1.050 ± 0.01	0.881 ± 0.01	1.06 ± 0.01	-0.091 ± 0.01	0.52 ± 0.02
2.0	$(0.661659, 0.662)$	0.212 ± 0.01	1.073 ± 0.01	0.922 ± 0.01	1.07 ± 0.01	-0.129 ± 0.01	0.52 ± 0.02
2.1	$(0.663511, 0.683)$	0.184 ± 0.01	1.100 ± 0.01	0.961 ± 0.01	1.08 ± 0.01	-0.180 ± 0.01	0.52 ± 0.02
2.2	$(0.664880, 0.703)$	0.172 ± 0.01	1.150 ± 0.01	0.992 ± 0.01	1.09 ± 0.01	-0.211 ± 0.01	0.52 ± 0.02
2.4	$(0.666269, 0.742)$	0.123 ± 0.01	1.211 ± 0.01	1.045 ± 0.01	1.12 ± 0.01	-0.288 ± 0.01	0.52 ± 0.02
2.6	$(0.666487, 0.769)$	0.105 ± 0.01	1.22 ± 0.01	1.055 ± 0.01	1.14 ± 0.01	-0.334 ± 0.01	0.52 ± 0.02
2.8	$(0.666001, 0.792)$	0.098 ± 0.01	1.22 ± 0.01	1.055 ± 0.01	1.15 ± 0.01	-0.353 ± 0.01	0.52 ± 0.02
∞	$(0.6606466, 0.879)$	0.09 ± 0.01	1.22 ± 0.008	1.055 ± 0.005	1.15 ± 0.005	-0.35 ± 0.008	0.52 ± 0.02

Table C.2: Critical exponents for the LTDP model in one dimension. For $\sigma < 2/3$, the universality class belongs to the mean-field LTDP. For $2/3 < \sigma < 1.0$, the universality class belongs to the LTDP. Finally, for $\sigma > 1.0$, the tricritical point does not exist.

σ	(κ_t, ω_t)	δ	δ'	$\bar{z} \equiv z/d$	$\nu_\parallel$	η	ϕ
0.2	(0.603919, 0.388)	0.50 ± 0.005	1.000 ± 0.01	0.666 ± 0.005	1.00 ± 0.01	0.00 ± 0.005	0.50 ± 0.02
0.4	(0.616681, 0.471)	0.50 ± 0.005	0.99 ± 0.01	0.666 ± 0.005	1.00 ± 0.01	0.00 ± 0.005	0.50 ± 0.02
0.6	(0.631031, 0.576)	0.49 ± 0.01	0.96 ± 0.01	0.670 ± 0.005	1.01 ± 0.01	0.00 ± 0.005	0.50 ± 0.02
0.7	(0.637510, 0.654)	0.34 ± 0.01	0.91 ± 0.01	0.701 ± 0.01	1.05 ± 0.01	0.00 ± 0.005	0.52 ± 0.02
0.8	(0.637551, 0.744)	0.25 ± 0.01	0.88 ± 0.01	0.878 ± 0.01	1.09 ± 0.01	-0.013 ± 0.01	0.54 ± 0.02
0.9	(0.622539, 0.846)	0.14 ± 0.01	0.83 ± 0.01	1.05 ± 0.01	1.18 ± 0.01	-0.04 ± 0.01	0.56 ± 0.02
1.0	(0.556705, 0.960)	0.04 ± 0.01	0.76 ± 0.01	1.43 ± 0.01	1.34 ± 0.01	-0.09 ± 0.01	0.58 ± 0.02
1.05	Tricritical point does not exist						

Appendix D

Appendix of chapter 6

D.1 Classical contact process using the quantum jump Monte Carlo method

In this section, we consider $\omega \to 0$. When $\kappa \ll \gamma$, inactive particles become more abundant with time, and eventually the system is fully occupied by inactive particles. Thus, the system is no longer dynamic and falls into an absorbing state. When $\kappa \gg \gamma$, the system remains in an active state with a finite density of active particles. Thus, the classical CP exhibits a phase transition from an active to an absorbing state as κ is decreased.

The critical exponents of $1d$-QCP were obtained using the finite-size scaling from the data of QJMC method in the main text. To check the validity of the finite-size scaling with the small system size, we consider the $1d$ classical contact process (CCP) where κ is finite and $\omega = 0$ (see Eqs. (2-5) in the main text). At the critical point, we perform the finite-size scaling to $1d$-CCP using the QJMC method. The observables correspond to the definitions of the main text.

First, we obtain the exponents $\delta + \delta'$, η, δ', z, δ, and α directly by measuring the slopes in the double-logarithmic plots shown in Figs. D.1 and D.2. Then, we collapse the data by using the obtained exponents to compute the dynamic exponent z. Specifically, we plot $\rho_d t^{\delta + \delta'}$ versus $t N^{-z}$ in Fig. D.1(a), $N_a t^{-\eta}$ versus $t N^{-z}$ in Fig. D.1(b), and $P(t) t^{-\delta'}$ versus $t N^{-z}$ in Fig. D.1(c) for different system sizes N. We measure the exponent z directly using the plot of $R^2(t)$ versus t in Fig. D.1(d). In classical contact

process, we can classify the surviving runs and thus we measure the exponent $-\delta$ directly using the plot of $\rho_{\mathrm{d,s}}(t)$ versus t in Fig. D.1(e). Next, we plot $n(t)t^{-\alpha}$ versus tN^{-z} in Fig. D.2(a) for different system sizes N. The exponent $\nu_\parallel$ is obtained from the rescaling plot of $n(t)t^\alpha$ versus $t(\omega_c - \omega)^{\nu_\parallel}$ for different ω values in Fig. D.2(b).

The critical exponents are thus obtained as $\delta + \delta' = 0.32 \pm 0.01$, $\eta = 0.31 \pm 0.02$, $\delta' = 0.16 \pm 0.01$, $\delta = 0.16 \pm 0.02$, $z = 1.58 \pm 0.03$, and $\alpha = 0.16 \pm 0.01$. Note that $\delta = \alpha$. In addition, $\alpha = \delta'$ implying that rapidity-reversal symmetry holds. All the critical exponents are in good agreement with the DP values within the error bars. Thus we verified that the critical exponents on classical contact process can be successfully obtained using QJMC method with the same system size in main text.

D.2 Test of scaling relations using classical Monte Carlo simulations

We mentioned that $\rho_d(t)$ and $n(t)$ show the same asymptotic behavior, which means that $\delta = \alpha$ holds [174, 175]. In this section, we shall test this relation using classical Monte Carlo simulations. The models we consider here are $1d$ contact process and $2d$ tricritical contact process. It was revealed that rapidity reversal symmetry holds for $1d$ contact process [28] and does not hold for $2d$ tricritical contact process [54, 55]. By measuring the slopes in the double-logarithmic plots, we measure the complete set of critical exponents.

In Fig. D.3(a), the values of all critical exponents for $1d$ contact process are $z = 1.58$, $\delta = 0.16$, $\eta = 0.31$, $\delta' = 0.16$, and $\alpha = 0.16$. Note that $\delta' = \alpha$ and the generalized hyperscaling relation $\eta - D/z = -\delta - \delta'$ hold. In addition, $\delta = \delta'$ because rapidity-reversal symmetry holds. Next, in Fig. D.3(b), the values of all critical exponents for $2d$ tricritical contact process are $z = 2.11$, $\delta = 0.09$, $\eta = -0.35$, and $\delta' = 1.21$. Note that $\delta' = \alpha$ and the generalized hyperscaling relation $\eta - D/z = -\delta - \delta'$ hold. However, $\delta \neq \delta'$ because rapidity-reversal symmetry is broken.

Thus, the scaling relations $\delta = \alpha$ and $\eta - D/z = -\delta - \delta'$, which is believed to be satisfied with the single absorbing state phase transition, hold; however $\delta = \delta'$ when the rapidity-reversal symmetry holds.

D.3 Critical behavior by neural network approach with different training regions

For supervised learning, it is advantageous to take a narrower test region [white region in Fig. D.4(a)], because more information can be taken in the training region. However, if the test region is too narrow to include the crossing point, the crossing point of the outputs would not be the critical point. To avoid this case, it is desirable to take a test region with an appropriate size.

We took the left boundary $\omega = 4$ in the main text, because this is the value at which the order parameter $n(t)$ decays exponentially, i.e., at which the system is in the subcritical region, as shown in Fig. D.5. This result was obtained using the QJMC method. However, the boundary $\omega = 8$ was taken, because $n(t)$ behaves as it does in the supercritical state.

To check the sensitivity of the positions of the left and right boundaries, we also considered a test region of $(3 \leq \omega \leq 9)$ and then estimated the transition point ω_c in the thermodynamic limit and the value of the exponent $\nu_\perp$. As shown in Fig. D.4, we obtained the same values of ω_c and $\nu_\perp$.
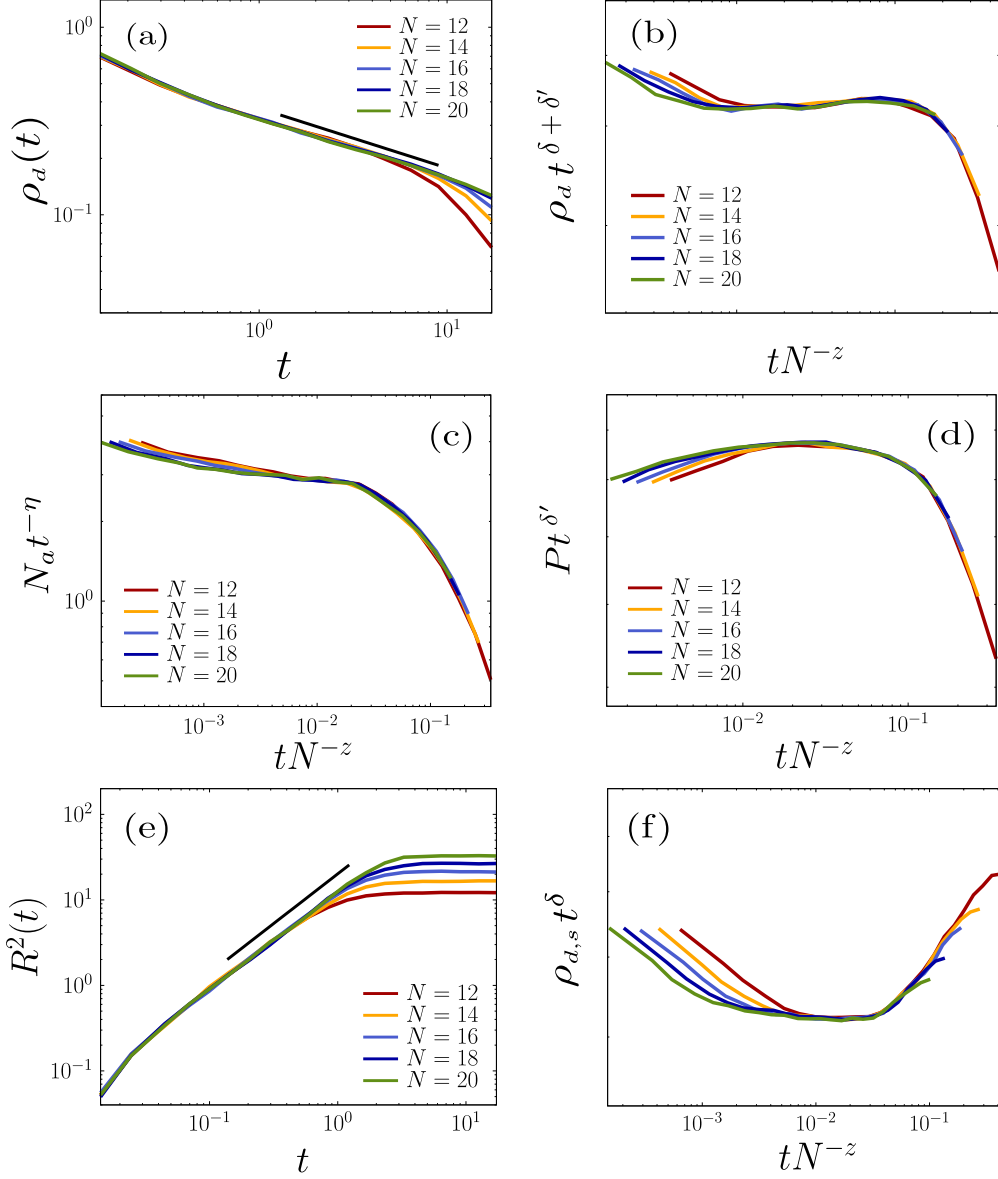
Figure D.1: Estimates of the critical exponents of the $1d$-CCP starting from the single active initial state. (a) Plot of $\rho_d(t)$ versus t, which behaves as $\rho_d(t) \sim t^{-\delta-\delta'}$. The solid line is a guideline with slope -0.32. Inset: scaling plot of $\rho_d(t)t^{\delta+\delta'}$ versus tN^{-z} for $\delta + \delta' = 0.32$ and $z = 1.58$. (b) Scaling plot of $N_a(t)t^{-\eta}$ versus tN^{-z} for $\eta = 0.30$ and $z = 1.58$. (c) Scaling plot of $P(t)t^{\delta'}$ versus tN^{-z} for $\delta' = 0.16$ and $z = 1.58$. (d) Plot of $R^2(t)$ as a function of t. The solid line is a guideline with slope $2/z$ for $z = 1.58$. (e) Scaling plot of $\rho_{d,s}(t)t^{\delta}$ versus tN^{-z} for $\delta = 0.16$ and $z = 1.58$. The parameter t is given in units of $1/\gamma$.
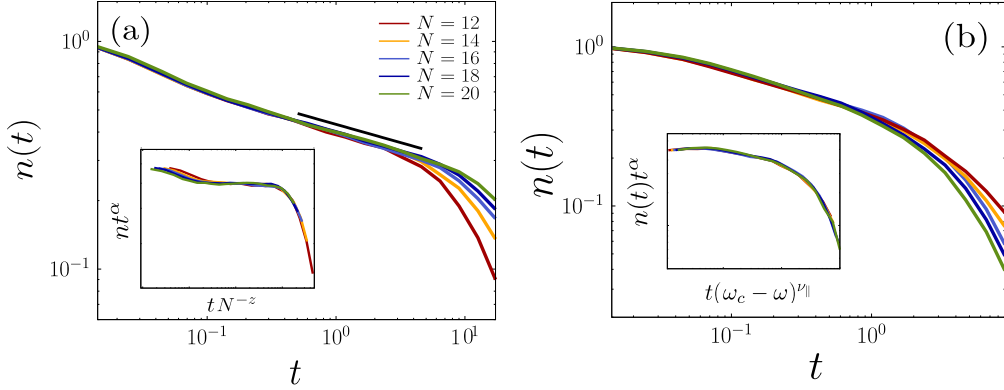
Figure D.2: Estimates of the critical exponents of the $1d$-CCP starting from the fully active initial state. (a) Plot of $n(t)$ as a function of t, which shows $n(t) \sim t^{-\alpha}$. The solid line is a guideline with slope -0.16. Inset: the scaling plot of $n(t)t^{\alpha}$ versus tN^{-z} for $\alpha = 0.16$ and $z = 1.58$. (b) Plot of $n(t)$ as a function of t for different values of $\omega < \omega_c$. Inset: Data points collapse well onto a single curve for $\alpha = 0.16$, and $\nu_{\parallel} = 1.73$. The parameter t is given in units of $1/\gamma$.
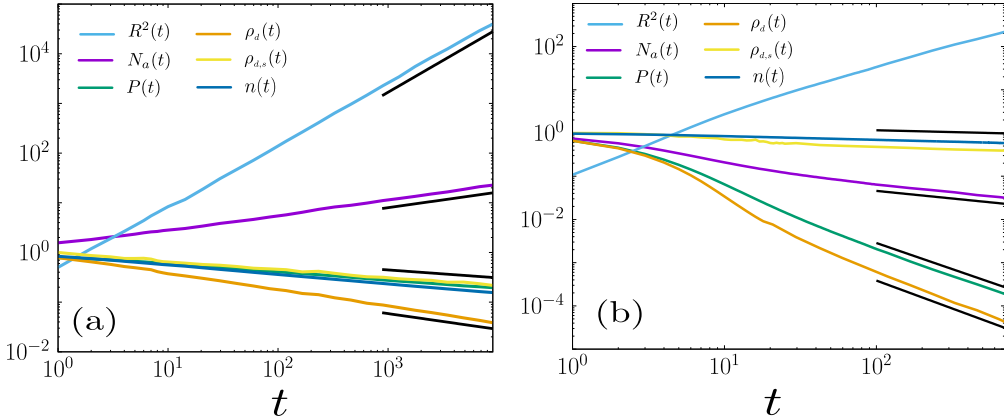
Figure D.3: The behaviors of physical quantities as a function of time t at the transition point. (a) For the classical CP. The solid lines are a guideline with slope $2/z$, η, $-\delta = -\delta' = -\alpha$, $\eta - 1/z$, from top to bottom. The values of all critical exponents are $z = 1.58$, $\delta = 0.16$, $\eta = 0.31$, $\delta' = 0.16$, and $\alpha = 0.16$. Note that $\delta' = \alpha$ and rapidity-reversal symmetry holds. (b) For the $2d$ classical tricritical contact process starting from a single active site. The solid lines are a guideline with slope $2/z$, $-\delta = -\alpha$, η, $-\delta'$, and $\eta - 1/z$ from top to bottom. The values of all critical exponents are $z = 2.11$, $\delta = 0.09$, $\eta = -0.35$, and $\delta' = 1.21$. Note that rapidity-reversal symmetry is broken.
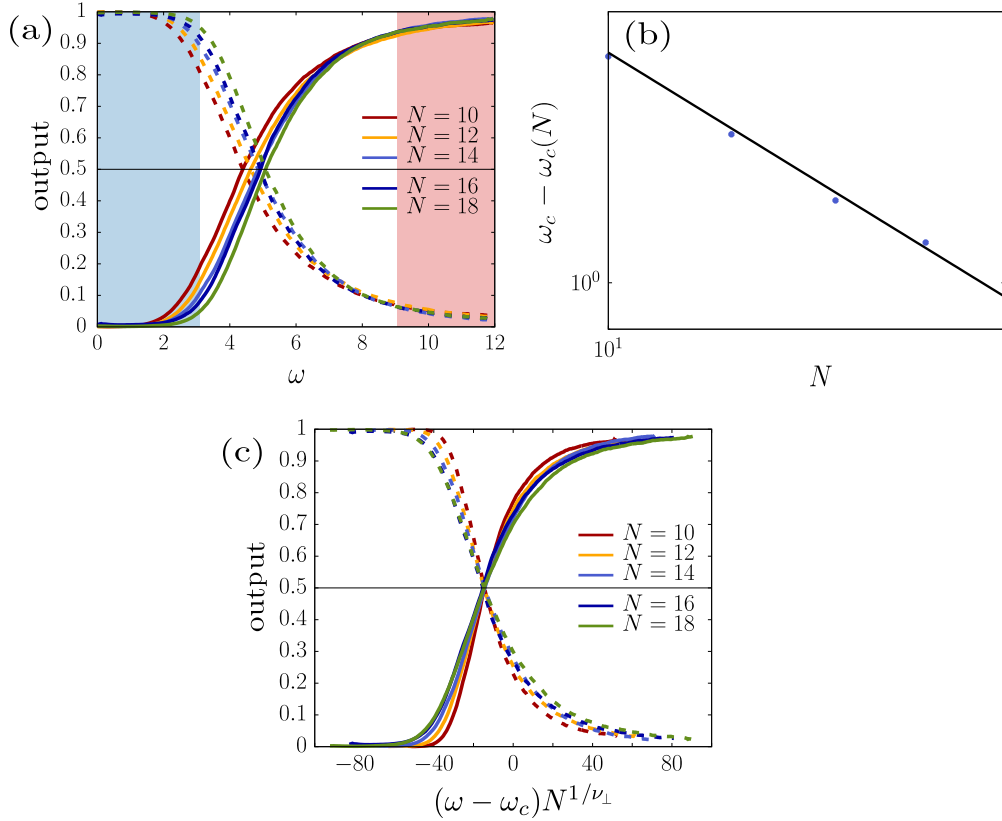
Figure D.4: Plots using the neural network approach. (a) Plot of the output averaged over a test set as a function of ω for different system sizes. The value of the first (second) output neuron is represented as solid (dashed) line. From this plot, we estimate the crossing point of the two outputs and regard it as the transition point $\omega_c(N)$ for a given system size N. The shaded regions $\omega \in [0,3]$ and $\omega \in [9,12]$ indicate the training sets used in the convolutional NN (CNN) analysis. (b) Plot of $\omega_c - \omega_c(N)$ versus N, where ω_c is chosen so as to yield power-law behavior, which is typical near the transition point ω_c. The slope represents the value of the critical exponent $-1/\nu_\perp$. (c) Scaling plot of the output versus $(\omega - \omega_c)N^{1/\nu_\perp}$. For the obtained numerical values of $\nu_\perp$ and ω_c, the data collapse well for system sizes $N = 10, 12, 14, 16,$ and 18. From (b) and (c), we obtain $\omega_c \approx 6.04$ and $\nu_\perp = 1.06 \pm 0.04$. The units of control parameter is given as γ.
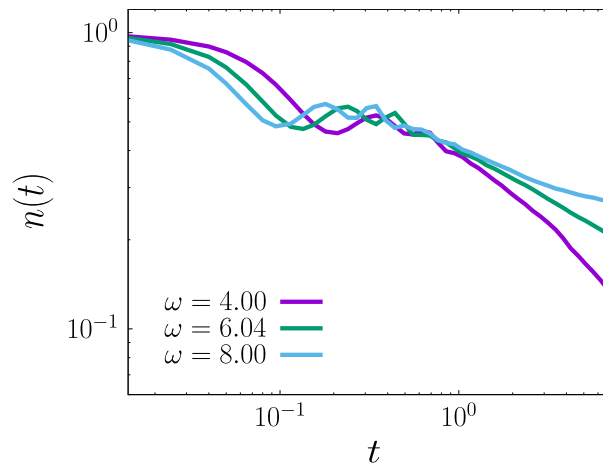
Figure D.5: Plot of $n(t)$ as a function of t for different ω. For $\omega = 4.00$, an exponentially decaying curve is observed. On the other hand, for $\omega = 8.00$, a stationary state converges to a finite density. At the critical point $\omega = 6.04$, it exhibits power-law behavior. System size is taken as $N = 20$.

Appendix E

Appendix of chapter 7

E.1 Fluctuationless mean-field approach for DTI

To explore the MF phase transition, we extract the MF equation from the DQIM, one may explore the equation of motion of observables. The equations of motion of an observable O we employ the conjugate Master equation,

$$\partial_t \hat{O} = i\left[\hat{H}_S, \hat{O}\right] + \sum_{\ell=1}^{N} \left[\hat{L}_\ell^\dagger \hat{O} \hat{L}_\ell - \frac{1}{2}\left\{\hat{L}_\ell^\dagger \hat{L}_\ell, \hat{O}\right\}\right]. \tag{E.1}$$

Ignoring correlations and taking uniform fields, we arrive at the MF equations, which are given by

$$\partial_t \sigma^x = 4J\sigma^y\sigma^z - \Gamma(1+\sigma^x),$$
$$\partial_t \sigma^y = -4J\sigma^x\sigma^z - 2\Delta\sigma^z - \frac{\Gamma}{2}\sigma^y,$$
$$\partial_t \sigma^z = 2\Delta\sigma^y - \frac{\Gamma}{2}\sigma^z. \tag{E.2}$$

Then we find the transition line as follows:

$$\Gamma/J = 4\sqrt{2(\Delta/J) - (\Delta/J)^2},$$
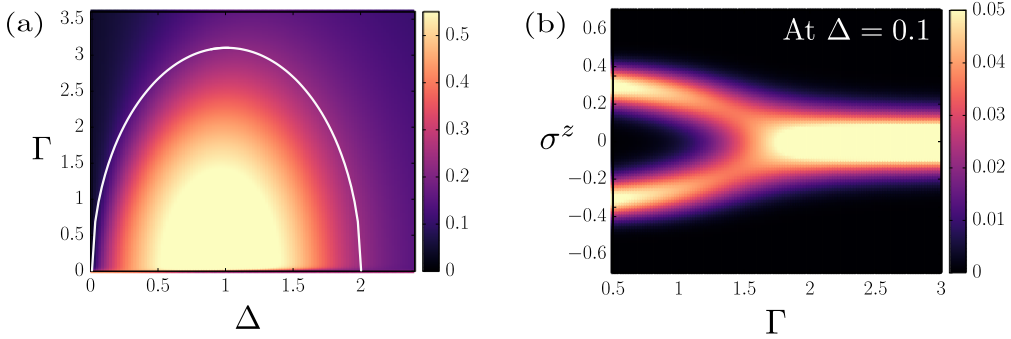
Figure E.1: (a) Phase diagram of the fully-connected DTI in the parameter space (Δ, Γ). Continuous transitions (solid line) occur. (b) Histogram of order parameter in steady states as a function of Γ at $\Delta = 0.1$. Continuous transition occurs with Z_2 symmetry. System size is taken as $N = 128$.

or equivalently

$$J/\Gamma = \frac{1 + 16(\Delta/\Gamma)^2}{32(\Delta/\Gamma)},$$

which corresponds to Fig. 7.1(a) or E.1(a), respectively.

E.2 Phase transition in parameter space (Δ, Γ) at $J = 1$

To verify the mean-field behavior, we use our exact numerical solution approach to DTI model. The phase diagram in the parameter space (Δ, Γ) is shown in Fig. E.1(a), and the order parameter curve at $\Delta = 0.1$ is shown in Fig. E.1(b). It seems to be continuous, and we perform the finite-size scaling for various Δ. When the transition type is continuous, then the critical behavior is shown and the critical exponent can be measured. In Fig. E.2, we perform the finite-size scaling at $\Delta = 0.1$ and obtain the critical exponents $\beta = 0.5$ and $\bar{\nu} = d_c \nu = 1.5$. Thus, we conclude that the transition type of DTI model in all parameter spaces is continuous. Furthermore, we find that the transition type and line are exactly the same as the result of the fluctuationless mean-field approach instead of Keldysh formalism. The universality class belongs to the trans-
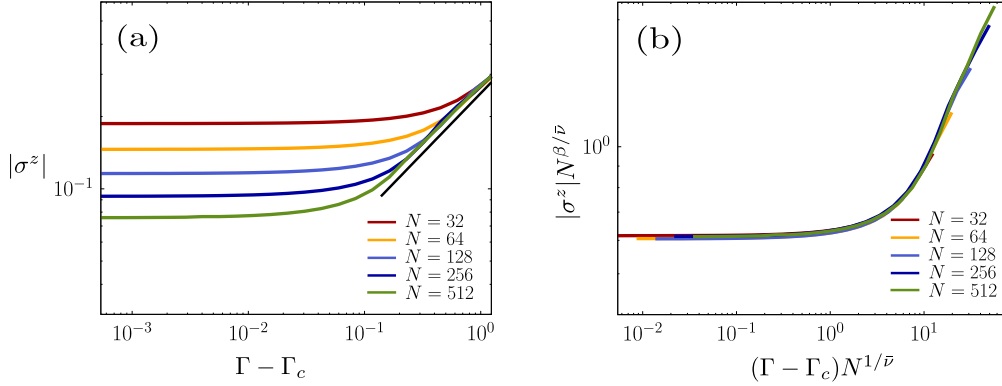
Figure E.2: (a) Plot of $|\sigma^z|$ as a function of $\Gamma - \Gamma_c$ at $\Delta = 0.1$ for different system sizes, which shows that $|\sigma^z| \sim (\Gamma - \Gamma_c)^\beta$ for $\beta = 0.5$. (b) Scaling plot of the rescaled order parameter $|\sigma^z|N^{\beta/\bar{\nu}}$ versus $(\Gamma - \Gamma_c)N^{1/\bar{\nu}}$. The data are well collapsed onto a single curve with $\beta = 0.5$ and $\bar{\nu} = 1.5$.

verse Ising class where $\beta = 0.5$ and $d_c = 3$, which is the results of conserving Z_2 symmetry.

E.3   Fluctuationless mean-field approach for driven-dissipative XY model

The fluctuationless mean-field equations for $\sigma^x(t)$, $\sigma^y(t)$, and $n(t)$ is expressed

$$\partial_t \sigma^x = -2\Delta\sigma^y - 2J\sigma^y\sigma^z - \frac{\Gamma}{2}\sigma^x \tag{E.3}$$

$$\partial_t \sigma^y = 2\Delta\sigma^x - 2\Omega\sigma^z + 2J\sigma^x\sigma^z - \frac{\Gamma}{2}\sigma^y \tag{E.4}$$

$$\partial_t \sigma^z = 2\Omega\sigma^y - \Gamma(1 + \sigma^z). \tag{E.5}$$

For steady state,

$$(\sigma^z + 1)\left(\Gamma^2 + 16(\Delta + J\sigma^z)^2\right) + 8\Omega^2\sigma^z = 0, \tag{E.6}$$

which results in

$$\Omega = \left(\frac{(\sigma^z + 1)\left(\Gamma^2 + 16\Delta^2 + 16J^2(\sigma^z)^2 + 32\Delta J\sigma^z\right)}{-8\sigma^z} \right)^{1/2}. \tag{E.7}$$

This mean-field equation exhibits a discontinuous phase transition for $(J,\Delta)/\Gamma = (4,0.5)$. The full phase diagram of the model is more complex, but it is out of the scope of this paper.

E.4   Fluctuationless mean-field approach for QCP

One can derive fluctuationless mean-field equations for $\sigma^x(t)$, $\sigma^y(t)$, and $n(t)$.

$$\dot{n} = \omega n\sigma^y + (\kappa - 1)n - 2\kappa n^2,$$

$$\dot{\sigma}^x = -\omega\sigma^x\sigma^y - \frac{1+\kappa}{2}\sigma^x - \kappa n\sigma^x,$$

$$\dot{\sigma}^y = \omega\left\{2n + (\sigma^x)^2 - 4n^2\right\} - \frac{1+\kappa}{2}\sigma^y - \kappa n\sigma^y, \tag{E.8}$$

where we rescale time, $t\gamma \to t$, $\omega/\gamma \to \omega$, and $\kappa/\gamma \to \kappa$. Then, the two solutions for each region can be obtained. The first solution becomes

$$\kappa = 1, \omega \leq 1, \tag{E.9}$$

and the second solution is

$$\omega = \left(1 + \kappa - \kappa^2 + \sqrt{(1+\kappa-\kappa^2)^2 - \kappa^4}\right)^{1/2} \text{ at } \kappa \leq 1. \tag{E.10}$$

The first (second) solution is the solid (dashed) line in Fig. 3(a) in the main text.

We remark that the universality class can be obtained using the Martin–Siggia–Rose formalism (See Table S1), which has the same transition lines.

Table E.1: Critical exponents at a tricritical point for the MF-QCP.

	Exact solution	QJMC	TDP[1]	DP
α	0.49 ± 0.02	0.47 ± 0.05	0.50	1.00
z	2.00 ± 0.01	2.00 ± 0.04	2.00	2.00
δ'	1.00 ± 0.02	1.00 ± 0.05	1.00	1.00
η	0.00 ± 0.01	0.00 ± 0.04	0.00	0.00

E.5 Observables of a single initial condition for QCP

First, we consider an initial state in which a single active seed is present at $\ell = 0$, and the remaining sites are inactive. This configuration is expressed as $\hat{\rho}(0) = \hat{\sigma}_0^+ \hat{\rho}_{ab} \hat{\sigma}_0^-$. We measure the following quantities: i) the survival probability, that is, the probability that the system does not fall into an absorbing state, $P(t) = 1 - \text{Tr}[\hat{\rho}(t)\hat{\rho}_{ab}]$; ii) the number of active sites, $N_a(t) = \sum_\ell \text{Tr}[\hat{\rho}(t)\hat{n}_\ell]$; iii) the mean square distance of the active sites from the origin, $R^2(t) = \sum_\ell \text{Tr}[\ell^2 \hat{\rho}(t)\hat{n}_\ell]/N_a(t)$. At the transition point, these quantities exhibit the following power-law behaviors: $P(t) \propto t^{-\delta'}$, $N_a(t) \propto t^\eta$, and $R^2(t) \propto t^{2/z}$, $\rho_d(t) \propto t^{\eta-1/z}$. We estimate the exponents δ', η, and z by direct measurement of the slopes in the double-logarithmic plots, as shown in Fig. 7.4. We estimate the exponent z using the data collapse technique. For instance, for the survival probability $P(t)$, we plot $P(t)t^{\delta'}$ versus tN^{-z} for different system sizes N. We determine z as the value at which the data for different system sizes collapse onto a single curve.

Bibliography

[1] P. W. Anderson, "More is different," *Science*, vol. 177, no. 4047, pp. 393–396, 1972. [Online]. Available: https://science.sciencemag.org/content/177/4047/393

[2] P. Hohenberg and A. Krekhov, "An introduction to the ginzburg–landau theory of phase transitions and nonequilibrium patterns," *Physics Reports*, vol. 572, pp. 1 – 42, 2015, an introduction to the Ginzburg–Landau theory of phase transitions and nonequilibrium patterns. [Online]. Available: http://www.sciencedirect.com/science/article/pii/S0370157315000514

[3] K. G. Wilson and J. Kogut, "The renormalization group and the expansion," *Physics Reports*, vol. 12, no. 2, pp. 75 – 199, 1974. [Online]. Available: http://www.sciencedirect.com/science/article/pii/0370157374900234

[4] M. Suzuki, "Relationship between d-Dimensional Quantal Spin Systems and (d+1)-Dimensional Ising Systems: Equivalence, Critical Exponents and Systematic Approximants of the Partition Function and Spin Correlations," *Progress of Theoretical Physics*, vol. 56, no. 5, pp. 1454–1469, 11 1976. [Online]. Available: https://doi.org/10.1143/PTP.56.1454

[5] L. M. Sieberer, S. D. Huber, E. Altman, and S. Diehl, "Dynamical critical phenomena in driven-dissipative systems," *Phys. Rev. Lett.*, vol. 110, p. 195301, May 2013. [Online]. Available: https://link.aps.org/doi/10.1103/PhysRevLett.110.195301

[6] ——, "Nonequilibrium functional renormalization for driven-dissipative bose-einstein condensation," *Phys. Rev. B*, vol. 89, p. 134310, Apr 2014. [Online]. Available: https://link.aps.org/doi/10.1103/PhysRevB.89.134310

[7] J. Lang and F. Piazza, "Critical relaxation with overdamped quasiparticles in open quantum systems," *Phys. Rev. A*, vol. 94, p. 033628, Sep 2016. [Online]. Available: https://link.aps.org/doi/10.1103/PhysRevA.94.033628

[8] S. Diehl, A. Tomadin, A. Micheli, R. Fazio, and P. Zoller, "Dynamical phase transitions and instabilities in open atomic many-body systems," *Phys. Rev. Lett.*, vol. 105, p. 015702, Jul 2010. [Online]. Available: https://link.aps.org/doi/10.1103/PhysRevLett.105.015702

[9] E. G. Dalla Torre, E. Demler, T. Giamarchi, and E. Altman, "Quantum critical states and phase transitions in the presence of non-equilibrium noise," *Nature Physics*, vol. 6, no. 10, pp. 806–810, Oct 2010. [Online]. Available: https://doi.org/10.1038/nphys1754

[10] ——, "Dynamics and universality in noise-driven dissipative systems," *Phys. Rev. B*, vol. 85, p. 184302, May 2012. [Online]. Available: https://link.aps.org/doi/10.1103/PhysRevB.85.184302

[11] U. C. Täuber and S. Diehl, "Perturbative field-theoretical renormalization group approach to driven-dissipative bose-einstein criticality," *Phys. Rev. X*, vol. 4, p. 021010, Apr 2014. [Online]. Available: https://link.aps.org/doi/10.1103/PhysRevX.4.021010

[12] A. Mitra, S. Takei, Y. B. Kim, and A. J. Millis, "Nonequilibrium quantum criticality in open electronic systems," *Phys. Rev. Lett.*, vol. 97, p. 236808, Dec 2006. [Online]. Available: https://link.aps.org/doi/10.1103/PhysRevLett.97.236808

[13] E. G. D. Torre, S. Diehl, M. D. Lukin, S. Sachdev, and P. Strack, "Keldysh approach for nonequilibrium phase transitions in quantum optics: Beyond the dicke model in optical cavities," *Phys. Rev. A*, vol. 87, p. 023831, Feb 2013. [Online]. Available: https://link.aps.org/doi/10.1103/PhysRevA.87.023831

[14] R. Rota, F. Storme, N. Bartolo, R. Fazio, and C. Ciuti, "Critical behavior of dissipative two-dimensional spin lattices," *Phys. Rev. B*, vol. 95, p. 134431, Apr 2017. [Online]. Available: https://link.aps.org/doi/10.1103/PhysRevB.95.134431

[15] R. Rota, F. Minganti, C. Ciuti, and V. Savona, "Quantum critical regime in a quadratically driven nonlinear photonic lattice," *Phys. Rev. Lett.*, vol. 122, p. 110405, Mar 2019. [Online]. Available: https://link.aps.org/doi/10.1103/PhysRevLett.122.110405

[16] W. Verstraelen, R. Rota, V. Savona, and M. Wouters, "Gaussian trajectory approach to dissipative phase transitions: The case of quadratically driven photonic lattices," *Phys. Rev. Research*, vol. 2, p. 022037, May 2020. [Online]. Available: https://link.aps.org/doi/10.1103/PhysRevResearch.2.022037

[17] J. Marino and S. Diehl, "Driven markovian quantum criticality," *Phys. Rev. Lett.*, vol. 116, p. 070407, Feb 2016. [Online]. Available: https://link.aps.org/doi/10.1103/PhysRevLett.116.070407

[18] E. Domany and W. Kinzel, "Equivalence of cellular automata to ising models and directed percolation," *Phys. Rev. Lett.*, vol. 53, pp. 311–314, Jul 1984. [Online]. Available: https://link.aps.org/doi/10.1103/PhysRevLett.53.311

[19] H. Takayasu and A. Y. Tretyakov, "Extinction, survival, and dynamical phase transition of branching annihilating random walk," *Phys. Rev. Lett.*, vol. 68, pp. 3060–3063, May 1992. [Online]. Available: https://link.aps.org/doi/10.1103/PhysRevLett.68.3060

[20] T. E. Harris, "Contact interactions on a lattice," *Ann. Probab.*, vol. 2, no. 6, pp. 969–988, 12 1974. [Online]. Available: https://doi.org/10.1214/aop/1176996493

[21] M. Saffman, T. G. Walker, and K. Mølmer, "Quantum information with rydberg atoms," *Rev. Mod. Phys.*, vol. 82, pp. 2313–2363, Aug 2010. [Online]. Available: https://link.aps.org/doi/10.1103/RevModPhys.82.2313

[22] B. Olmos, R. González-Férez, and I. Lesanovsky, "Creating collective many-body states with highly excited atoms," *Phys. Rev. A*, vol. 81, p. 023604, Feb 2010. [Online]. Available: https://link.aps.org/doi/10.1103/PhysRevA.81.023604

[23] M. Marcuzzi, E. Levi, W. Li, J. P. Garrahan, B. Olmos, and I. Lesanovsky, "Non-equilibrium universality in the dynamics of dissipative cold atomic gases," *New Journal of Physics*, vol. 17, no. 7, p. 072003, jul 2015. [Online]. Available: https://doi.org/10.1088%2F1367-2630%2F17%2F7%2F072003

[24] R. Gutiérrez, C. Simonelli, M. Archimi, F. Castellucci, E. Arimondo, D. Ciampini, M. Marcuzzi, I. Lesanovsky, and O. Morsch, "Experimental signatures of an absorbing-state phase transition in an open driven many-body quantum system," *Phys. Rev. A*, vol. 96, p. 041602(R), Oct 2017. [Online]. Available: https://link.aps.org/doi/10.1103/PhysRevA.96.041602

[25] M. Marcuzzi, M. Buchhold, S. Diehl, and I. Lesanovsky, "Absorbing state phase transition with competing quantum and classical fluctuations," *Phys. Rev. Lett.*, vol. 116, p. 245701, Jun 2016. [Online]. Available: https://link.aps.org/doi/10.1103/PhysRevLett.116.245701

[26] M. Buchhold, B. Everest, M. Marcuzzi, I. Lesanovsky, and S. Diehl, "Nonequilibrium effective field theory for absorbing state phase transitions in driven open quantum spin systems," *Phys. Rev. B*, vol. 95, p. 014308, Jan 2017. [Online]. Available: https://link.aps.org/doi/10.1103/PhysRevB.95.014308

[27] H.-P. Breuer, F. Petruccione *et al.*, *The theory of open quantum systems*. Oxford University Press on Demand, 2002.

[28] H. Hinrichsen, "Non-equilibrium critical phenomena and phase transitions into absorbing states," *Advances in Physics*, vol. 49, no. 7, pp. 815–958, 2000. [Online]. Available: https://doi.org/10.1080/00018730050198152

[29] M. Henkel, H. Hinrichsen, S. Lübeck, and M. Pleimling, *Non-equilibrium phase transitions*. Springer, 2008, vol. 1.

[30] A. Altland and B. D. Simons, *Condensed Matter Field Theory*, 2nd ed. Cambridge University Press, 2010.

[31] M. Jo, J. Um, and B. Kahng, "Nonequilibrium phase transition in an open quantum spin system with long-range interaction," *Phys. Rev. E*, vol. 99, p. 032131, Mar 2019. [Online]. Available: https://link.aps.org/doi/10.1103/PhysRevE.99.032131

[32] M. Jo and B. Kahng, "Tricritical directed percolation with long-range interaction in one and two dimensions," *Phys. Rev. E*, vol. 101, p. 022121, Feb 2020. [Online]. Available: https://link.aps.org/doi/10.1103/PhysRevE.101.022121

[33] M. B. Plenio and P. L. Knight, "The quantum-jump approach to dissipative dynamics in quantum optics," *Rev. Mod. Phys.*, vol. 70, pp. 101–144, Jan 1998. [Online]. Available: https://link.aps.org/doi/10.1103/RevModPhys.70.101

[34] G. Vidal, "Efficient classical simulation of slightly entangled quantum computations," *Phys. Rev. Lett.*, vol. 91, p. 147902, Oct 2003. [Online]. Available: https://link.aps.org/doi/10.1103/PhysRevLett.91.147902

[35] F. Verstraete, J. J. García-Ripoll, and J. I. Cirac, "Matrix product density operators: Simulation of finite-temperature and dissipative systems," *Phys. Rev. Lett.*, vol. 93, p. 207204, Nov 2004. [Online]. Available: https://link.aps.org/doi/10.1103/PhysRevLett.93.207204

[36] M. Jo, J. Lee, K. Choi, and B. Kahng, "Anomalous crossover from a quantum to a classical DP transition," *arXiv e-prints*, p. arXiv:2004.02672, Apr. 2020.

[37] M. Jo, B. Jhun, and B. Kahng, "Phase transitions in the infinite dimensional dissipative quantum systems," *in preparation*.

[38] J. Marro and R. Dickman, *Nonequilibrium phase transitions in lattice models*. Cambridge University Press, 2005.

[39] W. Kinzel, "Phase transitions of cellular automata," *Zeitschrift für Physik B Condensed Matter*, vol. 58, no. 3, pp. 229–244, Sep 1985. [Online]. Available: https://doi.org/10.1007/BF01309255

[40] R. M. Ziff, E. Gulari, and Y. Barshad, "Kinetic phase transitions in an irreversible surface-reaction model," *Phys. Rev. Lett.*, vol. 56, pp. 2553–2556, Jun 1986. [Online]. Available: https://link.aps.org/doi/10.1103/PhysRevLett.56.2553

[41] R. Dickman and I. Jensen, "Time-dependent perturbation theory for nonequilibrium lattice models," *Phys. Rev. Lett.*, vol. 67, pp. 2391–2394, Oct 1991. [Online]. Available: https://link.aps.org/doi/10.1103/PhysRevLett.67.2391

[42] P. Grassberger and K. Sundermeyer, "Reggeon field theory and markov processes," *Physics Letters B*, vol. 77, no. 2, pp. 220 – 222, 1978. [Online]. Available: http://www.sciencedirect.com/science/article/pii/0370269378906263

[43] S. Obukhov, "The problem of directed percolation," *Physica A: Statistical Mechanics and its Applications*, vol. 101, no. 1, pp. 145 – 155, 1980. [Online]. Available: http://www.sciencedirect.com/science/article/pii/0378437180901053

[44] J. L. Cardy and R. L. Sugar, "Directed percolation and reggeon field theory," *Journal of Physics A: Mathematical and General*, vol. 13, no. 12, pp. L423–L427, dec 1980. [Online]. Available: https://doi.org/10.1088/0305-4470/13/12/002

[45] G. Ódor, "Universality classes in nonequilibrium lattice systems," *Rev. Mod. Phys.*, vol. 76, pp. 663–724, Aug 2004. [Online]. Available: https://link.aps.org/doi/10.1103/RevModPhys.76.663

[46] M. Sano and K. Tamai, "A universal transition to turbulence in channel flow," *Nature Physics*, vol. 12, no. 3, pp. 249–253, Mar 2016. [Online]. Available: https://doi.org/10.1038/nphys3659

[47] P. Grassberger, "On phase transitions in schlögl's second model," *Zeitschrift für Physik B Condensed Matter*, vol. 47, no. 4, pp. 365–374, Dec 1982. [Online]. Available: https://doi.org/10.1007/BF01313803

[48] H. K. Janssen, "On the nonequilibrium phase transition in reaction-diffusion systems with an absorbing stationary state," *Zeitschrift für Physik B Condensed Matter*, vol. 42, no. 2, pp. 151–154, Jun 1981. [Online]. Available: https://doi.org/10.1007/BF01319549

[49] H. Hinrichsen and M. Howard, "A model for anomalous directed percolation," *The European Physical Journal B - Condensed Matter and Complex Systems*, vol. 7, no. 4, pp. 635–643, Feb 1999. [Online]. Available: https://doi.org/10.1007/s100510050656

[50] H. Hinrichsen, "Non-equilibrium phase transitions with long-range interactions," *Journal of Statistical Mechanics: Theory and Experiment*, vol. 2007, no. 07, pp. P07006–P07006, jul 2007. [Online]. Available: https://doi.org/10.1088/1742-5468/2007/07/p07006

[51] H.-K. Janssen and O. Stenull, "Field theory of directed percolation with long-range spreading," *Phys. Rev. E*, vol. 78, p. 061117, Dec 2008. [Online]. Available: https://link.aps.org/doi/10.1103/PhysRevE.78.061117

[52] H. K. Janssen, "Influence of long-range interactions on the critical behavior of systems with a negative fisher exponent," *Phys. Rev. E*, vol. 58, pp. R2673–R2676, Sep 1998. [Online]. Available: https://link.aps.org/doi/10.1103/PhysRevE.58.R2673

[53] T. Ohtsuki and T. Keyes, "Nonequilibrium critical phenomena in one-component reaction-diffusion systems," *Phys. Rev. A*, vol. 35, pp. 2697–2703, Mar 1987. [Online]. Available: https://link.aps.org/doi/10.1103/PhysRevA.35.2697

[54] P. Grassberger, "Tricritical directed percolation in 2+1 dimensions," *Journal of Statistical Mechanics: Theory and Experiment*, vol. 2006, no. 01, pp. P01 004–P01 004, jan 2006. [Online]. Available: https://doi.org/10.1088%2F1742-5468%2F2006%2F01%2Fp01004

[55] S. Lübeck, "Tricritical directed percolation," *Journal of Statistical Physics*, vol. 123, no. 1, pp. 193–221, 2006.

[56] A. Windus and H. J. Jensen, "Phase transitions in a lattice population model," *Journal of Physics A: Mathematical and Theoretical*, vol. 40, no. 10, pp. 2287–2297, feb 2007. [Online]. Available: https://doi.org/10.1088/1751-8113/40/10/005

[57] ——, "Cluster geometry and survival probability in systems driven by reaction–diffusion dynamics," *New Journal of Physics*, vol. 10, no. 11, p. 113023, nov 2008. [Online]. Available: https://doi.org/10.1088/1367-2630/10/11/113023

[58] C. Ates, T. Pohl, T. Pattard, and J. M. Rost, "Antiblockade in rydberg excitation of an ultracold lattice gas," *Phys. Rev. Lett.*, vol. 98, p. 023002, Jan 2007. [Online]. Available: https://link.aps.org/doi/10.1103/PhysRevLett.98.023002

[59] T. Amthor, C. Giese, C. S. Hofmann, and M. Weidemüller, "Evidence of antiblockade in an ultracold rydberg gas," *Phys. Rev. Lett.*, vol. 104, p. 013001, Jan 2010. [Online]. Available: https://link.aps.org/doi/10.1103/PhysRevLett.104.013001

[60] A. de Paz, A. Sharma, A. Chotia, E. Maréchal, J. H. Huckans, P. Pedri, L. Santos, O. Gorceix, L. Vernac, and B. Laburthe-Tolra, "Nonequilibrium quantum magnetism in a dipolar lattice gas," *Phys. Rev. Lett.*, vol. 111, p. 185305, Oct 2013. [Online]. Available: https://link.aps.org/doi/10.1103/PhysRevLett.111.185305

[61] B. Yan, S. A. Moses, B. Gadway, J. P. Covey, K. R. A. Hazzard, A. M. Rey, D. S. Jin, and J. Ye, "Observation of dipolar spin-exchange interactions with lattice-confined polar molecules," *Nature*, vol. 501, no. 7468, pp. 521–525, Sep 2013. [Online]. Available: https://doi.org/10.1038/nature12483

[62] K. R. A. Hazzard, S. R. Manmana, M. Foss-Feig, and A. M. Rey, "Far-from-equilibrium quantum magnetism with ultracold polar molecules," *Phys. Rev. Lett.*, vol. 110, p. 075301, Feb 2013. [Online]. Available: https://link.aps.org/doi/10.1103/PhysRevLett.110.075301

[63] X. Deng, B. L. Altshuler, G. V. Shlyapnikov, and L. Santos, "Quantum levy flights and multifractality of dipolar excitations in a random system," *Phys. Rev. Lett.*, vol. 117, p. 020401, Jul 2016. [Online]. Available: https://link.aps.org/doi/10.1103/PhysRevLett.117.020401

[64] I. L. Aleiner, B. L. Altshuler, and K. B. Efetov, "Localization and critical diffusion of quantum dipoles in two dimensions," *Phys. Rev. Lett.*, vol. 107,

p. 076401, Aug 2011. [Online]. Available: https://link.aps.org/doi/10.1103/PhysRevLett.107.076401

[65] G. A. Álvarez, D. Suter, and R. Kaiser, "Localization-delocalization transition in the dynamics of dipolar-coupled nuclear spins," *Science*, vol. 349, no. 6250, pp. 846–848, 2015. [Online]. Available: https://science.sciencemag.org/content/349/6250/846

[66] G. Günter, H. Schempp, M. Robert-de Saint-Vincent, V. Gavryusev, S. Helmrich, C. S. Hofmann, S. Whitlock, and M. Weidemüller, "Observing the dynamics of dipole-mediated energy transport by interaction-enhanced imaging," *Science*, vol. 342, no. 6161, pp. 954–956, 2013. [Online]. Available: https://science.sciencemag.org/content/342/6161/954

[67] E. Urban, T. A. Johnson, T. Henage, L. Isenhower, D. D. Yavuz, T. G. Walker, and M. Saffman, "Observation of rydberg blockade between two atoms," *Nature Physics*, vol. 5, no. 2, pp. 110–114, Feb 2009. [Online]. Available: https://doi.org/10.1038/nphys1178

[68] M. O. Scully and M. S. Zubairy, *Quantum Optics*. Cambridge University Press, 1997.

[69] P. C. Martin, E. D. Siggia, and H. A. Rose, "Statistical dynamics of classical systems," *Phys. Rev. A*, vol. 8, pp. 423–437, Jul 1973. [Online]. Available: https://link.aps.org/doi/10.1103/PhysRevA.8.423

[70] H.-K. Janssen, "On a lagrangean for classical field dynamics and renormalization group calculations of dynamical critical properties," *Zeitschrift für Physik B Condensed Matter*, vol. 23, no. 4, pp. 377–380, Dec 1976. [Online]. Available: https://doi.org/10.1007/BF01316547

[71] DE DOMINICIS, C., "Techniques de renormalisation de la théorie des champs et dynamique des phénomènes critiques," *J. Phys. Colloques*,

vol. 37, no. C1, pp. C1–247–C1–253, 1976. [Online]. Available: https://doi.org/10.1051/jphyscol:1976138

[72] W. H. Louisell and W. H. Louisell, *Quantum statistical properties of radiation*. Wiley New York, 1973, vol. 7.

[73] D. Banerjee, B. C. Bag, S. K. Banik, and D. S. Ray, "Solution of quantum langevin equation: Approximations, theoretical and numerical aspects," *The Journal of Chemical Physics*, vol. 120, no. 19, pp. 8960–8972, 2004. [Online]. Available: https://doi.org/10.1063/1.1711593

[74] E. W. MONTROLL and B. J. WEST, "Chapter 2 - on an enriched collection of stochastic processes**this work was partially supported by the fluid dynamics branch of the office of naval research." in *Fluctuation Phenomena*, E. MONTROLL and J. LEBOWITZ, Eds. Elsevier, 1979, pp. 61 – 175. [Online]. Available: http://www.sciencedirect.com/science/article/pii/B9780444852489500054

[75] C. Pérez-Espigares, M. Marcuzzi, R. Gutiérrez, and I. Lesanovsky, "Epidemic dynamics in open quantum spin systems," *Phys. Rev. Lett.*, vol. 119, p. 140401, Oct 2017. [Online]. Available: https://link.aps.org/doi/10.1103/PhysRevLett.119.140401

[76] B. Jhun, M. Jo, and B. Kahng, "Quantum contact process in scale-free networks," *in preparation*.

[77] T. Ohtsuki and T. Keyes, "Crossover in nonequilibrium multicritical phenomena of reaction-diffusion systems," *Phys. Rev. A*, vol. 36, pp. 4434–4438, Nov 1987. [Online]. Available: https://link.aps.org/doi/10.1103/PhysRevA.36.4434

[78] H.-K. Janssen, "Survival and percolation probabilities in the field theory of growth models," *Journal of Physics: Condensed Matter*, vol. 17, no. 20,

pp. S1973–S1993, may 2005. [Online]. Available: https://doi.org/10.1088/0953-8984/17/20/021

[79] H. Hinrichsen, "First-order transitions in fluctuating 1+1-dimensional nonequilibrium systems," *arXiv e-prints*, pp. cond–mat/0 006 212, Jun. 2000.

[80] M. E. Fisher, S.-k. Ma, and B. G. Nickel, "Critical exponents for long-range interactions," *Phys. Rev. Lett.*, vol. 29, pp. 917–920, Oct 1972. [Online]. Available: https://link.aps.org/doi/10.1103/PhysRevLett.29.917

[81] J. Sak, "Recursion relations and fixed points for ferromagnets with long-range interactions," *Phys. Rev. B*, vol. 8, pp. 281–285, Jul 1973. [Online]. Available: https://link.aps.org/doi/10.1103/PhysRevB.8.281

[82] E. Luijten and H. Meßingfeld, "Criticality in one dimension with inverse square-law potentials," *Phys. Rev. Lett.*, vol. 86, pp. 5305–5308, Jun 2001. [Online]. Available: https://link.aps.org/doi/10.1103/PhysRevLett.86.5305

[83] J. Sak, "Low-temperature renormalization group for ferromagnets with long-range interactions," *Phys. Rev. B*, vol. 15, pp. 4344–4347, May 1977. [Online]. Available: https://link.aps.org/doi/10.1103/PhysRevB.15.4344

[84] Y. Yamazaki, "Critical exponent η of isotropic spin systems with long and short-range interactions," *Physics Letters A*, vol. 61, no. 4, pp. 207 – 210, 1977. [Online]. Available: http://www.sciencedirect.com/science/article/pii/0375960177901396

[85] T. Horita, H. Suwa, and S. Todo, "Upper and lower critical decay exponents of ising ferromagnets with long-range interaction," *Phys. Rev. E*, vol. 95, p. 012143, Jan 2017. [Online]. Available: https://link.aps.org/doi/10.1103/PhysRevE.95.012143

[86] H. K. Janssen, K. Oerding, F. van Wijland, and H. J. Hilhorst, "Lévy-flight spreading of epidemic processes leading to percolating clusters," *The European Physical Journal B - Condensed Matter and Complex Systems*, vol. 7, no. 1, pp. 137–145, Jan 1999. [Online]. Available: https://doi.org/10.1007/s100510050596

[87] C. Bezuidenhout and G. Grimmett, "The critical contact process dies out," *Ann. Probab.*, vol. 18, no. 4, pp. 1462–1482, 10 1990. [Online]. Available: https://doi.org/10.1214/aop/1176990627

[88] R. S. Sander, G. S. Costa, and S. C. Ferreira, "Sampling methods for the quasistationary regime of epidemic processes on regular and complex networks," *Phys. Rev. E*, vol. 94, p. 042308, Oct 2016. [Online]. Available: https://link.aps.org/doi/10.1103/PhysRevE.94.042308

[89] U. C. Täuber, *Critical dynamics: a field theory approach to equilibrium and non-equilibrium scaling behavior*. Cambridge University Press, 2014.

[90] A. Kamenev, *Field theory of non-equilibrium systems*. Cambridge University Press, 2011.

[91] B. J. Brosilow and R. M. Ziff, "Effects of a desorption on the first-order transition in the a-b_2 reaction model," *Phys. Rev. A*, vol. 46, pp. 4534–4538, Oct 1992. [Online]. Available: https://link.aps.org/doi/10.1103/PhysRevA.46.4534

[92] F. Carollo, E. Gillman, H. Weimer, and I. Lesanovsky, "Critical behavior of the quantum contact process in one dimension," *Phys. Rev. Lett.*, vol. 123, p. 100604, Sep 2019. [Online]. Available: https://link.aps.org/doi/10.1103/PhysRevLett.123.100604

[93] E. Gillman, F. Carollo, and I. Lesanovsky, "Numerical simulation of critical dissipative non-equilibrium quantum systems with an absorbing state," *New*

Journal of Physics, vol. 21, no. 9, p. 093064, sep 2019. [Online]. Available: https://doi.org/10.1088%2F1367-2630%2Fab43b0

[94] D. Roscher, S. Diehl, and M. Buchhold, "Phenomenology of first-order dark-state phase transitions," *Phys. Rev. A*, vol. 98, p. 062117, Dec 2018. [Online]. Available: https://link.aps.org/doi/10.1103/PhysRevA.98.062117

[95] I. Iacopini, G. Petri, A. Barrat, and V. Latora, "Simplicial models of social contagion," *Nature Communications*, vol. 10, no. 1, p. 2485, Jun 2019. [Online]. Available: https://doi.org/10.1038/s41467-019-10431-6

[96] B. Jhun, M. Jo, and B. Kahng, "Simplicial SIS model in scale-free uniform hypergraph," *Journal of Statistical Mechanics: Theory and Experiment*, vol. 2019, no. 12, p. 123207, dec 2019. [Online]. Available: https://doi.org/10.1088/1742-5468/ab5367

[97] D. Lee, M. Jo, and B. Kahng, "Critical behavior of *k*-core percolation: Numerical studies," *Phys. Rev. E*, vol. 94, p. 062307, Dec 2016. [Online]. Available: https://link.aps.org/doi/10.1103/PhysRevE.94.062307

[98] N. Araújo, P. Grassberger, B. Kahng, K. J. Schrenk, and R. M. Ziff, "Recent advances and open challenges in percolation," *The European Physical Journal Special Topics*, vol. 223, no. 11, pp. 2307–2321, Oct 2014. [Online]. Available: https://doi.org/10.1140/epjst/e2014-02266-y

[99] T. Blanchard, M. Picco, and M. A. Rajabpour, "Influence of long-range interactions on the critical behavior of the ising model," *EPL (Europhysics Letters)*, vol. 101, no. 5, p. 56003, mar 2013. [Online]. Available: https://doi.org/10.1209/0295-5075/101/56003

[100] M. Picco, "Critical behavior of the Ising model with long range interactions," *arXiv e-prints*, p. arXiv:1207.1018, Jul. 2012.

[101] P. Grassberger, "Two-dimensional sir epidemics with long range infection," *Journal of Statistical Physics*, vol. 153, no. 2, pp. 289–311, Oct 2013. [Online]. Available: https://doi.org/10.1007/s10955-013-0824-7

[102] M. B. Plenio and P. L. Knight, "The quantum-jump approach to dissipative dynamics in quantum optics," *Rev. Mod. Phys.*, vol. 70, pp. 101–144, Jan 1998. [Online]. Available: https://link.aps.org/doi/10.1103/RevModPhys.70.101

[103] A. J. Daley, "Quantum trajectories and open many-body quantum systems," *Advances in Physics*, vol. 63, no. 2, pp. 77–149, 2014. [Online]. Available: https://doi.org/10.1080/00018732.2014.933502

[104] U. Schollwöck, "The density-matrix renormalization group in the age of matrix product states," *Annals of Physics*, vol. 326, no. 1, pp. 96 – 192, 2011, january 2011 Special Issue. [Online]. Available: http://www.sciencedirect.com/science/article/pii/S0003491610001752

[105] I. Carusotto and C. Ciuti, "Quantum fluids of light," *Rev. Mod. Phys.*, vol. 85, pp. 299–366, Feb 2013. [Online]. Available: https://link.aps.org/doi/10.1103/RevModPhys.85.299

[106] C. Noh and D. G. Angelakis, "Quantum simulations and many-body physics with light," *Reports on Progress in Physics*, vol. 80, no. 1, p. 016401, nov 2016. [Online]. Available: https://doi.org/10.1088%2F0034-4885%2F80%2F1%2F016401

[107] H. J. Carmichael, "Breakdown of photon blockade: A dissipative quantum phase transition in zero dimensions," *Phys. Rev. X*, vol. 5, p. 031028, Sep 2015. [Online]. Available: https://link.aps.org/doi/10.1103/PhysRevX.5.031028

[108] M. Müller, S. Diehl, G. Pupillo, and P. Zoller, "Engineered open systems and quantum simulations with atoms and ions," in *Advances in Atomic, Molecular, and Optical Physics*. Elsevier, 2012, vol. 61, pp. 1–80.

[109] K. Baumann, C. Guerlin, F. Brennecke, and T. Esslinger, "Dicke quantum phase transition with a superfluid gas in an optical cavity," *Nature*, vol. 464, no. 7293, pp. 1301–1306, Apr 2010. [Online]. Available: https://doi.org/10.1038/nature09009

[110] K. Baumann, R. Mottl, F. Brennecke, and T. Esslinger, "Exploring symmetry breaking at the dicke quantum phase transition," *Phys. Rev. Lett.*, vol. 107, p. 140402, Sep 2011. [Online]. Available: https://link.aps.org/doi/10.1103/PhysRevLett.107.140402

[111] I. Bloch, "Ultracold quantum gases in optical lattices," *Nature Physics*, vol. 1, no. 1, pp. 23–30, Oct 2005. [Online]. Available: https://doi.org/10.1038/nphys138

[112] J. M. Fink, A. Dombi, A. Vukics, A. Wallraff, and P. Domokos, "Observation of the photon-blockade breakdown phase transition," *Phys. Rev. X*, vol. 7, p. 011012, Jan 2017. [Online]. Available: https://link.aps.org/doi/10.1103/PhysRevX.7.011012

[113] T. Fink, A. Schade, S. Höfling, C. Schneider, and A. Imamoglu, "Signatures of a dissipative phase transition in photon correlation measurements," *Nature Physics*, vol. 14, no. 4, pp. 365–369, Apr 2018. [Online]. Available: https://doi.org/10.1038/s41567-017-0020-9

[114] M. Fitzpatrick, N. M. Sundaresan, A. C. Y. Li, J. Koch, and A. A. Houck, "Observation of a dissipative phase transition in a one-dimensional circuit qed lattice," *Phys. Rev. X*, vol. 7, p. 011016, Feb 2017. [Online]. Available: https://link.aps.org/doi/10.1103/PhysRevX.7.011016

[115] S. Helmrich, A. Arias, G. Lochead, T. M. Wintermantel, M. Buchhold, S. Diehl, and S. Whitlock, "Signatures of self-organized criticality in an ultracold atomic

gas," *Nature*, vol. 577, no. 7791, pp. 481–486, Jan 2020. [Online]. Available: https://doi.org/10.1038/s41586-019-1908-6

[116] T. E. Lee, S. Gopalakrishnan, and M. D. Lukin, "Unconventional magnetism via optical pumping of interacting spin systems," *Phys. Rev. Lett.*, vol. 110, p. 257204, Jun 2013. [Online]. Available: https://link.aps.org/doi/10.1103/PhysRevLett.110.257204

[117] J. Jin, A. Biella, O. Viyuela, L. Mazza, J. Keeling, R. Fazio, and D. Rossini, "Cluster mean-field approach to the steady-state phase diagram of dissipative spin systems," *Phys. Rev. X*, vol. 6, p. 031011, Jul 2016. [Online]. Available: https://link.aps.org/doi/10.1103/PhysRevX.6.031011

[118] A. Le Boité, G. Orso, and C. Ciuti, "Steady-state phases and tunneling-induced instabilities in the driven dissipative bose-hubbard model," *Phys. Rev. Lett.*, vol. 110, p. 233601, Jun 2013. [Online]. Available: https://link.aps.org/doi/10.1103/PhysRevLett.110.233601

[119] J. Klinder, H. Keßler, M. Wolke, L. Mathey, and A. Hemmerich, "Dynamical phase transition in the open dicke model," *Proceedings of the National Academy of Sciences*, vol. 112, no. 11, pp. 3290–3295, 2015. [Online]. Available: https://www.pnas.org/content/112/11/3290

[120] L. J. Zou, D. Marcos, S. Diehl, S. Putz, J. Schmiedmayer, J. Majer, and P. Rabl, "Implementation of the dicke lattice model in hybrid quantum system arrays," *Phys. Rev. Lett.*, vol. 113, p. 023603, Jul 2014. [Online]. Available: https://link.aps.org/doi/10.1103/PhysRevLett.113.023603

[121] D. Nagy and P. Domokos, "Nonequilibrium quantum criticality and non-markovian environment: Critical exponent of a quantum phase transition," *Phys. Rev. Lett.*, vol. 115, p. 043601, Jul 2015. [Online]. Available: https://link.aps.org/doi/10.1103/PhysRevLett.115.043601

[122] A. A. Houck, H. E. Türeci, and J. Koch, "On-chip quantum simulation with superconducting circuits," *Nature Physics*, vol. 8, no. 4, pp. 292–299, Apr 2012. [Online]. Available: https://doi.org/10.1038/nphys2251

[123] E. Gillman, F. Carollo, and I. Lesanovsky, "Nonequilibrium phase transitions in $(1+1)$-dimensional quantum cellular automata with controllable quantum correlations," *Phys. Rev. Lett.*, vol. 125, p. 100403, Sep 2020. [Online]. Available: https://link.aps.org/doi/10.1103/PhysRevLett.125.100403

[124] E. Gillman, F. Carollo, and I. Lesanovsky, "Numerical Simulation of Critical Quantum Dynamics without Finite Size Effects," *arXiv e-prints*, p. arXiv:2010.10954, Oct. 2020.

[125] A. Caldeira and A. Leggett, "Quantum tunnelling in a dissipative system," *Annals of Physics*, vol. 149, no. 2, pp. 374 – 456, 1983. [Online]. Available: http://www.sciencedirect.com/science/article/pii/0003491683902026

[126] S. Chakravarty, "Quantum fluctuations in the tunneling between superconductors," *Phys. Rev. Lett.*, vol. 49, pp. 681–684, Aug 1982. [Online]. Available: https://link.aps.org/doi/10.1103/PhysRevLett.49.681

[127] J. Carrasquilla and R. G. Melko, "Machine learning phases of matter," *Nature Physics*, vol. 13, no. 5, pp. 431–434, May 2017. [Online]. Available: https://doi.org/10.1038/nphys4035

[128] D. Kim and D.-H. Kim, "Smallest neural network to learn the ising criticality," *Phys. Rev. E*, vol. 98, p. 022138, Aug 2018. [Online]. Available: https://link.aps.org/doi/10.1103/PhysRevE.98.022138

[129] W. Zhang, J. Liu, and T.-C. Wei, "Machine learning of phase transitions in the percolation and *xy* models," *Phys. Rev. E*, vol. 99, p. 032142, Mar 2019. [Online]. Available: https://link.aps.org/doi/10.1103/PhysRevE.99.032142

[130] Y. LeCun, Y. Bengio, and G. Hinton, "Deep learning," *Nature*, vol. 521, no. 7553, pp. 436–444, May 2015. [Online]. Available: https://doi.org/10.1038/nature14539

[131] G. Carleo, I. Cirac, K. Cranmer, L. Daudet, M. Schuld, N. Tishby, L. Vogt-Maranto, and L. Zdeborová, "Machine learning and the physical sciences," *Rev. Mod. Phys.*, vol. 91, p. 045002, Dec 2019. [Online]. Available: https://link.aps.org/doi/10.1103/RevModPhys.91.045002

[132] P. Broecker, J. Carrasquilla, R. G. Melko, and S. Trebst, "Machine learning quantum phases of matter beyond the fermion sign problem," *Scientific Reports*, vol. 7, no. 1, p. 8823, Aug 2017. [Online]. Available: https://doi.org/10.1038/s41598-017-09098-0

[133] J. Venderley, V. Khemani, and E.-A. Kim, "Machine learning out-of-equilibrium phases of matter," *Phys. Rev. Lett.*, vol. 120, p. 257204, Jun 2018. [Online]. Available: https://link.aps.org/doi/10.1103/PhysRevLett.120.257204

[134] A. Canabarro, F. F. Fanchini, A. L. Malvezzi, R. Pereira, and R. Chaves, "Unveiling phase transitions with machine learning," *Phys. Rev. B*, vol. 100, p. 045129, Jul 2019. [Online]. Available: https://link.aps.org/doi/10.1103/PhysRevB.100.045129

[135] B. S. Rem, N. Käming, M. Tarnowski, L. Asteria, N. Fläschner, C. Becker, K. Sengstock, and C. Weitenberg, "Identifying quantum phase transitions using artificial neural networks on experimental data," *Nature Physics*, vol. 15, no. 9, pp. 917–920, Sep 2019. [Online]. Available: https://doi.org/10.1038/s41567-019-0554-0

[136] A. Bohrdt, C. S. Chiu, G. Ji, M. Xu, D. Greif, M. Greiner, E. Demler, F. Grusdt, and M. Knap, "Classifying snapshots of the doped hubbard model

with machine learning," *Nature Physics*, vol. 15, no. 9, pp. 921–924, Sep 2019. [Online]. Available: https://doi.org/10.1038/s41567-019-0565-x

[137] M. Schuld, I. Sinayskiy, and F. Petruccione, "Neural networks take on open quantum systems," *Physics*, vol. 12, p. 74, 2019.

[138] N. Yoshioka and R. Hamazaki, "Constructing neural stationary states for open quantum many-body systems," *Phys. Rev. B*, vol. 99, p. 214306, Jun 2019. [Online]. Available: https://link.aps.org/doi/10.1103/PhysRevB.99.214306

[139] M. J. Hartmann and G. Carleo, "Neural-network approach to dissipative quantum many-body dynamics," *Phys. Rev. Lett.*, vol. 122, p. 250502, Jun 2019. [Online]. Available: https://link.aps.org/doi/10.1103/PhysRevLett.122.250502

[140] A. Nagy and V. Savona, "Variational quantum monte carlo method with a neural-network ansatz for open quantum systems," *Phys. Rev. Lett.*, vol. 122, p. 250501, Jun 2019. [Online]. Available: https://link.aps.org/doi/10.1103/PhysRevLett.122.250501

[141] F. Vicentini, A. Biella, N. Regnault, and C. Ciuti, "Variational neural-network ansatz for steady states in open quantum systems," *Phys. Rev. Lett.*, vol. 122, p. 250503, Jun 2019. [Online]. Available: https://link.aps.org/doi/10.1103/PhysRevLett.122.250503

[142] D. M. Harris and S. L. Harris, "Introductory digital design & computer architecture curriculum," in *2013 IEEE International Conference on Microelectronic Systems Education, MSE 2013, Austin, TX, USA, June 2-3, 2013*. IEEE Computer Society, 2013, pp. 14–16. [Online]. Available: https://doi.org/10.1109/MSE.2013.6566693

[143] S. Ioffe and C. Szegedy, "Batch normalization: Accelerating deep network training by reducing internal covariate shift," *CoRR*, vol. abs/1502.03167, 2015. [Online]. Available: http://arxiv.org/abs/1502.03167

[144] M. Abadi, A. Agarwal, P. Barham, E. Brevdo, Z. Chen, C. Citro, G. S. Corrado, A. Davis, J. Dean, M. Devin *et al.*, "Tensorflow: Large-scale machine learning on heterogeneous distributed systems," *arXiv:1603.04467*, 2016.

[145] D. P. Kingma and J. Ba, "Adam: A Method for Stochastic Optimization," *arXiv e-prints*, p. arXiv:1412.6980, Dec. 2014.

[146] J. F. F. Mendes, R. Dickman, M. Henkel, and M. C. Marques, "Generalized scaling for models with multiple absorbing states," *Journal of Physics A: Mathematical and General*, vol. 27, no. 9, pp. 3019–3028, may 1994. [Online]. Available: https://doi.org/10.1088%2F0305-4470%2F27%2F9%2F017

[147] L. M. Sieberer, M. Buchhold, and S. Diehl, "Keldysh field theory for driven open quantum systems," *Reports on Progress in Physics*, vol. 79, no. 9, p. 096001, aug 2016. [Online]. Available: https://doi.org/10.1088/0034-4885/79/9/096001

[148] S. Choi, J. Choi, R. Landig, G. Kucsko, H. Zhou, J. Isoya, F. Jelezko, S. Onoda, H. Sumiya, V. Khemani, C. von Keyserlingk, N. Y. Yao, E. Demler, and M. D. Lukin, "Observation of discrete time-crystalline order in a disordered dipolar many-body system," *Nature*, vol. 543, no. 7644, pp. 221–225, 2017. [Online]. Available: https://doi.org/10.1038/nature21426

[149] F. M. Gambetta, F. Carollo, M. Marcuzzi, J. P. Garrahan, and I. Lesanovsky, "Discrete time crystals in the absence of manifest symmetries or disorder in open quantum systems," *Phys. Rev. Lett.*, vol. 122, p. 015701, Jan 2019. [Online]. Available: https://link.aps.org/doi/10.1103/PhysRevLett.122.015701

[150] B. Kraus, H. P. Büchler, S. Diehl, A. Kantian, A. Micheli, and P. Zoller, "Preparation of entangled states by quantum markov processes," *Phys. Rev. A*, vol. 78, p. 042307, Oct 2008. [Online]. Available: https://link.aps.org/doi/10.1103/PhysRevA.78.042307

[151] F. Verstraete, M. M. Wolf, and J. Ignacio Cirac, "Quantum computation and quantum-state engineering driven by dissipation," *Nature Physics*, vol. 5, no. 9, pp. 633–636, 2009. [Online]. Available: https://doi.org/10.1038/nphys1342

[152] T. Tomita, S. Nakajima, I. Danshita, Y. Takasu, and Y. Takahashi, "Observation of the mott insulator to superfluid crossover of a driven-dissipative bose-hubbard system," *Science Advances*, vol. 3, no. 12, 2017. [Online]. Available: https://advances.sciencemag.org/content/3/12/e1701513

[153] R. Ma, B. Saxberg, C. Owens, N. Leung, Y. Lu, J. Simon, and D. I. Schuster, "A dissipatively stabilized mott insulator of photons," *Nature*, vol. 566, no. 7742, pp. 51–57, Feb 2019. [Online]. Available: https://doi.org/10.1038/s41586-019-0897-9

[154] M. F. Maghrebi and A. V. Gorshkov, "Nonequilibrium many-body steady states via keldysh formalism," *Phys. Rev. B*, vol. 93, p. 014307, Jan 2016. [Online]. Available: https://link.aps.org/doi/10.1103/PhysRevB.93.014307

[155] F. Verstraete and J. I. Cirac, "Renormalization algorithms for quantum-many body systems in two and higher dimensions," *arXiv preprint cond-mat/0407066*, 2004.

[156] A. Kshetrimayum, H. Weimer, and R. Orús, "A simple tensor network algorithm for two-dimensional steady states," *Nature Communications*, vol. 8, no. 1, p. 1291, Nov 2017. [Online]. Available: https://doi.org/10.1038/s41467-017-01511-6

[157] A. H. Werner, D. Jaschke, P. Silvi, M. Kliesch, T. Calarco, J. Eisert, and S. Montangero, "Positive tensor network approach for simulating open quantum many-body systems," *Phys. Rev. Lett.*, vol. 116, p. 237201, Jun 2016. [Online]. Available: https://link.aps.org/doi/10.1103/PhysRevLett.116.237201

[158] N. Shammah, S. Ahmed, N. Lambert, S. De Liberato, and F. Nori, "Open quantum systems with local and collective incoherent processes: Efficient numerical simulations using permutational invariance," *Phys. Rev. A*, vol. 98, p. 063815, Dec 2018. [Online]. Available: https://link.aps.org/doi/10.1103/PhysRevA.98.063815

[159] N. Malossi, M. M. Valado, S. Scotto, P. Huillery, P. Pillet, D. Ciampini, E. Arimondo, and O. Morsch, "Full counting statistics and phase diagram of a dissipative rydberg gas," *Phys. Rev. Lett.*, vol. 113, p. 023006, Jul 2014. [Online]. Available: https://link.aps.org/doi/10.1103/PhysRevLett.113.023006

[160] C. Carr, R. Ritter, C. G. Wade, C. S. Adams, and K. J. Weatherill, "Nonequilibrium phase transition in a dilute rydberg ensemble," *Phys. Rev. Lett.*, vol. 111, p. 113901, Sep 2013. [Online]. Available: https://link.aps.org/doi/10.1103/PhysRevLett.111.113901

[161] C. Ates, B. Olmos, J. P. Garrahan, and I. Lesanovsky, "Dynamical phases and intermittency of the dissipative quantum ising model," *Phys. Rev. A*, vol. 85, p. 043620, Apr 2012. [Online]. Available: https://link.aps.org/doi/10.1103/PhysRevA.85.043620

[162] J. Jin, A. Biella, O. Viyuela, C. Ciuti, R. Fazio, and D. Rossini, "Phase diagram of the dissipative quantum ising model on a square lattice," *Phys. Rev. B*, vol. 98, p. 241108, Dec 2018. [Online]. Available: https://link.aps.org/doi/10.1103/PhysRevB.98.241108

[163] D. C. Rose, K. Macieszczak, I. Lesanovsky, and J. P. Garrahan, "Metastability in an open quantum ising model," *Phys. Rev. E*, vol. 94, p. 052132, Nov 2016. [Online]. Available: https://link.aps.org/doi/10.1103/PhysRevE.94.052132

[164] A. Hu, T. E. Lee, and C. W. Clark, "Spatial correlations of one-dimensional driven-dissipative systems of rydberg atoms," *Phys. Rev. A*, vol. 88, p. 053627,

Nov 2013. [Online]. Available: https://link.aps.org/doi/10.1103/PhysRevA.88.053627

[165] S. Sachdev, *Quantum Phase Transitions*, 2nd ed.   Cambridge University Press, 2011.

[166] T. E. Lee, H. Häffner, and M. C. Cross, "Antiferromagnetic phase transition in a nonequilibrium lattice of rydberg atoms," *Phys. Rev. A*, vol. 84, p. 031402, Sep 2011. [Online]. Available: https://link.aps.org/doi/10.1103/PhysRevA.84.031402

[167] H. Weimer, "Variational principle for steady states of dissipative quantum many-body systems," *Phys. Rev. Lett.*, vol. 114, p. 040402, Jan 2015. [Online]. Available: https://link.aps.org/doi/10.1103/PhysRevLett.114.040402

[168] V. R. Overbeck, M. F. Maghrebi, A. V. Gorshkov, and H. Weimer, "Multicritical behavior in dissipative ising models," *Phys. Rev. A*, vol. 95, p. 042133, Apr 2017. [Online]. Available: https://link.aps.org/doi/10.1103/PhysRevA.95.042133

[169] R. Uzdin, A. Levy, and R. Kosloff, "Equivalence of quantum heat machines, and quantum-thermodynamic signatures," *Phys. Rev. X*, vol. 5, p. 031044, Sep 2015. [Online]. Available: https://link.aps.org/doi/10.1103/PhysRevX.5.031044

[170] R. Sridhar and R. Jagannathan, "On the q-analogues of the zassenhaus formula for disentangling exponential operators," *Journal of Computational and Applied Mathematics*, vol. 160, no. 1, pp. 297 – 305, 2003, proceedings of the International Conference on Special Functions and their Applications. [Online]. Available: http://www.sciencedirect.com/science/article/pii/S0377042703006332

[171] A. N. Vasil'ev, *The field theoretic renormalization group in critical behavior theory and stochastic dynamics*.   CRC press, 2004.

[172] C. Behan, L. Rastelli, S. Rychkov, and B. Zan, "Long-range critical exponents near the short-range crossover," *Phys. Rev. Lett.*, vol. 118, p. 241601, Jun 2017. [Online]. Available: https://link.aps.org/doi/10.1103/PhysRevLett.118.241601

[173] M. F. Paulos, S. Rychkov, B. C. van Rees, and B. Zan, "Conformal invariance in the long-range ising model," *Nuclear Physics B*, vol. 902, pp. 246 – 291, 2016. [Online]. Available: http://www.sciencedirect.com/science/article/pii/S0550321315003703

[174] P. Grassberger and A. de la Torre, "Reggeon field theory (schlögl's first model) on a lattice: Monte carlo calculations of critical behaviour," *Annals of Physics*, vol. 122, no. 2, pp. 373 – 396, 1979. [Online]. Available: http://www.sciencedirect.com/science/article/pii/0003491679902070

[175] F. Landes, A. Rosso, and E. Jagla, "Tuning spreading and avalanche-size exponents in directed percolation with modified activation probabilities," *Phys. Rev. E*, vol. 86, p. 041150, Oct 2012. [Online]. Available: https://link.aps.org/doi/10.1103/PhysRevE.86.041150

초 록

최근 차가운 원자 가스 실험의 발전은 열린 양자 다체계 시스템에서 비평형 상전이를 연구 할 수 있는 환경을 제공했다. 이러한 비평형 상전이는 양자 요동(결맞은 해밀토니안)과 고전적인 요동(비결맞은 소실) 사이의 경쟁에서 비롯한다. 이와 관련하여 시스템이 양자 요동이 관련있는 새로운 보편성 군을 볼 수 있을지에 대한 근본적인 질문이 있었다. 만일 보편성이 새로운 보편성을 보이지 않는다면, 고전적인 보편성으로 될 것이고 이것은 양자-고전 매핑에 의해 설명 될 수 있다. 이 질문에 대한 많은 연구들이 진행되었지만, 아직 완전히 이해되지 않았다.

본 학위논문에서 우리는 디렉티드 스미기 군에 속하는 고전적인 접촉 과정 모델의 일반화인 양자 접촉 과정의 다체계 물리학을 고려함으로써 이 질문에 대해 탐구하려고 한다. 디렉티드 스미기 군은 고전적인 비평형 계에서 많은 모델이 속하고 잘 연구 된 보편성 군이다. 양자 접촉 과정은 디렉티드 스미기 군에 추가적으로 양자 과정이 있으므로 이러한 양자 효과로 인해 새로운 보편성으로 바뀔 수 있다. 또한 양자 접촉 과정은 극저온 리드버그 원자 계에서 실험적으로 구현 가능하다.

구체적으로 본 학위 논문에서는 최근 양자 접촉 과정에서의 임계 현상을 다룬다. 먼저, 쌍극자 상호 작용하는 리드버그 원자의 실험에서의 구현 가능성을 통해 우리는 먼거리 상호 작용하는 양자 접촉 과정을 연구한다. 일반적으로 보편성의 관점에서 봤을 때, 먼거리 상호 작용하는 계는 단거리 상호 작용하는 계와 다른 보편성 군을 갖는다. 이와 관련하여 우리는 먼거리 상호 작용이 관련있는 구간에 대해 새로운 고전적 보편성이 얻어지는 것을 발견하였고 이를 "먼거리 삼중 임계 스미기 군"라고 불렀다. 먼거리 상호 작용이 관련이 없는 영역의 경우 먼거리 모델의 평균 장 위상 다이어그램은 단거리 상호작용하는 양자 접촉 과정의 상 다이어그램에 해당한다. 다음으로, 우리는 장거리 상호 작용하는 삼중 디렉티드 스미기 군의 낮은 차원 물리를 재규격화 군과 몬테 카를로 시뮬레이션을 이용하여 공부한다. 먼거리 상호 작용의 강도에 따라 평균장 먼거리 삼중 임계 스미기 군에서 단거리 삼중 임계

스미기 군으로 연속적으로 바뀌는 것을 확인 했다.

　일차원과 이차원 양자 접촉 과정을 탐구하기 위해, 우리는 기계 학습과 양자 점프 몬테카를로 시뮬레이션과 텐서 네트워크 같은 양자 시뮬레이션을 이용했다. 우리는 일차원에서 양자 스미기 군에서 디렉티드 스미기 군으로 바뀌는 교차 구간을 발견했다. 이 교차 구간은 양자적인 과정이 임계 현상에 관련이 있는 것을 보여준다. 또한, 우리는 이러한 교차 구간을 확인할 실험적인 구성을 제안 했다.

　추가적으로 우리는 소실 양자 상전이의 평균장 현상을 모두 연결된 그래프에서의 순열 대칭을 이용하여 탐구하였다. 구체적으로 우리는 소실 양자 이징 모델, 소실 XY 모델, 양자 접촉 프로세스를 고려하였다. 소실 양자 이징 모델에 대해 모든 영역에서 연속 상전이를 보았고 소실 XY 모델에서는 불연속 상전이를 보았다. 이는 켈디쉬 방법과는 상반되는 결과이고 요동없는 평균장 이론의 방법과 일치한다. 또한 양자 접촉 프로세스의 상전이는 준고전적 방법을 이용한 풀이와 상전이 선과 보편성은 일치했지만, 일차원 양자 접촉 프로세스에서 본 것과 같이 교차 구간을 확인했다. 최종적으로 우리는 양자 접촉 과정의 평균장과 낮은 차원에서의 상전이 다이어그램을 보였다.